



**Investigation of atomic and molecular  
fluorescence spectroscopy of helium in  
different pressures and temperatures using  
a corona discharge**

Thesis submitted for the degree of  
Doctor of Philosophy  
at the University of Leicester

by  
Naghham Muhee Kadhum Shiltagh  
Department of Physics and Astronomy  
University of Leicester

June 2018

# Investigation of atomic and molecular fluorescence spectroscopy of helium in different pressures and temperatures using a corona discharge

Naghm Muhee Kadhum Shiltagh

## Abstract

Fluorescence spectroscopy is a powerful tool for obtaining information on microscopic processes in discharge (corona) plasmas in dense media, such as high pressure supercritical gases and even liquids. Spectroscopic observations of the light emitted from an ionization zone near a tip electrode can be used to determine structural information of the local environment of the emitting atoms or molecules. The spectra observable are sensitive to the immediate surroundings of the emitting species, making them useful for the study of cold non-equilibrium plasmas at varying pressures and temperatures.

The aim of this project is to further our understanding of helium ( $^4\text{He}$ ) in different phases, providing information to help understand the nature of the interaction between the helium atoms within this environment.

In this work, spectra have been recorded for a corona discharge in gaseous and liquid helium. The experimental conditions covered a wide region of thermodynamic states in two different designs. The first experiment was carried out at cryogenic temperatures at 3.8, 4.0, 4.5 and 5.0 K under a range of pressure (0.1-5.0 bar). The second set of experiments were carried out at room temperature with range of pressures 0.1-30 bar. Several thousand spectra were recorded in the visible and near-infrared regions. Analyses were conducted on spectra including the atomic  $3s\ ^1S \rightarrow 2p\ ^1P$  and  $3s\ ^3S \rightarrow 2p\ ^3P$  transitions. These transitions showed line shifts, spectral broadening and intensity changes that were dependent on the magnitude of the pressure and temperature, and therefore on the thermodynamic phase. In addition to atomic lines, rotationally-resolved molecular emission bands arising from the  $d\ ^3\Sigma_u^+ \rightarrow b\ ^3\Pi_g$  and  $D\ ^1\Sigma_u^+ \rightarrow B\ ^1\Pi_g$  transitions of the electrically excited helium dimer (excimer),  $\text{He}_2^*$ , were recorded.

Remarkably, and similarly to the analysis of atomic lines, the molecular (excimer) emission showed sharp and distinct lines at low temperature in the region below the saturated vapor pressure (SVP) of helium. However, lineshifts, linewidths and line intensities of the excimers increased strongly upon an increase in pressure, indicating that solvated  $\text{He}_2^*$  in the liquid phase exhibits hindered rotation. The rotation of excimers

within the liquid phase was attributed to the location of the excimer within a large bubble.

A further interesting observation was the abrupt changes of lineshift and linewidths with pressures that occurred by crossing the SVP curve for both atomic and molecular transitions. A model was developed to explain this in which clusters form around excimers and excited helium atoms before the helium liquefies.

In a separate application of the corona discharge, it was employed to make plasmas from a mixture of pure air and perfume. The idea here was collecting spectra of this mixture with and without helium to explore and understand some of the emitted species generated in this mixture of plasmas at atmospheric pressure and to the first time.

# Acknowledgements

All praises to Almighty ALLAH who gave me the courage and strength to complete this project.

To my parents, brothers and sisters who are the dearest to me, great thanks for him with their support and prayers.

My greatest appreciation and thanks to my beloved husband Naseer who gives me unlimited moral support, encouragement and attention.

I would like to express my very great appreciation to Dr. Klaus von Haefen, Dr. Steve Baker and Prof. Andrew Ellis for their supervision, valuable suggestions and guidance throughout my PhD. I gratefully acknowledge Mr Stuart Thornton for his unlimited assistance throughout all time of my experimental work. I would also like to extend my great thanks to Dr. Mark Watkins for his assistance in the lab for the second experiment in my project and for his help with proofreading this thesis.

Many thanks to the staff of the mechanical workshop; Andrew Underhill, Nick Boldra and Phil Stapleton in the Physics Department, University of Leicester for the manufacture of the most of parts of experiments. I acknowledge Phil Worth, Nigel Fisher and Kiri Humphreys for their clerical support during my PhD. Also, I would also like to extend my great thanks to Mr Ray McErlean and, Dipali Thanki to help me in issues of programs and software installer and for and, Dipali Thanki to help me from the Electrical Support Laboratory, and for all staff in Physics Department

I acknowledge my friends in Condensed Matter Physics group Luis Guillermo Mendoza for his assistance, also for Mümin Mehmet Koç, Mustafa Şükrü Kurt, Hanieh Yazdanfar and Michael McNally and all members of the CMP group.

I dearly thank my friend and colleague Dr. Khawla Tahir from University of Karbala in Iraq for her kind and help to finish my own official issues in Karbala University.

I would like to give my special thanks to the Ministry of Higher Education and Scientific Research in Iraq for giving me to opportunity to get study for my PhD in the UK and for funding this project. Without their support, I was not have been able to afford or complete this research. Great thanks also to the Iraqi Cultural Attaché in London for their support.

I would like to express my deep gratitude to the Department of Physics, College of Science, University of Karbala to support me through my PhD study.

# Contents

<b>Chapter 1 Introduction</b>	<b>1</b>
1.1 Helium and its general properties	1
1.2 Properties of superfluid helium	3
1.3 Rotational spectroscopy in Superfluid He	5
1.4 Rotational spectroscopy of excimer in LHe	8
1.5 Objectives and thesis overview	12
<b>Chapter 2 Theoretical background</b>	<b>14</b>
2.1 Rotational Spectroscopy of Diatomic Molecules	14
2.2 Molecular spectra	16
2.2.1 Total energy of the diatomic molecule	17
2.2.2 Vibrational structure of the electronic transition	17
2.2.3 Rotational structure of non-rigid rotator	18
2.2.4 Rotational-Vibrational interaction for a rotor	18
2.3 Electronic structure of diatomic molecule	19
2.4 Classification of electronic states-Structure multiplet	20
2.5 Hund's coupling cases of the rotations and electronic motion	22
2.5.1 Hund's coupling case (b)	23
2.5.2 Hund's coupling case (d)	23
2.6 Generation of electronic excitation in bulk He	24
2.6.1 A corona discharge	24
2.6.2 Excited helium atom and molecule (Excimers)	25
2.7 Electronic structure of the He transitions	27
2.7.1 Atomic lines	27
2.7.2 Molecular band	28
2.7.2.a Electronic structure of $D \ ^1\Sigma_u^+ \rightarrow B \ ^1\Pi_g$ transition	29
2.7.2.b Electronic structure of $d \ ^3\Sigma_u^+ \rightarrow b \ ^3\Pi_g$ transition	29
2.8 A bubble formation around $\text{He}_2^*$ and $\text{He}^*$ embedded in LHe	31
<b>Chapter 3 Experimental and Measurement Techniques</b>	<b>32</b>
3.1 Part I- Cryogenic temperature experiment	32
3.1.1 General description of the cryogenic system	33
3.1.2 HelioxAC-V $^3\text{He}$ Refrigerator	34

3.1.3	Heat transfer by radiation and conduction	36
3.1.4	Vacuum pump and minimization of convection	39
3.1.5	Operation HelioxAC-V <sup>3</sup> He Refrigerator	42
3.1.6	Gas installation and pressure measurement	43
3.1.7	ITC Temperature Controller and thermometer	45
3.1.8	High pressure cryogenic cell and components	47
3.1.9	The Optical Layout	51
3.1.10	The electrical layout	53
3.1.11	Assembly of the experimental setup	54
3.1.12	Experimental procedure	60
3.1.13	Methodology of the data collection	61
3.2	Part II- Room temperature experiment	66
3.2.1	High pressure cell at room temperature	66
3.2.2	Electrodes configuration with A Lumina Ceramic tube	67
3.2.3	Optical layout	69
3.2.4	Assembly of the setup of experiment &	71
<b>Chapter 4 Results and discussion</b>		<b>75</b>
4.1	Introduction	77
4.2	Experimental data	78
4.3	Treatment of the spectra	80
4.3.2	Glow discharge spectra as a reference and calibration	83
4.4	Atomic Fluorescence	86
4.5.1	Line-Shift versus pressure	89
4.5.2	Linewidth versus pressure	93
4.5.3	Line Intensity versus pressure	98
4.6	Prospective phase transition of He for different parameters	101
4.7	Discussion	102
4.8	Error determination for the data	105
4.9	Theoretical treatment using the Static Approximation	107
4.11	Conclusion and structural model	115
<b>Chapter 5 Results and discussion</b>		<b>119</b>
5.1	Introduction	121
5.2	Experimental data of Molecular bands	122
5.3	Treatment of the spectra	123
5.4	Molecular band	125

5.4.1	$d\ ^3\Sigma_u^+ \rightarrow b\ ^3\Pi_g$ transition	130
5.4.2	$D\ ^1\Sigma_u^+ \rightarrow B\ ^1\Pi_g$ transition	137
5.4.3	Analysis of the $D\ ^1\Sigma_u^+ \rightarrow B\ ^1\Pi_g$ transition	139
5.5	Predicted phase transition of the SVP of LHe	145
5.6	Conclusion and general observations	147
5.7	Error determination	150

## **Chapter 6 Results and discussion** **152**

6.1	Introduction	153
6.2	Experimental data	155
6.3	Current and voltage relationship with pressure	157
6.4	Spectral lines of the $3s\ ^1,^3S \rightarrow 2p\ ^1,^3P$ transitions	158
6.5	Analysis of atomic lines	159
6.6.1	Simulation of the triplet 706 nm line	167
6.6.2	Simulation of the singlet 728 nm line	168
6.7	Molecular bands	170
6.8	Analysis of molecular bands	172
6.8.2	A comparison with results at low temperature	173
6.9	Conclusion	177

## **Chapter 7 Results and discussion** **179**

7.1	Introduction	180
7.2	Experimental data	182
7.3	Analysis of Spectra	183
7.3.1	Spectra of air and air plus helium at atmospheric Pressure	185
7.3.2	Spectra of air and air plus perfume plasmas	186
7.3.3	Spectra of air, helium and perfume plasmas	191
7.4	General observations and plan	192

## **Chapter 8 Summary and outlook** **194**

### **Publications and Activities** **197**

### **Appendix** **198**

### **Bibliography** **207**

# List of Figures

1.1 Phase diagram of $^4\text{He}$ at low temperature. . . . .	2
1.2 (a) Andronikashvili's experiment, immersing of pile of disks in LHe, as torsional oscillation to demonstrate the effective division of He II into normal and superfluid components. (b) The two fluid model (normal and superfluid) densities as a function of T. . . . .	4
1.3 Spectra of the $\text{SF}_6$ molecule embedded in $^4\text{He}$ droplets are shown in different sizes. . . . .	5
1.4 Infrared spectra of the OCS molecule in four cases. . . . .	6
1.5 The $d\ ^3\Sigma_u^+ \rightarrow b\ ^3\Pi_g$ and $D\ ^1\Sigma_u^+ \rightarrow B\ ^1\Pi_g$ transitions at high resolution, from spectra of electron-bombarded liquid helium in the (a) gas phase, and (b) liquid phase. . . . .	8
1.6 Luminescence spectroscopy of (A) $^3\text{He}$ and (B) $^4\text{He}$ droplets excited by monochromatic synchrotron radiation at 23.39 eV. . . . .	9
1.7 Fluorescence spectrum showing the $d$ - $b$ and $D$ - $B$ transitions observed in liquid helium at 4.2 K and 1.0 bar by corona discharge. . . . .	10
2.1 Diagram representing the energy levels of a molecule and various transitions . . . . .	16
2.2 Energy level diagram of the rovibrational band with P-, R- and Q-branches transition from the upper state $J'$ to the lower state $J''$ . . . . .	20
2.3 Vector diagram for Hund's case (b) on the left-hand side of the figure, and case (d). . . . .	24
2.4 Diagram of the energy levels of helium atomic lines for the singlet, triplet transitions. . . . .	27
2.5 Diagram of the energy levels that give rise to the molecular bands for the singlet and triplet transitions. . . . .	28
2.6 Energy levels and transitions between the $D\ ^1\Sigma_u$ and $B\ ^1\Pi_g$ states as per Hund's coupling case (b). . . . .	29
2.7 Energy levels and transitions between $d\ ^3\Sigma_u^+$ and $b\ ^3\Pi_g$ states as per Hund's coupling case (b). . . . .	30
3.1 Operation principle of a HelioxAC-V sorption pumped $^3\text{He}$ insert. . . . .	33
3.2 Schematic diagram of the cryostat vacuum and $^3\text{He}$ handling system. . . . .	35
3.3 Schematic diagram of the pumping station shows. . . . .	40
3.4 Photo of pumping cart utilized in experiment shown the main valves that are responsible from evacuation process out OVC. . . . .	41
3.5 Image of the cryostat in the lab, showing the valve system drawn in section 3.2. . . . .	43

3.6 Schematic diagram of the gas installation. . . . .	44
3.7 Detailed image of the ITC503 temperature controller is illustrated. . . . .	46
3.8 Physical description of the plane-tip electrode array. . . . .	48
3.9 Image of macor ceramic piece holding the tip-plane electrodes. . . . .	50
3.10 Cross-sectional view of the discharge region of the high pressure copper cell. . . . .	50
3.11 Schematic diagram of the optical pattern that used in experiment to merge the emitted fluorescence light from inside the cell (vacuum regime) to the out of the chamber . . . . .	51
3.12 Cross section of the optical setup explained mathematically in Fig. 3.10 . . . . .	52
3.13 Circuit diagram of the experiment. . . . .	53
3.14 Image of device used to measure high voltage-current applied to the electrodes . . . . .	54
3.15 Image of cross section of the inner section of fridge showing . . . . .	56
3.16 cross section cryostat after assembling all components . . . . .	58
3.17 The entire experimental setup including the inner section of fridge, gas installation, optical setup and data collection by the computer. . . . .	59
3.18 Images of optical setup outside vacuum chamber to optimize the alignment of emitted light from the cell. . . . .	61
3.19 Images of emitted light nearby to the tip electrode were recorded using the Andor Solis software accompanying the hardware. . . . .	63
3.20 Photo of the tip electrode within the cell was observed during recording the image of the spot of glow discharge. . . . .	64
3.21 A section of the PT diagram for the gaseous and liquid phases in the experiment. . . . .	65
3.22 Photos of high pressure cells that used in experiment. . . . .	67
3.23 Cross-sectional view of discharge region of the high pressure stainless steel cell. . . . .	68
3.24 Schematic diagram of optical pattern using in experiment of room temperature . . . . .	70
3.25 Photograph of the optical board showing the optical setup for focussing the light emitted from the cell into the spectrometer. . . . .	71
3.26 The setup of the experimental procedure at room temperature. . . . .	73
3.27 Photos of corona discharges nearby the tip electrode after applying high voltage. . . . .	73
4.1 A section of the PT diagram for the gaseous and liquid phases probed in experiment. . . . .	79
4.2 Fit of atomic line of the $3s - 2p$ singlet and triplet transitions at 3.8 K and 1.3 bar. . . . .	83

4.3 Overview of normalized and calibrated glow discharge spectrum. . . . .	84
4.4 The linear relationship used to calibrate the corona spectra in terms of actual NIST-reported wavelength as a function of row number. . . . .	86
4.5 Fluorescence spectra of gaseous and liquid helium excited by a corona discharge in the region of the atomic $2p^1P_1 \leftarrow 3s^1S_0$ transition of singlet helium. . . . .	87
4.6 Fluorescence spectra of gaseous and liquid helium in the region of the atomic triplet transition $2p^3P_{0,1,2} \leftarrow 3s^3S_1$ . . . . .	88
4.7 Overview of fluorescence spectra of gaseous and liquid helium in the region of atomic triplet transition $2p^3P \leftarrow 3s^3S$ at 4.0 K. Intensities have been normalised. . . . .	89
4.8 Pressure dependence of the $2p^1P \leftarrow 3s^1S$ atomic singlet transition in the gas and liquid phases at 3.8, 4.0, 4.5 and 5.0 K . . . . .	90
4.9 As per Figure 4.7 but for the triplet $2p^3P \leftarrow 3s^3S$ transition . . . . .	91
4.10 Pressure dependence of the linewidth of the $2p^1P \leftarrow 3s^1S$ atomic singlet transition in the gas and liquid phases at 3.8, 4.0, 4.5 and 5.0 K. . . . .	94
4.11 Pressure dependence of the linewidth of the $2p^3P \leftarrow 3s^3S$ atomic triplet transition in the gas and liquid phases at 3.8, 4.0, 4.5 and 5.0 K . . . . .	95
4.12 Shifts for the 706 nm line at 4.2 K at different pressures. . . . .	97
4.13 FWHM of the 706 nm line as a function of pressure at 4.2 K . . . . .	97
4.14 Our results with simulations of lineshift for the singlet 728 nm line at 4.2 K . . . . .	98
4.15 Overview of the spectra for the 3.8 K isotherm at different pressures for the triplet transition at 706 nm and the singlet transition at 728 nm . . . . .	99
4.16 Pressure dependence of the intensity ratio of triplet ( $2p^3P \leftarrow 3s^3S$ ) and singlet ( $2p^1P \leftarrow 3s^1S$ ) lines at 3.8, 4.0, 4.5 and 5.0 K. . . . .	100
4.17 Linewidths and lineshifts (solid blue line and dashed red line, respectively) for the (a) triplet $3s^3-2p^3$ and the (b) singlet $3s^1-2p^1$ transitions . . . . .	102
4.18 FWHM of the 728 nm (on the left-hand side) and 706 nm (on the right-hand side) atomic lines as a function of pressure in gas and liquid helium. . . . .	111
4.19 Comparison between measured lineshifts and theory for the singlet line at 728 nm and the triplet line at 706 nm as a function of pressure. . . . .	114
4. 20 Schematic diagram of an excited helium atom $He^*$ . . . . .	118
4. 21 Schematic diagram of excited helium atom $He^*$ enclosed in a bubble that has formed cluster with ground state helium atoms in the gas phase before <i>SVP</i> . . . . .	118
5.1 Fit of spectra using Lorentzian functions provided in the Fityk program . . . . .	125

5.2 Selection of spectra of He <sub>2</sub> <sup>*</sup> in helium as a function of pressure for four isotherms . . .	127
5.3 Comparison of the $d^3 \Sigma_u^+ \rightarrow b^3 \Pi_g$ and $D^1 \Sigma_u^+ \rightarrow B^1 \Pi_g$ bands at high resolution in the gas and liquid phases . . . . .	128
5.4 Spectra of the triplet d–b transition at 3.8 K as a function of pressure. . . . .	129
5.5 Lineshifts as obtained through fitting with Lorentzians . . . . .	131
5.6 As a consequence of fitting with Lorentzians, linewidths can be obtained as a function of pressure of the triplet d-b transition for different isotherms. . . . .	134
5.7 Pressure dependence of the intensity ratio of the Q branch and averaged P lines . . .	136
5.8 Spectra of He <sub>2</sub> <sup>*</sup> in helium as a function of pressure for four isotherms. . . . .	138
5.9 Lineshifts gained by fitting with Lorentzian lineshapes as a function of pressure. . .	140
5.10 Pressure dependence of the linewidth of the Q- and P <sub>avg</sub> branches features. . . . .	142
5.11 Pressure dependence of the line intensity ratio of the Q branch and the P(2) line . .	144
5.12 Hypothetical phase diagram for the excimer-helium mixed system showing the comparison between the saturated vapour pressure (SVP) of pure <sup>4</sup> He . . . . .	146
5.13 Schematic diagram of excited helium molecule (He <sub>2</sub> <sup>*</sup> excimer) in different species. . . . .	150
6.1 Overview of the spectra of He gas at 300 K and up to 26 bar of pressure . . . . .	155
6.2 Expanded wavelength range from Fig. 6.1. . . . .	156
6.3 Voltage versus current as a function of pressure at room temperature. . . . .	158
6.4 Spectra of atomic lines of the singlet and triplet 3s-2p transitions at 300 K. . . . .	159
6.5 Fluorescence spectra of helium excited by a corona discharge at 300 K in the region of the atomic 3s1S→2p1P transition of singlet and triplet transition 3s3S→2p3P. . . . .	160
6.6 Pressure dependence of the 3s 1,3S→2p 1,3P atomic singlet and triplet transitions as a function of pressure at room temperature . . . . .	161
6.7 Pressure dependence of the linewidth of the 3s <sup>1,3</sup> S→2p <sup>1,3</sup> P atomic singlet and triplet transition at 300 K . . . . .	162
6.8 Pressure dependence of the intensity ratio of the triplet 706 nm and singlet 728 nm lines at 300 K. . . . .	162
6.9 Comparison of lineshifts observed for the atomic triplet line as function of pressure. . . . .	163
6.10 Comparison between the lineshifts that measured low temperatures and 300 K as a function of pressure for the singlet line. . . . .	164
6.11 Linewidth as a function of pressure for the singlet line for measurements at cryogenic temperatures and at room temperature . . . . .	164

6.12 Comparison of the lineshifts for the 706 nm line as a function of pressure. . . . .	165
6.13 Comparison of the linewidths for triplet 3s-2p transition as a function of pressure. .	166
6.14 Linewidth of the 706 nm line of helium gas at 300 K and various pressures. . . . .	166
6.15 Lineshift of the 706 nm line as a function of pressure of the helium gas at 300 K. .	169
6.16 Broadening of the 728 nm line of helium gas at 300 K at different pressures. . . .	169
6.17 Lineshifts of the 728 nm line as a function of pressure of helium gas at 300 K . . .	171
6.18 Spectra of the triplet d-b and singlet D-B transitions of the He <sub>2</sub> <sup>*</sup> excimer as a func- tion of pressure at room temperature. . . . .	171
6.19 Lineshifts and lonewidths as obtained by fitting with Lorentzians at 300 K. . . . .	172
6.20 Pressure dependence of the intensity ratio of the Q-branch and P <sub>avg</sub> -branch excluding P(2), for 3.8, 4.0, 4.5, and 5.0 K. . . . .	174
6.22 Measurements of linewidth as a function of pressure in different temperatures for the singlet D-B and triplet d-b transitions. . . . .	176
6.23 Comparison of the lineshift for the 706 nm line as a function of pressure between previous and the current studies at low and room temperatures. . . . .	176
7.1 The emission spectrum obtained by atmospheric-pressure glow discharge (APGD) at 0.5 and 1 atm at 300 K. . . . .	184
7.2 Overview of spectra at room temperature of the plasma of pure helium at 1 bar. .	185
7.3 A comparison between the spectrum of air and spectrum of an unspecified perfume and air mixture at atmospheric pressure . . . . .	186
7.4 High resolution spectrum of the range 350-400 nm of Fig . . . . .	187
7.5 Typical emission spectra of air and perfume at atmospheric pressure from a corona discharge in the UV, visible and NIR regions (300-1000 nm). . . . .	190
7.6 Development of the spectra for atmospheric pressure glow discharges of different cases of plasma. . . . .	192
Appendix A- Atomic and molecular transitions of helium. . . . .	197
Appendix B- Potential energy curves for states of He <sub>2</sub> . . . . .	198
Appendix C- Drawing of copper high pressure cell (low temperatures) . . . . .	199
Appendix D.1- Technical drawings of the tip bearer electrodes. . . . .	200

Appendix D.2- Technical drawings of the flat electrodes . . . . .	201
Appendix E- High-Voltage monitor. . . . .	202
Appendix F- Drawing of stainless steel cell (room temperature). . . . .	203
Appendix G- The standard error deviation data for the simulation treatment of the line-shifts for the atomic singlet and triplet transitions. . . . .	204
Appendix H- The standard error deviation data for the simulation treatment of the line-widths for the atomic singlet and triplet transitions . . . . .	205
Bibliography . . . . .	206

# Chapter 1

## Introduction

### 1.1 Helium and its general properties

Helium (He) is a chemical element and inert gas belonging to the group of the noble gases from the periodic table. Helium is characterized by being an odourless, a tasteless, colourless, non-toxic, and the second-lightest element. The boiling point of helium is the lowest among all the elements at 4.2 K, and has a critical point of 5.2 K. Helium exists as two stable isotopes,  $^3\text{He}$  and  $^4\text{He}$ , but  $^4\text{He}$  is the most abundant type at roughly  $10^6$  times greater than  $^3\text{He}$  [16]. Liquid helium has fascinated scientists and led to much research in condensed matter physics. This is due to its extensive quantum-like behaviour caused by its small mass and the weak interaction between its atoms, keeping it liquid down to absolute zero [17]. Moreover, helium-4 ( $^4\text{He}$ ) is unique due in having two liquid forms [18] that are:

#### 1.1.1 Helium I (He I)

This kind is a normal liquid and is called helium I (He I). It exists below the critical temperature ( $\sim 5.2$  K) down to the lambda temperature<sup>1</sup> ( $T_\lambda$ ) of  $\sim 2.17$  K; i.e.,  $2.17 \text{ K} < T < 5.2 \text{ K}$ . He I has a very low viscosity and a density of 0.145–0.125 g/mL (between about 0 and 4 K) [2].

#### 1.1.2 Helium II (He II)

Interestingly, below  $T_\lambda$  ( $0 \text{ K} < T < 2.17 \text{ K}$ ), the onset of superfluidity occurs, where the thermal conductivity of helium-4 becomes more than  $\sim 100$  times greater than that of copper or silver [19, 20]. This form of liquid is called He II [2].

So consequently, the two kinds of liquid helium (LHe) or two phases that are distinguished by the labels He I and He II are separated by the lambda line ( $\lambda$ ) as shown in Fig. 1.1.

---

<sup>1</sup>  $T_\lambda$  so named because the shape of the corresponding specific heat anomaly is similar to a Greek lambda.  $T_\lambda$  has a value at saturated vapour pressure (SVP) of 2.17 K that upon increased pressure decreases to 1.80 K at the solidification point.

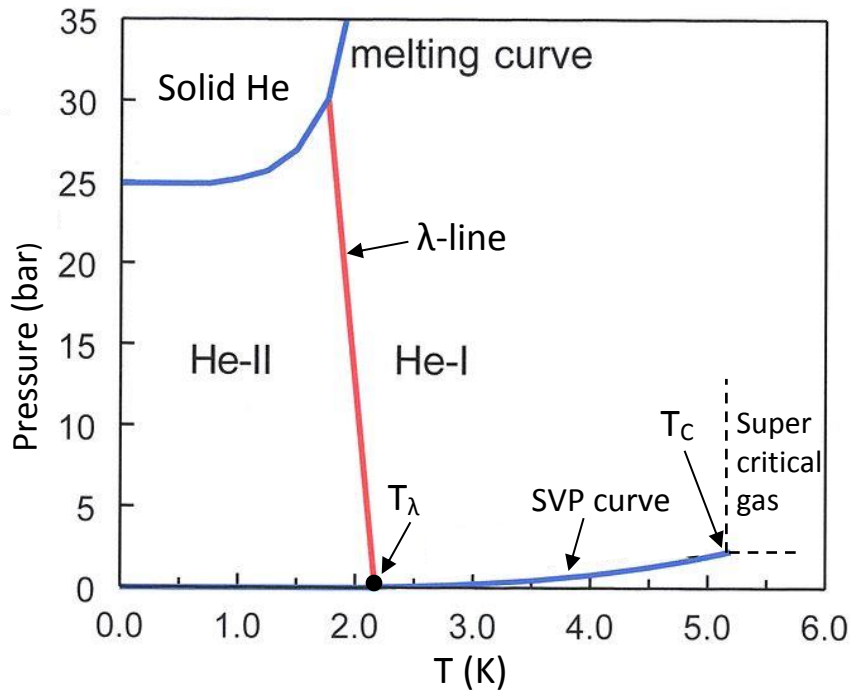


Figure 1.1: Phase diagram of  $^4\text{He}$  at low temperature. He-I represents normal liquid helium and He-II designates superfluid liquid helium.  $T_c$  is the critical temperature after there is only a gas phase called the super-critical phase. This diagram was reproduced from reference [2].

One might well ask why this feature of helium being liquid at low temperatures occurs. This is due to the extremely weak interatomic forces between helium atoms. Indeed, the helium atom possesses the structure of an inert gas [21], including two electrons forming a closed K shell. The electric dipole fluctuation between a pair of helium atoms has the smallest polarizability of any atom, and therefore this weak van der Waals force is the only attraction between a pair of helium atoms [18]. Moreover, due to the low He-He potential well depth with its large zero point energy [22], helium does not solidify under its own vapour pressure, even at absolute zero, unless the pressure is increased to more than 25 bar, which will ultimately obtain the solid phase [20].

## 1.2 Properties of superfluid helium

As mentioned, at the lambda point of 2.17 K, superfluidity can be obtained. Superfluidity in helium-4 was discovered by the Russian physicist Pyotr Leonidovich Kapitsa in the 1930s [21]. There is no other liquid that behaves in this manner, except the other lighter isotope of helium ( $^3\text{He}$ ) at low temperature ( $T < 3$  mK), which was first observed

by Douglas D. Osheroff, David M. Lee, and Robert C. Richardson of the United States in 1972 [23]. The nature of a superfluid arises from the bosonic character of  $^4\text{He}$  atoms (they have zero nuclear and electronic spins). However,  $^3\text{He}$  is fermionic on account of a net nuclear spin of  $\frac{1}{2}$  (due to having two protons and only one neutron) [24].

Superfluidity implies that liquid helium has a small viscosity (which is almost non-existent), where helium flows through surfaces against the force of gravity [20]. This is due to the low resistance to flow, allowing microscopic objects to be mobile within the LHe without friction. The first phenomenon of superfluidity is superconductivity, which was discovered by H. Kamerlingh Onnes in Leiden in 1911 [20]. He II possesses numerous other unusual and interesting properties, such as the thermomechanical (fountain) effect, the mechanocaloric effect and quantized vortices [25].

The next indication relates to the model of two fluid densities which was initially explored by Tisza in 1947 [26], after which an accurate description was proposed by Landau [21], as shown in Fig. 1.2 (b), that can be summarized as follows;

- a) He II behaves as though it is a mixture of two separate fluids: a normal fluid component and a superfluid component.
- b) The two fluids interpenetrate freely, passing through each other fully without any interaction.
- c) The total density  $\rho$  of the liquid is made up of the sum of the densities of the two components, so that:

$$\rho = \rho_n + \rho_s \dots \dots \dots (1.1)$$

Where  $n$  and  $s$  denote to quantities of the normal fluid and superfluid respectively. From Fig. 1.2 (b) we will find that:  $\rho_n = 0$  at  $T = 0$  and,  $\rho_n = \rho$  at  $T = T_\lambda$

- d) The superfluid component possesses no entropy and no resistance to flow whatsoever, indicating its viscosity is identically zero and no turbulence is produced within it. However, the normal fluid carries the whole entropy content  $S$  of the liquid and has an infinite viscosity [20, 26].

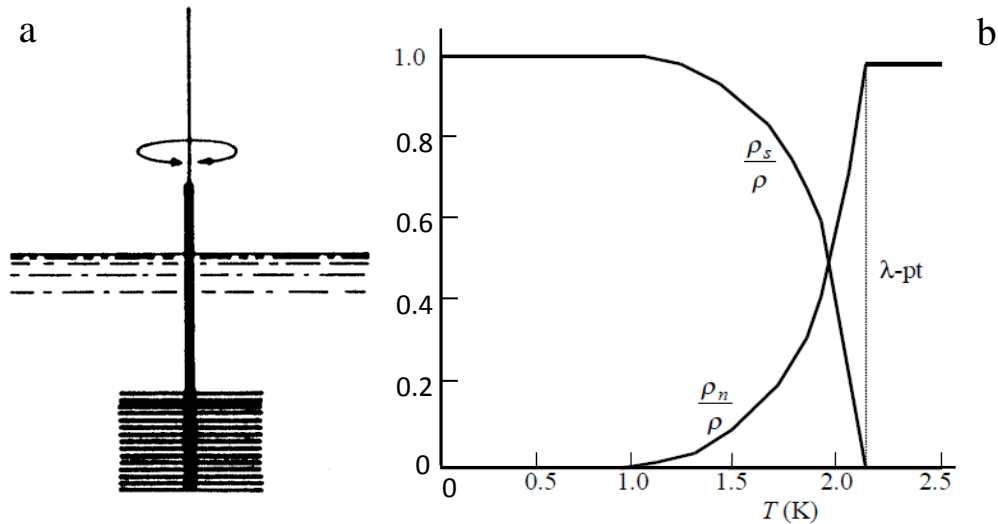


Figure 1.2: (a) Andronikashvili's [1] experiment, immersing of pile of disks in LHe, as a torsional oscillation to demonstrate the effective division of He II into normal and superfluid components. (b) The two fluid model (normal and superfluid) densities as a function of temperature. It can be seen that the sum of densities is constant according to eq. 1.1. The normal and superfluid densities are divided by the total density of system. This figure was taken from ref. [11].

The density of the normal fluid as a function of temperature was investigated by Andronikashvili in one of the most important experiments conducted on helium in 1946 [27] that confirmed Landau theory about the division of the liquid into two components. This experiment defined the torsional oscillations, and consisted of a stack of thin metal disks spaced about 0.2 mm apart from each other and immersed in LHe [1] as shown in Fig. 1.2 (a). It was observed that the normal fluid, which was confined between the discs due to their close spacing, constrained the discs to oscillate and increased the moment of inertia of the pendulum. However, the superfluid had no effect on the moment of inertia or on the period of oscillation, hence the rotation of the disks was consistent. Thus, by measurements of the period of oscillation, first-hand evidence for the dependence of the normal fluid density on temperature was provided [11, 18, 27].

### 1.3 Rotational spectroscopy in Superfluid He

The electronically excited states of condensed helium have attracted considerable attention in the literature. Unlike the other condensed rare gases, the spectra of helium clusters, droplets and liquid helium show discrete, atomic- and molecular-like features [9, 28]. The ability to investigate superfluidity in helium-4 at the nanoscale using single

molecules as probes for rotational motion at low temperatures provides a considerable amount of detail about molecular interactions. The first attempts to immerse ions and electrons in LHe II [29] were undertaken in the 1930s [30]. For instance, X-ray and radioactive sources [31] were used to produce electrons and ions of  $\text{He}^+$  in LHe in 1943. After that, in the early 1990s, an alternative means was proposed for studying dopants in superfluid helium by using nanoscale helium droplets [32]. For example, in 1995, the first rotationally resolved Infrared spectra were observed by J. P. Toennies and coworkers for molecules of sulphur hexafluoride ( $\text{SF}_6$ ) embedded within a liquid helium cluster of around 20000 atoms, and excited by a diode laser. In this experiment, sharp and discrete spectral lines were displayed indicating the free rotation and superfluidity of the  $^4\text{He}$  droplets and providing experimental evidence for the cluster temperature, which was 0.37 K [32, 33] as shown in Fig. 1.3.

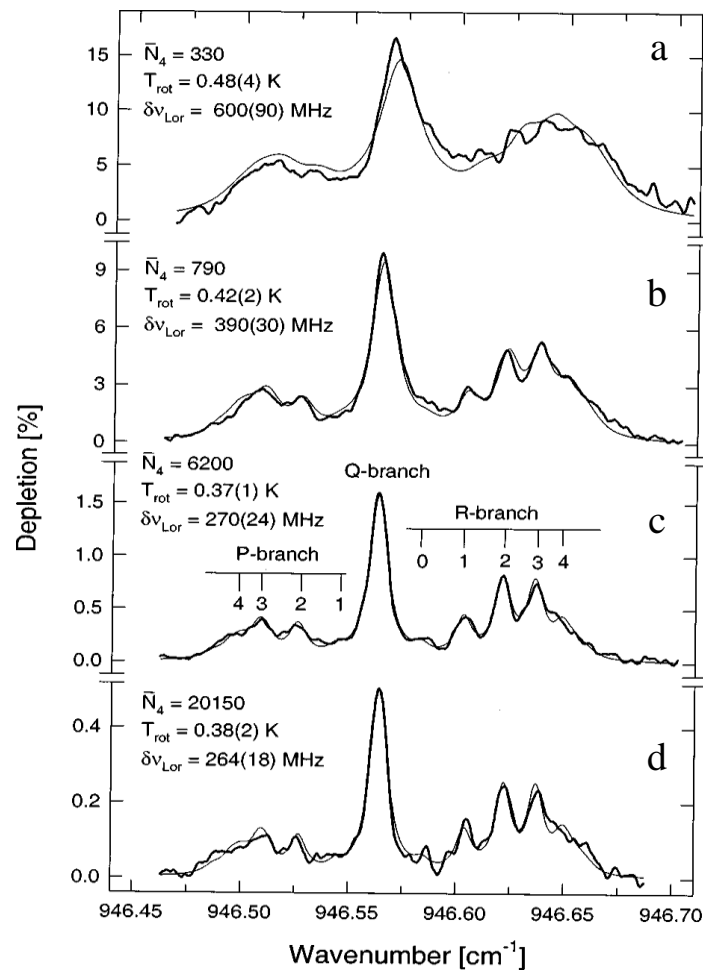


Figure 1.3: Spectra of the  $\text{SF}_6$  molecule embedded in  $^4\text{He}$  droplets are shown in four different sizes,  $N_4$ , where the size increases from  $3.3 \times 10^2$  to  $2 \times 10^4$  as presented from panel (a) to (d) with a reduction in the source temperature ( $T_0$ ) from 26 to 14.5 K under pressure ( $P_0$ ) = 44 bar. The individual rotation-vibrational lines of the P and R branches are observed in spectrum (c). The rotational temperatures  $T_{\text{rot}}$  and the widths  $\delta v_{\text{Lor}}$  (FWHM) of the line profiles were yielded by the simulations of the spectra plotted in thin solid lines. This figure is taken from Fig.1, ref. [10].

Furthermore, additional proof to test the superfluid nature of  $^4\text{He}$  droplets was reported by Grebenev *et al.*[34] in 1998, when a carbonyl sulphide (OCS) molecule was embedded in  $^4\text{He}$  droplets and sharp rotational lines in the infrared vibration-rotation spectrum of OCS were observed. However, by repeating the same experiment but this time with pure  $^3\text{He}$  droplets, it was realized that the rotational structure had broadened to the point of being unresolved. This was interpreted to be due to the non-free rotation of OCS with  $^3\text{He}$  droplets, which was attributed to a normal liquid state. This experiment went further by adding  $^4\text{He}$  atoms to a mixture of  $^3\text{He}$  with the OCS molecule to find that a sharp spectrum was recovered after adding 60 atoms [34, 35]. The conclusion from this experiment is that to achieve superfluidity, the minimum number of  $^4\text{He}$  atoms required is 60 atoms, as shown in Fig. 1.4. The appearance of sharp rotational spectra of a single molecule was proposed to be a microscopic manifestation of  $^4\text{He}$  superfluidity [12, 13].

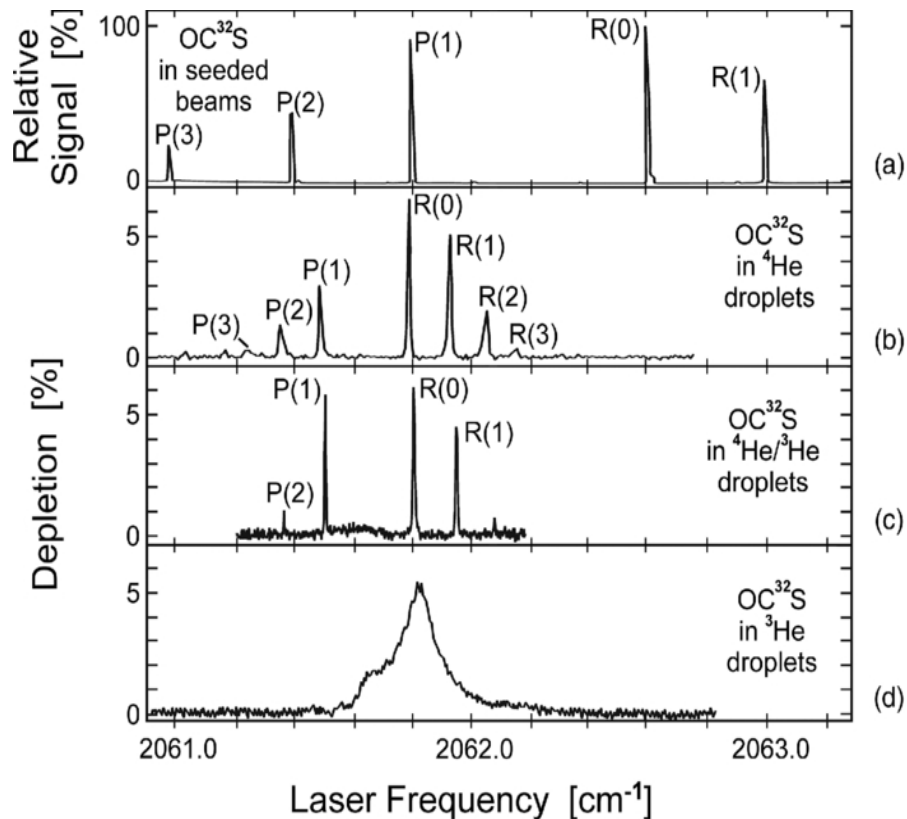


Figure 1.4: Infrared spectra of the OCS molecule in four cases: panel (a) spectrum of single OCS molecule in an Ar seeded beam. (b) The spectrum in a pure  $^4\text{He}$  droplet where the size of the droplet is around  $N_4 \approx 3 \times 10^3$ . (c) The OCS molecule immersed in size of a mixed  $^4\text{He}/^3\text{He}$  droplet ( $N_4 \approx 10^3$ ,  $N_3 \approx 104$ ). The spectrum in (d) was in a pure  $^3\text{He}$  droplet ( $N_3 \approx 12 \times 10^3$ ). The moment of inertia increases by a factor of 2.8 in going from the free rotation of the molecule in panel (a) to the molecule in  $^4\text{He}$  in panel (b) [12]. The figure is taken from Fig. 1 in ref. [13, 14].

In view of these exciting features and the distinct temperature effects in helium droplets mentioned above, this would seem a very promising starting point from which to perform rotationally resolved spectroscopy with control over a wide range of temperatures, beyond 0.15 and 0.4 K, particularly in combination with pressure control and thermodynamic phase. However, this control is difficult to accomplish in helium droplets in a free beam. Therefore, a solution using bulk helium is of more benefit and it is relatively straightforward to achieve such conditions.

On the other hand, embedding single foreign molecules directly into bulk helium is rather challenging to prove. This is because at low temperatures in helium, all other substances will be frozen to the wall of the container [36], so the question arises as to how this problem can be tackled; clearly, additional sophisticated techniques are required [37-39]. The solution to this problem was achieved by creating molecules and atoms from the helium itself, as shown in the next section.

## 1.4 Rotational spectroscopy of excimer in LHe

As mentioned, to overcome the above problem, the generation of short-lived helium excimers ( $\text{He}_2^*$ ) as single-molecule probes represents an alternative way to embed molecules in liquid helium.

An excimer (originally the terminology for an excited dimer) is a short-lived dimeric molecule that is often diatomic and composed of two atoms or molecules that would not bond if both were in the ground state [40]. The lifetime of an excimer is generally very short, in the order of nanoseconds [41]. Binding a larger number of excited atoms to form Rydberg matter clusters can extend the lifetime to exceed many seconds - see the formation and decay of excimers in chapter 2.6.2. The first singlet excimer was identified from that of helium (He) when an intense continuum line of between 60 and 100 nm wavelength was observed by Hopfield (1930) [42-44], in the vacuum ultraviolet emission spectrum of a high-pressure helium discharge. This was attributed to a transition from an excited dimer He to the dissociated ground state.

The atomic and molecular fluorescence spectra consist of a series of lines that result from allowed radiative transitions between different electronically excited states [40]. The coupling between the excited helium atom ( $\text{He}^*$ )/excited helium molecule ( $\text{He}_2^*$ ) and the surrounding liquid helium was studied using the techniques of optical absorption and fluorescence spectroscopies. The emitting  $\text{He}^*$  and  $\text{He}_2^*$  species are common forms

of excitations in bulk superfluid helium that have been used recently [45-48] and in the past to probe the bulk phases of helium by imaging [49].

In the 1970s, several researchers studied the optical absorption and emission spectra of excimers in LHe, in particular in the visible and near infrared spectral range due to its intensity in these regions. Different methods were used to excite LHe; in some of these studies this was achieved by bombarding bulk superfluid helium with a 160 keV electron beam [9, 50-53]. However, most of these investigations were just absorption rotational spectroscopy, but not emission spectroscopy, even if, like Soley and Fitzsimmons, some transitions were not resolved in the emission such as  $d^3\Sigma_u^+ \rightarrow b^3\Pi_g$  and  $D^1\Sigma_u^+ \rightarrow B^1\Pi_g$  transitions [53].

Further investigation by Dennis and co-workers considered the infrared emission spectra of electron-bombarded LHe. Though rotational emission pertaining to the  $D$ - $B$  and  $d$ - $b$  transitions was readily observed in the gas spectra, but it was not observed for the liquid phase of helium, as shown in Fig. 1.5; more details about these molecular transitions can be found in chapter 5.

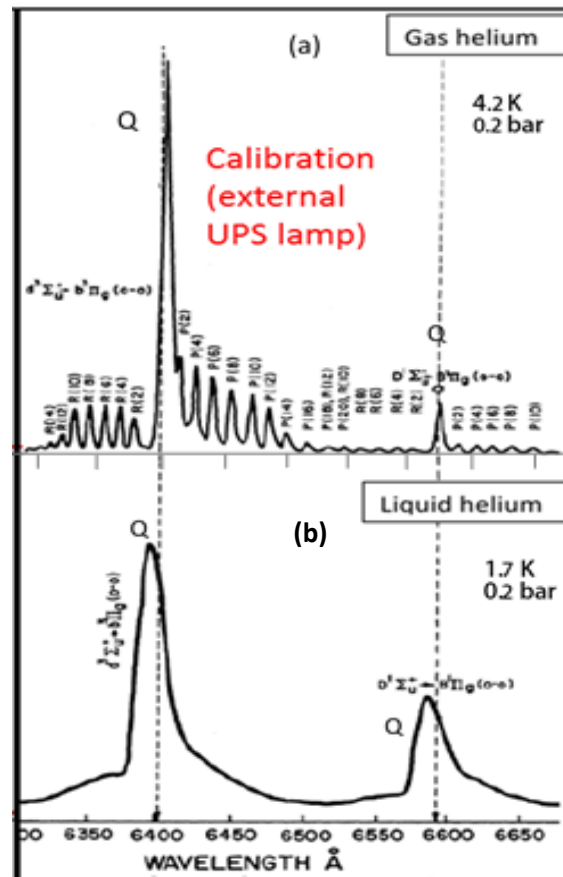


Figure 1.5: The  $d^3\Sigma_u^+ \rightarrow b^3\Pi_g$  and  $D^1\Sigma_u^+ \rightarrow B^1\Pi_g$  transitions at high resolution, observed from spectra of electron-bombarded liquid helium in the (a) gas phase at 150 Torr and 4.5 K, and (b) liquid phase at 1.7 K. This figure has been reproduced from Fig. 3 of ref. [9]

However, although the above research used bulk helium and excimers, many atomic and molecular transitions were not observed and there was no opportunity to investigate the shape of the emitted lines over a range of pressures.

Further studies regarding the rotational spectroscopy of the excimer using luminescence spectroscopy produced rotationally resolved emission spectra for the  $D^1\Sigma_u^+ \rightarrow B^1\Pi_g$  (0-0) transition, as observed in  $^3\text{He}$  and  $^4\text{He}$  clusters by this study, but this time the clusters were electronically excited by monochromatic synchrotron radiation [7, 54]. However, the sharp rotational lines seem to originate from excited atoms and molecules that are ejected from clusters after the excitation process, in other words that the emitted lines were not characteristic of excimers in droplets due to excimer ejection from the cluster [54]. Hence, there was no emission from excimers inside LHe (more details about rotational emission of excimers in chapter 5). Fig. 1.6 shows the rotational features of the luminescence spectroscopy of the singlet  $D$ - $B$  transition.

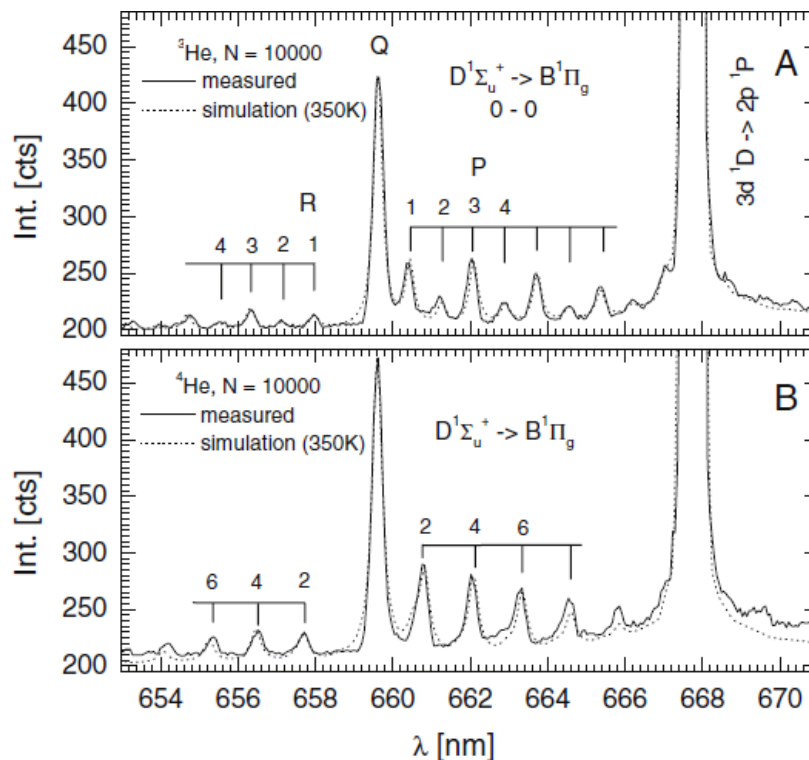


Figure 1.6: Luminescence spectroscopy of (A)  $^3\text{He}$  and (B)  $^4\text{He}$  droplets excited by monochromatic synchrotron radiation at 23.39 eV. Both isotopes' spectra show rotational features of the molecular  $^1D$ - $^1B$  transition covering the R, Q and P branches. This figure was taken from Fig. 1 of ref. [7].

Consequently, in order to assess the problem of light emission from excimers within liquid helium, a corona discharge, which is capable of being run at high helium densities, is employed to excite helium atoms and molecules in a high-pressure cell (more details about corona discharges can be found in chapter 2.6.1).

In the same manner, recently Li and co-workers excited normal-liquid helium with a corona discharge and observed the fluorescence emission of  $\text{He}_2^*$ , similar to Dennis, but where in this instance sharp, discrete lines were observed in liquid helium at 4.2 K [8], as shown in Fig. 1.7.

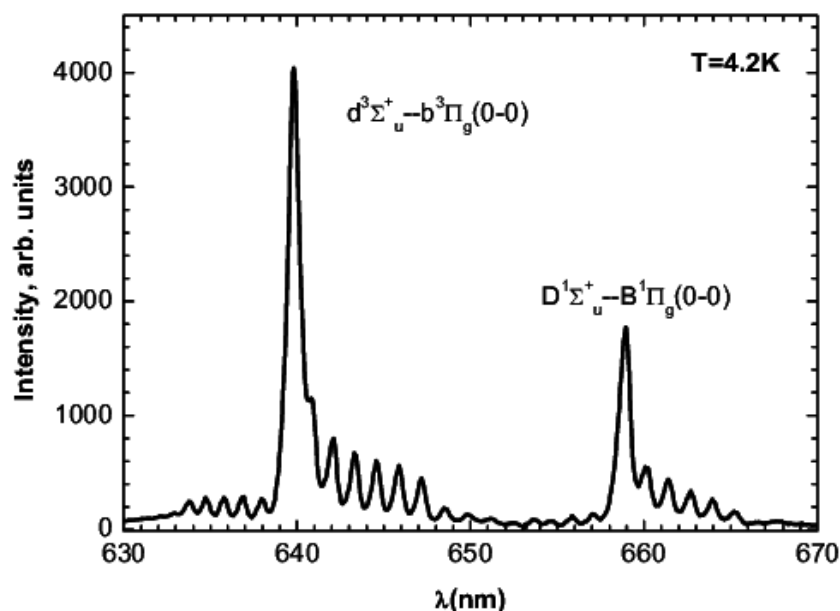


Figure 1.7: Fluorescence spectrum showing the  $d$ - $b$  and  $D$ - $B$  transitions observed in liquid helium at 4.2 K and 1.0 bar by corona discharge. Figure is taken from Fig. 1 of ref. [8].

However, in all these experiments the effects of temperature and the pressure have not been addressed. Furthermore, though the case of solvated excimers was suggested in the work on helium droplets, experimental evidence has not been produced or analysed to support this hypothesis (see chapter 5).

On the other hand, atomic spectral lines have been investigated by several research groups. For instance, Li and Bonifaci [8, 55-58] have recently investigated atomic spectra above the SVP in normal liquid helium. However, data and analysis of such at pressures and temperatures in the region below the SVP have not yet been undertaken.

Therefore, from a more generic point of view, another question that can be raised is whether one can apply the assumption of solvated excimers on excited atoms as well. The current work aims to address the above-mentioned questions, providing additional information in order to understand the interaction between excimers, excited atoms and their environment in the gas and liquid phases by controlling pressure and temperature, as this also adds the possibility of predicting the origin of contribution of rotational lines, whether from the solvated or unsolvated state, by knowing the pressure broadening coefficients. Hence, investigation of the microscopic origin of superfluidity (onset of superfluidity) is possible by investigation an unhindered rotation of helium excimers in LHe. Finally, the ability to change the temperatures and pressures in this project to control the interactions of  $\text{He}^*$  and  $\text{He}_2^*$  with surrounding helium atoms, motivated us to determine the origin of the formation of helium clusters around an excimer and excited helium atom. Possibly, this formation can be in the region below the SVP curve of pure helium or after crossing SVP curve.

## 1.5 Objectives and thesis overview

The principle aim of this thesis was to explore the potential corona discharge method for the study of the fluorescence spectroscopy of excimers  $\text{He}_2^*$  and  $\text{He}^*$  in different phases through analysis of different parameters, namely the lineshifts, linewidths and the intensities of emitted lines. This is to examine the answers to the following questions:

- What are the coefficients that can be investigated to control the interaction between the excited atoms and molecules and their environment by changing the pressure and temperature?
- What are the generic differences in the solvation behaviour of the singlet  $D-B$  (in the present work) and triplet  $d-b$  transitions? (The latter investigated by Mendoza-Lua [3, 59] - see chapter 5).
- How can we explain the rotational line broadening in superfluid helium and predict the origin of the contribution to the Q-branch as arising from the solvated or unsolvated state?
- How can we disentangle the spectra of a cold molecules and those of the equivalent species in the gas-phase?

- Why are excimers able to rotate in a liquid helium environment even though it is in a solvated state?
- Is it possible to apply the assumptions made about solvated excimers to excited helium atoms too?
- Is it possible to employ corona discharge to excite other environments at atmospheric pressure to detect other emissions?

In this section, an overview of the content of the thesis has been provided. A brief introduction into helium and its properties, including superfluidity, has been given, followed by an overview of studies of rotational spectroscopy in superfluid helium, the rotational spectroscopy of excimers in LHe and atomic spectral lines.

The second chapter, background of rotational spectroscopy and molecular spectra of diatomic molecules is given. This background of diatomic molecule covers total energy, vibrational structures, rotation-vibration interaction for rotor and electronic states structure with classification of these states. This chapter also describes Hund's coupling cases (b) and (d) then show energy level schematics for the atomic and molecular lines of interest transitions. This chapter also focuses on a derivation of the theoretical framework in order to understand the creation of excimers in Rydberg state and how corona discharge excites helium atoms and molecules. Finally, an idea about the formation of clusters and bubble around excited helium atoms and excimers is given.

The third chapter is dedicated to the description of the experimental setup, which is divided into various sections. The first describes the design of the low temperature ( $\leq 5$  K) experiment, whilst the second relates the setup of the room temperature experiment.

The data recorded, with associated analysis, is described in chapter 4 including investigations into the pressure dependence of line broadening and lineshifts under a wide range of pressures. This chapter focus on the spectra of atomic lines for the singlet and triplet  $3s-2p$  transitions.

In chapter 5 molecular bands associated with the  $D-B$  and  $d-b$  transitions at 3.8, 4.0, 4.5 and 5.0 K and range of pressures will be analysed to investigate the effects of pressure on the lineshape.

Chapter 6 and 7 are specific to the results carried out at room temperature, with chapter 6 covering the molecular bands and atomic lines observed of helium in emission spectra

at pressures of up to 25 bar. Chapter 7 will present the spectra of different cases at atmospheric pressure and, for the first time, will consider the effects of a perfume dopant, a perfume with air and mixture of all these substances with helium, where corona discharge and helium are used as a means of tracing other, unknown transitions.

Potential future work and summary will be described in chapter 8, which will be followed by publications, finally then will be an Appendix.

# Chapter 2

## Theoretical background

### 2.1 Rotational Spectroscopy of Diatomic Molecules

The wave function can be used to describe quantum mechanical systems. Thus, the Schrödinger Equation can be used to solve the energy of a model from which valuable explanations of atomic and molecular spectra will be produced [60] as long as the rigid rotor is assumed to be a good model of the rotation of a diatomic molecule. The rigid rotor consists of two masses ( $m_1$ ,  $m_2$ ) bound together and separated by the internuclear distance, i.e., the separation between the masses, ( $r$ ), that rotate around their centre of mass (COM). Additionally, diatomic molecules have rotational spectra associated with their vibrational spectra [14, 60, 61].

The bond length ( $r$ ), which is the distance between the centres of the two masses, was set to be constant, as this model can be treated as a single system by using the reduced mass concept ( $\mu$ ) [62]. Therefore, instead of considering the rotation of dumbbell, it can be consider the rotation of a single mass point of ( $\mu$ ) at a fixed distance ( $r$ ) from the axis of rotation, where [14];

$$m_1 r_1 = m_2 r_2 \dots \dots \dots (2.1)$$

and:

$$\mu = \frac{m_1 m_2}{m_1 + m_2} \dots \dots \dots (2.2)$$

where;  $r = r_1 + r_2$ ,  $r_1$  and  $r_2$  are the distance of masses  $m_1$  and  $m_2$  from the center of gravity

The moment of inertia ( $I$ ) for such a linear system of two molecules is given by [14, 62]:

$$I = m_1 r_1^2 + m_2 r_2^2 \dots \dots \dots (2.3)$$

$$I = \frac{m_1 m_2}{m_1 + m_2} r^2 \dots \dots \dots (2.4)$$

So the moment of inertia of a single body is given as a function of reduced mass and rotational length [62]:

$$I = \mu r^2. \dots\dots\dots (2.5)$$

The rotational energy ( $E$ ) for this model is given classically by [14]:

$$E = \frac{1}{2} I \omega^2. \dots\dots\dots (2.6)$$

Where  $\omega$  is the angular velocity. The classical angular momentum ( $P$ ) is another important factor in a rotating system and is defined by  $P = I\omega$ , hence the kinetic energy becomes:

$$E = \frac{P^2}{2I} \dots\dots\dots (2.7)$$

On the other hand, by solving the Schrödinger Equation, the quantized result of rotational energy is given by [63]:

$$E_r = \frac{h^2 J(J+1)}{8\pi^2 \mu r^2} = \frac{h^2 J(J+1)}{8\pi^2 I} \dots\dots\dots (2.8)$$

Since  $I = \mu r^2$ , and  $\hbar = h/2\pi$ , Eq. (2.8) then becomes;

$$E_r = \frac{J(J+1) \hbar^2}{2I} \dots\dots\dots (2.9)$$

Where,  $J$  is the rotational quantum number which is equal to 0, 1, 2, ... (non-negative),  $h$  is Planck's constant and  $\hbar$  is the Reduced Planck's constant (or Dirac constant). When the rotator changes from the upper energy level to the lower, the emission between these two levels occurs according to quantum theory. Hence Eq. (2.9) can be divided by the term  $hc$  to obtain the rotational energy  $F(J)$  in wavenumbers due to the energy associated with this transition [63]:

$$F(J) = \frac{E}{hc} = \frac{h}{8\pi^2 c I} J(J+1) = B J(J+1) \dots\dots\dots (2.10)$$

Where  $c$  is the light speed and  $B$  is the rotational constant in wavenumbers, which is defined as:

$$B = \frac{h}{8\pi^2 c I} \dots\dots\dots (2.11)$$

For a transition to be allowed, a selection rule that describes the probability of transition between sequential rotational levels must equal to [64]:

$$\Delta J = J' - J'' = \pm 1 \dots \dots \dots (2.12)$$

Where a single prime mark denotes the upper state and a double prime mark denotes the lower state. Also, this requires the (diatomic) molecule to contain a permanent dipole moment [64].

## 2.2 Molecular spectra

It is possible to observe different transitions corresponding to the different states of the molecule. Fig. 2.1 shows the commonly observed molecular spectra.

Pure rotational transitions within a given electronic state and vibration level can take place; this is called a pure rotational spectrum. When transitions occur between two levels of a given vibration, within the same electronic state, this spectrum is called vibration-rotation, as accompanied by a rovibrational transition.

Finally, transitions between two electronic levels can be observed, most often in the visible or near visible domain. These transitions represent rotational transitions between two electronic levels of the molecule, depending on the state of vibration of each of the electronic state [65], in what is referred to as a rovibronic transition.

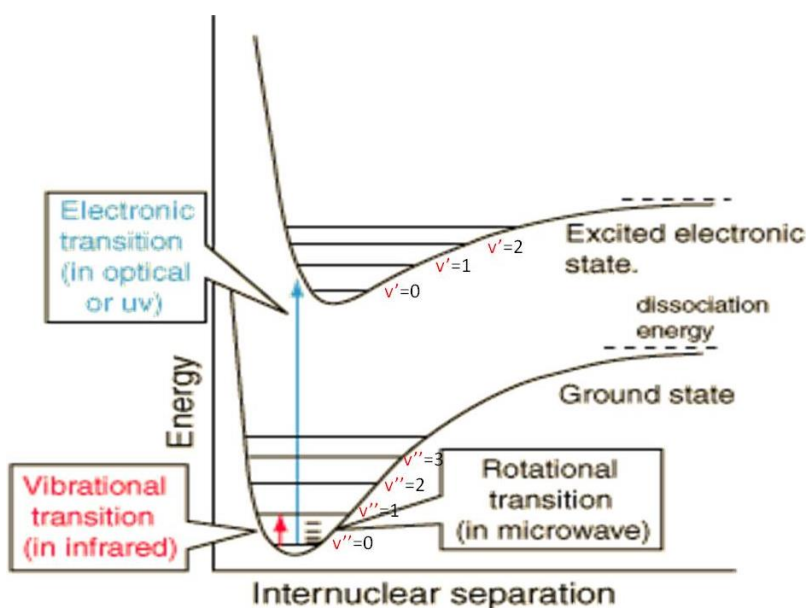


Figure 2.1: Diagram representing the energy levels of a molecule and various transitions. a: rotational transition; b: rovibrational transition; c: rovibronic transition. Figure taken from ref. [15].

### 2.2.1 Total energy of the diatomic molecule

The total energy of a diatomic molecule, according to the Born-Oppenheimer approximation, is given by

$$E = E_e + E_v + E_r \dots \dots \dots (2.12)$$

Where  $E_e$ ,  $E_v$  and  $E_r$  are the electronic excitation energy, the vibration and the rotation energy respectively.

As mentioned, rotational transitions within a given electronic state and vibration can occur, in what we call a rotational spectrum. When transitions are between two levels of a vibration, in a single electronic state, a vibration-rotation spectrum is observed. Hence, in spectral terms, equation (2.12) can be written the total energy of molecule as per the following expression [64]:

$$T = T_e + G(v) + F_v(J) \dots \dots \dots (2.13)$$

It seems from the equation the  $T_e \gg G(v) \gg F_v(J)$ , where  $v$  and  $J$  are, respectively, the number of vibrational and rotational quanta.  $T = E / hc$ ,  $T$  is expressed in wavenumbers.

A molecular energy level is defined by its quantum numbers  $n, v, K$  or  $J$ ;

- The principal quantum number  $n$  indicates the electron shell, or energy level of an electron. It is characterized by the electronic term value,  $T_e$ .
- The quantum number of vibration  $v$  describes the vibrational state of the molecule. It is characterized by the vibrational term value,  $G(v)$ .
- The quantum number of the total angular momentum  $J$  indicates the state of rotation of the molecule in the electronic state  $n$  and vibration  $v$ . it characterizes the rotational term value,  $F_v(J)$  (or  $F_v(N)$ ).

### 2.2.2 Vibrational structure of the electronic transition

$G(v)$  is the vibrational term value; its expression is specific to each electronic state studied,  $n$ , and is given by [14]:

$$G(v) = \omega_e \left( v + \frac{1}{2} \right) - \omega_e x_e \left( v + \frac{1}{2} \right)^2 + \omega_e y_e \left( v + \frac{1}{2} \right)^3 + \dots \dots \dots (2.14)$$

Where;  $\omega_e$ ,  $x_e$  and  $y_e$  and are constants for a given molecule.

### 2.2.3 Rotational structure of a non-rigid rotator

When the vibrations in a diatomic molecule do not correspond with those predicted for a rigid rotor, the concept of non-rigidity of the rotator, or a deviation from the ideal rigid rotor case, will arise. Consequently, a massless spring between the two atoms can be considered instead of a rigid connection, leading to an increase in internuclear distance with increasing rotational velocity (increase quantum number,  $J$ ) due to centrifugal force. Additionally, the constant of rotation  $B$  in Eq. (2.11) will be dependent on  $J$ , which decreases with increasing  $J$ . The value of  $F$  will now be given by [14, 63];

$$F(v) = BJ(J + 1) - DJ^2 (J + 1)^2 \dots \dots \dots (2.15)$$

Where  $B$  is the rotational constant and  $D$  is the centrifugal distortion constant, which depends on the stiffness of the bond.

### 2.2.4 Rotation-Vibration interactions for a rotor

For the model of a rigid rotor, where the bond length is fixed between the atoms in a diatomic molecule, rotations and vibrations can take place together. However, the spacing between energy levels would be expected to decrease according to the correction for anharmonicity, leading to an increase in bond length expectation value for higher vibrational levels. In this model, the rotational constants,  $B_v$ , and the centrifugal distortion,  $D_v$ , in a given vibrational state are dependent on the vibrational level,  $v$  [64];

$$B_v = B_e - \alpha_e \left( v + \frac{1}{2} \right) + \dots \dots \dots (2.16)$$

$$D_v = D_e - \beta_e \left( v + \frac{1}{2} \right) + \dots \dots \dots (2.17)$$

Here,  $\alpha_e$  is a constant of the rotation-vibration interaction in  $B_v$ , which is small in comparison to  $B_e$  [14],  $D_e$  is the constant translating centrifugal distortion and  $\beta_e$  translates the rotation-vibration interaction in  $D_v$  [66].

Accordingly, for a given vibrational level, the rotational terms are:

$$F_v(J) = B_v J (J + 1) - D_v J^2 (J + 1)^2 + \dots \dots \dots (2.18)$$

The second term can be neglected because  $D_v$  is very small compared to the first term.

Finally, according to the vibration-rotation interaction, the term values of a *vibrational rotator* are given by:

$$T = G(v) + F_v(J) = \omega_e \left( v + \frac{1}{2} \right) - \omega_e x_e \left( v + \frac{1}{2} \right)^2 + \omega_e y_e \left( v + \frac{1}{2} \right)^3 + \dots \\ + B_v J(J+1) - D_v J^2(J+1)^2 + \dots \quad \dots \dots \dots (2.19)$$

## 2.3 Electronic structure of diatomic molecule

Rovibrational (or ro-vibrational) is an abbreviated term for transitions between energy levels that involve changes in both vibrational and rotational states. This makes the energy level of diatomic molecule more complicated than for an atom due to the rovibrational states that are added to the electronic transition. The spectra are usually detected by lines obtained due to transitions from one rotational level in the ground vibrational state to another rotational level in the vibrationally excited state. These lines are called bands, and correspond to sequences of quantized rotational levels.

Formally, the allowed transitions from one quantum state to another for any system are dominated by a selection rule (transition rule). The selection rules for rotational transitions are given by [14]:

$$\Delta J = J' - J'' = 0, \pm 1 \dots \dots \dots (2.20)$$

Where  $J'$  represents the upper state and  $J''$  the lower state. The electronic angular momenta,  $\Lambda$ , for the upper and lower states determine the possible transitions of a system. If the  $\Lambda$  of the upper and the lower levels is different ( $\Delta\Lambda \neq 0$ ), then  $\Delta J = 1, 0$ , and  $-1$  for the transitions. Consequently, this makes it possible to define the branches of the rotational transitions, which are named the P, Q and R branches of a sequence for  $\Delta J = 0, \pm 1$ , respectively, as follows:

$$\Delta J = 0 \quad \text{Q - branch} \quad \dots \dots \dots (2.21)$$

$$\Delta J = 1 \quad \text{R - branch} \quad \dots \dots \dots (2.22)$$

$$\Delta J = -1 \quad \text{P - branch} \quad \dots \dots \dots (2.23)$$

However, it is anticipated that only two branches only of the rotational transitions will be observed when  $\Lambda = 0$ . In this case, the transition  $\Delta J = 0$  (Q-branch) is prohibited and only the  $\Delta J = \pm 1$  transitions will be apparent (P and R branches). Generally, the

frequencies of the resulting two or three series of lines are indicated by the following formulae:

$$v = v_0 + F'_V(J) - F''_V(J - 1) \quad \text{R - branch} \dots\dots\dots (2.24)$$

$$v = v_0 + F'_V(J) - F''_V(J) \quad \text{Q - branch} \dots\dots\dots (2.25)$$

$$v = v_0 + F'_V(J) - F''_V(J + 1) \quad \text{P - branch} \dots\dots\dots (2.26)$$

Where,  $F'_V(J)$  and  $F''_V(J)$  are the spectral rotation terms of the upper and lower states, respectively, and  $\nu_0$  is the zero line of band origin, as shown in Fig. (2.2).

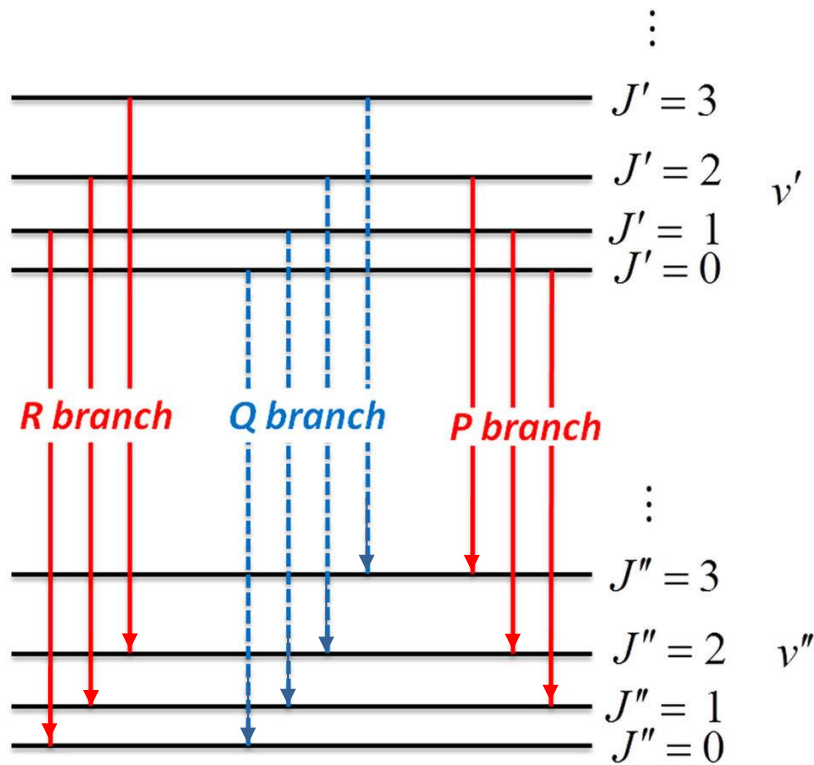


Figure 2.2: Energy level diagram of the rovibrational band with P-, R- and Q-branches transition from the upper state  $J'$  to the lower state  $J''$  according to the one-photon selection rule. This figure is reproduced from Fig. 1 in ref. [6]

## 2.4 Classification of electronic states-Structure multiplet

A diatomic molecule has several electronic states which are classified in a similar manner to that used for the classification of atomic energy states. The difference is that electrons in a diatomic molecule are subjected to an axially symmetric field of force determined by the internuclear axis, rather than a central field force, as per an atom. This

is due to the a strong electrostatic field of the two nuclei along the internuclear axis [67]. Therefore, the projection of the orbital angular momentum ( $\mathbf{L}$ ) of the electrons about the internuclear axis is a constant of motion with its component  $M_L(h/2)$ , where  $M_L$  can take the values (integer values) [63];

$$M_L = L, L - 1, L - 2, \dots, -L. \quad \dots \dots \dots (2.27)$$

In an electric domain, the energies of the states of the diatomic molecule remain unchanged, although the direction of the electrons is inverted and although the change in the sign of the  $M_L$  from positive to the negative. Consequently, the energy of states will differ only when  $M_L$  changes. From this point another a quantum number will arise with these changes of energy states, which determines the constant component of the resultant orbital angular momentum on internuclear axis and is symbolized by vector  $\Lambda$  [14, 67].

The quantum number  $\Lambda$  can take the values 0, 1, 2, 3, ..., L, with these values corresponding to the molecular states which are designated  $\Sigma$ ,  $\Pi$ ,  $\Delta$ ,  $\Phi$ , ..... state. Since  $M_L$  can take two values of  $+\Lambda$  and  $-\Lambda$ , thus  $\Pi$ ,  $\Delta$ ,  $\Phi$  are doubly degenerate, while  $\Sigma$  states are not [14].

Another case can be taken into account due to the spins of the individual electrons, whereby the multiplet structure of the spectral lines can be observed. The spins of the individual electrons which form a resultant  $\mathbf{S}$ , can have integer or half-integer values depending on the total number of electrons in the molecule (*even* or *odd*), with two cases;

- In case  $\Lambda \neq 0$ : There is an internal magnetic field resulting from the orbital motion of the electrons whose direction is along the internuclear axis. The component of the angular momentum of spin on this axis is a constant of the motion  $\hbar M_L$ ,  $M_S$  noted  $\Sigma$  is the projection of the spin  $S$  on the internuclear axis. The quantum number  $\Sigma$  can take  $2S + 1$  values such that  $\Sigma = -S, -S + 1, \dots, S$ .
- Case where  $\Lambda = 0$ : There is no internal magnetic field resulting from the orbital motion of electrons from where  $\Sigma$  is not defined.

Finally, the total angular momentum of the electrons around the internuclear axis is denoted  $\mathbf{\Omega}$  and defined as:

$$\mathbf{\Omega} = |\Lambda + \Sigma| \quad \dots \dots \dots (2.28)$$

The absolute value in Eq. 2.28 is because  $\Sigma$  and  $\Lambda$  have the same direction.

$2S + 1$  is defined as the multiplicity of a spin state, where the value of this process is added to the left superscript of the symbol.

The symmetry properties of the electronic eigenfunction are important to the classification of molecular states. In a diatomic molecule, any level through the internuclear axis is a plane of symmetry. Therefore, the electronic eigenfunction of a (non-degenerate)  $\Sigma$  state changes by a factor of  $\pm 1$ , when reflected through any plane passing through both nuclei. However, the state is designated as  $\Sigma^+$  if the factor is positive; and the state is designated by  $\Sigma^-$ , if the factor is -1,

Another symmetry property that applies to homonuclear molecules is symmetry with respect to the centre of symmetry. If the electronic eigenfunction remains unchanged it is said to be even (and designated by a “g” subscript, meaning *gerade* or “even” in German); if it changes sign it is said to be odd (and designated by a “u” subscript, meaning *ungerade* or “odd” in German) [3, 14].

## 2.5 Hund's coupling cases of the rotations and electronic motion

In the molecule, there are several angular momenta that can be defined. Depending on the mode of their association, several of these cases can couple, but also other cases are decoupled according to the value of the quantum number of rotation,  $J$ . Moreover, all the interactions between the different angular momenta of the molecule play an important role in the expressions of energies of rotation,  $F_v(J)$ . In the diatomic molecule, the different angular momenta such as the electron spin, the electronic orbital angular momentum, and the angular momentum of nuclear rotation, form a resultant that we denote  $J$ . The simplest case, which does not require any particular treatment, is the electronic state  $^1\Sigma$  since, in this case,  $\Lambda = 0$  and  $S = 0$ , hence  $J = N$ , we are dealing with a simple rotator. Other states are distinguished according to the different modes of coupling which were studied by Hund.

There are five Hund's coupling cases, traditionally notated with the letters (a) through (e). Most diatomic molecules are somewhere between these cases [14, 68]. In this section we will examine cases (b) and (d) in detail as they will be shown to be important to the  $\text{He}_2$  molecule.

### 2.5.1 Hund's coupling case (b)

In this case, spin-orbit coupling disappears, then  $\Lambda = 0$  and  $S \neq 0$  such that the spin vector  $\mathbf{S}$  is not coupled to the internuclear axis at all. Sometimes, even if  $\Lambda \neq 0$ , the spin vector  $\mathbf{S}$  may only be very weakly coupled to the internuclear axis, as happens for the light molecules. The zero coupling of  $\mathbf{S}$  in this manner is defined as Hund's case (b).

Angular momentum vectors  $\mathbf{\Lambda}$  and  $\mathbf{R}$  ( $\mathbf{R}$  represents the rotation of the molecule) form a resultant  $\mathbf{N}$ , whose corresponding quantum number  $N$  can have integer values from  $\Lambda$  onwards.  $\mathbf{N}$  and  $\mathbf{S}$  form the resultant designated  $\mathbf{J}$ . From angular momentum theory, the only possible values for the quantum number  $J$  range from  $|N-S|$  to  $N+S$  in integer steps. According to the coupling, the quantum numbers of Hund's coupling case (b) are  $\Lambda$ ,  $N$ ,  $S$  and  $J$ , as shown in Fig. 2.3 (a).

### 2.5.2 Hund's coupling case (d)

When the coupling between  $\mathbf{L}$  and the internuclear axis is very weak, and the interaction between  $\mathbf{L}$  and the rotation axis is strong, we obtain case (d). In this case,  $\mathbf{K}$  can be obtained by adding the angular momentum  $\mathbf{L}$  to  $\mathbf{R}$ . Meanwhile, similar to case (b), this vector can be coupled to  $\mathbf{S}$  to give  $\mathbf{J}$ , as shown in Fig. 2.3 (b).

The quantum number  $K$  can take on integer values between  $|R-L|$  and  $R+L$ . In addition,  $K$  can take  $2L+1$  different values for each  $R$ , except in the case where  $R < L$ . In this case,  $L$ ,  $R$ ,  $K$ ,  $S$  and  $J$  are the quantum numbers used.

These coupling cases are an adequate characterization for electronic states such as *Rydberg* states in molecules, where the interaction between the *Rydberg* electron and molecular core is quite weak [3].

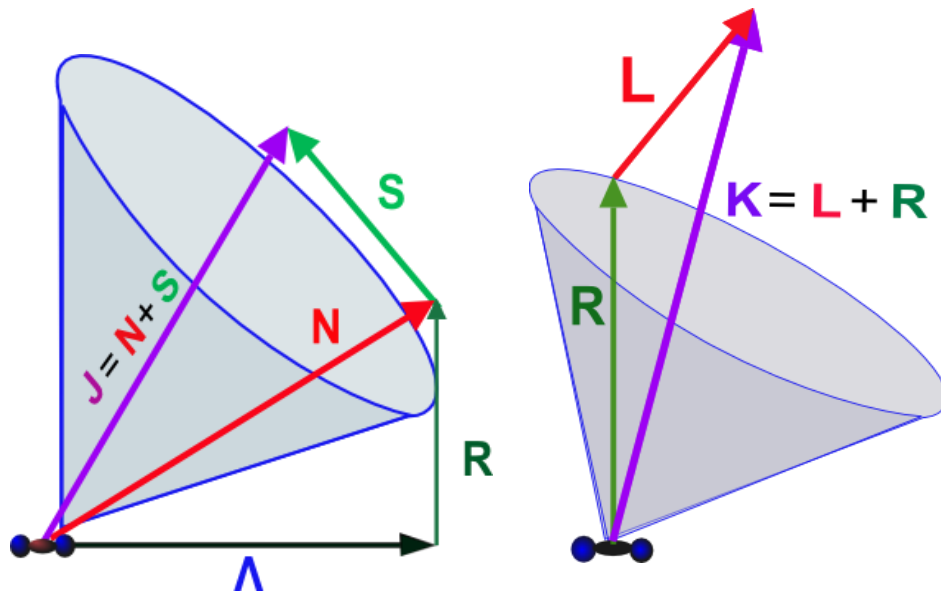


Figure 2.3: Vector diagram for Hund's case (b) on the left-hand side of the figure, and case (d) on the right.

## 2.6 Generation of electronic excitation in bulk He

In this section, some of the aspects relating to the electronic excitation process of helium atoms and molecules (excimers) in the gas and liquid helium will be discussed. We will start with a corona discharge, which is the first step in the generation of an excitation.

### 2.6.1 A corona discharge

The methodology in chapter 3 of experimental procedure – section 3.1.12, using a corona discharge in the excitation of helium atoms and molecules will give a detailed description of this technique; here, we provide a quick overview.

A corona discharge is an electrical discharge transported by an ionized fluid surrounding a conductor which is electrically energized. A major factor in obtaining a discharge is applying a sufficiently large electric field between the conductors (electrodes in our case). A coloured spot near the ionization region indicates the occurrence of a discharge. Commonly, a bluish (or other colour such as like purplish) glow in the plasma adjacent to the tip-point tungsten electrode carrying high voltages is seen [69].

The process of discharge begins when the current flows with a high potential on an electrode towards a neutral fluid (helium in this project), producing a plasma region around the electrode. When electrons flow, their energy is transferred to the surrounding

fluid and ions, excited atoms and molecules were generated; for more details of the ionized region around electrodes see chapter 3. The corona may be a positive or negative depending on the polarity of the applied voltage [70, 71].

The corona can be used in several applications [69]:

- It can be used to generate charged surfaces, to use in electrostatic copying.
- It can also be used to remove matter from air streams by first charging the air, and then passing the charge through a comb of alternating polarity to deposit charged particles onto oppositely charged plates.
- The free radicals and ions generated in the corona reactions can be used to scrub the air of certain noxious products, through chemical reactions, and can be used to produce ozone.

## 2.6.2 Excited helium atom and molecule (Excimers)

One of the problems mentioned in chapter 1 was the difficulty inherent to exciting molecules in liquid helium. Therefore, using an electrical discharge (a corona discharge) was in our case the solution to overcoming this problem, and can be run easily in high helium densities to continuously generate excited helium atoms,  $\text{He}^*$ , and excited helium molecules,  $\text{He}_2^*$ , in Rydberg states [72, 73].

The high voltage across the electrodes is sufficient to inject electrons into the cell which transfer their energy to He atoms as mentioned in the preceding section. This energy is sufficient to excite He atoms and molecules, ionizing them and thus leading to the formation of excimers which were employed as molecular probes [4].

*What is an excimer?* Originally, excimer was the terminology for excited state dimer (short for excited dimer). Often excimers are diatomic, composed of two species of atoms or molecules that would not bond if both were in their respective ground states. Furthermore, excimers are short-lived, with lifetimes in the order of nanoseconds [40]. One way in which excimers can be formed is when one of the components of the dimer is in its excited state. Then its components will dissociate when the excimer decays into the ground state leading mostly to repulsion of its components. An excimer can thus be measured by fluorescence emission. The next step is one of a series of  $\text{He}^*$  and  $\text{He}_2^*$  formation by using corona discharge.

Basically, electrons that flow by corona discharge transfer their kinetic energy to excite or ionize helium atoms from the ground state. We therefore have the two following processes to obtain  $He^*$ , depending upon whether the atom is excited or ionized.

The first process so when electrons excite helium atoms directly to an excited helium atom, as shown in the following equation [73-75]:



Secondly,  $He^*$  can be obtained by a *two-body* process; starting when the atomic ionization energy reaches of 22-25 eV, to ionize helium atoms [75];



Then helium ion can react to form helium molecule-ions which are generated in helium relatively early by [76], to recombine again with an electron to produce  $He^*$  [77]:



A further way to produce excited He atoms but in the reverse manner to the above step, where  $He_2^+$  can produced from associative ionisation of  $He^*$ , followed by dissociative recombination with an electron as shown in the following equations [78]:



Helium ions can react to form helium molecule-ions which recombine again with an electron to create an excited helium molecule (excimer). The series of equations below shows the steps of collisions to generate a single molecule in liquid helium.

Regarding the formation of excimers, the helium molecule-ions produced in Eq. 2.32 recombine with electrons to form the excited helium molecule [74, 75];



In summary, in fact no experimental observation or theoretical explanation for the formation of  $He_2^*$  by other processes than this one has ever been proposed. Additionally, the main ionic species of  $He_2^+$  in plasma can be obtained from  $He^+$  that is rapidly converted to the  $He_2^+$ . This features of a fast process from excitation to decay on a nanosecond timescale for different species of helium, all of which motivated us to

generate excited species of helium in different environments to extend our investigations. By doing this, the second problem was solved by using this species of excited helium as probes in LHe.

## 2.7 Electronic structure of the He transitions

In this subsection, we will present the electronic states of  $^4\text{He}$  transitions of interest in this work covering atomic lines and molecular bands. Since  $^4\text{He}$  has a zero spin, only transitions between fully symmetric levels are allowed. Allowed transitions of atomic and molecular transitions are listed in Appendix A.

### 2.7.1 Atomic lines

In this paragraph we only analyse the spectral atomic lines of the triplet,  $2p\ ^3\text{P} \leftarrow 3s\ ^3\text{S}$  at 706 nm, and singlet  $2p\ ^1\text{P} \leftarrow 3s\ ^1\text{S}$  at 728 nm. The main interest of this choice is related to the fact that these lines are sufficiently intense that they appear over a large pressure domain and that they have been studied by numerous authors (the information and results of these transitions are discussed in chapter 4). The transitions of associated with these lines are in the energy range 20-23 eV, where Fig. 2.4 shows a diagram of the energy levels for the lines observed.

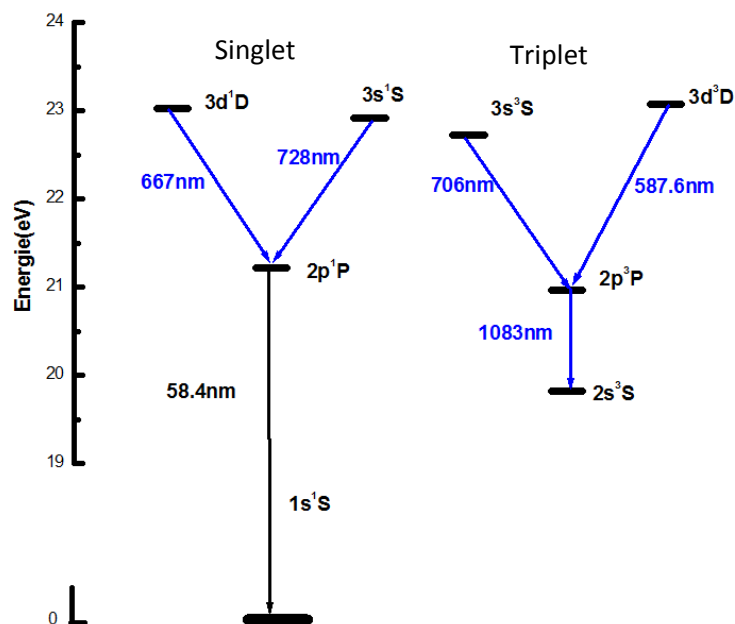


Figure 2.4: Diagram of the energy levels of the helium atomic lines for the singlet and triplet transitions. This figure is taken from Fig. 6.1 from ref. [4].

## 2.7.2 Molecular bands

As known, the potential energy for the ground state of He<sub>2</sub> molecule is repulsive and unstable. However, the excited states are bound strongly, therefore we can investigate spectroscopic features of the helium molecule [15]. As a result, several electronic states are known for He<sub>2</sub>, as investigated by Günter and co-workers [14, 41, 79, 80]. Based on the levels of nuclear rotation interaction with the momenta of the electron, there are different modes of angular momentum coupling, as mentioned in the preceding sections. Additionally, a He atom can exist either in the singlet or triplet states with a total spin  $S = 0$  or  $1$  respectively, where the spin of the electron is  $\frac{1}{2}$ . The energy levels of molecular bands of the He<sub>2</sub> singlet and triplet are shown in Fig. 2.5. The potential energy curves for several transitions for He<sub>2</sub> states investigated by Günter are shown in Appendix B. In this work, we will focus on the singlet and triplet  $d^3\Sigma_u^+ \rightarrow b^3\Pi_g$  and  $D^1\Sigma_u^+ \rightarrow B^1\Pi_g$  transitions, respectively.

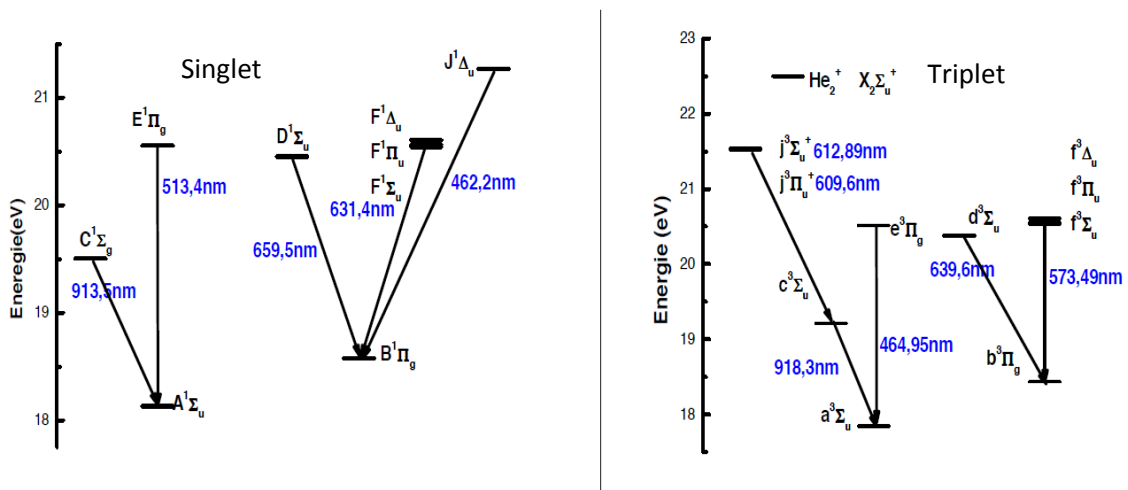


Figure 2.5: Diagram of the energy levels that give rise to the molecular bands for the singlet and triplet transitions. This figure is reproduced from Fig. II.5 of ref. [15].

### 2.7.2.a Electronic structure of $D^1\Sigma_u^+ \rightarrow B^1\Pi_g$ transition

This is the energy level of  $D^1\Sigma_u^+$  level is at 20.57 eV and  $B^1\Pi_g$  is at 18.70 eV. The transition between these two states follows Hund's case (b). The spin and the orbital angular momenta ( $\Lambda = 0$ ) of the electron are equal to zero ( $S = 0$ ), therefore it is a singlet state due to rule  $(2S + 1 = 1)$  and every N level = J level. On the other hand, the orbital

angular momentum  $\Lambda = 1$  for  $B^1\Pi_g$ , so  $J$  takes the values:  $J = 1, 2, 3 \dots J \geq \Lambda$ . The transition between these two states follows Hund's case (b). The allowed lines for the associated transitions are shown in Fig. 2.6. It may be noted that the transitions have been classified into three branches named Q, R and P, as deduced according to the one-photon selection rules (2.21), (2.22) and (2.23). When the state is  $u$ , only odd levels for the quantum number ( $N'$ ) are populated.

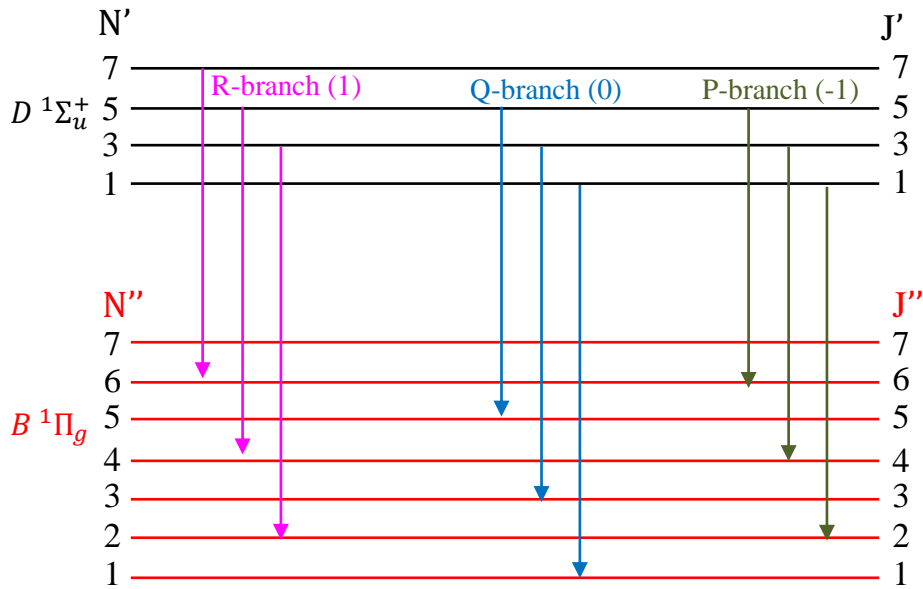


Figure 2.6: Energy levels and transitions between the  $D^1\Sigma_u^+$  and  $B^1\Pi_g$  states as per Hund's coupling case (b). The bands are indicated by arrows of different colours; purple arrows represent R-branch transitions that are equal to +1 due to the one-photon selection rule (2.22), blue lines indicate to the Q-branch (2.21) and green lines are the P-branch that is equal to -1 (2.23). Diagram reproduced from Fig. II.9 of ref. [15].

### 2.7.2.b Electronic structure of $d^3\Sigma_u^+ \rightarrow b^3\Pi_g$ transition

This transition is between the level  $d^3\Sigma_u^+$  located at 20.38 eV and  $b^3\Pi_g$  at 18.44 eV. The upper electronic state  $d^3\Sigma_u^+$  is such that  $\Lambda = 0$  and  $S = 1$ , and belongs strictly to Hund's case (b). The spin of  $^4\text{He}$  is zero, so the electron wavelength function is symmetrical. Since  $S = 1$ , every  $N$  state splits into three different levels according to the rule  $(2S + 1)$ , with levels  $J = N - 1, J = N$  and  $J = N + 1, J \geq \Lambda = 0$  [3].

Again, the symbol  $u$  in the upper molecular state implies the quantum number  $N$  only odd which is permitted. Regarding the order of levels,  $J$  is that the maximum energy level at  $J = N$ , while the lower one is when  $J = N-1$  and the middle level at  $J = N + 1$  [8]. On the other hand, the symbol  $g$  in the lower state ( $\Pi_g$ ) means the molecular state has even symmetry, and the quantum number  $N$  can take integer values from  $\Lambda = 1$ . Therefore, the values of  $N$  are 1, 2, 3, 4, ..., for the lower  $\Pi_g$  state and equal to 1, 3, 5, 7, ..., for the upper  $\Sigma_u$  state.

The rotational constants of the vibrational bands (0-0) of the upper and lower states are very close at 7.34 and 7.45  $\text{cm}^{-1}$  [14]. Consequently, the rotational lines of the Q-branch are not resolved because they are close in energy, with the overlapping of these lines leading to an intense central Q band.

Fig. 2.7 shows the structure of the allowed transitions between  $d^3\Sigma_u$  state and  $b^3\Pi_g$  state.

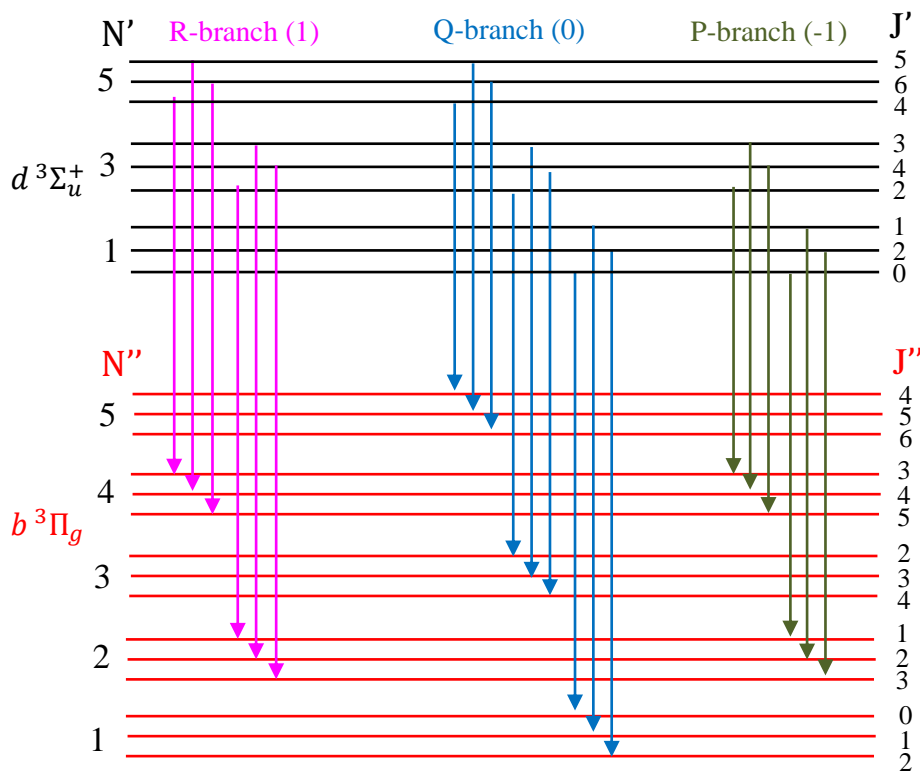


Figure 2.7: Energy levels and transitions between  $d^3\Sigma_u^+$  and  $b^3\Pi_g$  states as per Hund's coupling case (b). Due to the *ungerade* upper state, only odd levels of quantum number  $N$  are allowed. Every value of  $N$  splits into three levels with values of  $J = N - 1, N + 1$  and  $N$  for the upper state, while for lower state  $J = N + 1, N$  and  $N-1$ . These transitions can be categorized into three branches; the R-branch, represented by purple arrows, blue arrows for the Q-branch transitions, and finally green arrows for the P-branch. This electronic dynamics were analysed following ref. [15].

## 2.8 A bubble formation around $\text{He}_2^*$ and $\text{He}^*$ embedded in LHe

After applying electrical discharge by using corona discharges, excited helium atoms and excimer molecules are generated and reside in Rydberg states which gives rise to form structure around excited particles. Then a repulsive force is established between the Rydberg electron orbital and surrounding ground state helium atoms. As a consequence, a cavity is created around the  $\text{He}_2^*$  and  $\text{He}^*$  due to pushing the surrounding helium atoms away at a short time [81, 82]. Usually, this void is called a *bubble* or *cavity* which has radius between 10-15 Å [83]. The existence of localized excited helium atoms and molecules in cavities within LHe was investigated by Hickman [84], where it was found that the size of cavity around excited helium atoms within LHe is smaller than that one surrounding a free electron. Because even if with a large separations between the excited atom and neighbouring atoms, attractive forces dominate the interaction potential between them, leading to a smaller cavity [84].

On the other hand, Localized heating was produced, even if in the LHe, due to electrical field applied on the electrodes. As a result, gas pocket is expected to form around excited species in liquid helium (see chapters 4 and 5). For this case, solvation layers with high density of helium atoms can be formed around a gas pocket.

So the final picture of this system will be excited helium atoms and excimers are caged or solvated in the bubble within liquid helium

Schematic diagrams of an excited helium atom  $\text{He}^*$  and molecule ( $\text{He}_2^*$  excimer) enclosed in a bubble in different phases is presented in Figs. 4.21 and 5.13 respectively.

# Chapter 3

## Experimental and Measurement Techniques

This chapter describes experimental design and explains details of the technique used to study the dynamics and structure of helium atoms and molecules by employing a corona discharge method.

Different thermodynamic phases of helium are required for investigation in this experiment, covering low (liquid helium) temperatures in addition to room temperature. Therefore, two experimental setups will be described in this chapter: the first will characterize the cryogenic experiment and the second part the 300 K experiment, involving the liquid and gas phases of helium, respectively.

Additionally, the method of collecting fluorescence spectroscopy will be given in this chapter.

### **3.1 Part I- Cryogenic temperature experiment**

An understanding of the concept of the fundamental atomic and molecular processes in gases has been bringing the motivation for research to investigate cryogenic plasmas. For instance, the investigations of the electron or He ions mobilities in helium and measuring the momentum transfer collision cross section of electrons in helium gas, has been the focus of research [85-87]. Furthermore, several studies [88-90] have been carried out to understand the properties of plasmas in ultracold conditions. Conceptually, a cryogenic system is a comprehensive system dealing with the practical application of very low temperatures.

In our experiment, the main goal in the low temperature experiment is to study and determine the properties of helium plasma in the gas and liquid phases, mainly the

effects of pressure, temperature and thermodynamic phase on the fluorescence of He atoms and molecules over a wider range of pressures. Therefore, we designed and built a new apparatus, conceptually similar to that previously used by Li *et al.* [8], but with better performance in a number of areas. A requirement was that the cell could operate at high pressures and at cryogenic temperatures of around 4 K. Another objective was to measure a larger number of spectra in a given time per experimental run than was possible with the apparatus used by Li and co-workers. To accomplish this, sensitivity had to be increased by several orders of magnitude. This was achieved by a newly designed lens system which was able to collect fluorescence over a larger solid angle and deliver the light to our spectrometer with significantly reduced losses in intensity. Additionally, the use of a closed-cycle Oxford Instruments HelioxAC-V  $^3\text{He}$  cryostat gave resalable results.

### 3.1.1 General description of the cryogenic system

The system we used in our experiments consists of a  $^3\text{He}$  insert and cryostat, a two-stage pulse tube cryocooler (PTC) and a compressor. A  $^3\text{He}$  pot, a sorption pump and a heat switch are the major components of the  $^3\text{He}$  insert, as shown in Fig 3.1.

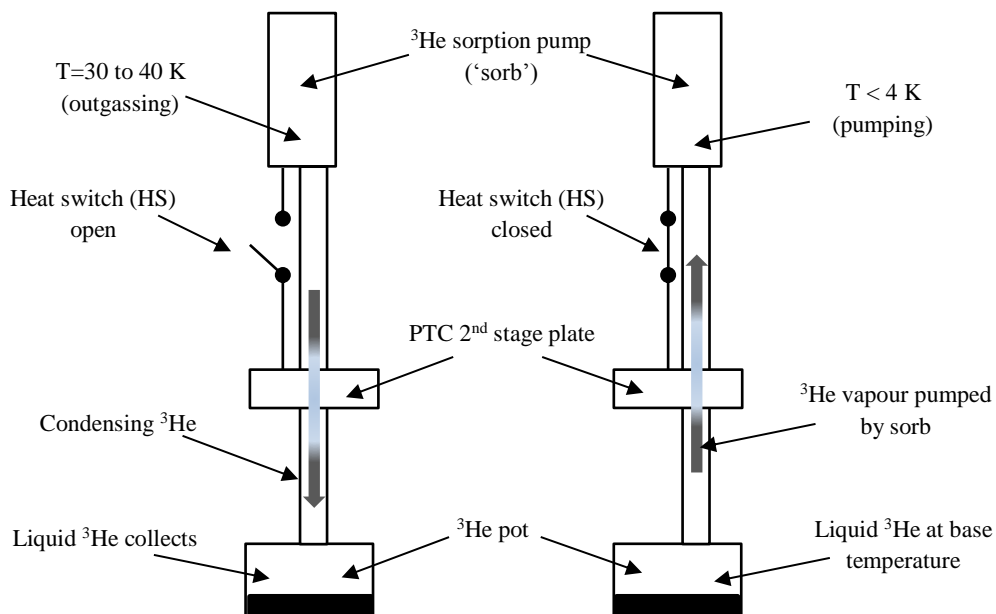


Figure 3.1: Operation principle of a HelioxAC-V sorption pumped  $^3\text{He}$  insert. Figure reproduced from [5]

The thermal link between the PTC second stage and the sorption pump<sup>2</sup> is weak at the opening to the heat switch (HS); when the heat switch is closed (operating), the thermal link between the PTC second stage and sorption pump becomes strong.

The system of external pumping is required to evacuate the cryostat vacuum space before the <sup>3</sup>He insert operation (evacuation process will be explained in the following sections). The operation of the <sup>3</sup>He insert is dominated by two temperature controllers (ITC503). One ITC controls the temperature of the sample stage (<sup>3</sup>He pot) and the sorption pump. The other ITC controls the heat switch and allows us to monitor the temperature of the second stage of the PTC (more details will be given in subsequent sections). At the bottom of the line, the pot is where liquid <sup>3</sup>He is ultimately condensed.

### 3.1.2 HelioxAC-V <sup>3</sup>He Refrigerator<sup>3</sup>

The HelioxAC-V <sup>3</sup>He refrigerator is the mechanical fridge. Broadly, "refrigerator" is used as a replacement for the word "cryorefrigerator", which refers to the system of pulse tube which is based on a cold head (an expansion chamber inside the fridge) and the compressor package and lines which are capable of attaining cryogenic temperatures. To cool to 4 K with a mechanical cooler requires a two-stage system, with the first stage (PTC 1<sup>st</sup>) operating at a temperature of 40 to 80 K. The first stage typically has a large cooling power (e.g., 40 W at 45 K, compared with 0.3 W at 4 K), and can thus be used to cool radiation shields in a similar manner to helium with a liquid nitrogen bath. Then, the systems is cooled down to 4 K on the second stage of the fridge, which is made of a gold-plated copper plate [91]. Fig. 3.2 shows schematic diagram of the fridge used in this experiment.

The <sup>3</sup>He insert consists of two sections: the dump, which is a large vessel used to release any overpressure in the gas line; the other section is the pot side of the gas line that includes the SORB, where these two sections are separated by valves as per Fig. 3.2. When the sample has been mounted in vacuum on the base of the <sup>3</sup>He pot, the jacket of

---

<sup>2</sup> Cryogenic pumping is the cold surfaces that will freeze out any remaining impurities and start collecting them at the cold surfaces, thus acting as pumps. It was found that the pressure in the OVC drops when the fridge is isolated under closing PV5.

<sup>3</sup> This refrigerator is covered by US patent 6782712 and European patent application 1387133, and was supplied by Oxford Instruments Superconductivity (Oxon, OX13 5QX, England)

the cryostat vacuum should be sealed and the vacuum space evacuated. Swagelok valve V1 on the insert top plate should be opened to allow  $^3\text{He}$  to flow freely from the dump vessel to the sorption pump and  $^3\text{He}$  pot.

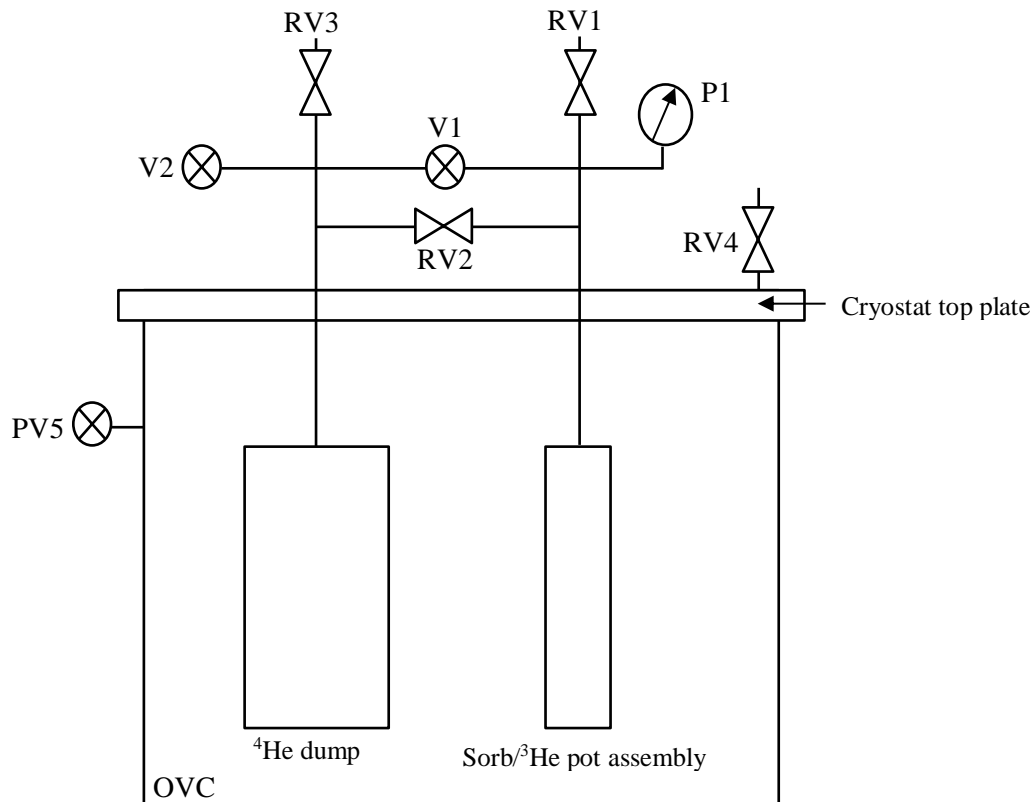


Figure 3.2: Schematic diagram of the cryostat vacuum and  $^3\text{He}$  handling system. Figure reproduced from ref. [5].

From Fig. 3.2, valves V1 and V2 are Swagelok bellow-sealed valves. Valve V1 links the  $^3\text{He}$  dump to the sorb/ $^3\text{He}$  pot assembly (this valve only needs to be opened or closed during normal operation of the insert). Valve V2 is the  $^3\text{He}$  fill port the insert (this valve should never be opened during normal operation). P1 is the mechanical pressure gauge with a range of 0.0-14.5 bar absolute. This gauge can be used to check the  $^3\text{He}$  pressure when the insert occurs at room temperature, and the  $^3\text{He}$  pressure in the sorb/ $^3\text{He}$  pot assembly during the condensation process. Relief valves RV1, RV2 and RV3 prevent the dump, sorb and  $^3\text{He}$  pot from being over-pressurized. Valve VP5 is known as an Edward's NW25 Speedivalve which is utilized to evacuate the cryostat OVC. Finally, relief valve RV4 prevents the outer vacuum chamber (OVC) from being over-pressurized [5].

### 3.1.3 Heat transfer by radiation and conduction

There are many ways that can allow the heat to be transferred between the specimen and its surroundings such as convection, conduction and radiation. Often, the partial evacuation of a gas from the interior of the cryostat can assist thermal isolation in low temperature applications, hence convection is eliminated. On the other hand, conduction during the residual low temperature gas requires the effective heat transfer be taken into account and also conduction over the solids that interconnect the various cryostat parts and also by radiation. Moreover, there are other factors that can contribute to the heat transfer, such as Joule heating in electrical connections, mechanical vibration, eddy current heating and gas adsorption or desorption [92].

Usually, heatshields are considered as an important part used in cryostats to reduce the effects of radiation. A heatshield is a cylindrical metallic container that connects directly at a certain temperature with a fridge stage. Then the heatshield is at the same temperature as the stage to which it is attached (although temperature gradients may arise when the material of the heatshield does not have a high enough thermal conductivity). Hence, the shielded surface is exposed to a surface at a lower temperature. A black body is absorbing all of the radiation that falls upon it. Thus, the absorptivity ( $a$ ) for such a body and its emissivity ( $\epsilon$ ) are unity, and its reflectivity ( $R$ ) is zero;  $R = 1 - \epsilon = 1 - a = 0$  [92].

According to the Stefan Boltzmann law for black bodies, the total radiant energy emitted at a temperature  $T$ , per second per unit area is given by [93]:

$$E = \sigma T^4 \dots\dots\dots (3.1)$$

Or, the total power radiated in eq. (3.1) can be written by surface area and given by [94]:

$$P = A e \sigma T^4 \dots\dots\dots (3.2)$$

Where;

- $\sigma$  is the constant of Stefan Boltzmann =  $5.67 \times 10^{-8} \text{ W/m}^2\text{K}^4$
- $A$  is the surface area
- $e$  is the emissivity (for most objects is taken to be 1)
- $T$  is the temperature of the object in Kelvin

The feature of such calculations that deal with radiant heat transfer at low temperatures are not limited to the black body only. However, calculations can be applied on the metallic surface, which has an emissivity between 0.01 - 1.0, to some extent.

From this point of view, therefore, the rate of heat transfer from the ambience temperature of a room (say 300 K) can be calculated for a small aperture on a heatshield in direct connection with part of the fridge held at the lowest temperature. For instance, for a 1 mm aperture radius ( $r$ ), and its area of  $\pi r^2$ , the radiated power from eq. (3.2) is  $1.443 \times 10^{-3}$  W. However, in case of the heatshield with dimensions of the cylinder where radius is 73.5 mm, the height is 257.34 mm, the area of heatshield is  $A = 2\pi r^2 + 2\pi rh$ . So, if the heatshield contacts with the coldest point in the setup of fridge (assume 4 K), the loading of the heat would be  $2.217 \times 10^{-6}$  W.

### 3.1.3.1 Joule heating effects

As mentioned, Joule heating in electrical connections (leads, connections) and resistance thermometers is one of the factors of heat transfer that gives rise to the rate of heat input [95]:

$$Q = I^2 R = I^2 (V/I) = VI \dots \dots \dots (3.3)$$

In our experiment, the electrical field applied to the electrode-tip contributes to the heat-load in the fridge via joule heating. The value of the voltage that was required to ignite discharge in liquid phase is around 10 kV (this will be explained in chapter 4 and 5) and the discharge current about 1  $\mu$ A. So, the estimated value of the power of joule heating ( $Q$ ) is 10 mW, and we assume this heat loading affects stabilization of discharge and hence on the ambient temperature in the fridge.

### 3.1.3.2 Heat conduction through solids

Here, we indicate the rate of heat flow ( $Q$ ) in solid sections in the cryostat, which is obtained through the temperature gradient ( $dT/dx$ ) over the cross-section ( $A$ ). Hence, it is easy to estimate the heat transfer ( $Q$ ) as determined by [95]:

$$\dot{Q} = \lambda(T) A \frac{dT}{dx} \dots \dots \dots (3.4)$$

Where  $\lambda(T)$  is the temperature-dependent thermal conductivity of the solid that gives an idea about the ability of a substance to conduct heat at temperature,  $T$ .

However, if the ends of a solid bar of uniform cross-section ( $A$ ) and length ( $l$ ) are  $T_1$  and  $T_2$ , then the rate of transfer heat ( $Q$ ) is given by:

$$\dot{Q} = \frac{A}{l} \int_{T_1}^{T_2} \lambda(T) dT \dots \dots \dots (3.5)$$

To resolve the integral in eq. (3.5) a particular theory was needed such as the mean value theorem [96] for integrals to overcome difficulties in such calculations, which gives:

$$\bar{\lambda} = \frac{1}{T_1 - T_2} \int_{T_1}^{T_2} \lambda(T) dT \dots \dots \dots (3.6)$$

From eq. (3.5) and (3.6), we obtain the following:

$$\dot{Q} = \frac{A}{l} \bar{\lambda} (T_1 - T_2) \dots \dots \dots (3.7)$$

In our experiment, these calculations are relevant to the heat load contribution due to the gas supply line. Therefore, for a stainless steel tube with a length of 1.5 m between two stages in the fridge (at 77 K and 4 K), and with 0.020 m as the outer diameter of the tubing, the value of the rate of heat transfer according to eq. (3.7) is less than 0.5 mW at 77 K via stainless steel plumbing. The value of ( $\bar{\lambda}$ ) for stainless steel and for a numerous commonly used materials in experiments was taken from Table 3.1 [95].

Table 3.1: Mean values of thermal conductivity in (W/m.K) for diverse materials with different ends at of temperatures. Table reproduced from Table 4.1 of [95].

Material	$\bar{\lambda}$				
	T <sub>2</sub> =300 K T <sub>1</sub> =77 K	T <sub>2</sub> =300 K T <sub>1</sub> =4 K	T <sub>2</sub> =77 K T <sub>1</sub> = 4 K	T <sub>2</sub> =4 K T <sub>1</sub> =1 K	T <sub>2</sub> =1 K T <sub>1</sub> =0.1 K
St. steel 18/8	12.3	10.3	4.3	0.2	0.06
Copper (electrolytic)	410	570	980	200	40
Copper (phos-deoxid)	190	160	80	5	1
Brass (70Cu/30Zn)	81	67	26	1.7	0.35
Constantan (60Cu/40Ni)	20	18	14	0.4	0.05
Inconel X	10.7	8.9	4.6		
Machinable-glass ceramic (MGC)	2	1.6	1.3	0.03	0.004
Pyrex	0.82	0.68	0.25	0.06	0.006
Nylon	0.31	0.27	0.17	0.006	0.01

### 3.1.4 Vacuum pump and minimization of convection

The process of pumping a vacuum of the chamber plays a vital role in the experiment to reduce the effects of conduction and convection caused by the gas within the container. The typical levels of vacuum for cryogenic experiments is in the range of  $10^{-4}$ - $10^{-8}$  mbar. This process in a cryogenic experiment passes through different stages: a major stage of pumping is accomplished with mechanical pumps using a pumping station which is detached from the cryostat. In our experiment, the pumping station consists of a turbomolecular pump backed by a rotary pump which is mounted on a cart.

A vacuum pumping system is ideal and characterized by a valve system that enable us to operate the turbopump even after opening the fridge and removing it from the chamber. In this case we can save time re-setting up the fridge with no need to repeat pumping back down to vacuum. A diagram of the setup is shown in Fig. 3.3.

Through specific points in the pumping station, the vacuum can be measured at the pumping station through points marked as 1, 2 and 3 channels via two Pirani gauges and a Penning gauge, respectively, , where gauges 2 and 3 are placed at the turbomolecular pump.

The Penning gauge, which is placed at the bottom of the chamber, is responsible for measuring the vacuum in the cryostat chamber.

The procedure for operating the pumping station is as follows. Originally, the pumping methodology was devised by Robert Limpenny and Dr Gauthier Torricelli and carried out by a colleague, Dr Mendoza-Luna, then myself.

- First step/ To start up the pumping system:
  - Ensure that valves PV0, PV1, PV2, PV4 and PV6 are closed before starting pumping cart operation.
  - Start the rotary pump. Wait at least 5 minutes to standby before opening PV0.
  - We have to check the oil level in rotary pump is greater than the minimum.
  - Open PV0 and PV1.
  - The reading on CH2 must drop to  $5 \times 10^{-2}$  mbar or lower (all channels seen in green digit panel as shown in Fig. 3.4), then start to evacuate the turbo pump.
  - Check CH2 and CH3 to ensure the turbo is operating correctly and normally.
- Second step/ To operate the roughing system.

- Check roughing line by closing PV0, open PV2 to gain atmospheric pressure.
  - Check pressure of the roughing line at CH1 to ensure the pressure achieved is  $5 \times 10^{-2}$  mbar or less.
  - Ensure the pressure of the turbo backing line (CH2) does not go above the critical backing pressure for the turbopump ( $5 \times 10^{-2}$  mbar). If it does, close PV2 for few seconds, hence open PV0 to drop the pressure in the backing line of the turbopump.
  - When the pressures at channels CH2 and CH3 are stable at a reading of  $5 \times 10^{-4}$  mbar and  $5 \times 10^{-4}$  mbar respectively or less, roughing line check process can be resumed safely again.
- Third step/ To rough out OVC
- Connect the pumping line to the refrigerator.
  - The value of turbopump pressures should be  $5 \times 10^{-4}$  mbar on CH2 and less than  $5 \times 10^{-4}$  mbar on CH3
  - Close PV0, open PV2.
  - Ensure that pressure at CH1  $5 \times 10^{-2}$  mbar or less, then open PV4.
  - Open slowly PV5 and rough out OVC to  $5 \times 10^{-2}$  mbar or less.
  - When the OVC is at  $5 \times 10^{-2}$  mbar or less, close PV2, open PV0, then open PV3 to continue to evacuate the OVC to below  $10^{-2}$  mbar.

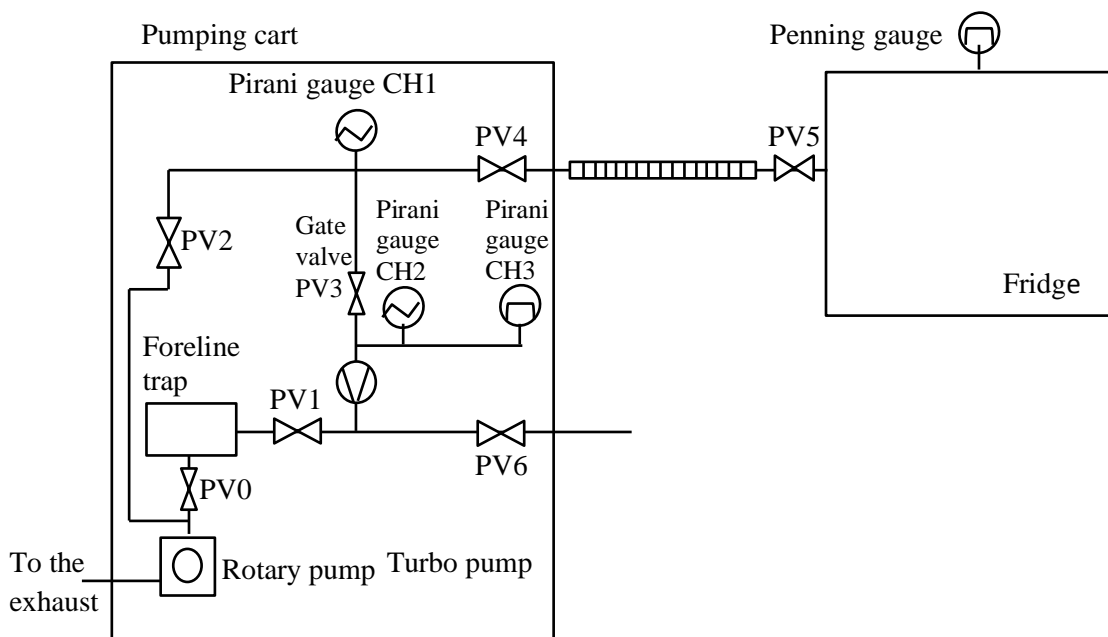


Figure 3.3: Schematic diagram of the pumping station shows the steps described above in the experiment. Figure reproduced from [3].

Next step, the process of the cooling-down can be started, once when the reading in the Penning gauge that measure the vacuum in the chamber achieves  $10^{-4}$ - $10^{-5}$  mbar. The cooling process, which will be explained in subsequent sections, enhances the pumping process by reducing the pressure in the chamber to  $10^{-6}$  mbar. Fig. 3.4 shows a photo of the vacuum pumping station utilized in the experiment.

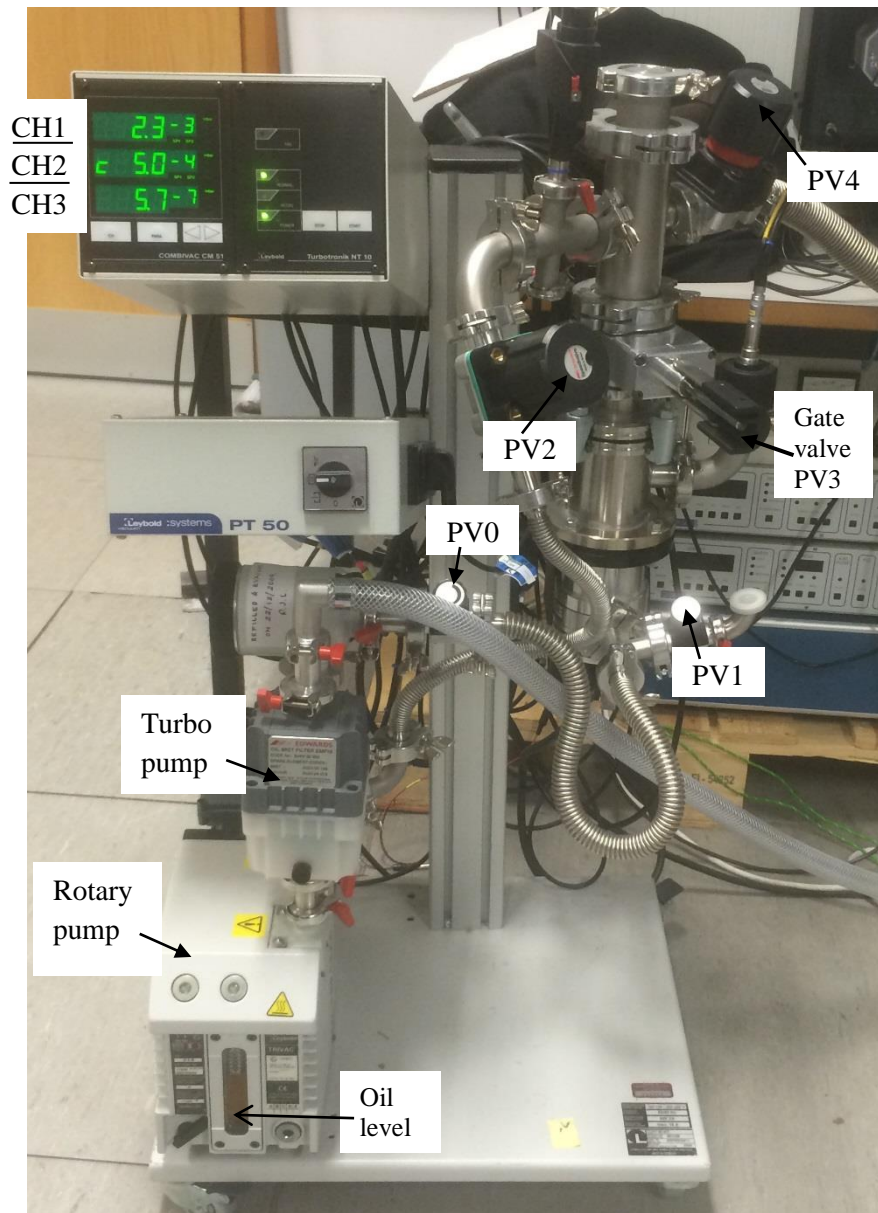


Figure 3.4: Photo of pumping cart utilized in experiment shown the main valves that are responsible from evacuation process out OVC. This photo was pictured in the Space Research Centre (SRC), at the University of Leicester.

### 3.1.5 Operation HelioxAC-V $^3\text{He}$ Refrigerator

The subsequent step after the pumping process is the cooling-down of the fridge. As mentioned, once when the reading in the Penning gauge that measures the vacuum in the chamber achieves  $10^{-4}$ - $10^{-5}$  mbar, the cooling-down process can be started.

Usually, at room temperature, the OVC should be vented by opening PV5 slightly to atmospheric pressure. Before proceeding any further, it should be ensured that valve VP1 is open too. To start cooling down the fridge, the outer edge of the top plate of the OVC has to be sealed to the cryostat by screwing down the six M4 bolts, then evacuated down to the range  $10^{-4}$ - $10^{-5}$  mbar. As explained in section 3.1.2, the cryo-refrigerator system is capable of attaining cryogenic temperatures. This system consists on the compressor package and pulse tube in which based on a cold head (an expansion chamber inside the fridge). So, cooling down the fridge is initially achieved by starting the compressor and cooling water. Hence, the cryogenic pumping has to be set after 24 hours of running the compressor under normal conditions. The electrical controls for the cold head motor are housed inside the compressor package which supplies the cold head with pressurized helium through flexible metal hoses.

As a complementary step to the previous procedure of pumping the OVC, the steps to operate the Heliox AC-V to cool down fridge are given below, where symbols for valves are relevant to Fig. 3.2 and 3.5:

- In order use the  $^3\text{He}$  as an exchange gas and to accelerate the cooling, close V1 when temperature is below 240 K.
- Set the SORB to 35-40 K. If the fridge runs during overnight, all the heaters have to be turned off for safety.
- Close PV5 and wait for the pot to cool down to 4 K.
- Open V1 to cool the refrigerator down to 300 mK.
- From ITC temperature controllers, set HS to 18 K and let it on until SORB cools down below 10 K (ideally 6-7 K), Then close V1.
- Heat SORB until reaching 35-40 K. Wait for 35 minutes or more until it stabilizes.
- Open V1 briefly. Opening V1 has a cooling effect.
- Set SORB to 0 and HS to 18 K.

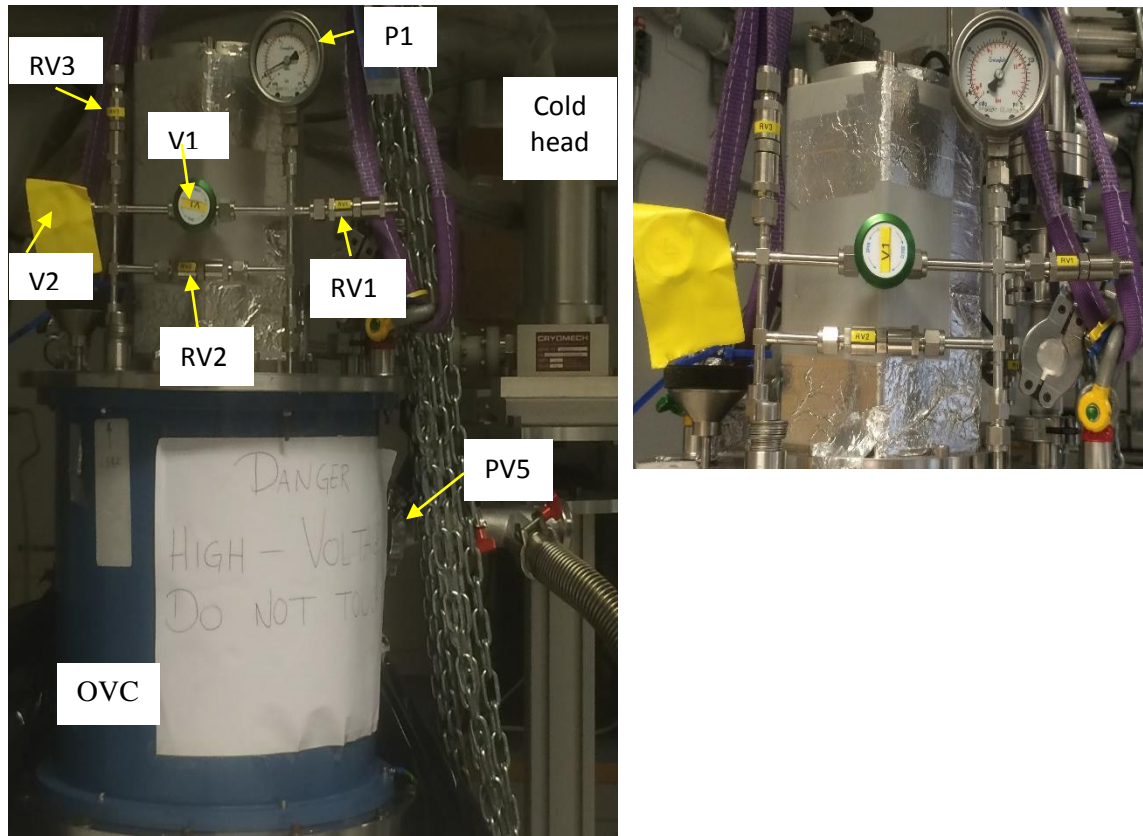


Figure 3.5: Image of the cryostat in the lab, showing the valve system drawn in section 3.2 (left side). On the right, the same image showing a close-up of the valves.

### 3.1.6 Gas installation and pressure measurement

As mentioned at the beginning of this chapter, the main equipment in this experiment was supplied by Oxford Instruments including; a  $^3\text{He}$  insert, cryostat, in addition to the refrigerator that consists from a pulse tube cryocooler and compressor. Also used was a high pressure cell with components from electrodes, lenses, etc (will explain in section 3.8.1) and the built-in gas supply line, which is an important part in itself and was specially built to feed the cryogenic cell. The pipes of the gas line used for this purpose were made of stainless steel with a Swagelok (part number SS-T1-S-020-6ME.) 6 mm O.D. (outer diameter) due to its ability to carry high pressure up to 100 bar. Furthermore, a high purity substance was required to pump to the cell, therefore the choice was to use helium of N6.0. To ensure a low leak rate, standard Swagelok seals were used.

Fig. 3.6 shows the set-up for the gas installation.

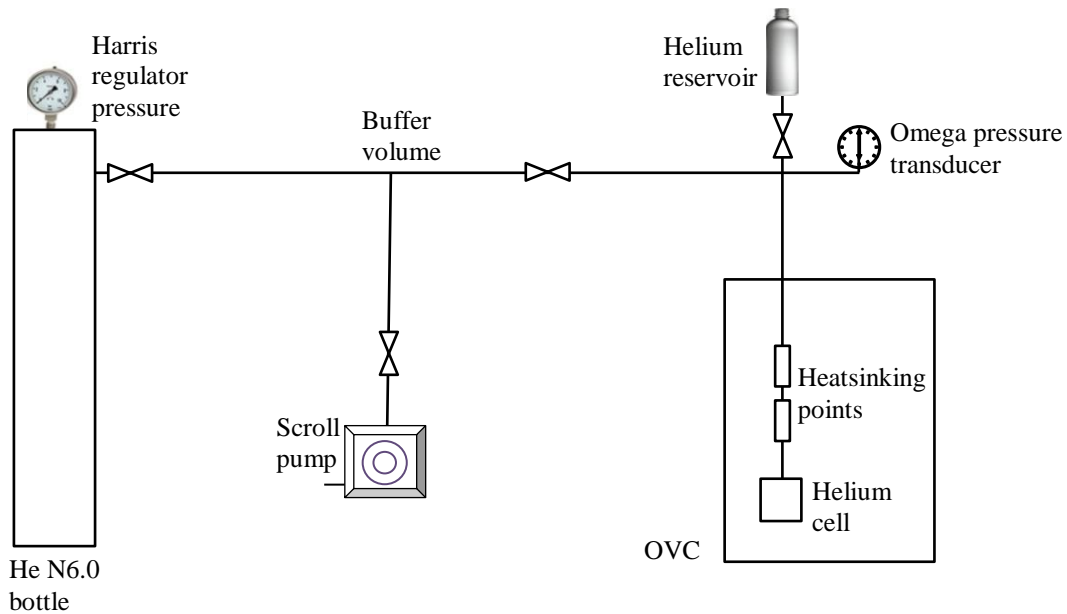


Figure 3.6: Schematic diagram of the gas installation. Figure reproduced from ref. [3].

In the present experiment, the gas line was divided into two sections (or even more, according to the need). The first section pumped the helium supply and the other the fridge part, where the process of evacuating and filling the gas line is easy each time the fridge is opened or closed. These two sections are connecting by a buffer volume. The first section that relates to the pumping-supply of the gas helium supply contains on a mechanical pump to evacuate gas lines, a series of ball valves that control the flow of gas through pipe, a big bottle of helium N6.0 and a Harris regulator pressure (up to 40 bar), while the second part of the gas installation (refrigerator part) is designed as a cross; the horizontal part from this cross connects to the buffer volume (in one end), so this part connected to the first, and the opposite end connects to the Omega pressure transducer. Either the vertical pipe, which is opposite to the fridge stand, the upper end of the gas pipe connects to the helium reservoir (0.3 litre) for the sake of maintaining a suitable volume of helium. This because when a high pressure of helium was required, this bottle provides and controls a big volume of helium through a ball valve. On the other hand, the bottle relieves the pressure in case we want to reduce pressure in the cell without losing the helium to atmosphere or contaminating the line. The fourth outlet of this structure accommodates a gas inlet system built for the Heliox cryostat.

The beginning of the inlet gas with a sector of 6 mm pipe is welded to the 25 KF flange to support vacuum seal. Inside the fridge, a three metre  $-1/16''$  O.D of the 6 mm pipe with pipe (0.020" wall thickness) was adapted inside the fridge, with a length of 1.5 m

between the two stages in the fridge (at 77 K and 4 K). In between these two stages a thin pipe was heatsunk by using copper bobbins (see Fig. 3.). Then, a pipe was connected to the cell via a flange.

In order to measure the pressure in the gas line and the cell, a PXM409-USBH Omega pressure transducer (0-100 bar absolute pressure USBH 0.14) was utilized. The PXM-409 High Speed USBH Series was connected directly to the computer. Free PC software made data logging and charting our readings a simple task. The pressure transducer has the following features [97]:

- USB output pressure transducer allowing up to 1000 readings per second.
- A major software update for USB transducers was involved; free OMEGA PC software took the data from the transducer directly to the digital domain, turning a laptop or Windows® tablet (with USB connection) into a virtual meter, chart recorder, or data logger.
- Charting window, which allowed us to see the data graphed in real time. The Y-axis is configurable to allow simultaneous graphing of multiple engineering units. An image of the data can be written directly to a png file.
- Channels Window, which displays all data from all sensors simultaneously. Each channel has configurable user alarms, three data filters, resettable low/high indication, and sample rates ranging from 30 minutes to 1000 Hz.
- The micro-machined silicon design is ideal for pressure or level applications in the laboratory that requires a high accuracy transducer. The micro-machined silicon sensor provides a very stable transducer with exceptional high accuracy of  $\pm 0.08\%$  and a broad compensated range of  $-29$  to  $85^{\circ}\text{C}$ .

### **3.1.7 ITC Temperature Controller and thermometer**

Two ITC503 temperature controllers were utilized in the previous steps (3.1.5) to control the HelioxAC-V  $^3\text{He}$  system. The first ITC503 (ITC-number 1) was used to control the temperature of the  $^3\text{He}$  pot and the sorption pump (SORB), through the entire operating range of the system. The second (ITC2) is used to monitor the temperature of the switch heat (SH) that indicates the thermal link between the sorption pump and the PTC 2<sup>nd</sup> stage, and to control the temperature of this stage [5]. The software provided with

ITC503 allows the range to be altered easily to cover a wide range of sensors. Fig. 3.7 shows images of the ITC503 devices (two controllers in top of each other) used in the experiment, and the second image (b) for panels showing type of sensors<sup>4</sup> for each controller. A Cernox resistor (CX-1030-CU-HT03L) has been selected for thermometry purposes. This is due its ability to measure temperatures in the range between 0.3 - 325 K. Once the cell has been placed in position in the chamber, the thermometer (wiped with acetone and rubbed with Apiezon-N) is mounted on the one side of the cell (the spark cell will be discussed in the next section).

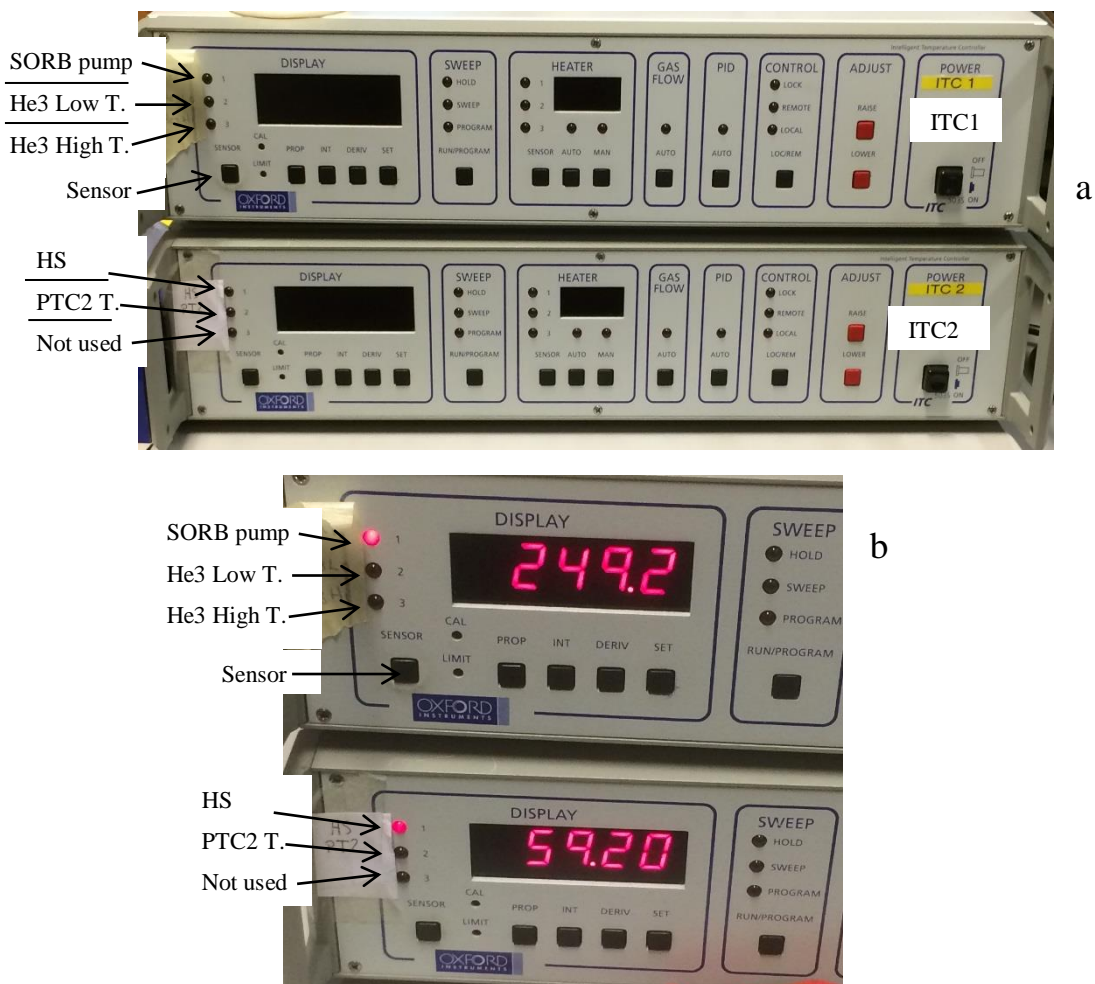


Figure 3.7: Detailed image of the ITC503 temperature controller is illustrated. The two controllers ITC1 and ITC2 were placed in top each other to run sensors easily as shown (a). Image of ITC 1,2 run which is zoomed in to show only the effective part of the panel with the sensors' buttons. The third sensor in ITC2 controller is not used (an example of using ITC- b).

<sup>4</sup> By pressing the sensor button (Fig. 3.7), one can cycle through the three stages of temperature monitoring for each kind of ITC503 temperature controller. Also, from the red buttons in the devices, we can adjust the temperature to lower or higher values.

### 3.1.8 High pressure cryogenic cell and components

The idea of using a spark cell to run the corona discharge at high pressure is not new. Due to the importance of the role of the cell, it is considered to be the very heart of the experiment. Conceptually similar to that previously used by our collaborators in Grenoble, France, Li *et al.* [8] used a cylindrical cell with an electrode spacing of 8 mm, but with better performance in a number of areas. One of these was a requirement that the cell could operate at high pressures and at cryogenic temperatures around 4 K. This was achieved by a newly designed high-pressure cell. A major difference in new design is the reduced gap between the tip and plane electrodes that existed in the cell by building a considerably smaller cell (4-6 mm) than the original one.

Generally, a cube-like design was chosen for the cell, providing faces for flanges for two high voltage electrodes, the helium gas supply and a window to couple out the fluorescence light. The approximately cubic cell had a side length of approximately 50 mm, providing an internal volume of 4 ml. The coaxial cell is rated to approximately 100 bar helium. Technical drawings of the cell were drawn up by one of the members of our group, Dr Luis Mendoza-Luna [3], and built by the Mechanical Workshop of the Physics Department at the University of Leicester, are given in Appendix C.

The cell is made of oxygen-free copper (OFHC) to improve performance of thermal conductivity at cryogenic temperatures by minimizing the size of the cell. The four flanges on the windows that provide the sides of cell allow for a system to feed the cell with helium gas (gas inlet) on one flange, on the opposite side of the gas inlet a mount for a lens (15 mm-diameter) to diverge the light from cell to the rest of the (external) optical layout (see schematic diagram of the optical system in Fig. 3.11). The last two opposing flanges accommodate the plane-tip electrode pair with a typical separation of 4-6 mm.

The high pressure cell consists of the following items:

#### 3.1.8.a The configuration of a plane-tip electrodes

The most important element in the spark cell are the tip-plane electrodes. Both the tip bearer and plane electrodes are made of stainless steel. The flat electrode that has cylindrically symmetric plate represents the anode (positively charged electrode) with  $\varnothing$  8.0 mm, 1.25 mm thickness and 43.5 mm length. Regarding the tip bearer, this has a

fine end that is triangular in shape containing a channel to hold the tip needle which is the source of electrons. The tip that is welded to the stainless steel brace is made of tungsten with a radius of curvature of around 200-250 nm (as determined from TEM), where the total length of tip and bearer is approximately 47.75 mm (3 mm length of tip). Technical drawings of the electrodes are shown in Appendix D. Fig. 3.8 shows a general plan for the tip-plane electrodes, with the figure was taken from ref. [3].

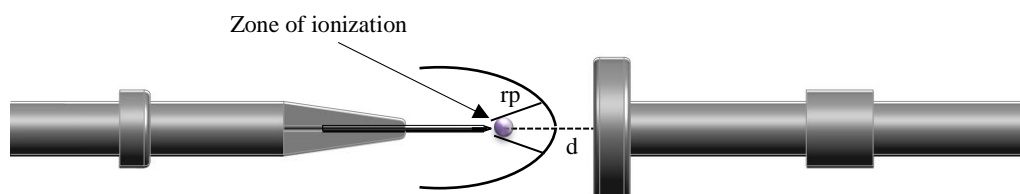


Figure 3.8: Physical description of the plane-tip electrode array. The tungsten needle (in black) has been spot welded on to the stainless steel pin (left). The plane electrode is grounded (right), while the tip can be either at positive or negative polarity with respect to ground.

The plane electrode is earthed while the tip electrode can be held at a positive or negative polarity (in our experiment, a negative polarity was used). The cell can withstand a DC voltage of  $\pm 10$  kV and produce currents of the order of hundreds of microamps (at room temperature), and is able to sustain the discharge for at least several hours in gas and liquid helium started at approximately 10 kV (negative polarity). The choice of a tip with a small radius of curvature is explained by the fact that we want a spatially well-defined discharge zone in order to carry out a spectroscopic study of the emitted light and the discharge current without ever reaching a breakdown that would destroy the tip and the measuring devices.

The tips are prepared by the electrolysis of a tungsten wire. The tungsten tips that we used in these experiments were prepared by Dr Mark Watkins, in a project for student Naomi Vellody Williams and the PhD project of Dr Mendoza-Luna, all at Leicester University. The procedure for preparing the tip is based on ref. [98]. The stability of the tip plays a crucial role whereby, a sharp tip is desired. The optimal parameters for achieving these characteristics of tip etching are: 8.0 g concentration of a solution of NaOH, 100 ml distilled from water and an applied voltage of roughly 5-10 V.

Either regarding tip-plane configuration, given the importance of understanding phenomena occurring in an intense electric field in liquid dielectrics, an approach to the original concept developed in the laboratory based on the study. The tip-plane geometry plays a vital role in the generation and transport of charges as a function of the density of the medium (from atmospheric pressure gas to liquid state).

In general, a very high electric field ( $\sim$ MV/cm) is required for the generation of charges in a liquid dielectric. The use of a tip-plane geometry makes it possible to obtain this generation field locally near the tip without this causing the dielectric breakdown of the liquid due to a low value average field between the electrodes. It can thus distinguish two different regions between the electrodes; a region located near the point (ionization zone) at a distance of the order of the radius of curvature of the point ( $r_p$ ) ( $\sim\mu\text{m}$ ), where the charges creation. The other region is the remainder of the distance point-plane ( $\sim$ mm) which is near to the plane space and under a weak middle field ( $\sim$ kV / cm) as shown in Fig. 3.8. In geometry nearby the tip-radius of curvature of the point; upon the high voltage application across this region, the charge generation occurs, is confined near the tip, which avoids the phenomenon of breakdown [99]. Most of the point-plane distance ( $d$ ) is, however, subjected to an insufficiently small field (because  $d \gg r_p$ ) so that no charge generation is possible there, only the transport of the charge created near the tip can occur. For this reason, a small distance between the electrodes is required.

### 3.1.8.b Macor ceramic insulator

In the cell, the metal electrodes (tip and plane) are supported by Macor insulators. Macor is both an electric and thermal insulator with little thermal expansion or outgassing. Macor can be considered unique as its composition comprises 55% fluorophlogopite mica and 45% borosilicate glass. Corning's unique production process results in Macor's microstructure, which is key to its versatile properties [100] [101]. Macor is a good thermal insulator and is stable up to temperatures of 1000°C, odourless, non-outgassing material that exhibits zero porosity, and unlike ductile materials, doesn't creep or deform. As an electric insulator, particularly at high temperatures, it is excellent at high voltages and a broad spectrum of frequencies.

After that sealing is ensured by indium seals ( $\varnothing$  1mm) and stainless steel flanges. The seals are made of indium which is a material of choice in the cryogenic regime. Indium is characterized by providing a low leak-rate seal and does not decay at low temperatures

at high pressures. The Macor holds the electrodes and is sealed using indium in the present experiment, as shown in Fig 3.9. A cross-section of an assembled copper cell design with its components is shown in Fig. 3.10 [3].



Figure 3.9: Image of Macor ceramic piece holding the tip-plane electrodes that are sealed with indium (indium does not appear in the image, and the Macor (the only item in the cell was bought from external company not built by the university).

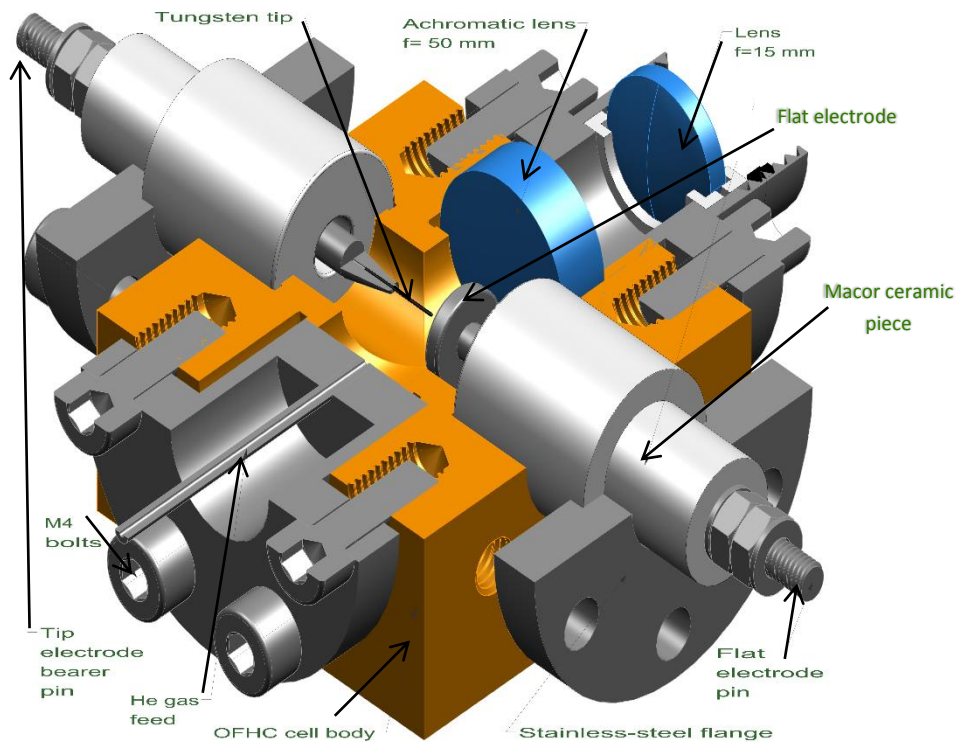


Figure 3.10: Cross-sectional view of the discharge region of the high pressure copper cell (assembled). This design was done and used by colleague Dr Mendoza Luna [3]

### 3.1.9 The Optical Layout

The fundamental objective from experiment was to measure a larger number of spectra in a given time per experimental run as possible with the apparatus used. This was achieved by a newly designed of a multiple lens system which was able to collect fluorescence light over a large solid angle and delivered the light to the detector with significantly reduced loss in intensity. Most important in the first step of this system is the distance between the object (spark of the discharge) and the first lens, which has to be placed as near to the object as possible. Therefore, using a lens that has focal length smaller than the mentioned distance is preferred. Otherwise, with a larger focal length, a virtual image is generated away from the discharge spark (behind the object) on the same side of the optical axis. Consequently, the beam of the light will diverge off the lens cause some loss of light on its way to the next lens (see Fig. 3.11). The proper distance between lenses and the tip electrode was measured according to the lens formula [102];

$$\frac{1}{f} = \frac{1}{u} + \frac{1}{v} \dots \dots \dots (3.8)$$

Where  $u$  is the distance of the object from the lens,  $v$  is the distance of the image from the lens and  $f$  is the focal length of lens, i.e., the distance of the focus from the lens.

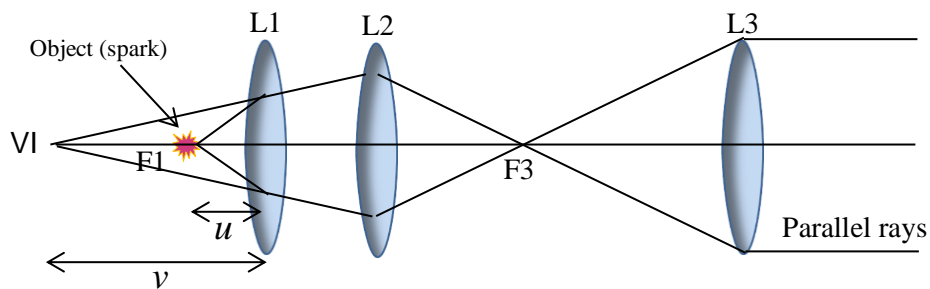


Figure 3.11: Schematic diagram of the optical pattern that used in experiment to merge the emitted fluorescence light from inside the cell (vacuum regime) to the out of the chamber (out the vacuum). The system consists of three lenses L1, L2 and L3, with focal lengths of 50, 15 and 50 mm respectively. The object represents the position of the spark of the discharge that is placed between the lens (L1) and its focal length (F1). A virtual image (VI) is created to be behind the tip according to the eq. (3.8). Then L2 (second lens) picks up the diverging beam from L1 and converges it on the optical axis at a point F3 (focal length of the third lens L3).

In the present experiment, the distance between the spark and first lens is 8 mm, but finding a lens with a focal length less than 8 mm was impossible. Therefore, an achromatic lens (Edmund Optics Dwg. No. 47702INK) with a focal length ( $f$ ) of 50 mm was used instead of. Consequently, the virtual image of discharge is generated behind the object, at a distance of -9.5 mm from L1. As we mentioned before, due to the large  $f$  of L1, the beam will diverge, and a second lens (L2),  $f = 15$  mm (Thorlabs Part No. LB1092) must be placed after L1. L2 was added to collimate and focus the diverge light from L1 to a pinhole (1 mm in diameter) that was etched on the flange of the first heatshield to prevent radiation from entering the cell. So, this aperture is considered to be a connection ring between cold regime (cell including L1 and L2) and the surrounding temperature (at the first heatshield). By placing a third lens (again achromatic lens /an Edmund Optics Dwg. No. 47702INK) on the flange of the second heatshield, the diverged light from pinhole is collected to send as a parallel beam to the next step. Fig. 3.12 clarifies the arrangement of optical system.

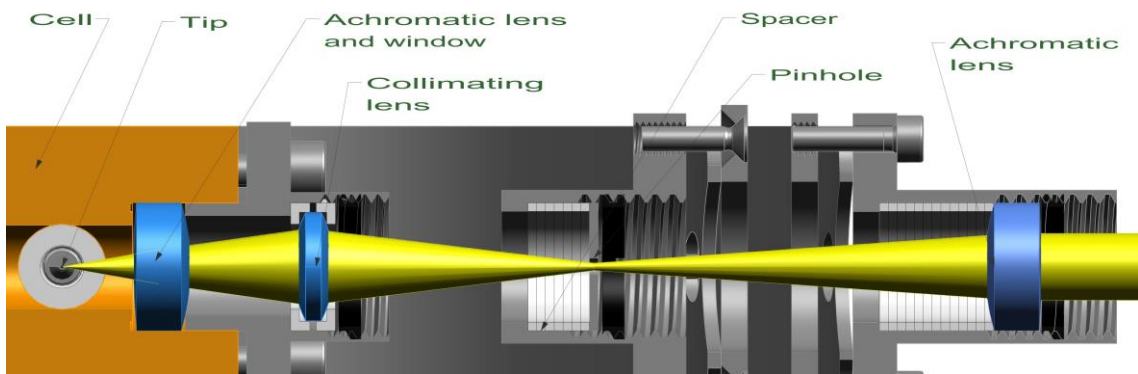


Figure 3.12: Cross section of the optical setup explained mathematically in Fig. 3.10. The divergent light is picked up by the achromatic lens ( $f = 50$  mm) with a 15 mm diameter, then collected by the second lens ( $f = 15$  mm) with a 12.7 mm diameter; a holder was built up to hold L2 to fit with bores 15 mm. The final step in the optical process within the chamber is with a third lens ( $f = 50$  mm) in 15 mm diameter, which converges the light to produce the parallel beam that is sent outside the chamber. Figure taken from ref. [3]

Either the optical setup outside the chamber (ambient at room temperature), includes a pair of mirrors (40 mm diameter) that were placed in parallel to lead the parallelized beam into the last lens ( $f = 150$  mm) with a 25 mm diameter (see Fig. 3.17), where the parallel beam was collected and focussed by L4 towards a slit of a Czerny-Turner

spectrograph [103], (Andor Technology Shamrock SR303i), and imaged onto a CCD chip (Andor CCD-12855 - iDus Camera DV420) to record in a computer for analysis. To minimize shot noise, the CCD camera is cooled to  $-65^{\circ}\text{C}$ .

### 3.1.10 The electrical layout

The process of igniting a discharge in plasma is dominated by the electrical installation that is run by the current-voltage values. The electrical circuit consists of the array of the tip-plane electrodes connected to a high-voltage ammeter and voltmeter by a coaxial cable. The stability of the current affects the sustainability of discharge in plasma. Voltage and current measurements are important to give an idea about the Joule heating that indicates the changes of phase of helium. Therefore, the typical value of current in the setup is  $300\ \mu\text{A}$  in the gas phase, while in the subcritical phase it is  $1\ \mu\text{A}$  in a stable discharge. Additionally, by knowing the values of current and discharge, the mobility of ions and electrons in helium can be calculated [99]:

$$I = C_t \mu \epsilon \frac{(V - V_0)^2}{d} \dots \dots \dots (3.9)$$

Where  $I$  represents the current,  $V$  is the potential difference,  $V_0$  is threshold voltage,  $C_t$  is a constant,  $\mu$  is the mobility and  $\epsilon$  is the dielectric constant ( $= \epsilon_0 \epsilon_r I$ ). Fig. 3.13 represents the circuit diagram of optical layout.

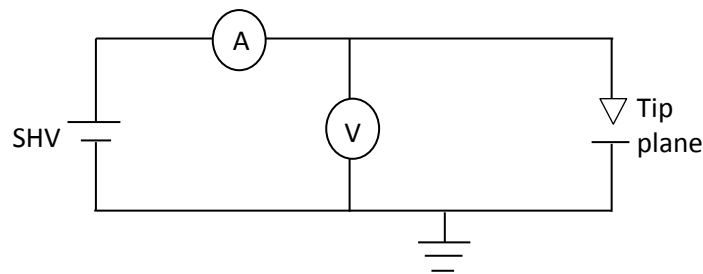


Figure 3.13: Circuit diagram of the experiment. The inatrucmental setup consists of an ammeter and voltmeter suitable for high-voltage uses connected in parallel with the electrodes. The plane electrode was earthed.

A high voltage was applied across tip-plane electrodes via a DC power supply (Spellman /MPS15N10/24/DCC2) under negative polarity and using high voltage cable (SHV); voltages in excess of 10 kV could be required at this stage. An instrument suitable for high-voltage use was constructed in-house. This consists of two pieces of equipment (an ammeter and voltmeter) coupled in one device to provide us with simultaneous readings of current ( $\mu\text{A}$ ) and voltage (kV). Fig 3.14 shows an image of this Avometer; see also the electronic map for more detail in Appendix E.

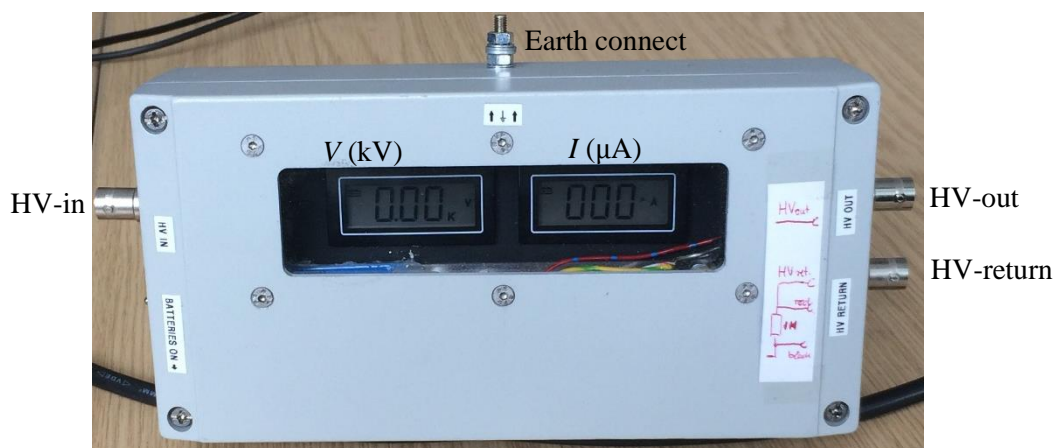


Figure 3.14: Image of the device used to measure high voltage-current applied to the tip-plane electrodes. A DC power supply (Spellman /MPS15N10/24/DCC2) feeds the cell through this avometer under negative polarity.

### 3.1.11 Assembly of the experimental setup

It is noteworthy that the copper cell in this experiment has a  $180^\circ$  symmetry, making the opposite faces of the cell identical, though not neighbouring faces. There are holes in all faces to accommodate the components of the cell, from the electrodes to the lenses and gas inlet. Therefore, an indium gasket must cut and placed against each of these components to ensure the cell is fully sealed. The dimensions of the gasket correspond to the size of the holes for each of the above cell components which are 15 mm, 13 mm and 1 mm outer and inner diameters and thickness, respectively. The lens is one of the most important components that needs delicate work to emplace, where the achromatic lens sits against the indium gasket in specific flange to hold it in place. An achromatic lens is used for two purposes; once to steer the light toward spectrometer and to obtain

a good seal. Then, the lens holder is inserted into the bore with a thin (1 mm-thick) PTFE spacer between them. After that, this arrangement is held in place and tightened against the indium seal by a flange on the front of the face of cell.

The Macor ceramic pieces that hold the tip-plane electrodes in place were also sealed with indium in addition to the flange's holes. The tungsten tip was spot welded onto the tip bearer electrode which is pushed against the inner face of the Macor pieces, as per Fig. 3.9. Then an indium gasket per electrode and the Macor piece (including the electrode) were inserted into the bore and pressed against the cell via the stainless steel flange.

Finally, the last face of the cell is that used for the gas inlet, which is opposite the lens, where the gas feed line linked into the corresponding bore and pressed against the cell to ensure a good seal with the indium gasket. To complete the cell, M4 fasteners with Belvoir washers were utilized on the walls and sides of the cell. The last step before attaching the cell to the rest of the experiment, was to test the cell with a helium leak detector.

When the copper cell is assembled, a "concentric-eccentric" adapter piece, which is also made from the copper, was used as a base on which to mount the copper cell. The component faces were wiped with acetone followed by Apiezon-N cryogenic grease.

Due to the softness of the cell, metric brass fasteners were used to screw the copper parts of the cell into position. When the cell was emplaced in the cryostat and ready to use, the thermometer was bolted onto one of its faces.

Next step is the thermal link between the first and second stage by cryogenic wires that would act as the heatsink between these two stages (typically phosphor-bronze, constantan or nichromel) which had a smaller thermal conductivity than the other metals, to the extent that it could be considered a thermal insulator compared with copper.

For the liquid phase experiments, high power would be needed to ignite the discharge, leading to increased Joule heating. The cooling power of the  $^3\text{He}$  pot was insufficient to overcome this Joule heating, as was discovered by the researchers. Therefore, to overcome such problem, strips of copper were used as a thermal bridge to link the cell to the second stage, to transfer the cooling power of the latter, and reduce Joule heating to keep a constant base temperature of 3.2 K (see Fig. 3.15).

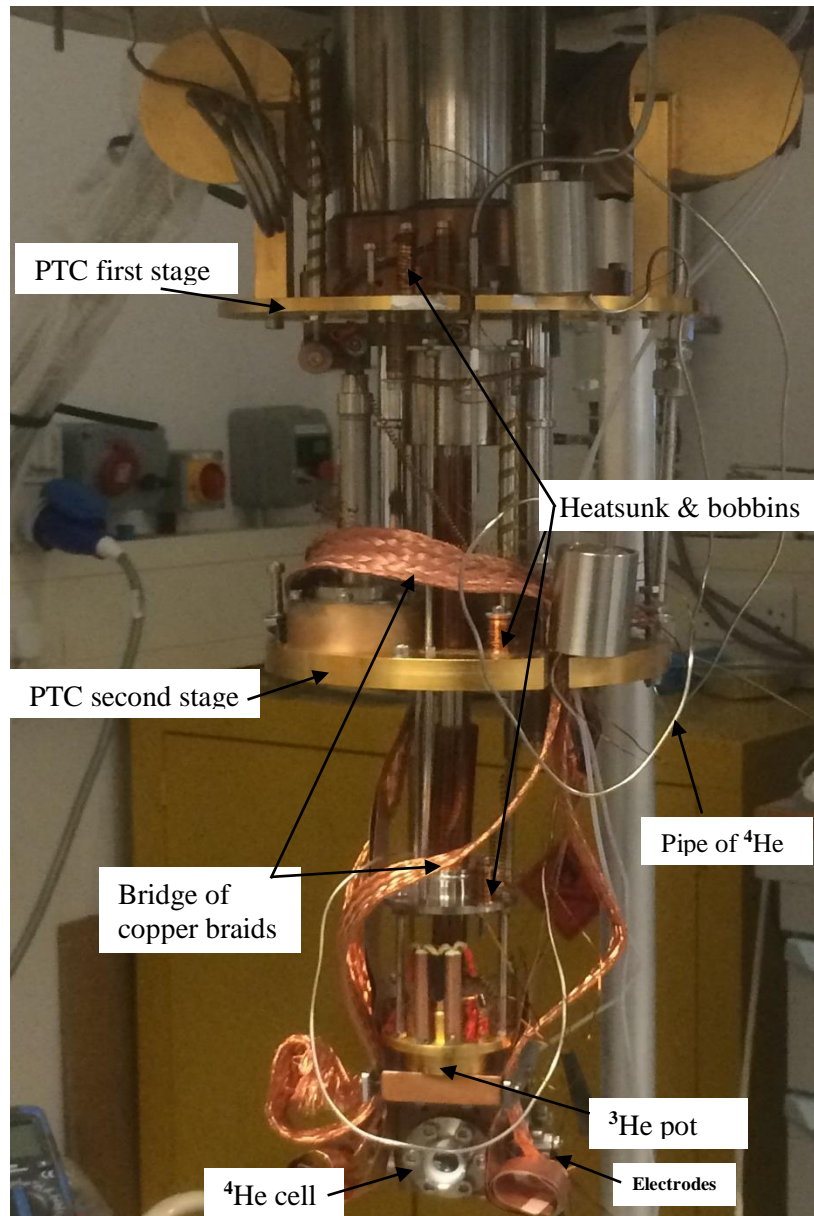


Figure 3.15: Image of cross section of the inner section of fridge showing; first and second stage, copper cell attached to the  $^3\text{He}$  pot, where copper braids were used to thermally link the cell to the second stage and cryogenic cables around a bobbin to allow for efficient heatsinking. This image was pictured in the Space Research Centre (SRC) lab, University of Leicester.

As mentioned, phosphor-bronze cables that to be heatsunk, were chosen to accommodate the high voltages utilized. A polyimide material was used for insulating these cables. However, the thickness of polyimide was not able to prevent short-circuits to ground that arise at potential differences of about 4 kV [3]. Hence, to use 10 kV at negative polarity (in present setup), a PTFE-sleeving (which cannot be heatsunk) was utilized. Another way reduce the thermal gradient between the ends of a cable was by using cryogenic wires inside the fridge being heatsunk. These cables were wrapped around copper bobbins then mostly placed on the two stages in the fridge (usually at 4 K and 80 K) as shown in Fig. 3.15. The subsequent cooling efficiency depends on the number of turns. To get efficient heatsinking, at least five turns of a wire around a bobbin are recommended [104].

Two heatshields are then mounted on the first and second stages of the fridge. These heatshields include cylindrical slots which accommodate lenses described above that include 1 mm-thick plastic spacers. The dimensions of these slots correspond to the dimensions of optical setup shown in Fig. 3.12. The inner heatshield sits around the pot of the fridge and is bolted to the first stage, while the outer one covers the first heatshield and was bolted to the second stage. The fridge was then lifted via a crane and dropped into the vacuum chamber, which is fitted with a window for coupling out the emitted light. The complementary parts of experiment, an electrical feed socket, a Penning gauge to assess the vacuum, compressor and pulse cold head were fitted to the outer vacuum chamber (OVC). Fig. 3.16 shows a drawing of the insides of the cryostat after the above assembly is complete, while Fig. 3.17 shows the entire setup including the inner section of fridge, gas installation, optical setup and data collection, which is the last step in procedure.

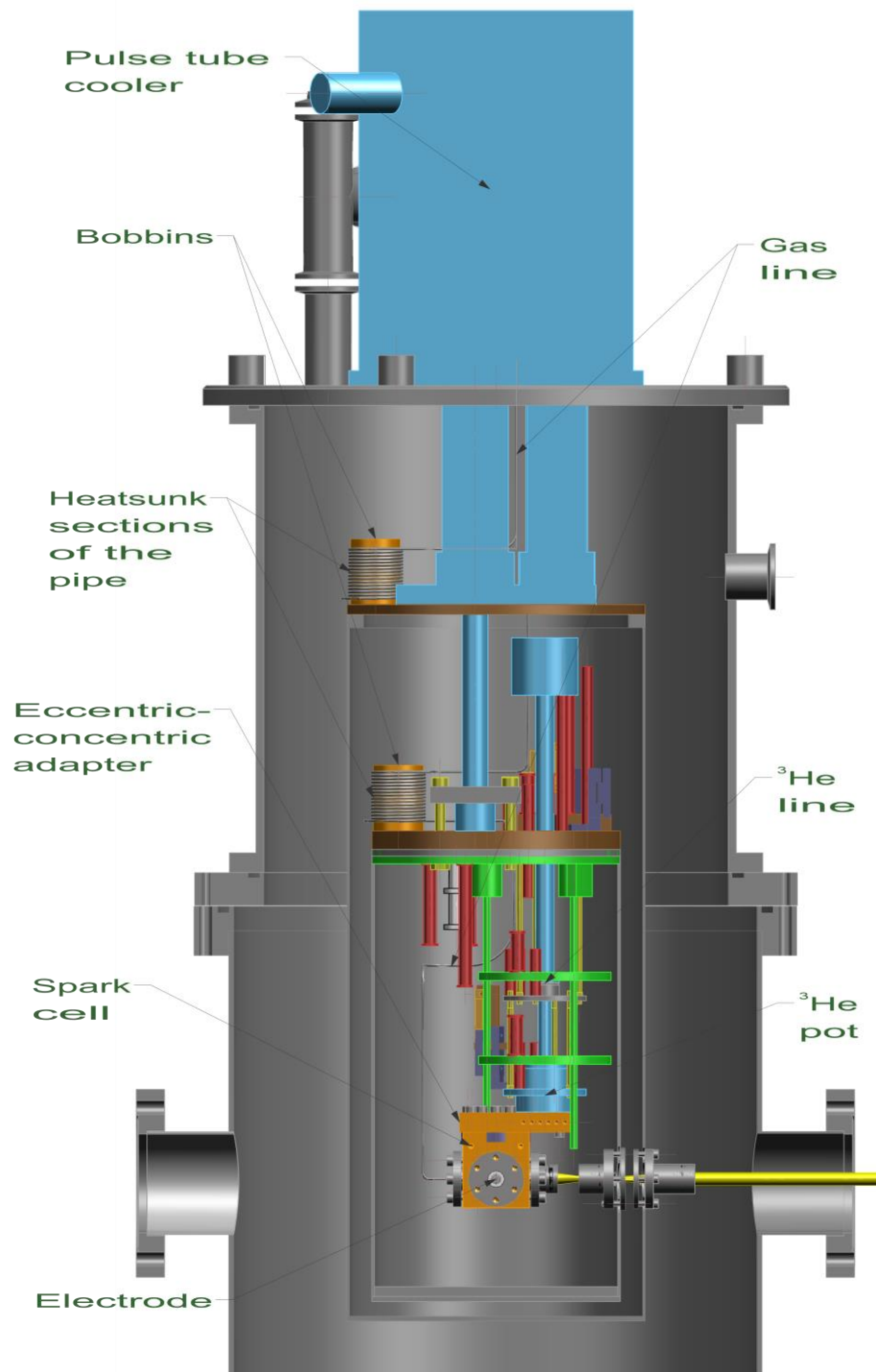


Figure 3.16: Cross section cryostat after assembling all components that has been mentioned in this section. Inner section of the tubing is shown clarifying the fine details and coherence of this design. This design already was used by collaborator in same our group [3].

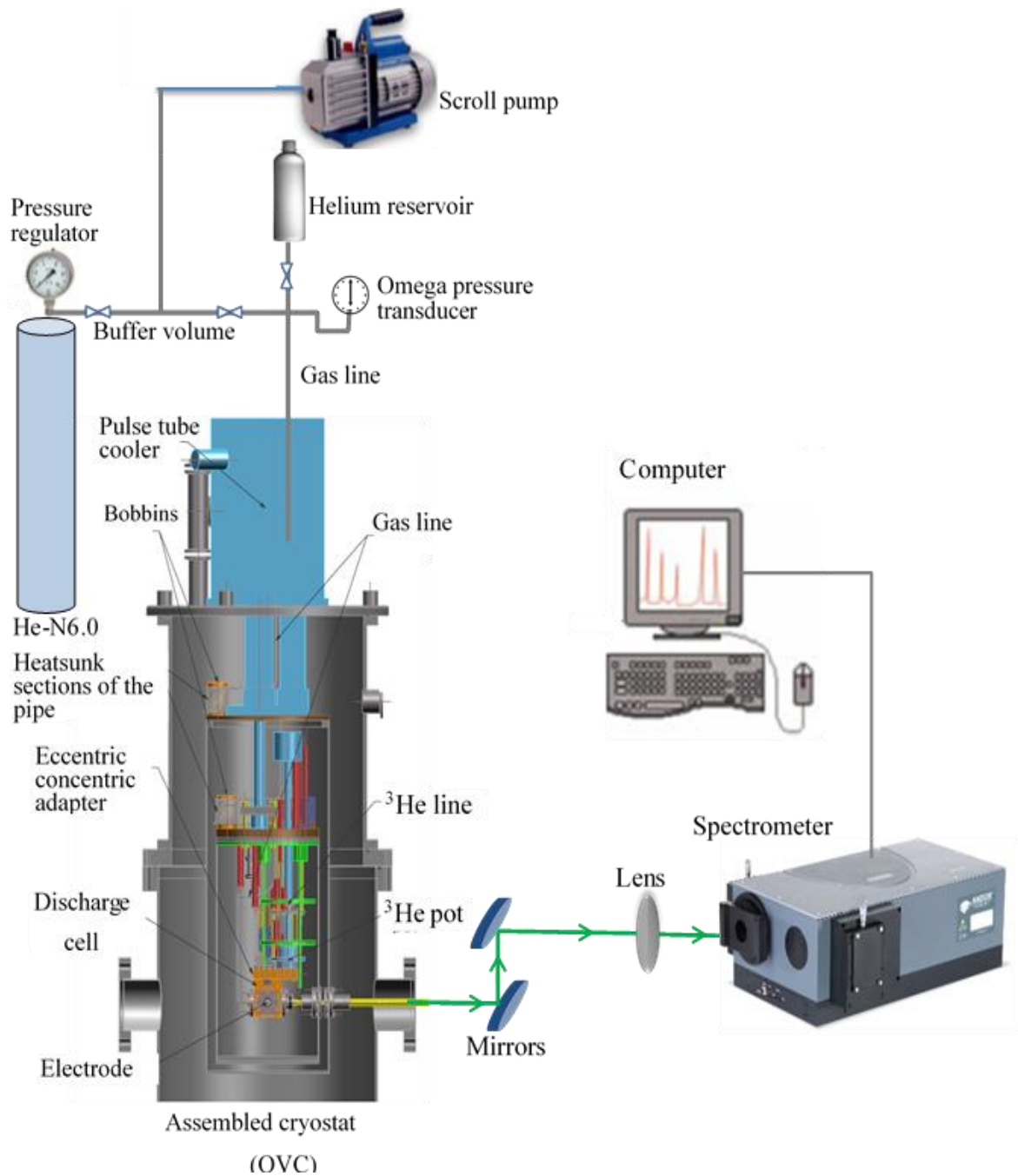


Figure 3.17: The entire experimental setup including the inner section of fridge, gas installation, optical setup and data collection by the computer, which is the last step in the procedure.

### 3.1.12 experimental procedure

This section explains the steps to run this experiment. After assembling the experiment parts explained in this chapter into the fridge and connecting electrical cables (SHV).

The experiment is ready to operate with the following steps;

- The first step as mentioned above in section 3.1.4 was routine of the pumping vacuum to the chamber and minimization of convection.
- Also the gas line was cleaned from impurities with the vacuum pump process by using scroll pump machine. Then the gas line was filled with 3-10 bar of He N6.0, then flushing out the helium, this process was repeated many times to flush all impurities. Although high purity of helium (99.9%) we used in present experiment, it still contains impurities such as hydrogen and oxygen.
- The cold process starts now for the fridge by the pulse tube cooler (typically below 20 K), when we reach to this temperature, all impurities have been frozen and stuck up upon container wall, consequently, no emission spectra were observed for this impurities as will we see in chapter of results (steps of cooling down in section 1.3.5).
- To test the electrical connectors and to run a corona discharge to be able recording fluorescence spectra, applying a high potential difference across the electrodes was required. By using different power supply depending on the value of voltage that discharge required. Once getting stabilized discharge, go to the next step.

In sake of follow up the emitted light from the cell after a corona discharge obtained, another optical setup was need. This setup can be done and aligned outside the vacuum chamber, this was upon an optical breadboard that lies between the cryostat chamber and spectrometer. This setup which includes two mirrors and lens is a complement to the first set inside the fridge. Where the parallel emitted beam from inside the cell through the (OVC) steer onto final lens in this arrangement in which focuses the beam onto the slit of the spectrograph (see Fig. 3.17, to follow up the green arrow as parallel light from OVC to spectrograph). Fig. 3.18 shows an image of the optical setup outside OVC. The spot of light that generated via corona discharge in the tip-plane space was considered as a typical source to the emitted light to follow the image on the entrance slit of the slit of an Andor Technology Shamrock SR303i Czerny Turner spectrometer. Hence, by manipulating with mirrors and lens an appropriate image can be obtained, then a suitable alignment of optics can be depended. The methodology of collecting

spectra will be shown in next section. So, with this optimization, the experimental procedure has been finished to go ahead towards data recording.

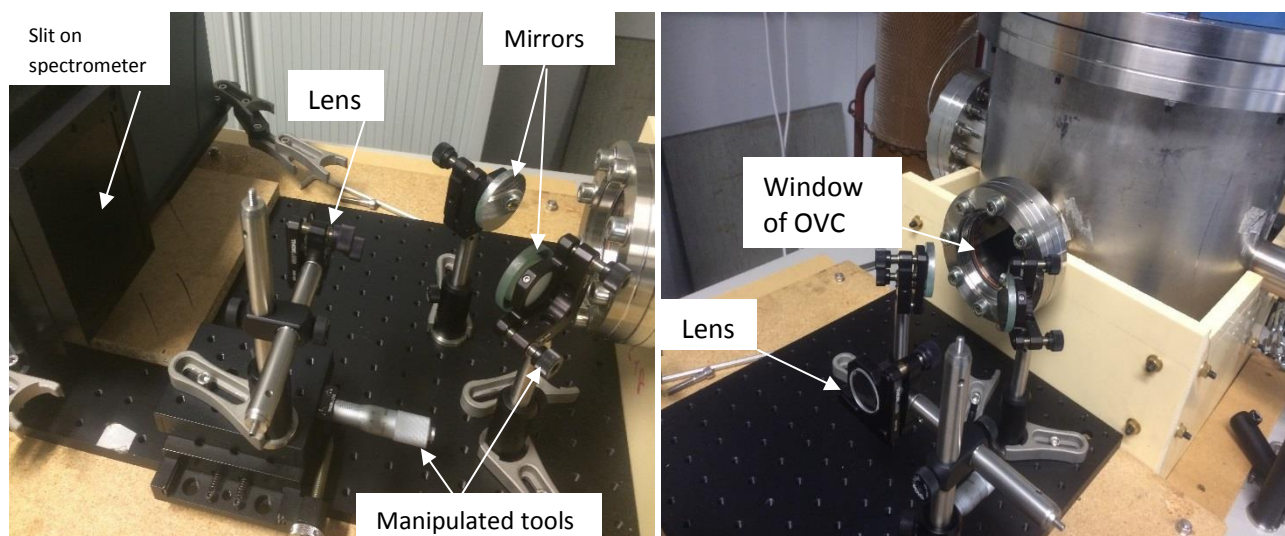


Figure 3.18: Images of optical setup outside vacuum chamber to optimize the alignment of emitted light from the cell. Both images in the same set but from different corner photos were pictured. This set lies on an optical breadboard that accommodates two mirrors and a lens that to lead and focus emitted light from the discharge zone within the cell to the slit of the spectrometer.

### 3.1.13 Methodology of the data collection

Once the system is aligned, it is ready to record and collect spectra. It is worthy to point out that during optical alignment in the previous section, the ignition of discharge that occurred to record the image of spot or spectra was at room temperature i.e., before starting of the cooling down process. Hence, such spectrum at room temperature is the first data and was used as a reference to the rest of spectra. This spectrum is called glow discharge and obtained at low-pressure (8 mbar) discharge spectra of helium by pumping on the cell with applying a high potential difference across the electrodes. Nevertheless, the pumping of the cell itself was conducted before applying discharges, the pumping of the cell was inefficient due to the length of pipe of helium gas. As a result, helium atoms remain at low pressure to get glow discharge spectrum. Spectra were recorded with a Peltier-cooled ( $-65\text{ }^{\circ}\text{C}$ ) CCD camera (Andor iDus DV420, CCD-12855). A  $1200\text{ mm}^{-1}$

grating blazed with a high-resolution diffraction along the range 300-1000 nm was employed and the resolution was 0.2 nm. The spectral line profile of the instrument followed to a good approximation a Lorentzian function.

As mentioned, the optimization of alignment resulted to get an image on the center of the slit of an Andor Technology Shamrock SR303i Czerny Turner spectrometer. So, either to record spectra or images in spectrometer, the Andor Solis software (version 4.19.30001.0) accompanying the hardware was used to change the setting of each case. In case recording images, the acquisition mode has to be changed to the single mode, and readout mode changed to the image choice, triggering to the internal and then select exposure time. Also, by selecting the zero-th order of the diffraction grating, the image can be record under these setting. In case spectrum was required, so acquisition mode has to be changed from single mode to the accumulation mode.

After recording glow spectrum at room temperature, to start cooling down process, the compressor was operated that will be ready after a couple of minutes. After that, the cooling water is controlled by specific valves that were opened to initiate cooling process according to the instruction of the fridge [5]. Now waiting until the  $^3\text{He}$  pot and second stage are linked thermally, if so, the cooling down process can take 9-10 hours. However, if not, this process will need up three days.

It was found that at cryogenic temperatures and during recording an image in similar way to that at room temperature, the position of image shifted slightly by 1 mm and thus modify the alignment must carry out, hence recording the images must been to repeated. Fig. 3.19, displays two cases both at low temperature; first case before alignment in (a) and (b) with 100  $\mu\text{m}$  and 2500  $\mu\text{m}$  slit width respectively. Another case after adjusting the lens and mirrors to get back image of discharge to the center of slit as shown in (c) and (d). Remarkably, during recording images of discharge at room temperature and low pressure, in which difficult to record image of discharge spot at low pressure, it was realized that one of this photos involved the shape of the sharp tip electrode nicely as shown in Fig. 3.20 .

Once the system is aligned the, applying a high potential difference across the electrodes, the fluorescence spectra are ready to record on computer that connecting to the spectrometer. Helium pressure and the temperatures are the parameters that is most depended in experiment. On the other hand, the amounts of used helium and temperature vary from experiment to another depending on what we plan to do. A routine work to collect spectra is as follow;

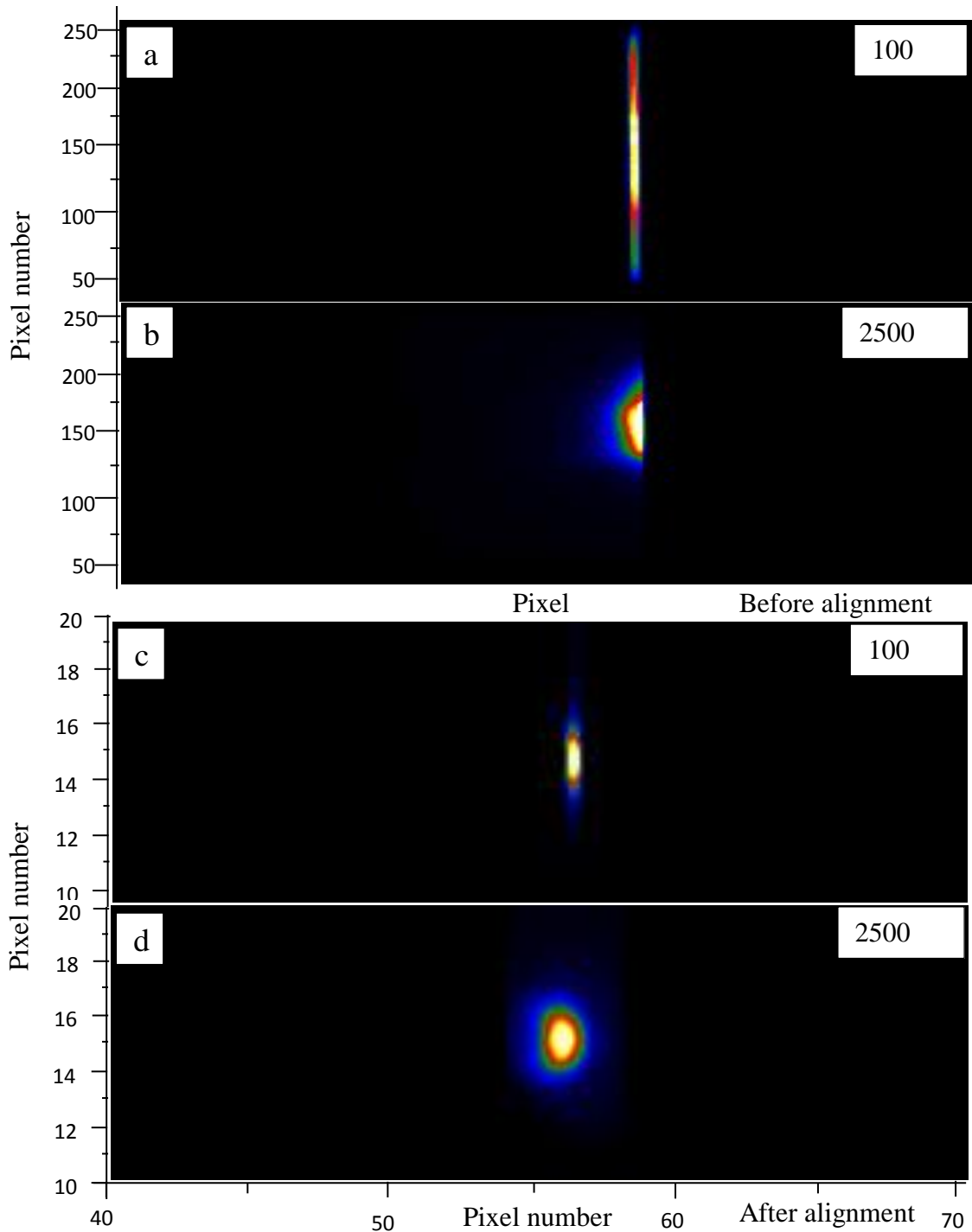


Figure 3.19: Images of emitted light nearby to the tip electrode were recorded using the Andor Solis software accompanying the hardware. All images recorded at  $T= 3.5$  K,  $P= 0.18$  bar,  $V= 0.68$  kV,  $I= 25$   $\mu$ A, Exposure time= 0.001 sec and accumulation No.= 20. The only difference is the realignment, where images (a) and (b) were recorded after cooling down and realized that the position of images has shifted from that one at room temperature (which were in the center of slit) due to the components suffering contractions at low temperature. Consequently, the setup of optics has to be modified, as a result, the image position returned back to the center of slit as shown in (c) and (d) after alignment. The widths of slit of spectrometer were 100  $\mu$ m for (a) and (c), while 2,500  $\mu$ m for (b) and (d). This is because with 100  $\mu$ m the centred image not clear such slit (fully) open at 2,500  $\mu$ m.

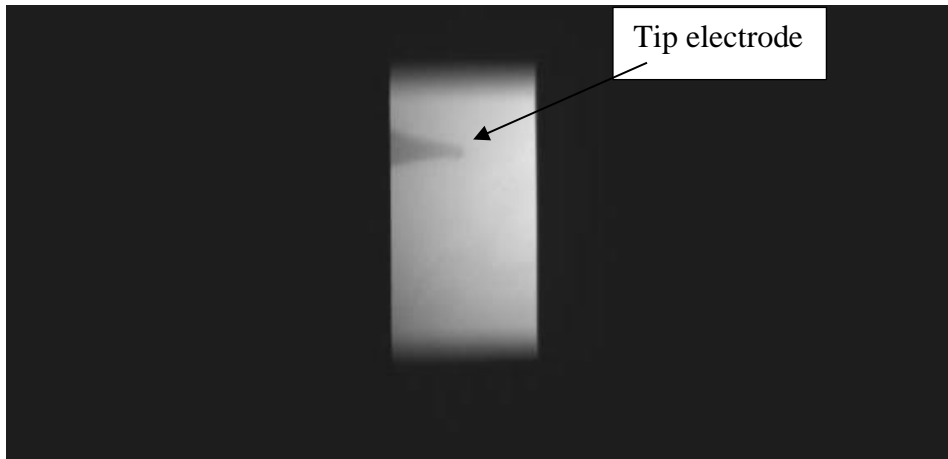


Figure 3.20: Photo of the tip electrode within the cell was observed during recording the image of the spot of glow discharge which is difficult to resolve at low pressure (7 mbar) and room temperature. This required high power under 1.23 kV, 146  $\mu$ A and 2,500 slit .width.

- Amount of helium at specific pressure has filled the gas line using buffer valve.
- High potential difference is applied across the electrodes to obtain electrical discharge. Where in the beginning of applied voltage there was no reading for current, which means the discharge not ignite yet. However, at some point of voltage, suddenly measurement of current appears on ammeter with fluctuation until getting on stabilization in a few seconds indicating to discharge ignition.
- On the other hand, a high voltage causes increase in temperature, therefore reducing the voltage and current slightly makes the temperature stable and in meantime stabilization of discharge.
- The acquisition time for each single spectrum was 10 ms for measurements in the gas phase and 100 ms in the liquid phase. Acquisition time usually always ranged between a few seconds up to one and a half minutes. Advantage of select specific acquisition time manages the need of acquiring to get a well resolved spectrum, the essential instability of the discharge and the fluctuations in the temperature (and pressure) of the helium.
- The acquisition was repeated 20 times or 10 times for the gas and liquid phase, respectively, during which the spectra were accumulated and corrected for noise (cosmic event removal, etc.). This led to an effective exposure time  $t_{eff} = t_{exp} \times N_{accu} = 0.2$  sec for the gas phase and 1.0 s for the liquid phase, respectively.

- Keep going on changing the pressure of helium and record spectra for each case. It can then raise or minimize the temperature in the cell via the heater at the pot of the fridge and temperature controller. So with repeating this procedure,  $PT$  diagram can be discovered and identify helium phases in a certain pressure and temperature. For instant as showed in results, by operating the heater of the pot and applying voltage the spectra at such conditions will be in supercritical regime ( $T= 5.2-20$  K). However, with starting from base temperature at 3.2-3.5 K and 0.150 bar, and upon increase pressure of helium this increase the temperature slightly and temporary until the system of refrigerator took it back to the original low temperature. With this action by adding helium gas atom to the cell without increase in temperature and the pressure, this is a signature that helium is upon the line of saturated vapor pressure (SVP). Noticeably, again with adding more helium gas the reading through pressure transducer has increased above SVP indicator to the condense phase of helium and liquid helium and below  $T_c$  was obtained (see Fig. 3.21 and Fig. 4.1).

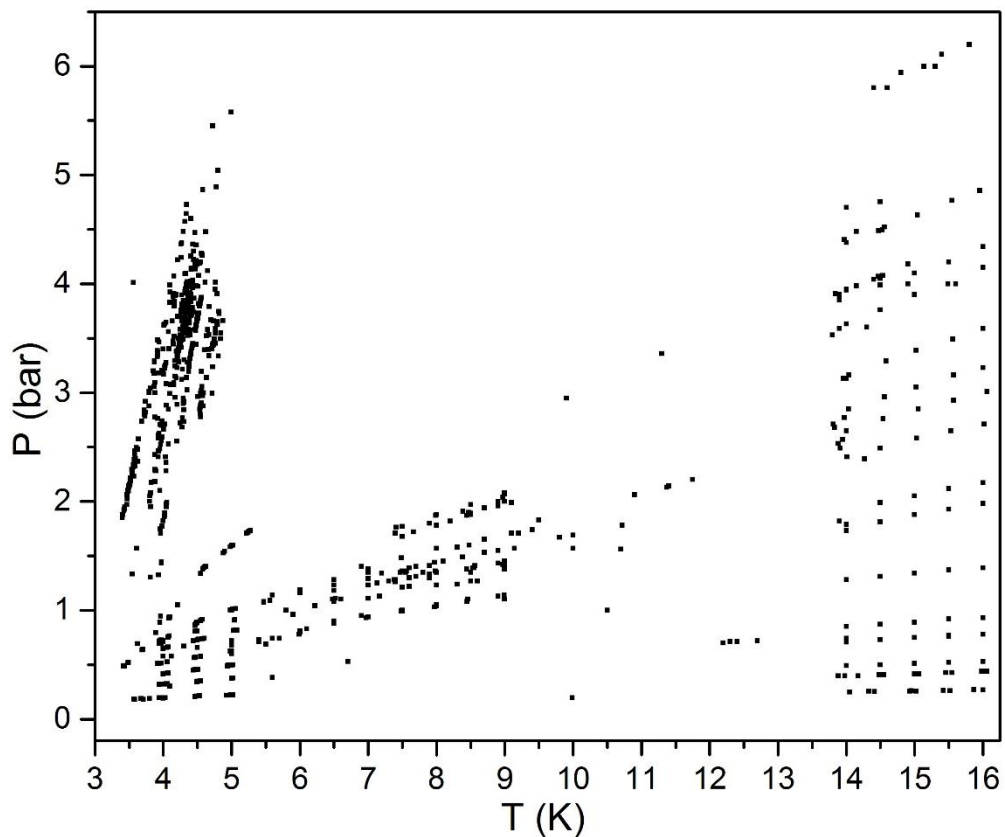


Figure 3.21: A section of the  $PT$  diagram for the gaseous and liquid phases probed in the experiment. Each point of this data represents a fluorescence spectrum which spans the range 300-1000 nm.

## 3.2 Part II- Room temperature experiment

The concept of this part in experiment is similar to the first part, where a corona discharge was employed or the electronic excitation and ionization of helium atoms at 298 K and over a range of pressures, from a small fraction of a bar up to 30 bar. The excited helium atoms and molecule-excimers undergo transitions between excited states electronically. Intense fluorescence in the visible and near infrared regions was observed in the wavelength range from 300-1000 nm. An Andor Solis Technology Shamrock SR303i spectroscopy (same means used at low temperatures) was used to record and collect the light emitted from the corona discharge in the vicinity of the tip of the top electrode through an optical setup similar to the one described in chapter 3-part I.

The differences with first experiment are; a major difference is cryorefrigerator that used only at low temperatures, while there was no need at room temperature. High pressure cell is the second change, where a stainless steel cell has been used at room temperature (will show in subsequent sections). The reason of this experiment was to compare the analysis of data that obtained at cryogenic temperature with these at 300 K. Overall, this experiment is much easier from the first one with simplest design.

### 3.2.1 High pressure cell at room temperature

A cube-like design was chosen, providing faces for flanges for two high voltage electrodes, the helium gas supply and a window to couple out the fluorescence light. The approximate cubic cell has two sides identical (in opposite top/bottom) with dimensions 55 x 55 mm. However, the others four adjacent faces are 45 x 55 mm, providing an internal volume of 5 ml, it was made of stainless steel metal (BS EN10088-3 (304S11; BS 970 PT1/3)). Pressure tests showed that it could withstand over 100 bar. A cell was built by the Mechanical Workshop of the Physics Department at the University of Leicester, Technical drawings of the cell is shown in Appendix F. In similar to the copper cell, In similar to the copper cell, the four adjacent faces of cell were accommodated by; a system that feed the cell with helium gas (gas inlet) sits one flange, on the opposite side to the gas inlet a lens sits in inner bore etched into cell then a flange places upon this lens (will explain in coming section). Finally, the last two opposing

flanges host a configuration of the plane-tip electrode with typical separations of 4-5 mm. Fig. 3.23 shows cross-sectional view of the high pressure stainless steel cell. Also, in Fig. 3.22, an image of the cryogenic temperature cell on left is compared with the room temperature cell on the right. Both photos are pictured in the lab of Physics Department.

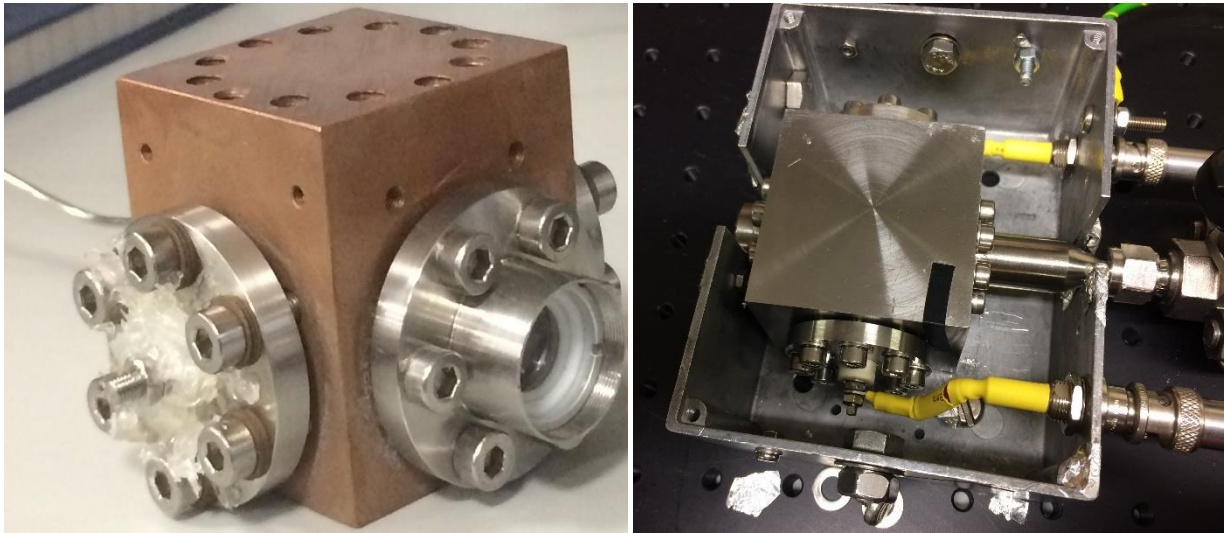


Figure 3.22: Photos of high pressure cells that used in experiment; on the left the copper cell used at low temperatures with a volume 4 ml, and Teflon material was placed around the electrodes for safety to prevent electricity spark that might distributes inside the fridge causing electricity everywhere. On the right an image of 5 ml of the stainless steel cell used at room temperature experiment with connections to the electrodes by coaxial SHV cables to supply cell high power.

### 3.2.2 Electrodes configuration with A Lumina Ceramic tube

The configuration of tip-plane electrodes in this experiment was based on by first experiment. The difference only is that the length of the tungsten tip is greater by 1 mm leading to make the separate distance between electrodes 4-5 mm instead of 4-6 mm. this is to reduce space between electrodes and to concentrate discharge as we can, especially in experiment of the atmospheric pressure air a high stabilization discharge was required. Also, M3 thread length in both electrodes are 17 mm i.e., longer than the length in first experiment about 7 mm, this to be, this to get more tolerance and space during tightening the nuts to the thread of the end of electrodes. The schematic drawing of electrodes is shown in Appendix X. A macor ceramics were replaced in the

experiment by Alumina tube to hold the electrodes. Alumina or as it known Aluminium Oxide,  $\text{Al}_2\text{O}_3$  is a major engineering material that offers a combination of good mechanical properties and electrical properties leading to a wide range of applications. Alumina can be produced with high purity with a minimum purity of 99.8% to enhance properties. Ceramic insulator tubes are used in vacuum interrupters for medium voltage (approx. 6kV to 80kV). Additionally, specialized Alumina is characterized that has superb material characteristics such as high electrical insulation, high mechanical strength, high wear and chemical resistance. According to the Possibility of a 50% size reduction with 1.6 times higher voltage resistance than conventional ceramic. Consequently, Alumina ceramic is preferred to use [105]. The rest information regarding assembling high pressure cell and sealing the slots see section 3.1.8.a. Fig. 3.23 shows the section of the stainless steel with its components. An image of the cell with Alumina

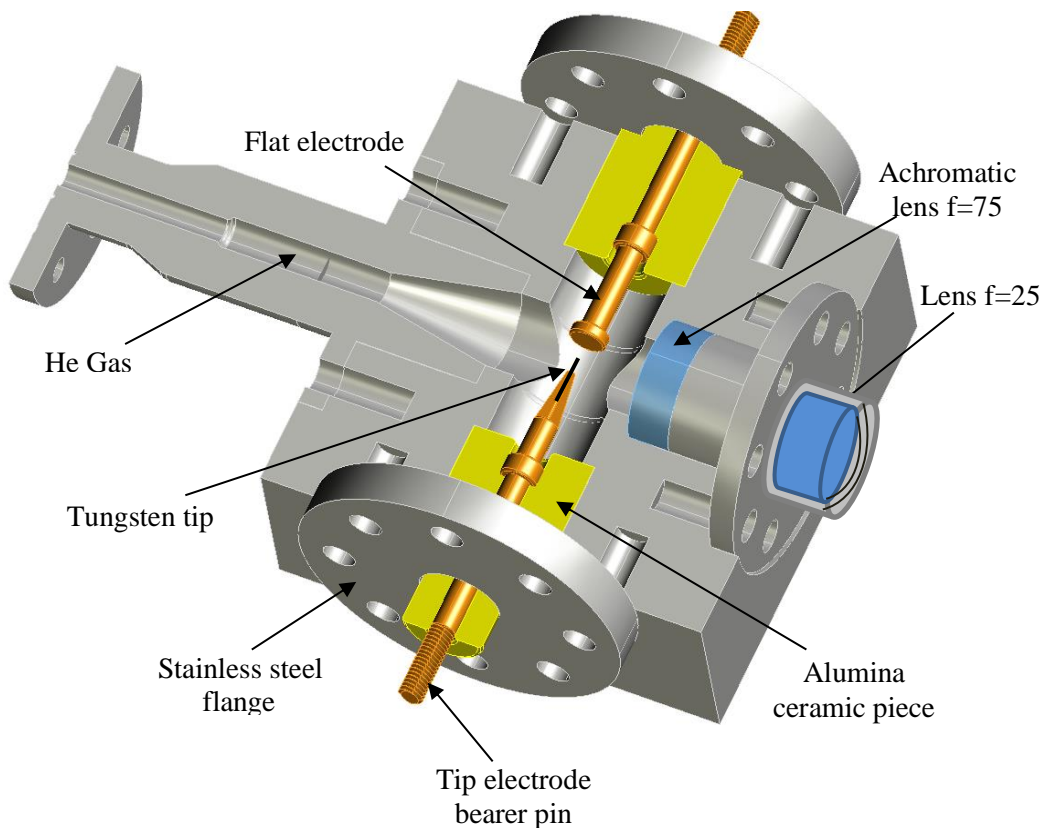


Figure 3.23: Cross-sectional view of the discharge region of the high pressure stainless steel cell (assembled).

### 3.2.3 Optical layout

The collection of emitted light from the cell needs an accurate system of lenses. The result of accuracy starts from the first image obtained from discharge region within the cell as explained in section 3.1.9. This can be obtained by making the first lens close to the spark of discharge as much we can. An achromatic lens (Edmund Optics Dwg. No. 47703INK) with focal length ( $f_1$ ) 75 mm x 15 mm diameter, is the first lens that was used in this set, nearby to the discharge point. This lens is apart away from the tip point in 16 mm ( $u$ ), in which created virtual image on a distance about -20.34 mm ( $V$ ) from the lens, behind the discharge region (a negative sign indicating to the virtual image that obtained in same side of discharge) according to the equation (3.8). This lens was placed inside the cell, underneath the flange in between two plastic rings, to protect it from scratch. In sake of collecting divergent beam from first lens ( $V$ ), positive focal length for Convex lenses (uncoated/LB1092-N-BK7) with ( $f_2$ )= 25 mm and diameter 15 mm, was placed after first lens on distance 12.5 mm. The divergent rays then concentrate in point in distance around  $100 \pm 4$  mm in front of second lens. Achromatic lens with focal length ( $f_3$ ) 75 mm and Dia. x 25 mm, was placed apart away from second lens in distance around 200 mm to produce parallel beams. Two mirrors in 40 mm diameter have passed this beams into fourth lens (Convex Lens Uncoated /LB1471-NBK7 which is the last lens in this set ( $f_4$ =50 mm) in 25 mm diameter. Where the parallel light were collected and focused by L4 towards a slit of a Czerny-Turner spectrograph (Andor Technology Shamrock SR303i), in which passed to a CCD chip (Andor CCD-12855 - iDus Camera DV420) to record in computer for analysis. To minimize shot noise, a CCD camera is cooled down to  $-65$  °C. The distances and calculations that dependent on the lenses law is shown by a schematic diagram (Fig. 3.24) of the optical pattern explained in above paragraph. Finally, the spectra of emitted light collect and record in computer for analysis.

In spite of the alignment of the light is complicated to somewhat, the manipulation with lenses in experiment at room temperature is easier than cryogenic experiment. On the other hand, the most important step in both the first and second experiment is the blackout of experiment along the optical path from the cell to the spectrometer to avoid cosmic ray and to reduce noise sign that conjugates spectra. Where, it was used a conventional way which is the cardboard box that is covered by fabric piece as well. Fig.

3.25 presents the optical board that accommodates the stainless steel cell within aluminum box, four lenses, two mirrors and spectrometer that were hold by a table.

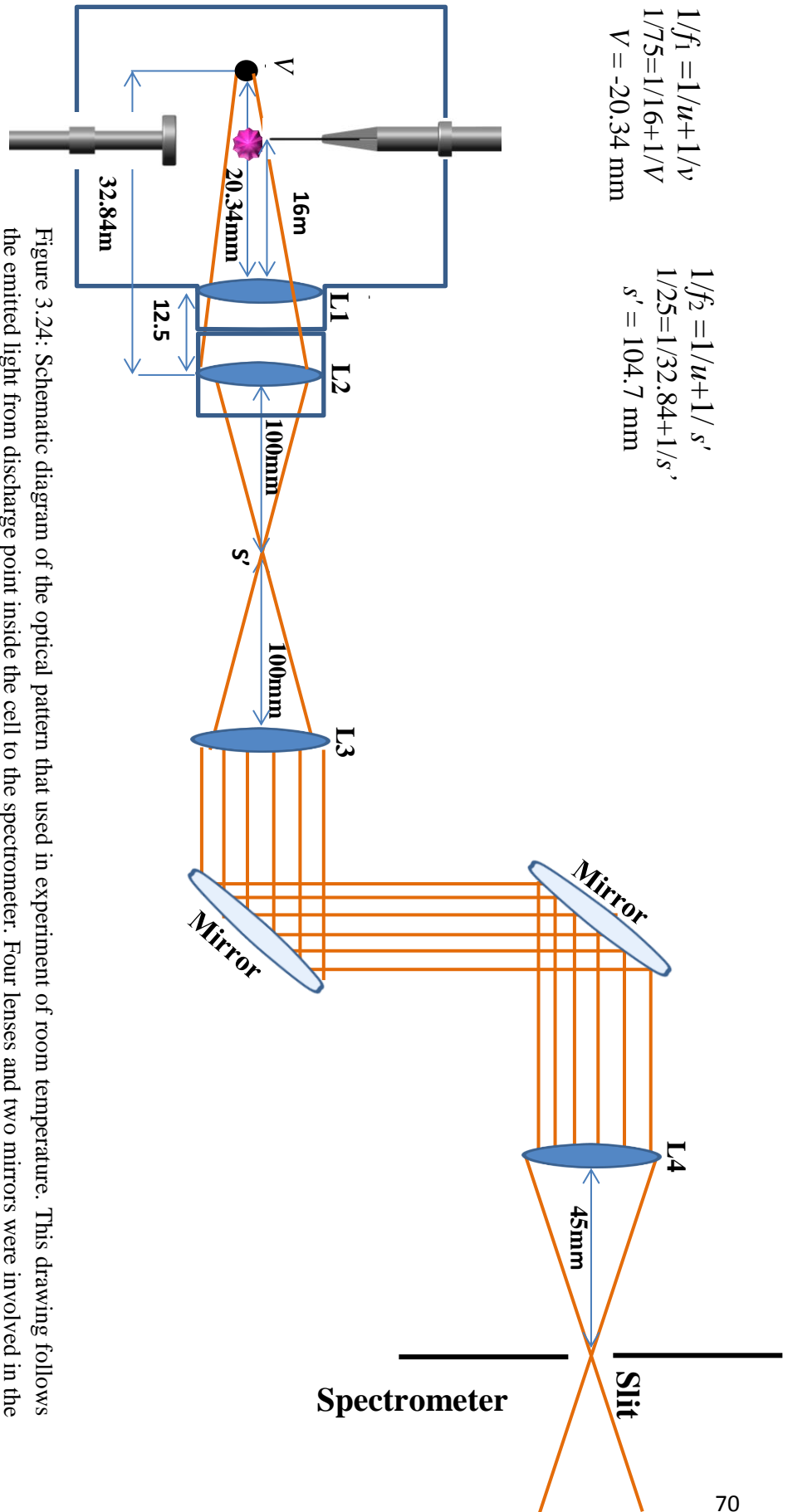


Figure 3.24: Schematic diagram of the optical pattern that used in experiment of room temperature. This drawing follows the emitted light from discharge point inside the cell to the spectrometer. Four lenses and two mirrors were involved in the optical set; the focal lengths for L1, L2, L3 and L4 are 75, 25, 75 and 50 mm respectively with diameter 15, 15, 25 and 25 mm. In top left corner calculations that showed how the distances between lenses, mirrors and virtual image (V) and real image (s') can be calculated by law of lenses. Although  $f_4 = 50$  mm, we have realized that a good resolution of image on the edge was observed at distance 45 mm, in which must be at 50 mm. This because the slit is behind the edge of spectrometer in 5 mm, hence the correct distance from L4 to slit would be  $45+5 = 50 \text{ mm} = f_4$ .

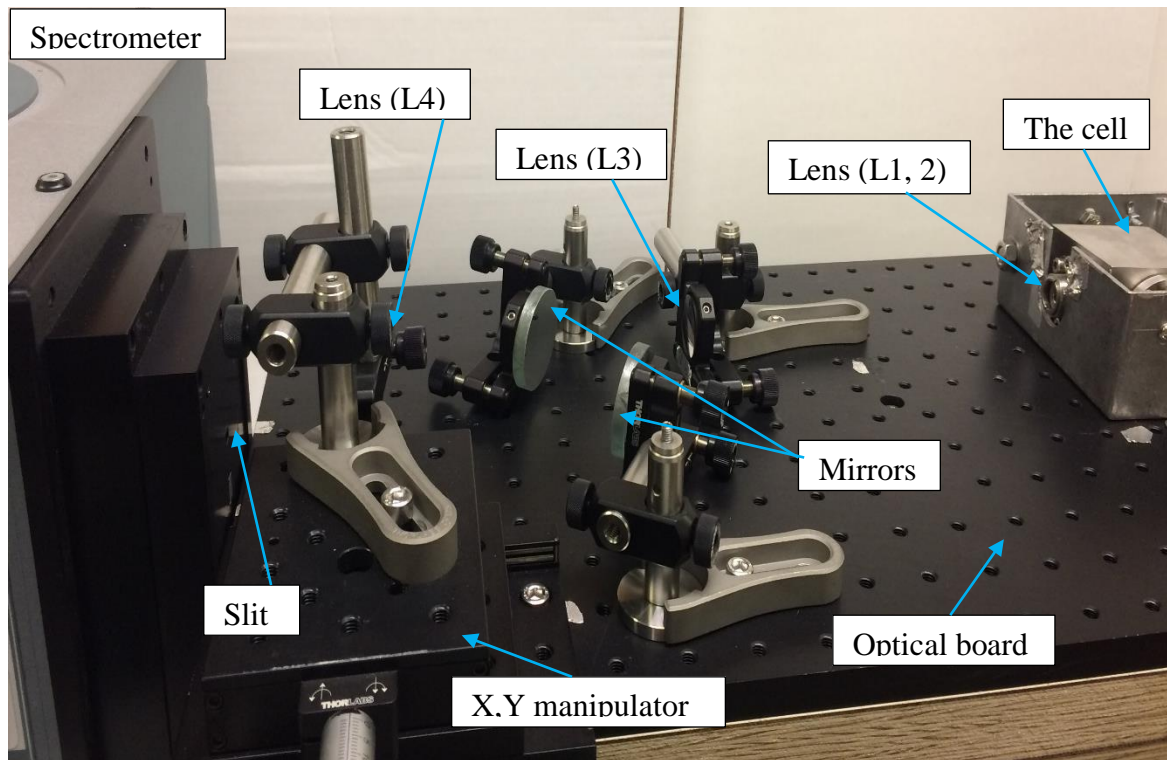


Figure 3.25: Photograph of the optical board showing the optical setup for focussing the light emitted from the cell into the spectrometer.

### 3.2.4 Assembly of the setup of experiment & Experimental procedure

As mentioned the setup for this experiment is simpler than for all cryogenic experiment. Only one thing remains we do not talking about, is the gas line installation which is not a big difference from the first experiment in terms of concept. Apparently, the only difference the gas line goes directly to the cell to feed the cell in this part, while in first experiment the gas line connects to the cell during the cryostat equipment's. A 3.5 m the length of the pipes of the gas line used in this experiment and is made of stainless steel with a Swagelok (part number SS-T1-S-020-6ME.) 6 mm O.D. (outer diameter) due to ability to carry high pressure up to 100 bar. Furthermore, a high purity substance was required to pump to the cell, therefore the choice was by using helium of N6.0. To get a low rate of leak, standard Swagelok seals were used. The connections of the gas line to

the cell and methodology of evacuation with pressure measurements explained in section 3.1.6. So, after preparing the gas line and connecting to the cell which is placed inside metal box (95x120x55) mm bolted to the optical board. This box holds the cell and SHV cables then closed by a cover that screwed to the box. After that this box bolted to the optical board that lays below the set of optical system as well to obtain on one level of alignment of light. Once the optical set and alignment are ready, the procedure of experiment to operate and record spectra as follow;

- The gas line was cleaned from impurities with the vacuum pump process by using scroll pump machine up to  $6 \times 10^{-2}$  mbar (reading on Pirani gauge). Then the gas line was filled with 3-10 bar of He N6.0 from bottle of helium, then flushing out the helium, this process was repeated many times to flush all impurities from the cell and pipes. Although high purity of helium (99.9%) we used in present experiment, it still contains impurities such as hydrogen and oxygen.
- To test the electrical connectors and to run a corona discharge to be able recording fluorescence spectra, applying a high potential difference across the electrodes was required. By using different power supply depending on the value of voltage that discharge required. First device of power supply (Fug-branch) was used in range 0-3 kV, then replaced by Spellman power supply when it was needed voltage up to 10 kV with negative polarity.
- Once getting stabilized discharge and already the alignment was done as well, the next step is blackout the whole optical board including the slit of spectrometer and excluding the gas line. Ignition of a corona discharge initiates by applying a high potential difference across the electrodes. Hence fluorescence spectra were recorded and observed on spectrometer. Fig. 3. 26 shows an image of experiment setup that was carried out in the lab (G33- Magnetic lab) in Physics Department.
- A small amendment was made in experiment by connecting a dragon valve to the gas line. This was for the second section from the second experiment (relating to results in chapter 7). Where, others gases have been mixed to the helium gas. Therefore, the ball valve on the buffer line of helium was closed, then evacuated the cell many times for cleaning from helium atoms. By turning on a dragon valve, regular perfume and air were allowed to enter to the cell and record spectra after applying high voltages (read the full story in chapter 7). Then the blackout of optical setup is the last step before recording spectra.

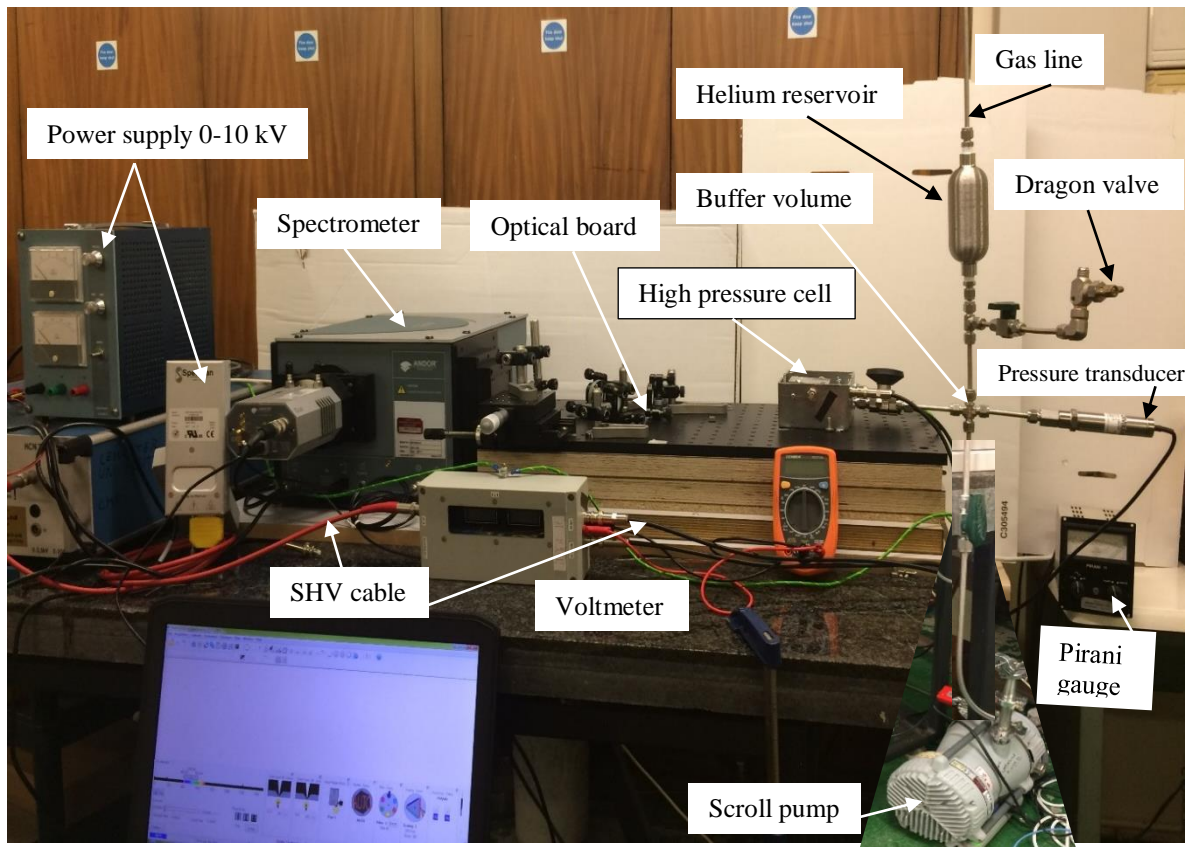


Figure 3.26 The setup of the experimental procedure at room temperature; including optical alignment setup, supplying potential difference across the electrodes, spectrometer and gas installation that divided into sections; one part for gas helium inlet and, the second part for air atmospheric pressure and perfume which is supplying from another inlet to the cell by using dragon valve.

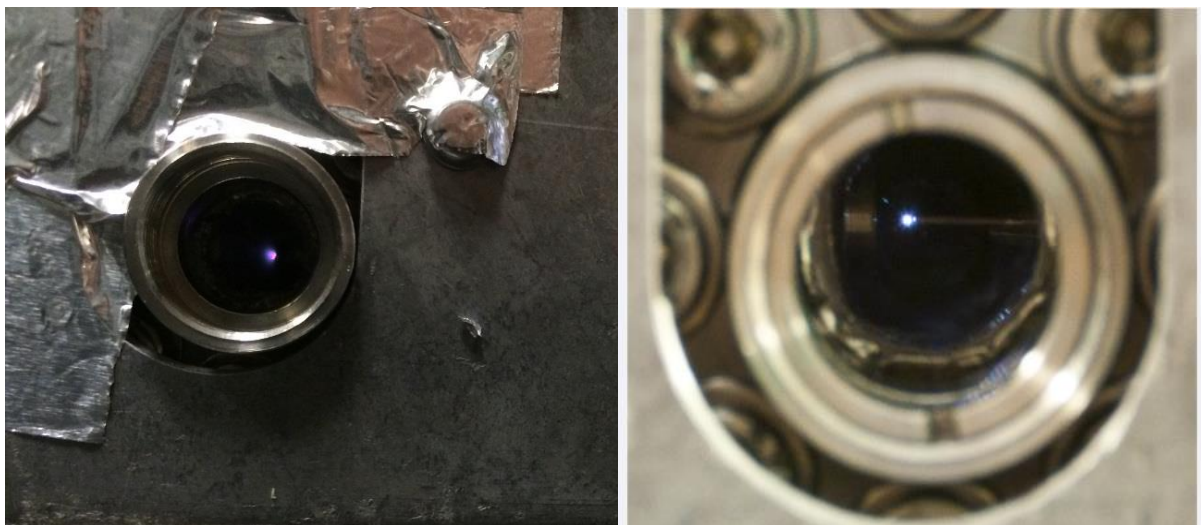


Figure 3.27: Photos of corona discharges nearby the tip electrode after applying high voltage. It seems that the spot of discharge tends to be in bluish color within copper cell at low temperature (on the right). However, with stainless steel cell at room temperature the discharge is in purplish color. This maybe returns to the effect of temperature on discharge environment.

### 3.3 General observations and experimental difficulties

A corona discharge has been employed to investigate the different thermodynamic phases of helium at low and at room temperatures. It has been used to excite helium atoms and helium excimers in Rydberg states at different pressures and temperatures. The general characteristics of the designed system are summarized below;

- A corona discharge can be used to excite short-lived helium excimers in Rydberg states
- The ability to ignite a corona discharge at cryogenic temperatures ( $\sim 3.2$  K) after reducing the temperature by cooling-down procedure.
- The high efficiency of spectra obtained from the ignition region, by using a solid base of lenses and mirrors to follow up the beam..
- Minimize heat transfer by radiation, conduction and joule heating as much as.
- The capability of obtained spectra of air atmospheric pressure and perfume plasmas.
- The ability to control temperature and pressure in this experiments.

On the other hand, the difficulties and obstacles that we faced during the experiment are;

- Losing the discharges during operation the experiment several times, pushed us to repeat ignition process also many times. Mostly, not getting a stable corona discharge this happened with air and perfume plasma at atmospheric pressure and room temperature.
- The elevated temperatures in the cell during applying high voltage and this was a big obstacle at cryogenic temperature with liquid phase, where LHe needs around 10 kV to ignite discharge and record spectra. However, it was realized that with high voltage the temperature increase leading to reduce number density of helium causing to obtain gas phase instead helium phase.
- The alignment of emitted light with black out of experiment also were required with high accuracy to avoid the noises and background with spectra.

## Chapter 4

### Results and discussion

# Atomic fluorescence emitted from a corona discharge in helium above and below saturated vapour pressure\* (SVP)<sup>5</sup>

This chapter presents the work originally published in

*Eur. Phys. J. D* (2018) 72: 5

<https://doi.org/10.1140/epjd/e2017-80322-4>

---

<sup>5</sup> Contribution to the Topical Issue “Dynamics of Molecular Systems (MOLEC 2016)”, edited by Alberto Garcia-Vela, Luis Banares, Maria Luisa Senent.

## Abstract

A new apparatus was constructed to investigate the visible and near-infrared fluorescence spectroscopy of electronically excited helium over a wide range of pressures and temperatures, covering both the gaseous and liquid phases. To achieve sufficient throughput, increased sensitivity was established by employing a micro discharge cell and a high-performance lens system that allowed for a large collection solid angle. With this setup, several thousand spectra were recorded. The atomic  $3s\ ^1S \rightarrow 2p\ ^1P$  and  $3s\ ^3S \rightarrow 2p\ ^3P$  transitions showed line shifts, spectral broadening and intensity changes that were dependent on magnitude on pressure, temperature, and thermodynamic phase. While in the gas phase, the lines showed little dependency on the discharge cell temperature; by contrast, the opposite was observed for the liquid phase, suggesting that a significant number of atoms were solvated. Triplet lines were up to a factor of 50 times stronger in intensity than the singlet lines, depending on pressure. When taking the particle density into account, this effect was stronger in the gas phase than in the liquid phase of helium. This was attributed to the recombination of  $\text{He}_2^+$ ,  $\text{He}_3^+$ , and  $\text{He}_4^+$  with electrons, which is facilitated in the gas phase because of the associated significantly higher mobility. Additionally, simulations were applied to calculate the lineshift and linewidth for atomic lines.

The structure of this chapter is as follows; Section 4.1 gives a concise introduction to atomic line transitions. Experimental data are reported in Section 4.2. The treatment of the spectra is described in Section 4.3, which involves line fitting and calibration processes. Section 4.4 presents spectral fluorescence lines that were resolved at low temperatures, namely 3.8, 4.0, 4.5 and 5.0 K, covering the singlet and triplet transitions. The analyses of said spectra are presented in Sections 4.5, including lineshifts, widths and intensities as functions of pressure. Section 4.6 reviews our perspective on phase transitions. We discuss the findings in Section 4.7. From Section 4.8 we present the error analysis for the data. Theoretical treatment of spectra is given in Section 4.9, and the results of the associated calculations are presented in Section 4.10, covering said parameters for both the singlet and triplet states. The structural model that arises from our findings is given in Section 4.11, and a number of concluding remarks are presented in Section 4.12.

## 4.1 Introduction

Collisional lineshape can yield information on the colliding atoms, and collisional conditions have attracted considerable attention in the literature. A large number of measurements of pressure broadening and line shift have been reported for atomic lines in the singlet (728 nm) transition of helium [106-111].

This is due to the simple comparison possible through formulating the theoretical description of interactions between the states of these atoms and in the analysis of the profiles measured for the spectral lines. Although there is a dipole-dipole coupling between the ground state and the lower  $n^1P$  levels for these transitions, most line broadening is dominated by the resonance interaction, hence it is expected that the broadening constant will be independent of temperature and there will be no shift of the central frequency [112].

However, later investigations [109, 110] elucidated how the broadening constant can be affected significantly by temperature. Further, they found that if the strength of the interaction potential is not entirely suppressed by the strong resonance interaction, then the shift parameters are not equal to zero [107]. Therefore, recently, there has only been concentricity and measurements of pressure broadening for the triplet lines (706 nm), despite the many studies that have also been conducted on the singlet lines (728 nm). Furthermore, helium atoms are an interesting test system for theory due to having only two electrons, which greatly facilitates high level ab initio calculations of clusters with (only) several helium atoms involved [113-119].

In this project, the fluorescence of excited helium atoms in its gaseous and liquid states has been investigated at cryogenic temperatures. A corona discharge has been employed to produce electronic excitation. Corona discharges operate over a wide range of pressures and densities, and can produce a rich fluorescence spectrum in liquid helium [8, 55, 56]. It is therefore possible to examine excited levels as a function of pressure, temperature and thermodynamic phase. Here, we report on atomic spectra that have been recorded from 0.1 to 5.6 bar and on isotherms between 3.8 and 5.0 K, covering the gas and the liquid phases of helium. Our goal was to explore solvation effects with specific regard to the thermodynamic phase. Our work adds to previously available datasets: Soley and Fitzsimmons reported lineshifts for atomic transitions between saturated vapour pressure (SVP) and 25 bar for temperatures between 1.4 and 2.0 K. Both absorption and emission were investigated, where all lines were observed to be blue-shifted

when pressure was increased [53]. Li and Bonifaci investigated atomic spectra above the saturated vapour pressure (SVP) in normal liquid helium [8, 55, 56, 120]; our results are in general agreement with these previously published; however, we report new data at pressures and temperatures that have not been previously investigated, including in the region below SVP. Depending on the temperature, a large section of the line profile in the region below the SVP is red-shifted. Our observations are important as a benchmark for theory [41, 121-126] and will contribute to a better understanding of collisional processes, including in the atmosphere of the sun, and indeed other stars and exoplanets [41, 112, 124-131]. Our studies are also relevant to an understanding of micro solvation. The excited helium atoms under consideration are in  $n = 3$  Rydberg states. The  $3s$  states are spherically symmetric and form bubbles of up to  $15 \text{ \AA}$  in diameter in liquid helium because of the Pauli repulsion between the excited electron and the  $1s^2$  electrons of neighbouring ground state atoms. Such states have similarities with anions which have recently been observed in helium clusters [132, 133]; theory confirms that these clusters appear to have a similar bubble-like solvation structure [132-136]. To make this advance, a significant number of spectra had to be recorded within a reasonable timeframe. This required the construction of a spectrometer with a highly efficient optical system which greatly reduced the data requisition time compared to the state-of-the-art instruments used and discussed in the literature. With the new setup (see chaprt3/ experiment chapter), we were able to record spectra in under 100 ms with excellent signal-to-noise ratios. Recently, this technique was adopted by our group in first investigation [59], for the study of excited helium molecules (excimers) in gaseous and liquid helium (all details for this study of excimers in chapter 5). The analysis of spectral features of excimers revealed that molecules exist in different environments leading to observe superposition of molecular lines from different sites. Therefore, the idea of this chapter to investigate spectral features of excited helium atoms in similar phases to see whether same observation of excimers we obtain or not.

## 4.2 Experimental data

Using a corona discharge allows for the electronic excitation and ionisation of helium atoms over very wide range of pressures. The excited helium atoms and molecule-excimers undergo transitions between electronically excited states, and into the dissociative state. Intense fluorescence spectroscopy in the visible and near infrared

regions is observed. The population mechanisms of the excited molecules and atoms are deduced through spectroscopy. Changing the pressure during operation was found to affect the discharge current and temperature of the cell. It was therefore not straightforward to record data along the isotherms; instead, we chose to record a large number of data points wherever we were able to establish stable conditions and select data points of interest from the large pool of data subsequently generated. Measurements at each point on the  $PT$  diagram were repeated at least three times. The criterion to select data points on a specific isotherm was that the temperature deviated by not more than 0.1 K from the isotherm - our measured error in temperature - and that the independently measured spectra were consistent. The procedure for selecting data points is illustrated in Fig. 4.1. Generally, the spectra that resolved were in the range of temperatures and pressures between 3.4 – 5.3 K and 0.2 to 7.0 bar. Fig. 4.1 shows a pressure and temperature  $PT$  diagram of the data points that we recorded and collected at low temperature using an Andor Solis Technology Shamrock SR303i spectroscopy. Each point represents a fluorescence spectrum in the range 300–1000 nm. The red line is the saturated vapour pressure (SVP) curve of  $^4\text{He}$  [137].

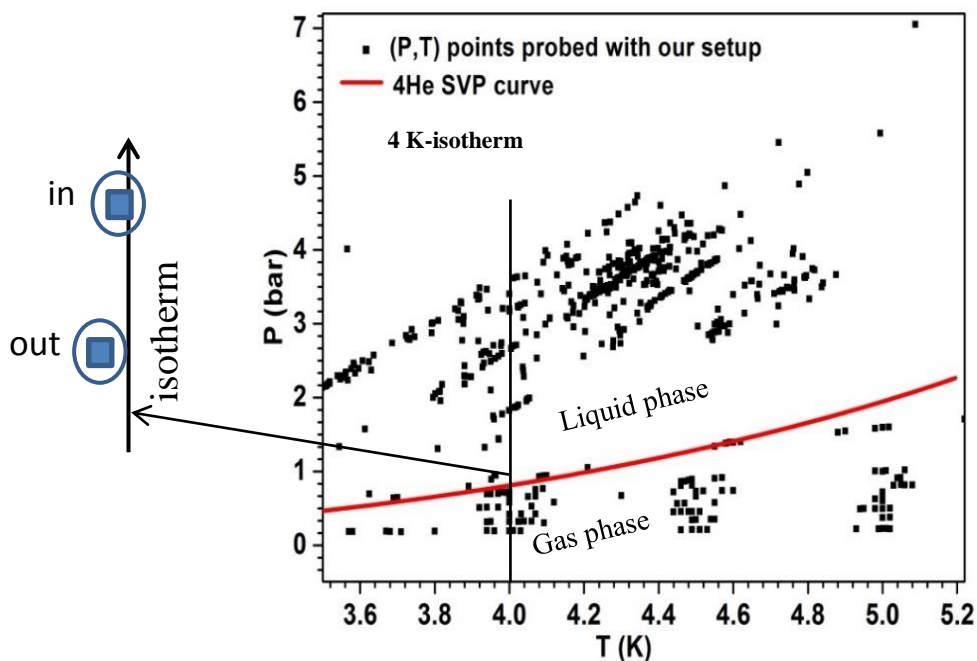


Figure 4.1: A section of the  $PT$  diagram for the gaseous and liquid phases probed in the experiment. The saturated vapour pressure (SVP) curve for  $^4\text{He}$  [37] is marked as a red line, showing the difference in the phases of helium. Also, as an example, the selection criterion for inclusion of data as being on the isotherm is shown. The blue circles around the example data points are 0.1 K in diameter, representing the error in the temperature measurements. Any data point considered to be isothermic or isobaric was measured independently.

However, the conditions to collect these spectra vary over time depending on the stability of the current and the voltage, and on the alignment of the optics. Table 4.1 clarifies the power required in Watts that were required to produce a stable discharge, where ignition voltages in the supercritical phase of liquid helium (LHe) are between 8.4 and 10 kV under a negative tip polarity, and currents are almost always less than or equal to 1  $\mu\text{A}$ . However, in gas phase only 0.6 to 1.5 kV was required to ignite corona discharge with a negative tip polarity. Additionally, experiments at room temperature (300 K) under vacuum conditions (base pressure  $\sim 70$  mbar) required a voltage of around 0.63 – 2.00 kV and current up to 289  $\mu\text{A}$  to obtain a discharge with vacuum. This was to collect glow discharge spectra to use as a reference for calibration (this will be explained in the following section).

Table 4.1: The required voltages and currents to ignite corona discharge using a negative tip polarity. LHe required a higher power and ignition voltage than the gas phase.

T / K	P / bar	- V / kV	- I / $\mu\text{A}$	Power / mW
300 (glow discharge)	0.07	0.63 – 2.00	20 – 289	12.6 – 578
14.0 – 18.0 (gas)	1.0 – 2.0	0.60 – 0.8	20 – 21	12.6 – 16.8
5.0 – 8.0 (gas)	0.5 – 1.5	0.60 – 0.9	10 – 15	6.00 – 13.5
4.0 – 5.0 (gas)	0.2 – 1.0	0.60 – 1.5	20 – 34	12.0 – 51.0
3.4 – 3.6 (liquid)	0.7 – 2.3	8.40 – 9.3	< 1.0	< 8.4 – 9.3
3.8 – 5.0 (liquid)	2.7 – 7.0	9.40 – 10	$\leq 1.0$ – 6.0	$\leq 9.4$ – 60

## 4.3 Treatment of the spectra

### 4.3.1 Lorentzian line fitting.

The methodology used to assess and analyse lineshifts, line broadening and intensity, was to fit the spectral lines of interest, systematically and individually, to a Lorentzian function while subtracting a constant baseline as necessary. Lorentzian functions produced equally good fits to the data as more complicated functions, but had fewer free parameters than, for example, Voigt functions. Also, compared to other ways for the assessment of linewidth such as full width at half maximum (FWHM), Lorentzian functions have the benefit of a greatly simplified deconvolution process, i.e., the

linewidth of two convoluted Lorentzians (and this was important for us) is simply the sum of the component Lorentzian widths. Gaussian linewidths have a Pythagorean relationship, as do the Voigt linewidths. The deviation between different methods was very small. Therefore, the Lorentzian lineshape was chosen.

There are important issues that go beyond the mere finding of best-fit parameters. Data are generally not fully accurate. They are subject to measurement errors (noise in the context of signal processing). Thus, typical data never exactly fit the model that is being used, even when that model is “correct”. Hence, some means to assess whether the model is appropriate is needed, that is, which here is manifest in the need to test the “goodness-of-fit” against some useful statistical standard. We usually also need to know the accuracy to which parameters can be determined with regards to the available dataset. In other words, we need to know the likely errors of the best-fit parameters. Not, “how good is this fit?” but rather, “how sure am I that there is not a very much better fit in some other region of parameter space?”

A function of merit in this regard is the weighted sum of squared residuals (WSSR), also called chi-squared, that is given in equation [138]:

$$\chi^2(a) = \sum_{i=1}^N \left[ \frac{y_i - \mathcal{Y}(x_i; a)}{\sigma_i} \right]^2 = \sum_{i=1}^N w_i [y_i - \mathcal{Y}(x_i; a)]^2 \quad (4.1)$$

So, we are looking for the minimum value of squares of residuals which is based on standard deviations,  $w_i = 1/\sigma_i^2$ , of the best-fit of  $N$  data points  $(x_i, y_i) i = 1, \dots, N$ .

Here, a few examples of the value of WSSR of the transitions studied at different pressures and temperatures might be noted, as reported in Table 4.2, where it can be seen that the values of standard deviation (uncertainty) for fitting atomic lines (singlet and triplet transitions) are very small. Also, the values of the Squared Residual ( $R^2$ ) that shows measures of goodness-of-fit indicates that our fits are good. Especially, these fittings were performed for spectra recorded at high pressures where some of the spectra become asymmetric and difficult to fit. Therefore, I would say these chi-squares are typical when the fits are good.

Table 4.2: The values of the uncertainty (SWRR), and goodness-of-fit of the atomic lines fitting for the  $3s-2p$  singlet and triplet transitions. These measurements were recorded at 4.8, 4.0, 4.5 and 5.0 K and high values of pressure only indicating to the good fitting.

Atomic transitions	T / K	P / bar	SWWR	R <sup>2</sup>
$2p\ ^1P \leftarrow 3s\ ^1S$ (singlet)	3.8	3.3	$1.29 \times 10^{-4}$	0.97
	4.0	3.8	$2.47 \times 10^{-4}$	0.95
	4.5	4.3	$8.94 \times 10^{-6}$	0.95
	5.0	3.7	$9.17 \times 10^{-5}$	0.95
$2p\ ^3P \leftarrow 3s\ ^3S$ (triplet)	3.8	3.3	$1.19 \times 10^{-3}$	0.96
	4.0	4.0	$3.19 \times 10^{-3}$	0.96
	4.5	4.3	$6.48 \times 10^{-2}$	0.95
	5.0	5.6	$3.74 \times 10^{-3}$	0.95

To conduct this curve fitting, the Fityk (Version 0.9.8) software was chosen [139]. This is to obtain a reasonable measure for the features of the different (molecular) rotational and atomic lines. The parameters determined by this software are as follows [140]:

Centre: to measure the absolute positions ( $\lambda$ ) and the lineshifts ( $\Delta\lambda$ ) of the transitions;

FWHM: to quantify the linewidth of the peak of each rotational and atomic lines,

Height: to determine the peak intensity as per below,

A: area of each peak = *height* x *HWHM*

Integral width (Int. Width) = peak area / peak maximum.

The precise form of the Lorentzian function is given by;

$$y = y_0 + \frac{2A}{\pi} \frac{w}{4(x-x_c)^2 + w^2} \quad (4.2)$$

Where;  $y_0$  = offset,  $x$  = wavelength,  $x_c$  = centre,  $w$  = FWHM of the  $i$ th peak,  $A$  = area.

An example of fitting with a Lorentzian function is shown in Fig. 4.2, for the  $3s-2p$  singlet and triplet transitions at 3.8 K and 1.3 bar. It can be seen how the fit is good and reliable for use in our data analysis. The line fitting analysis of the various atomic and molecular transitions of interest will be given in the following sections.

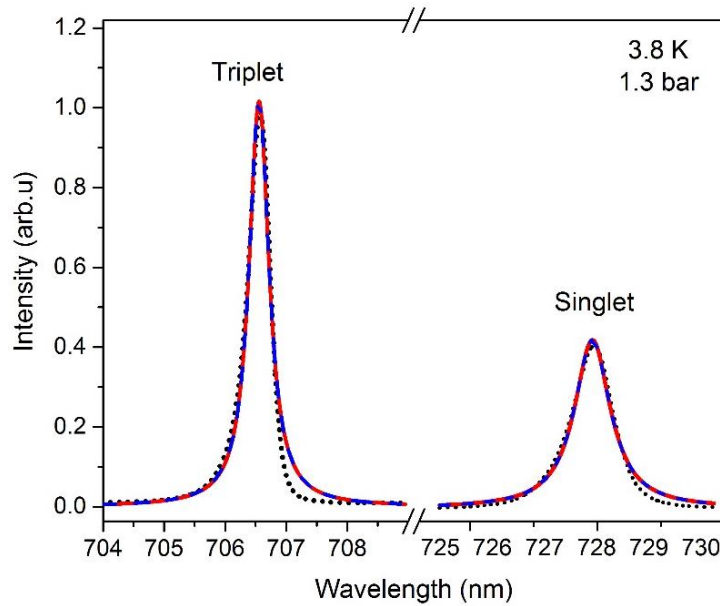


Figure 4.2: Fit of atomic line of the  $3s - 2p$  singlet and triplet transitions at 3.8 K and 1.3 bar. The black dotted line represents the actual spectrum; the overall fit is denoted by the red line, whilst the blue-dashed line represents the Lorentzian fitting.

### 4.3.2 Glow discharge spectra as a reference and calibration

As mentioned in the previous section that, the correct alignment of the optical setup is important to the collection of spectra. Every time the optical setup changes due to changing experimental conditions (as mentioned in chapter 3 – experimental process), this affects alignment. Hence, the position of the light spot on the entrance slit was readjusted as necessary. Therefore, to ensure consistency, some form of reference is necessary for comparison when new datasets are recorded. To better compare line profiles, the intensities have been normalized to the most intense peak in the spectrum, usually the 706 nm  $1s2p\ ^3P \leftarrow 1s3s\ ^3S$  triplet line of atomic helium. For comparison, a glow discharge spectrum of atomic helium lines was also recorded at room temperature (300 K) after evacuating the cell under low pressure helium of around 5 – 7 mbar. Accordingly, a number of reference glow discharge spectra were recorded under specific physical conditions, as pursuant to the physical conditions under which the investigated transitions were subsequently recorded.

The wavelength range that can be measured in a single scan (300 – 1000) nm, is dependent on the selected grating, the wavelength centre and physical width of the CCD detector. The recorded spectra needed to be recalibrated at high resolution spectra with a line as a standard reference for the position of spectral line. At this point, the glow discharge spectra recorded can employ another means of calibrating the measured

spectral lines; after collecting spectra under specific physical conditions (alignment, low temperature and pressure) each line of measured spectra was calibrated against the intense helium atomic lines positions reported in Table 4.3.

From Table 4.3, a number of species of standard atomic lines for helium, hydrogen and oxygen can be seen, and are compared to their standard values as available from the NIST database [141], where these lines are used to calibrate our spectra. To achieve this, the positions of these lines have been matched to the lines of glow discharge spectra measured in the range 300 – 1000 nm at room temperature.

The reference lines use to calibrate the atomic lines in this chapter were recorded under the following conditions: 300K, 78 mbar He, -1.07 kV, -94  $\mu$ A, 10 sec exposure time and 10 accumulations with effects due to transients such as dark current, cosmic rays, etc. removed in the software. Fig. 4.3 gives an example of a calibrated glow discharge spectrum. The intense atomic lines in this spectrum were used in the calibration process by matching them with the positions of the atomic lines reported in the NIST database [141], as reported in Table 4.3. The glow-discharge spectrum shown in Figure 4.3 contains atomic lines due to the transitions such as the hydrogen  $H_{\alpha}$  and oxygen lines in addition to the those of atomic helium itself; the additional atomic lines were due to impurities included in N6.0 He at room temperature, and vanish at low temperature when they are subsequently frozen out.

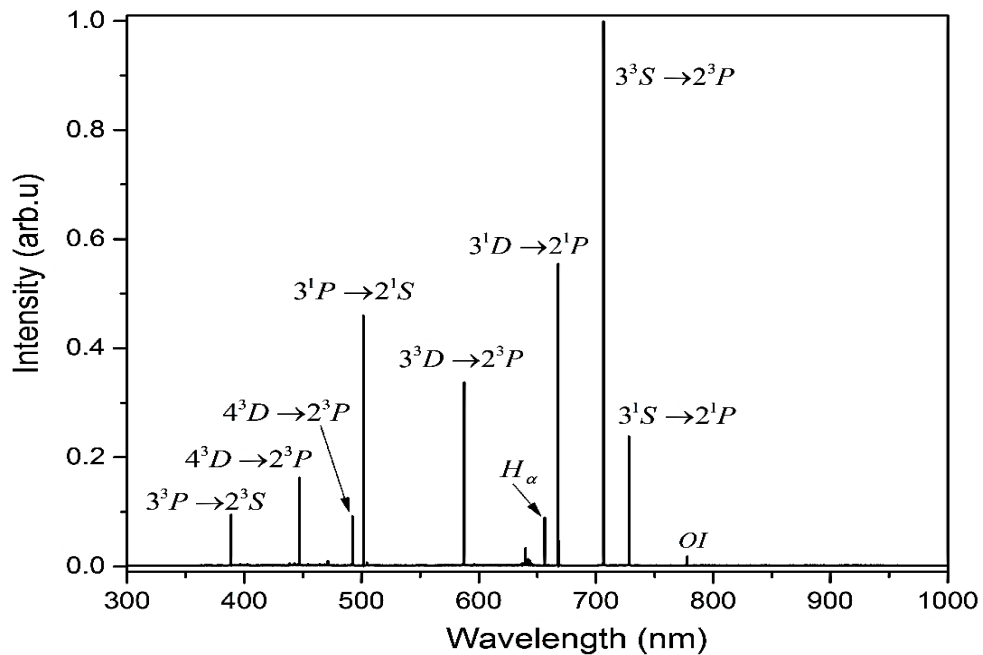


Figure 4.3: Overview of normalized and calibrated glow discharge spectrum. This spectrum was collected at room temperature conditions with a helium partial pressure of 78 mbar. Intense atomic lines transitions observed in the glow discharge were used for calibration purposes.

Table 4.3: Intense lines due to atomic transitions used to calibrate spectra. These include the lines due to atomic hydrogen and oxygen present in N6.0 He as impurities, in addition to helium atomic lines.

Species of atomic lines	Standard wave – length (nm)-NIST	n (number of rows)
atomic helium	388.865	1561
atomic helium	447.148	2566
atomic helium	493.193	3344
atomic helium	501.567	3506
atomic helium	587.562	4988
atomic hydrogen H <sub>α</sub> (3p → 2s)	656.277	6173
atomic helium	667.815	6372
atomic helium	706.518	7040
atomic helium	728.135	7413
Atomic oxygen OI (3p → 3s)	777.539	8264

Each fluorescence spectrum spans the range 300–1000 nm and consists of 12,081 rows ( $n$ ) corresponding to the data binned from the appropriate CCD photoreceptors across the width of the detector. The calibration formula of calibration is given by  $\lambda_{\text{cal}} = mn + b$ , where  $m$ ,  $n$ , and  $b$  correspond to the gradient, row number and an assumed offset for each datafile, respectively.

It was found from Fig. 4.4 that the relation between the row number in the datafile and the wavelength was linear. Hence the recalibration process consists of a linear fit in which characterizing the peak positions in terms of wavelengths vs. row number are as shown in Fig. 4.4. The result of calibration under these conditions gave  $m = 0.05795$  nm / bar,  $b = 298.6228$  nm.

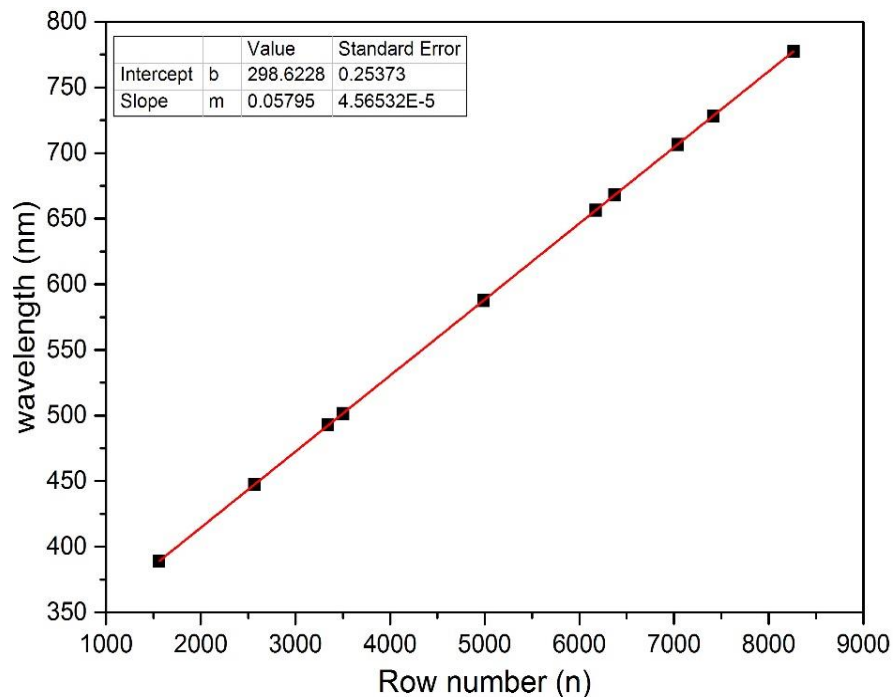


Figure 4.4: The linear relationship used to calibrate the corona spectra in terms of actual [NIST-reported] wavelength as a function of row number. The parameters utilized in the calibration are the gradient ( $m$ ) and the intercept ( $b$ ).

## 4.4 Atomic Fluorescence

Light emitted from a region in a point-plane geometry via a corona discharge that has employed to ionize helium with negative tip polarity was collected. Corona discharges lead to ionization of helium atoms, where helium ions ( $\text{He}^+$ ) can be produced via collisions with low  $\sim 25$  eV electrons. Then, through the process of recombination of electron-ion the helium excimers,  $\text{He}_2^*$ , are formed that dissociate to produce excited helium atoms,  $\text{He}^*$  (see chapter 2). Another possibility is the formation of excited helium atoms via direct electron excitation in the gaseous and the liquid helium. Hence, transitions to the lower-laying states can produce emissions for both singlet and triplet transitions of  $\text{He}^*$  [4, 8, 57]. Here, however, we concentrate on the  $2p^3\text{P} \leftarrow 3s^3\text{S}$  and  $2p^1\text{P} \leftarrow 3s^1\text{S}$  transitions.

Spectra were selected from four isotherms, those at 3.8, 4.0, 4.5 and 5.0 K, over a wide range of hydrostatic pressures. Figure 4.5 shows the transition of singlet helium in the region of 728 nm. Spectra have been recorded at various pressures, covering both the gas and the liquid phases. To better compare line profiles, the intensities have been normalised. For comparison, a glow discharge spectrum of atomic helium is also shown

(dashed line). At low pressure, the features consist essentially of only the atomic lines. With increasing pressure, the line broadens and begins to develop a blue-shifted wing. With increasing pressure, this wing becomes a separate band that takes on an increasingly symmetric line profile. The corresponding atomic triplet lines ( $2p^3P \leftarrow 3s^3S$ ) are shown in Figure 4.6. At low hydrostatic pressure, the atomic line is visible. This broadens with increasing pressure and develops a blue-shifted wing. With further increases in pressure, this wing becomes a symmetric band whose maximum shifts to shorter wavelengths with increasing pressure.

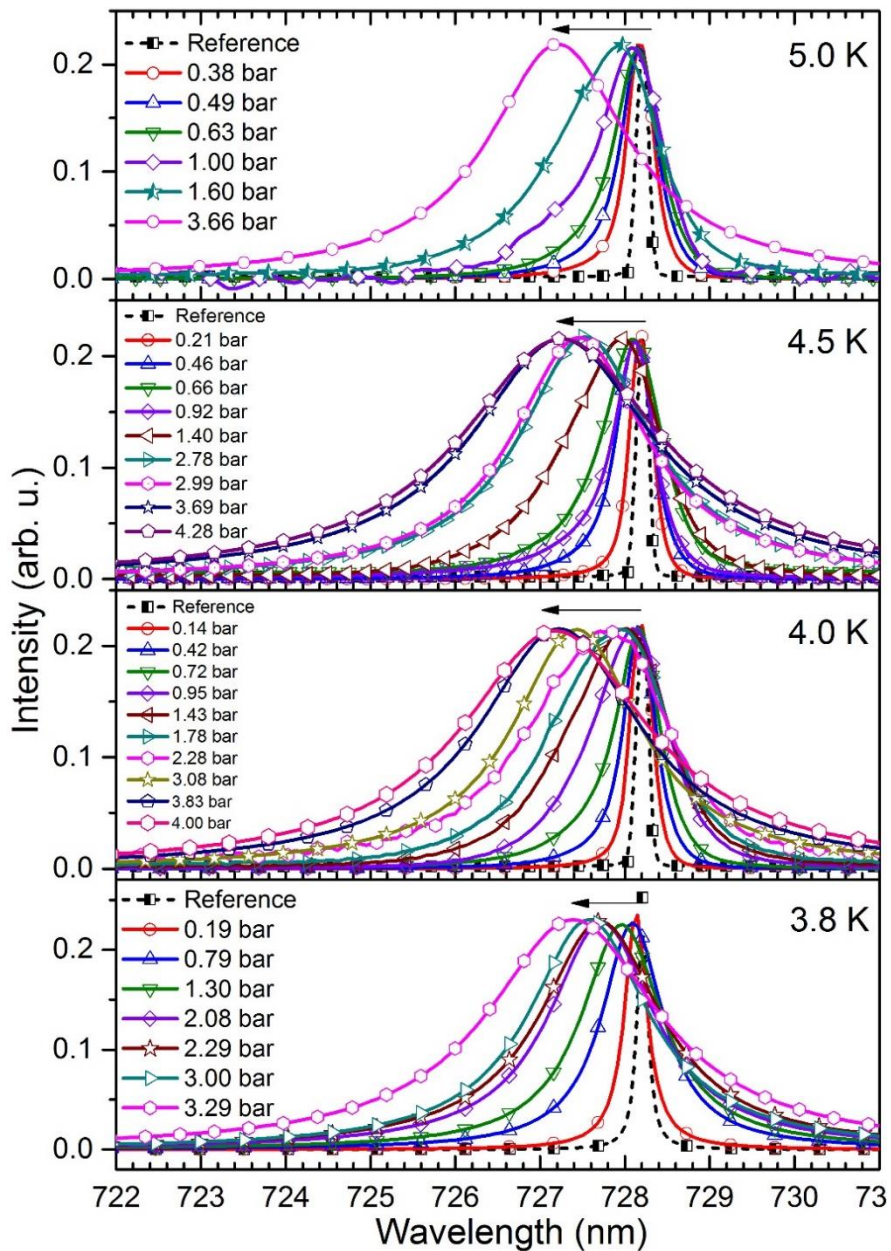


Figure 4.5: Fluorescence spectra of gaseous and liquid helium excited by a corona discharge in the region of the atomic  $2p^1P_1 \leftarrow 3s^1S_0$  transition of singlet helium. All intensities have been normalised. The dashed black line represents the reference spectrum from a glow discharge at room temperature

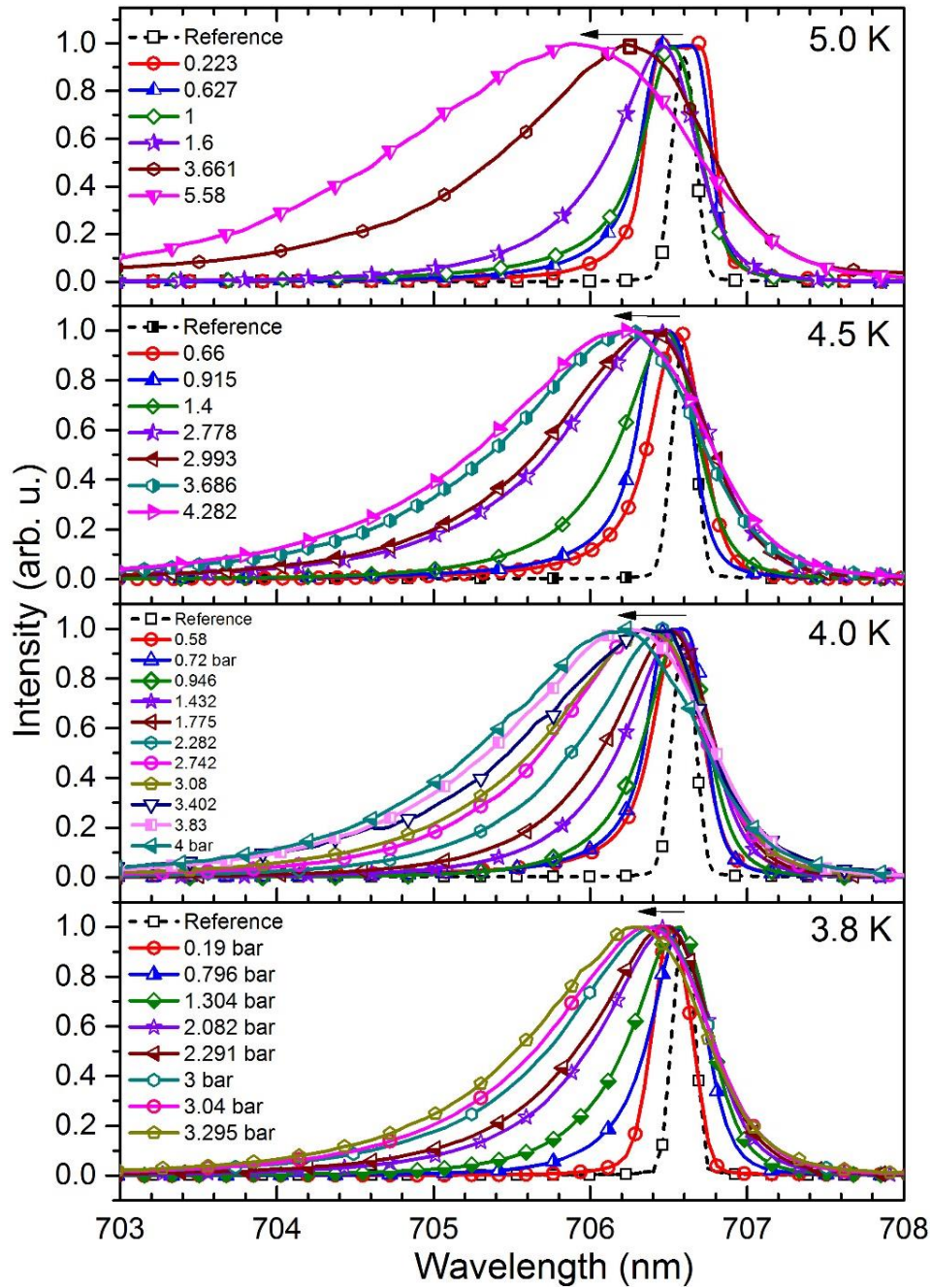


Figure 4.6: Fluorescence spectra of gaseous and liquid helium in the region of the atomic triplet transition  $2p \ ^3P_{0,1,2} \leftarrow 3s \ ^3S_1$ . Intensities have been normalised. A glow discharge spectrum in a dashed black line represents was used as the reference spectrum.

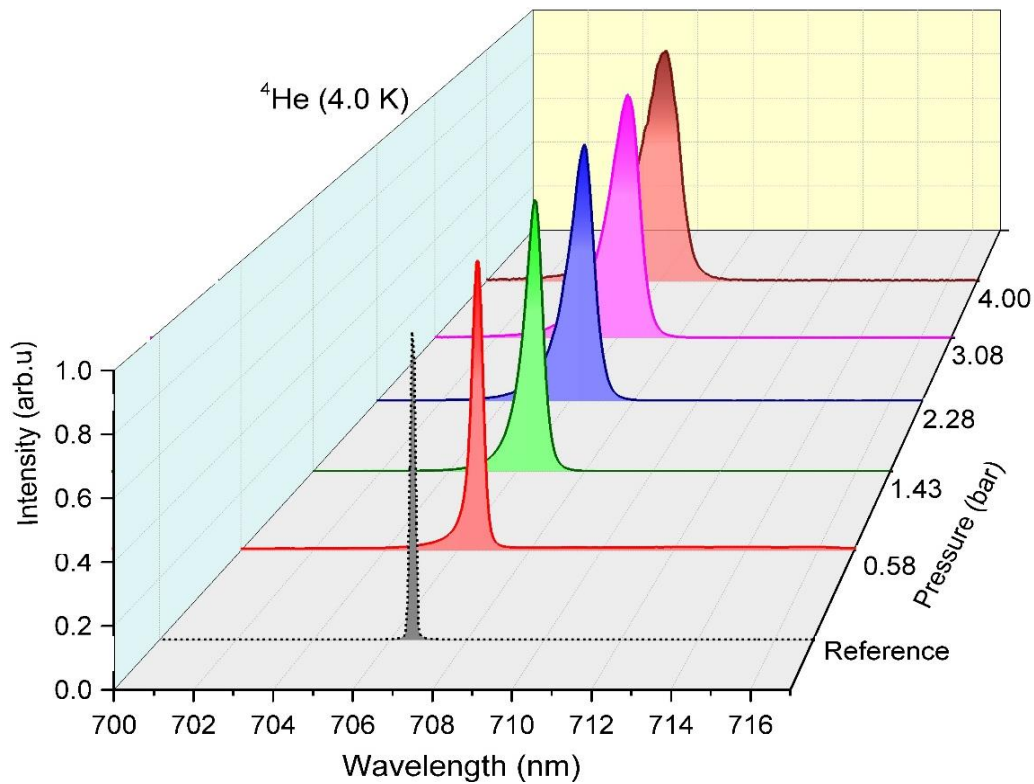


Figure 4.7: Overview of fluorescence spectra of gaseous and liquid helium in the region of the atomic triplet transition  $2p\ ^3P \leftarrow 3s\ ^3S$  at 4.0 K. Intensities have been normalised. A glow discharge spectrum in a dashed black line represents was used as the reference spectrum.

Fig. 4.7 showcases overview of fluorescence spectra of gaseous and liquid helium in the region of the atomic triplet transition  $2p\ ^3P \leftarrow 3s\ ^3S$ . This was recorded at 4.0 K over a variety of pressures. Intensities have been normalised to show the shift and broadening of spectral lines in three dimensions (3D). The dashed black line represents the glow discharge spectrum used as a reference.

## 4.7 Analysis of spectral atomic lines

### 4.7.1 Line-Shift versus pressure

To assess lineshifts, line broadening and intensity, the spectral lines were calibrated, normalized, and fitted to a Lorentzian function which produced good fits to the data.

The shift of spectral lines was measured from its maximum position relative to the maximum peak of the glow discharge line as a reference over a range of pressures (0.1 – 6.0 bar). Fig. 4.8 shows the lineshifts obtained from this fitting procedure as a function of pressure for four isotherms; 3.8, 4.0, 4.5 and 5.0 K. Correspondingly, Fig. 4.9 shows the lineshifts for the triplet line as a function of pressure for the same four isotherms.

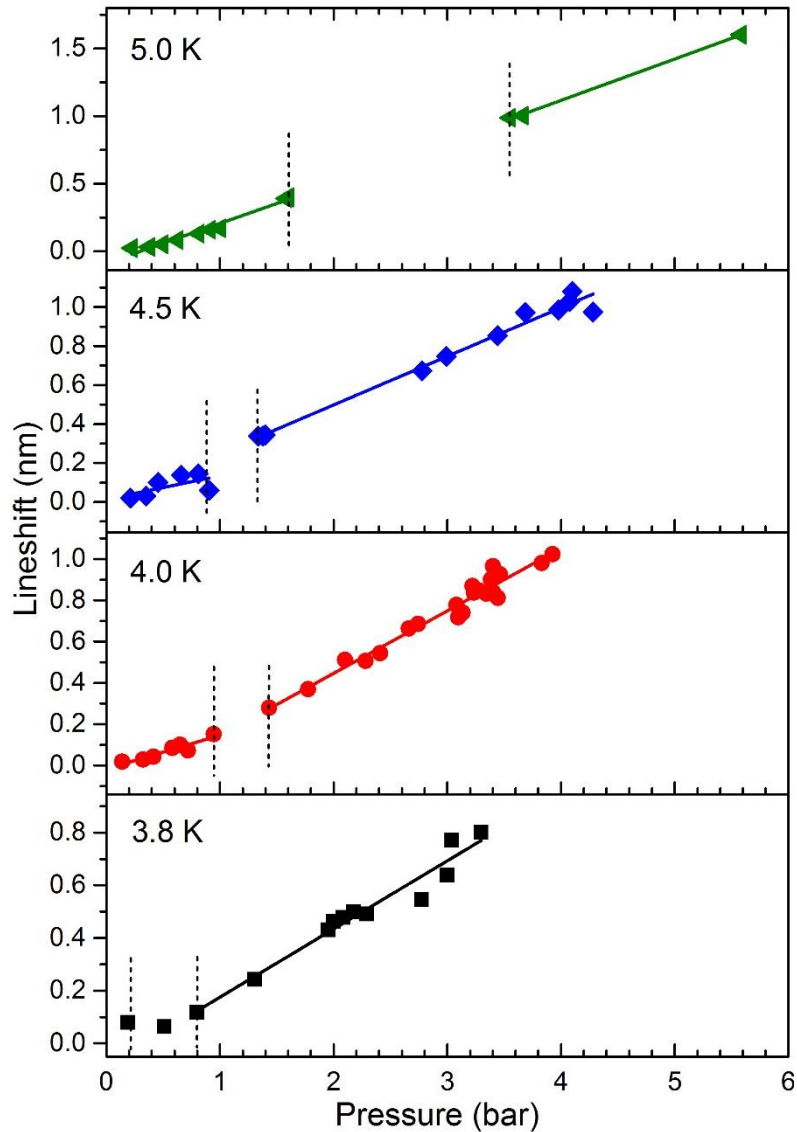


Figure 4.8: Pressure dependence of the  $2p\ ^1P \leftarrow 3s\ ^1S$  atomic singlet transition in the gas and liquid phases at 3.8, 4.0, 4.5 and 5.0 K. The straight lines indicate regions that show linear dependences on pressure. The dashed lines shows the region where the lineshift coefficient changes.

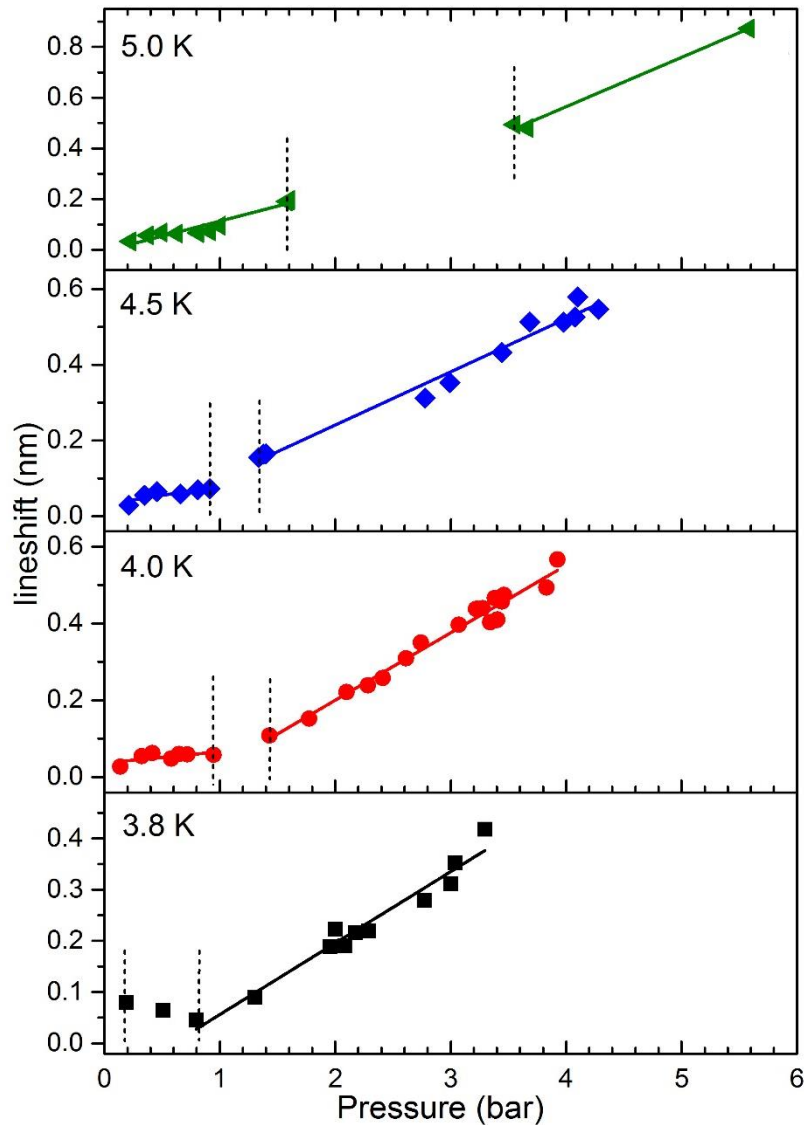


Figure 4.9: As per Figure 4.7 but for the triplet  $2p\ ^3P \leftarrow 3s\ ^3S$  transition. These lines were classified as gas phase at lower pressures and liquid phase at higher pressures; the region between them designated by dashed lines is believed to represent the associated phase transition.

The pressure dependence of the triplet  $2p\ ^3P \leftarrow 3s\ ^3S$  transition and the associated lineshifts have been measured previously by Soley and Fitzsimmons at pressures above *SVP* [53]. The lineshifts obtained from our measurements agree broadly with these results, and also with more recent measurements where corona discharge excitation has been employed [8, 120]. To the best of our knowledge, lineshifts below *SVP* pressure have not been previously reported, and will be contrasted with associated values in the liquid phase. Inspection of the pressure dependence of the lineshifts revealed regions where a linear dependence on pressure was apparent. These regions coincided with the gas and liquid phases; we note that this coincidence cannot be taken for granted as such. The

interaction between electronically excited helium atoms and ground state helium differs from the interaction between a helium ground state atom and another helium ground state atom. Also, the many-body effects of these systems may differ. As a consequence, one cannot expect the phase transition line of a mixed system of excited helium atoms solvated in ground-state atoms to coincide with the pressures and temperatures where the gas-liquid phase transition of pure helium occurs.

To establish trends, lineshifts were grouped depending on whether the data points lay in the gas or the liquid phase. The dashed lines in Figures 4.8 and 4.9 mark the boundaries of the crossover region where no data points were available, and hence whilst the phase transition could not be explored in finer detail, it was at least expected to lie in the region between the dashed lines. The function  $\Delta\lambda(p) = (\partial\Delta\lambda/\partial p)p + \Delta\lambda_0$  was fitted to the lineshifts by a linear fit that was performed in the OriginLab (Origin program) [142] with the equation  $y = a + bx$ , where  $y$  and  $x$  are the input data and represent lineshifts and pressures, respectively, and  $a$  and  $b$  are the intercept ( $\Delta\lambda_0$ ) and gradient ( $\partial\Delta\lambda/\partial p$ ), respectively. Lineshift coefficients,  $\partial\Delta\lambda/\partial p$  and intercept,  $\Delta\lambda_0$ , were obtained for the gas and solvated phases. The shift coefficients defined by the gradients of the lines for the singlet and triplet transitions are listed in Table 4.4, with the exception of the 3.8 K isotherm where too few data points below SVP were available to perform a reasonable analysis.

Table 4.4: Lineshift coefficients for singlet and triplet atomic lines in the gas and the liquid phases. There were too few data points available at 3.8 K in the gas phase to allow for a proper analysis, therefore coefficients for this region have not been determined.

$2p\ ^1P \leftarrow 3s\ ^1S$				$2p\ ^3P \leftarrow 3s\ ^3S$			
T [K]		slope, $\frac{\partial\Delta\lambda}{\partial p}$ [nm/bar]	intercept, $\Delta\lambda_0$ [nm]	T [K]		slope, $\frac{\partial\Delta\lambda}{\partial p}$ [nm/bar]	intercept, $\Delta\lambda_0$ [nm]
4.0	Gas	$0.16 \pm 0.03$	$-0.02 \pm 0.02$	4.0	Gas	$0.03 \pm 0.02$	$0.04 \pm 0.01$
4.5	Gas	$0.23 \pm 0.04$	$-0.03 \pm 0.02$	4.5	Gas	$0.05 \pm 0.02$	$0.03 \pm 0.01$
5.0	Gas	$0.30 \pm 0.02$	$-0.10 \pm 0.02$	5.0	Gas	$0.12 \pm 0.01$	$-0.01 \pm 0.01$
3.8	Liquid	$0.26 \pm 0.02$	$-0.10 \pm 0.05$	3.8	Liquid	$0.14 \pm 0.01$	$-0.10 \pm 0.02$
4.0	Liquid	$0.30 \pm 0.01$	$-0.16 \pm 0.04$	4.0	Liquid	$0.18 \pm 0.01$	$-0.15 \pm 0.02$
4.5	Liquid	$0.26 \pm 0.01$	$-0.03 \pm 0.03$	4.5	Liquid	$0.14 \pm 0.01$	$-0.04 \pm 0.02$
5.0	Liquid	$0.31 \pm 0.01$	$-0.11 \pm 0.03$	5.0	Liquid	$0.20 \pm 0.02$	$-0.21 \pm 0.10$

It can be seen from Table 4.4, the shift coefficients for the singlet transition, which are dominated by the resonance interaction, are larger than those for the triplet transitions in both the gas and liquid phases.

### **4.7.2 Linewidth versus pressure**

A similar procedure was undertaken to assess linewidths. According to the physical perturbation, line broadening can arise from different sources; it can be due to collisions in the gas phase or thermal motion in the condensed phase, where the perturbation shifts the energy levels and leads to line broadening. The retained symmetry of most rotational and atomic lineshapes allowed us to quantify the width of these lines by measuring the FWHM.

The linewidths obtained from fitting the spectral data with Lorentzian functions are shown in Figures 4.10 and 4.11 for the 3.8, 4.0, 4.5 and 5.0 K isotherms. Similar to the treatments given to lineshifts, the data were grouped together with respect to the thermodynamic phases and their apparent linear dependence on the pressure. A linear function was fitted to the data and linewidth coefficients thus obtained. The resulting linear functions are shown in Figures 4.10 and 4.11 as straight solid lines, and the calculated linewidth coefficients are listed in Table 4.5.

Again, the dashed vertical lines mark the gap in the data where we have reason to suspect that, within the crossover region between the gas and liquid phases, we can assume that for electronically excited helium the phase transition may not be exactly identical to that of pure helium. This assumption was based on the changing slope of the linewidth coefficient trend lines, and that this change was not always exactly coincident with the SVP. These crossovers were identified as being in the same regions as the lineshifts shown in Figures 4.8 and 4.9. We note that for the 5 K isotherm, the gradients of the linear functions in the gas and the liquid phase were very similar; also, however, the data are scarce. The grouping of the data is therefore somewhat ambiguous. Nominally, the data point recorded at 1.6 bar could be attributed to either the liquid or gas phases, either of which would produce an equally good fit. However, the crossover region would then lie between 1.0 and 1.6 bar, which would be significantly below the phase transition for pure helium at 1.6 bar.

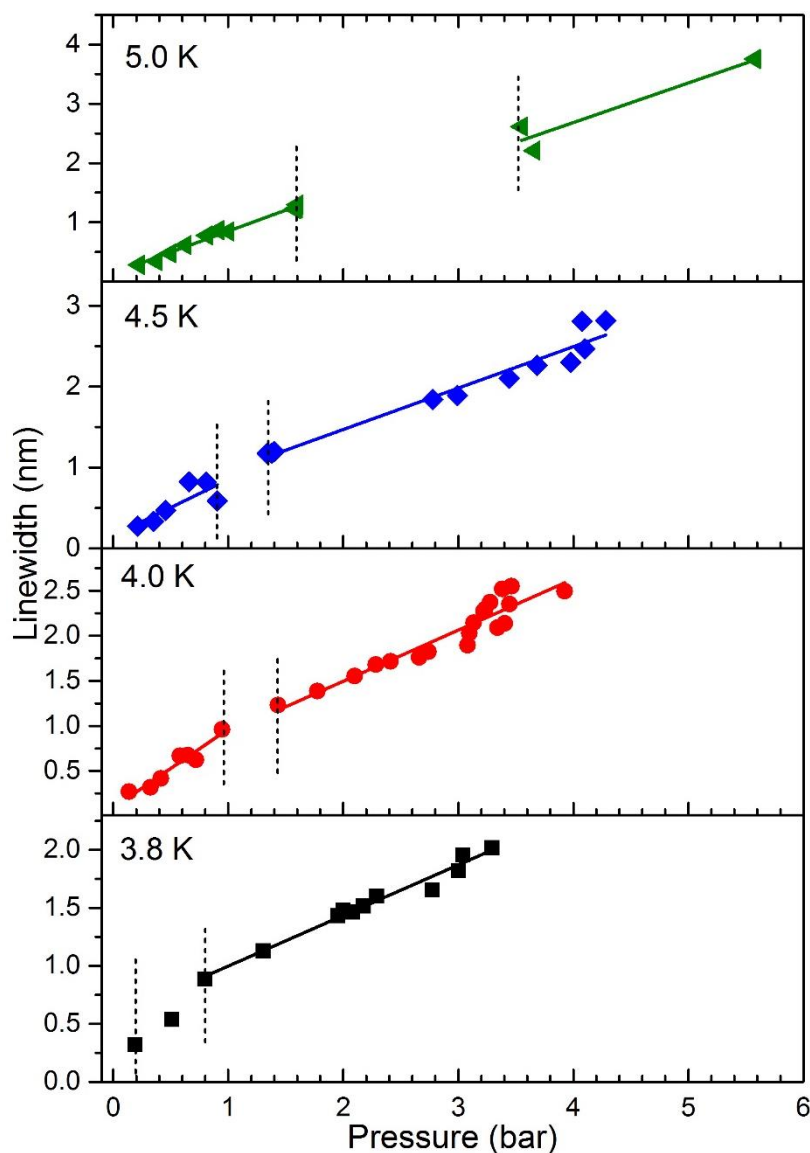


Figure 4.10: Pressure dependence of the linewidth of the  $2p\ ^1P \leftarrow 3s\ ^1S$  atomic singlet transition in the gas and liquid phases at 3.8, 4.0, 4.5 and 5.0 K. The straight lines indicate the regions that show a clear linear dependence on pressure. The dashed lines indicate the crossover regions. The unconvoluted, measured linewidths deduced from the fitting procedure are shown.

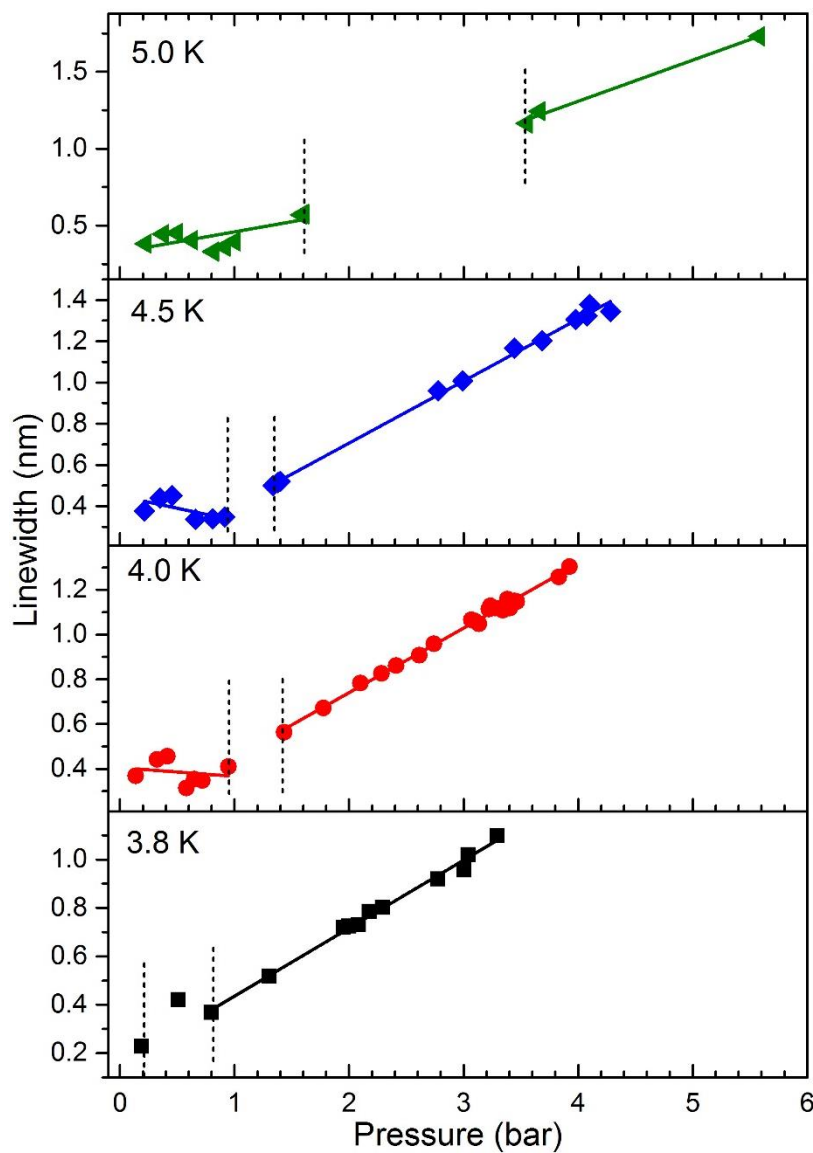


Figure 4.11: Pressure dependence of the linewidth of the  $2p\ ^3P \leftarrow 3s\ ^3S$  atomic triplet transition in the gas and liquid phases at 3.8, 4.0, 4.5 and 5.0 K. The straight lines indicate regions that show a linear dependence on pressure. The dashed lines illustrate the crossover regions. The measured linewidths deduced from the fitting procedure are shown.

Table 4. 5: Linewidth coefficients for singlet and triplet atomic lines in the gas and the liquid phases obtained from fitting the function  $\Delta\omega(p) = (\partial\Delta\omega/\partial p)p + \Delta\omega_0$ .

$3s\ ^1S \rightarrow 2p\ ^1P$				$3s\ ^3S \rightarrow 2p\ ^3P$			
T [K]		slope, $\frac{\partial\Delta\omega}{\partial P}$ [nm/bar]	intercept, $\Delta\omega_0$ [nm]	T [K]		slope, $\frac{\partial\Delta\omega}{\partial P}$ [nm/bar]	intercept, $\Delta\omega_0$ [nm]
4.0	Gas	$0.87 \pm 0.11$	$0.10 \pm 0.10$	4.0	Gas	$-0.04 \pm 0.10$	$0.41 \pm 0.10$
4.5	Gas	$0.70 \pm 0.30$	$0.16 \pm 0.20$	4.5	Gas	$-0.12 \pm 0.10$	$0.45 \pm 0.04$
5.0	Gas	$0.71 \pm 0.03$	$0.14 \pm 0.03$	5.0	Gas	$0.13 \pm 0.04$	$0.33 \pm 0.04$
3.8	Liquid	$0.44 \pm 0.02$	$0.56 \pm 0.10$	3.8	Liquid	$0.28 \pm 0.01$	$0.15 \pm 0.02$
4.0	Liquid	$0.50 \pm 0.06$	$0.52 \pm 0.20$	4.0	Liquid	$0.29 \pm 0.01$	$0.16 \pm 0.02$
4.5	Liquid	$0.51 \pm 0.04$	$0.45 \pm 0.12$	4.5	Liquid	$0.30 \pm 0.01$	$0.10 \pm 0.02$
5.0	Liquid	$0.67 \pm 0.21$	$0.01 \pm 1.00$	5.0	Liquid	$0.31 \pm 0.02$	$0.24 \pm 0.10$

Again, from Table 4.5, the magnitudes of broadening coefficients of the triplet transitions in both phases are smaller, as it was expected, than those for the corresponding singlet transitions, as controlled by the resonance interaction [110]. Line broadening constant almost increases continuously with temperature. Also, it is noticeable that linewidths of the singlet and triplet lines are twice as large as the lineshifts.

A comparison with previous studies [53, 57, 120, 143, 144] investigating the broadening and shifts of triplet lines at 706 nm are shown in Figures 4.12 and 4.13. On the other hand, for the singlet transition at 728 nm, only lineshifts studies were available for comparison with the literature, as shown in Fig 4.14, and to the best of our knowledge there has been no investigation into the effects of pressure on linewidth.

It can be seen from this comparisons that most of the results in these researches were in liquid phase, above the region of SVP curve of helium. Indeed, more time was needed to cover and understand the conditions of all such investigations.

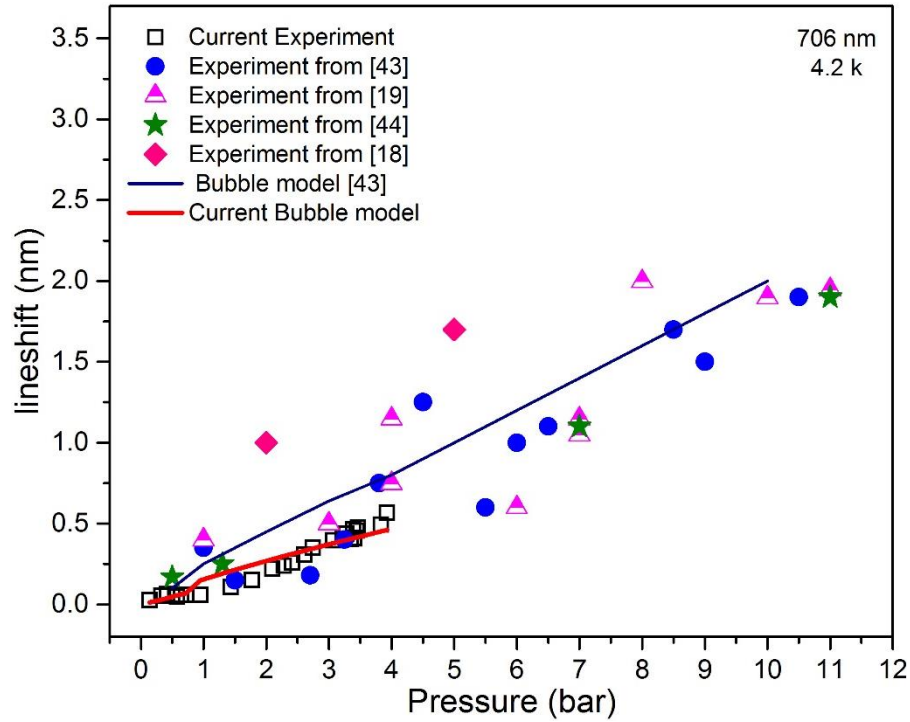


Figure 4.12 Shifts for the 706 nm line at 4.2 K at different pressures. Our experimental and theoretical results are represented using black squares and a solid red line. Other data from previous studies are also presented for comparative reasons.

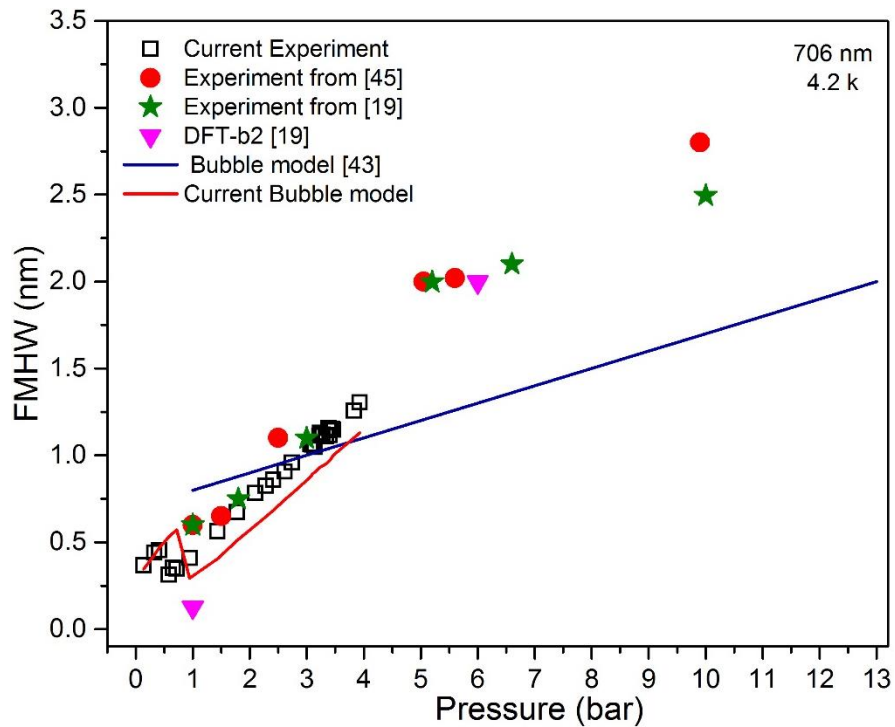


Figure 4.13: FWHM of the 706 nm line as a function of pressure at 4.2 K. Black squares are experimental data and the solid red line represents calculations that agree with experimental data, to a much greater extent than the calculation given by the blue line in [43] using the data therein.

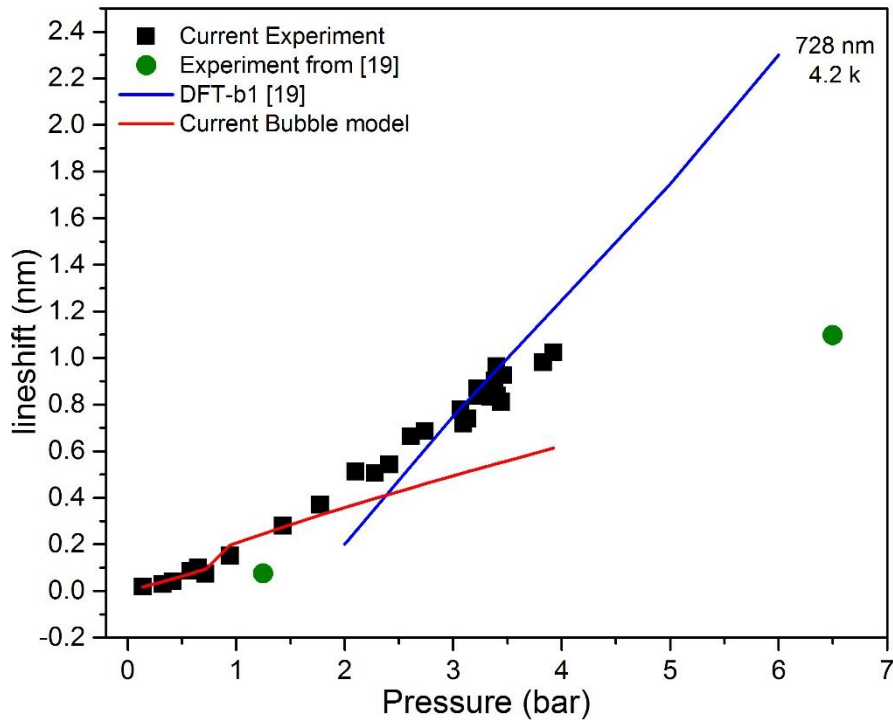


Figure 4.14: Our results with simulations of lineshift for the singlet 728 nm line at 4.2 K, as represented by the solid squares and red solid line, respectively. For this transition, there was insufficient data at high pressure to present additional linewidth results.

### 4.7.3 Line Intensity versus pressure

Another parameter which is interesting in addition to the lineshifts and linewidths is that of line intensities, as obtained herein from fitting the spectral data with Lorentzian functions. An apparent feature was that the intensity of the singlet lines was much lower than the intensity of the triplet lines (though this is not apparent from Figures 4.5, 4.6 and 4.7). However, Fig. 4.15 presents the original wavelength spectrum for singlet and triplet transition between 703–731 nm. This spectrum was recorded at 3.8 K at two different pressures, from which it is clear the difference in intensity between the triplet at 706 nm and singlet at 728 nm in the gas and the liquid phases of helium is quite considerable. This ratio was found to vary according to the pressure and temperature at which each spectrum was recorded.

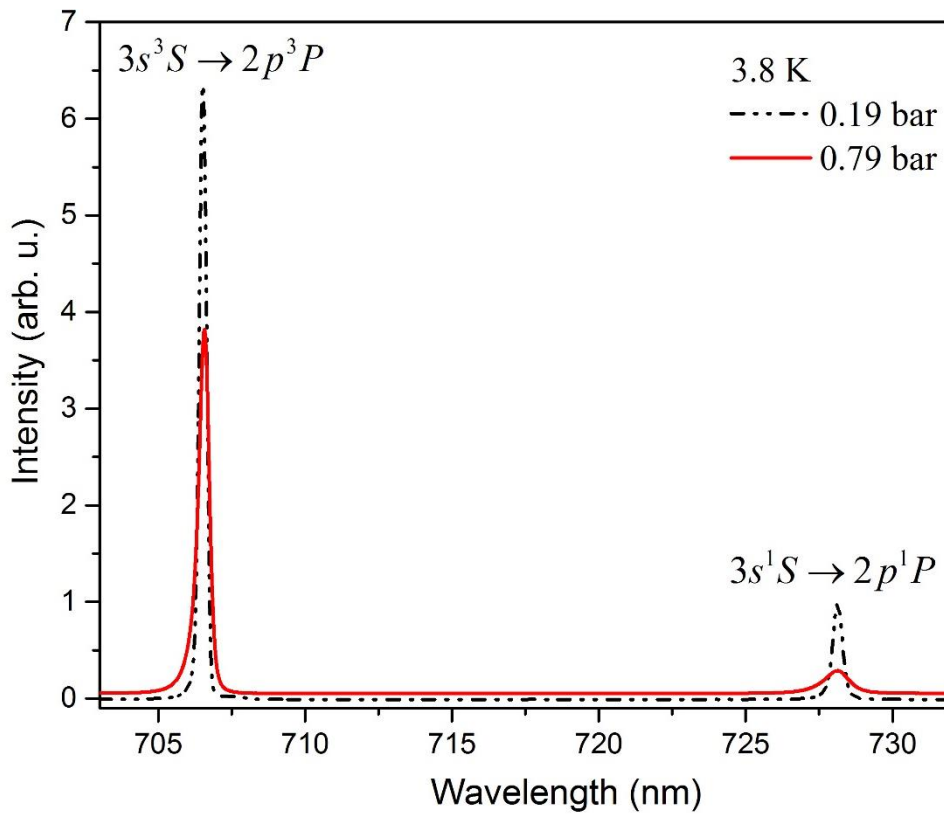


Figure 4.15: Overview of the spectra for the 3.8 K isotherm at different pressures for the triplet transition at 706 nm and the singlet transition at 728 nm. It is clear that the triplet transition is considerably more intense than the singlet transition in the gas and LHe phases.

Fluorescence intensity changes with pressure and temperature; from this, however, an analysis without meaningful calibration is rather challenging. We have therefore divided the intensity of the triplet line by that of the singlet prior to normalization, which eliminates the effects of intensity changes due to external factors. Fig. 4.16 shows the results of intensity ratio after fitting the spectral lines with a Lorentzian function for the isotherm of interest as a function of hydrostatic pressure. As previously, the dashed lines represent the region that it is thought to contain the phase transition from the gas phase to the liquid phase.

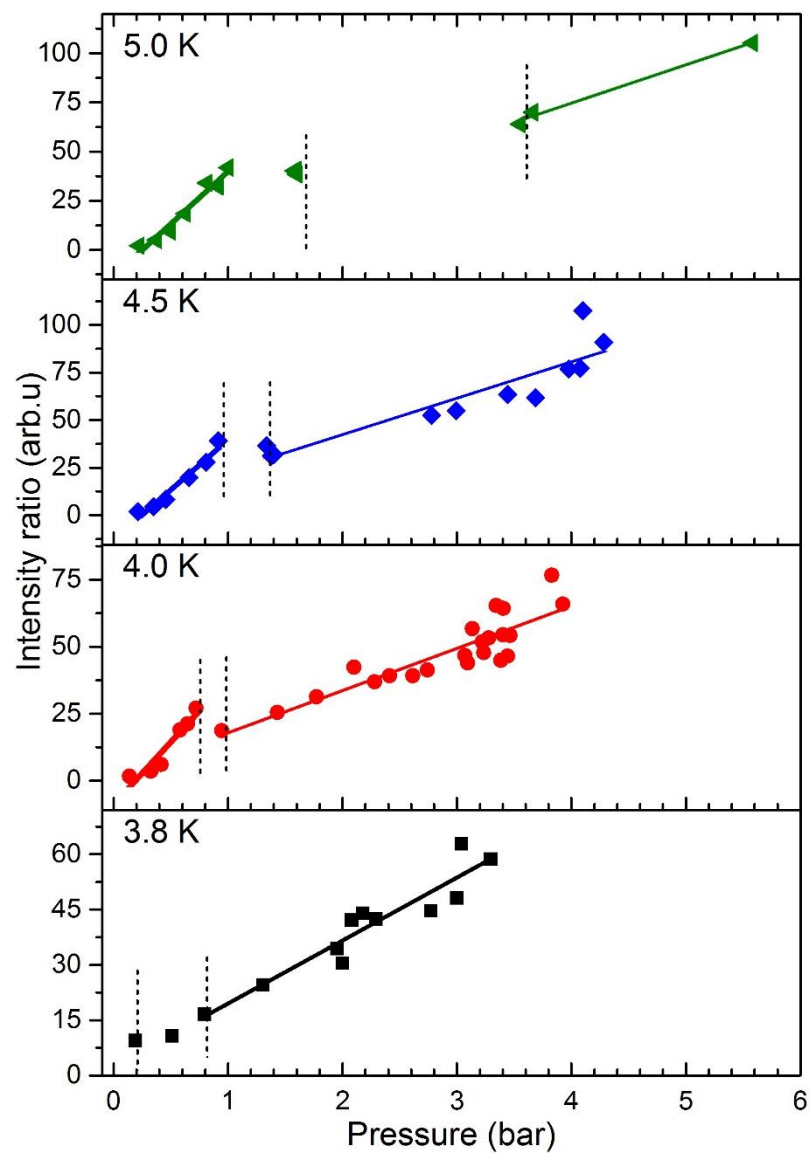


Figure 4.16: Pressure dependence of the intensity ratio of triplet ( $2p\ ^3P \leftarrow 3s\ ^3S$ ) and singlet ( $2p\ ^1P \leftarrow 3s\ ^1S$ ) lines at 3.8, 4.0, 4.5 and 5.0 K. The straight lines indicate regions that show a linear dependence on pressure. The dashed lines mark the boundaries of the crossover regions.

## 4.6 Prospective phase transition of He for different parameters

To reflect the importance of the above analysis, a comparison between the actual saturated vapour pressure SVP [137] and the SVP inferred from the pressure dependence of linewidths and lineshifts was undertaken. Fig. 4.14 presents this comparison for (a) the triplet and (b) the singlet transitions at 3.8, 4.0, 4.5 and 5.0 K. It can be seen that for the triplet transition, the phase transition takes place *below* the actual SVP of  $^4\text{He}$  for all studied isotherms, whereas for the singlet transition, both SVP curves are identical at 3.8 K and 4.0 K, and the measured SVP curve occurs at only a slightly lower pressure than the actual one at 4.5 K and 5.0 K. This is because the transitions for the excimer-helium mixed system are complex, and it should be noted that they differ considerably from those of the pure helium system. This indicates that the phase transition is likely to occur at slightly lower pressures than the values given by the actual SVP curve in the expected regions (as noted, between the parallel dashed lines in all the above analyses). Hence the change in the structure of the environments around atoms in these regions starts to allow the formation of a solvated shell of helium around individual helium atoms. From Fig 4.17, the shaded region between the hollow points indicates the region in the  $P$ - $T$  diagram where the hypothesized thermodynamic transition for the excimer- and excited helium atom mixed system is located. The function used to fit the data in Fig. 4.17 is known as EXP2PMod1 (Two-Parameter Exponential Function). This function is actually given by the relation  $y = a * \exp(b*x)$ , where the two parameters in this equation are temperature in K (corresponding to the  $x$  values) and pressure in bar (corresponding to the  $y$  values). Also,  $a$  and  $b$  represent the exponential parameters of the associated fit.

The relationships between the magnitudes of  $x$  and  $y$  ( $T$  and  $P$ , respectively) used in the exponential fit and the lineshifts and linewidths are reported in Table 4.6 for the atomic singlet and triplet lines.

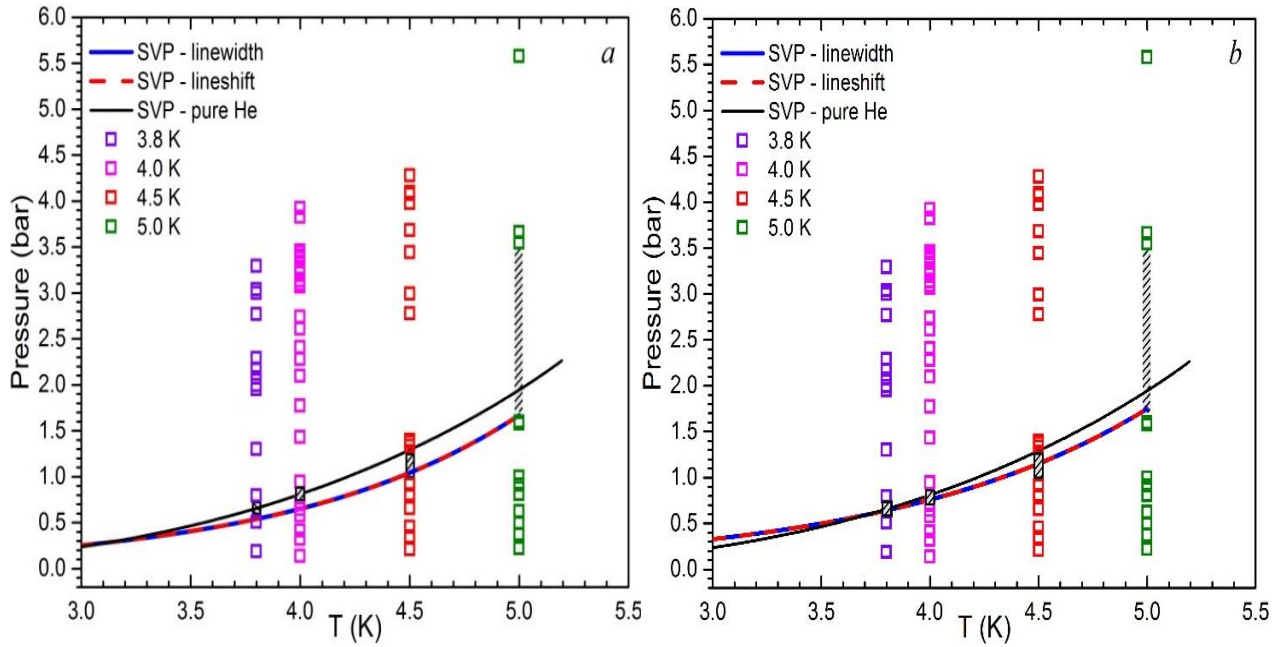


Figure 4.17: Linewidths and lineshifts (solid blue line and dashed red line, respectively) for the (a) triplet  $3s-2p$  and the (b) singlet  $3s-2p$  transitions. Hollow squares represent spectra measured for each of the indicated isotherms. The shaded region between the hollow points represents the region in the  $P$ - $T$  diagram where the hypothesized thermodynamic transition for the excimer-helium mixed system is anticipated.

Table 4.6: The values of pressure that quantify the hypothetical thermodynamic transition for the excimer-helium mixed system for both the singlet and triplet ( $3s-2p$ ) transitions at 3.8, 4.0, 4.5 and 5.0 K.

Atomic lines	Parameter	3.8 K	4.0 K	4.5 K	5.0 K
		Suspected pressure transition/bar	Suspected pressure transition/bar	Suspected pressure transition/bar	Suspected pressure transition/bar
singlet $3s-2p$	Line-Width	0.190 – 0.796	0.946 – 1.432	0.905 – 1.337	1.600 – 3.660
	Line-Shift	0.190 – 0.796	0.946 – 1.432	0.905 – 1.337	1.600 – 3.660
triplet $3s-2p$	Line-Width	0.190 – 0.796	0.946 – 1.432	0.915 – 1.337	1.600 – 3.550
	Line-Shift	0.190 – 0.796	0.946 – 1.432	0.915 – 1.337	1.600 – 3.550

## 4.7 Discussion

Corona discharges operating in a point-plane geometry in cryogenic helium create a confined region of excitation, producing a variety of localised electronically excited atomic and molecular transitions including the atomic transitions which are at the focus

of the present paper [145]. The lineshifts and linewidths observed for different pressures have been the topic of recent publications, though currently the associated results are still somewhat inconclusive. Allard *et al.* [145] pointed out that the large linewidths reported by Li *et al.* [8] are incommensurate with the temperatures of the discharge cell and liquid helium. Also, the same authors stress that it is important to include interaction potentials over a large range due to the Rydberg nature of the states involved in any analysis of lineshifts. Truncation at  $R = 16 \text{ \AA}$  would be insufficient and lead to false results.

We add to these findings that our data shows significant differences between the gas and liquid phases that rule out a quantitative analysis using the static or the impact approximation as these employ density as a key parameter. The differences between gas and liquid phase determined in the present study show that density alone cannot account for the observations.

Our recent publication shows  $\text{He}_2^*$  molecular spectral features and the population of high rotational quantum states equivalent to rotational temperatures of several hundred K, which is clearly incommensurate with a thermal equilibrium with liquid helium [59]. When the hydrostatic pressure of liquid helium was increased, these molecules were found to cool at a rate of at least  $10^{10}$  to  $10^{11}$  K/s via collisions with the liquid. At a pressure of a few bar, practically all molecules end up in the lowest allowed rotational quantum state before they fluoresce. These findings suggest a picture where helium gas bubbles, driven by the corona discharge, co-exist within the body of the liquid helium (see 2.8 about bubble formation).

The bubble size, which is pressure dependent, effects the lineshift and the broadening associated with spectral lines. Therefore, after increasing hydrostatic pressure, the size of the bubble decreases and hence the interactions between the surrounding atomic species will increase. This occurs as a result of the distance between the radiator and the perturbing ground state atoms being reduced. Consequently, linewidths and lineshifts will ultimately increase with increasing pressure. Moreover, previous studies have not, to the best of our knowledge, presented linewidth comparisons for the singlet 728 nm line due to the fact that experimental data were, in general, only obtained up to 6 bar due to the prevalent fluorescence quenching at, and beyond, this pressure [120]. Thus, the results of this study can be considered a benchmark for singlet state He.

Also upon increasing pressure, the volume available to the molecules in the bubbles decreases, equivalent to an increase of the concentration of helium in the gas bubbles

[59]. However, we also found that the concentration of gas bubbles in the cell decreases compared to the concentration of fully solvated molecules, suggesting that increased pressure stimulated the solvation of the molecules.

To test whether this assumption also holds for cryogenic gas, we compared the pressure dependence of the lineshift and linewidth coefficients, and the triplet to singlet intensity ratios, in the gas phase for the 3.8, 4.0, 4.5 and 5.0 K isotherms. All of these observables do not differ significantly with temperature over this range, with the exception of the 3.8 K isotherm. The most notable difference can be seen in the lineshift of the triplet atomic fluorescence, which decreases with increasing pressure in complete contrast to the trends observed at all other temperatures (Fig. 4.9).

In the liquid phase, lineshift and linewidth coefficients, and triplet to singlet intensity ratios, show a dependence on the cell temperature. The slope of the coefficients increases with temperature, with the exception of the 4.5 K isotherm. The intercepts of the lineshift coefficients are negative, indicating that the atoms are in a different environment than the gas phase. Also, the magnitude of the intercept increases with temperature, showing a greater sensitivity to the environment than might be expected for the gas phase.

In summary, there are many indicators to suggest atoms being solvated in liquid helium, or at least that a significant percentage of solvated atoms contribute to the spectral features. The possibility that atoms in gas bubbles contribute to the spectra cannot be excluded, however, as we do not have the tools to disentangle such a contribution.

The triplet-singlet intensity ratio shows an interesting dependency on both the pressure and temperature. In the gas phase, the intensity ratio of the two increases in a rather linear fashion. The slope of this increase is almost independent of cell temperature, indicating that plasma properties in the corona discharge region dictate the mechanisms of the energy transfer processes. A linear increase suggests that the higher-lying singlet states,  $E(3s\ ^1S) = 22.920$  eV, undergo collisions with ground state helium atoms to form the lower-lying triplet states with an energy of  $E(3s\ ^3S) = 22.718$  eV, which is 0.202 eV lower than the singlet.

However, such a conversion is rather unlikely. Not only does bridging this energy difference of 202 meV require rather high collisional temperatures, though this is in principle possible in a corona discharge plasma, but the Wigner Spin rule would also be violated [146]. Singlet-triplet transfers have been observed and investigated over many decades, including more recently in helium clusters and droplets that were electronically excited using monochromatic synchrotron radiation [147, 148]. Wellenstein and

Robertson showed that in a gas excited by a glow discharge, the Wigner Spin rule was not violated and that associative ionisation,  $\text{He}^* + \text{He} \rightarrow \text{He}_2^+ + \text{e}^-$ , followed by dissociative recombination,  $\text{He}_2^+ + \text{e}^- \rightarrow \text{He}^* + \text{He}$ , could satisfactorily explain experimental observations [129, 147, 149-155]. The  $\text{He}_2^+ + \text{e}^- \rightarrow \text{He}^* + \text{He}$  dissociation process has been investigated by Cohen [77] and Guberman [156]. The diabatic potential energy curves dissociating into the atomic  $3s^1\text{S}$  and  $3s^3\text{S}$  states cross the potential energy curve of vibrationally excited  $\text{He}_2^+$  [77]. In a simple picture, one would expect an intensity ratio of 3:1 dictated by the statistical weights of the atomic triplet and singlet states.

The fact that we observe a much stronger population of the triplet levels indicates that this simple picture does not fully account for the high densities and low temperatures presumed to be present in our cell. Glow discharges at pressures higher than a few millibars are characterised by a high concentration of  $\text{He}_2^+$  [157]. Studies under such conditions give also evidence of more complicated reactions involving, for example, three-body collisions, or  $\text{He}_3^+$  and  $\text{He}_4^+$  [157-159].

The strong increase of the triplet-singlet conversion rate observed with increasing pressure in our work could therefore have a number of explanations. Also, the number of data points in the gas phase is limited and, while a linear dependence on pressure is apparent, we cannot rule out higher-order contributions to the gradients in Figure 4.16. In the liquid phase, the triplet-singlet ratio is lower for pressures slightly above SVP than in the gas phase (at slightly below SVP). The ratio, then, increases with pressure, but not as rapidly as in the gas phase. Also, the triplet-singlet ratio depends on the temperature of the isotherm, where higher temperatures show higher singlet-triplet conversion rates. Given that the process appears to be more efficient in the gas phase at similar densities, a possible interpretation is that fewer particles are solvated at 5.0 K than at 3.8 K. At higher temperatures, the  $\text{He}_2^+$ ,  $\text{He}_3^+$  and  $\text{He}_4^+$  in gas bubbles would have a greater chance to recombine with electrons than at lower temperatures because solvated ions and electrons will have lower mobilities in liquid helium [160-163].

## 4.8 Error determination for the data

The estimation of the error from the determination of linewidths, lineshifts and line intensities could arise from various sources: (i) experimentally, due to inconstancy in the discharge current changes in temperature and pressure; (ii) analytically, with the

error inherent to the mathematical fitting procedures; (iii) the broadening of the spectral lines with increasing pressure and the concomitant overlap, and asymmetry, of the lineshape. Table 4.9 illustrates the values of the linear fits to the atomic lineshifts for the  $3s-2p$  singlet and triplet transitions, including the intercepts and the gradients for all isotherms studied. This is to show the magnitude of the standard error of each value and the magnitudes of the  $R$ -squared factor ( $R^2$ ) which represents the “goodness” of the linear fit process for each given phase. This was considered a highly convincing factor in the use of fits in our analysis. It was seen that the values of  $R^2$  in the gas phase are less than in liquid phase due to the reduced number of data points available to analyse the gas phase.

Table 4.7: The results of the linear fit of lineshifts of the  $3s-2p$  singlet and triplet transitions. This result includes the gradients in nm/bar and intercepts in nm of the gaseous (g) and liquid (solvated-s) phases for each given isotherm. The accuracy of the linear fit is quantified by the  $R^2$  factor.

Transition	T(K)	Phase	Intercept	Intercept	Slope	Slope	Statistics
			Value	Standard Error	Value	Standard Error	Adj. R-Square
Singlet	3.8	Liquid	-0.10	±0.05	0.26	±0.02	0.94787
	4.0	Gas	-0.02	±0.02	0.16	±0.03	0.86792
	4.0	Liquid	-0.16	±0.04	0.30	±0.01	0.95946
	4.5	Gas	-0.03	±0.02	0.23	±0.04	0.86944
	4.5	Liquid	-0.03	±0.03	0.26	±0.01	0.99316
	5.0	Gas	-0.10	±0.02	0.30	±0.02	0.97262
	5.0	Liquid	-0.11	±0.03	0.31	±0.01	0.99869
Triplet	3.8	Liquid	-0.10	±0.02	0.14	±0.01	0.95486
	4.0	Gas	0.04	±0.01	0.03	±0.02	0.58886
	4.0	Liquid	-0.15	±0.02	0.18	±0.01	0.96755
	4.5	Gas	0.03	±0.01	0.05	±0.02	0.61704
	4.5	Liquid	-0.04	±0.02	0.14	±0.01	0.97588
	5.0	Gas	-0.01	±0.01	0.12	±0.01	0.91126
	5.0	Liquid	-0.21	±0.10	0.20	±0.02	0.98725

## 4.9 Theoretical treatment using the Static Approximation

To get best comparison with our experimental results, the static equations used in reference [57] were also used in this treatment in an attempt to demonstrate the lineshifts and linewidths of the transitions of interest presented in previous sections. As mentioned previously, our findings show significant differences between the gas and liquid phases. This differences between the phases determined in the present study employ an important parameter, that of density, which would play a vital rule in any quantitative analysis using the impact or static approximations.

It is notable to mention that this is first time to use these equations in critical time of our research, therefore it need more repetitions to get further accuracy in results hoping to add new information about pressure dependence of the line shape. In this section, we will demonstrate a theoretical treatment via the static approximation used in [83] to model the emission observed for superfluid helium at 1.7 K, as used by publication [57] (but as per their experimental conditions, for LHe at 4.2 K). However, we carried out such calculations under our experimental conditions for gas and liquid helium at 3.8, 4.0, 4.5 and 5.0 K using a simple model of a spherical bubble with radius  $R_b$  and a trial function  $n(R)$  [164, 165].

The locative distribution of helium atoms around the excited helium atom is described on average by a density function which is equal to zero in the centre of the cavity ( $R = 0$ ), and which asymptotically (as  $R \rightarrow \infty$ ) approaches the bulk liquid density. A trial function of the form [166]:

$$n(R) = \begin{cases} n_{He}\{1 - [1 + \alpha(R - R_b)]e^{-\alpha(R-R_b)}\}, & \alpha(R - R_b) \geq 0 \\ 0, & \alpha(R - R_b) < 0 \end{cases} \quad (4.3)$$

Was used, where  $n_{He}$  is the helium number density, and  $R$  and  $\alpha$  are the variational parameters to be determined energy minimization. The value of  $\alpha$  was chosen as  $1 \text{ \AA}^{-1}$ , which appeared to be satisfactory in all cases. The radius of bubble or cavity ( $R_b$ ) is defined as the ‘‘centre of mass’’ of the area of transition from zero density to the normal bulk density,  $n_{He}$ , and it is given by the equation:

$$\int_0^{R_b} n(R)4\pi r^2 dR = \int_{R_b}^{\infty} [n_{He} - n(R)]4\pi r^2 dR. \quad (4.4)$$

Due to the reduction of the surface tension of the liquid ( $\sigma$ ) the energy term is required, and it is important to redistribute the liquid atoms and form the bubble. In this model, the classical expressions for the surface tension energy were used, as was the pressure-volume work term required to create a bubble of radius  $R_b$ , and the kinetic energy term due to the density gradient at the cavity edge [164]. Hence, the total energy of the spherical case is given by:

$$E_{total} = E_{int}(n(R)) + 4\pi R_b^2 \sigma + \frac{4}{3}\pi R_b^3 P + E_{kin}(n(R)) \quad (4.5)$$

By using the boundary profile in Eq. (4.4), the term in (4.5) was calculated as follows:

$$E_{kin} = \frac{\hbar^2}{8M_{He}} \int_{R_b}^{\infty} \frac{(\nabla n(R))^2}{n(R)} 4\pi R^2 dR = 1.67 \frac{\hbar^2}{8M_{He}} 4\pi n_{He} \alpha R_b^2 \quad (4.6)$$

Where  $P$  and  $M$  are the external pressure and the helium atomic mass (amu), respectively.

The parameter describing the repulsive interaction potential between the excited atom and surrounding atoms in the ground state was simulated as  $U(R) = C_{12}/R^{12}$ , where  $C_{12}$  and is the repulsive Lennard-Jones interaction [167] for interaction energy of two atoms separated by a distance  $R$ . It should be noted that  $C_{12} = qR^{12}$ , where  $q = (0.9 \pm 0.3) \times 10^{-16}$  erg. The data required to calculate the helium line broadening and shift of the  $2p \ ^3P \leftarrow 3s \ ^3S$  and  $2p \ ^1P \leftarrow 3s \ ^1S$  transitions are given.

$$E_{kin} = \int_{R_b}^{\infty} 4\pi R^2 \frac{C_{12}}{R^{12}} n(R) dR = 0.126 \frac{C_{12} n_{He} \alpha^{0.5}}{R_b^{8.5}} \quad (4.7)$$

At the equilibrium radius of the bubble, the total energy of the system in this model for the (excited helium atom  $He^*$  + bubble) in Equation (4.5) takes its minimum value. On increasing the pressure from  $P = 0$  to  $P = 3$  MPa, the radius decreases from 10.6 Å down to 8.6 Å.

The relationships used in reference [57] used to calculate the shift of the line centre relative to its location in vacuum and the FWHM are given by;

$$Shift = \frac{\lambda_o^2}{2\pi c \hbar} \left[ \frac{C_{12}^5 n_{He}^5 P^{18}}{\alpha^9} \right]^{\frac{1}{23}} \quad (4.8)$$

$$FWHM = \frac{\lambda_o^2}{2\pi c \hbar} \left[ \frac{C_{12}^4 P^{42}}{\alpha^{21} n_{He}^{19}} \right]^{\frac{1}{46}} \quad (4.9)$$

The value of interaction parameter  $C_{12}$  has only a weak effect on the lineshift and linewidth. On the other hand, the parameter describing the diffuseness of the boundary of the cavity,  $\alpha$ , which was chosen to be  $1 \text{ \AA}^{-1}$ , strongly affects the shift and width parameters. The results of the analysis conducted using these equations will be given in the following sections. The constants required in equation (4.8) and (4.9) are as follows:

$\lambda_o$ : the centre of atomic line (706 nm for the triplet, and 728 nm for the singlet)

$c$ : speed of the light (approximately  $3 \times 10^{10} \text{ cm/s}$ )

$\hbar = h/2\pi = 6.625 \times 10^{-27} \text{ erg.sec}$

$C_{12}$ : repulsive interaction constant ( $10^{-99} \text{ erg.cm}^{12}$ )

$\alpha$ : constant of diffuse boundary of the cavity ( $= 1 \text{ \AA}^{-1} = 10^{-8} \text{ cm}^{-1}$ )

$P$ : hydrostatic pressure in MPa ( $= 10 \text{ bar}$ )

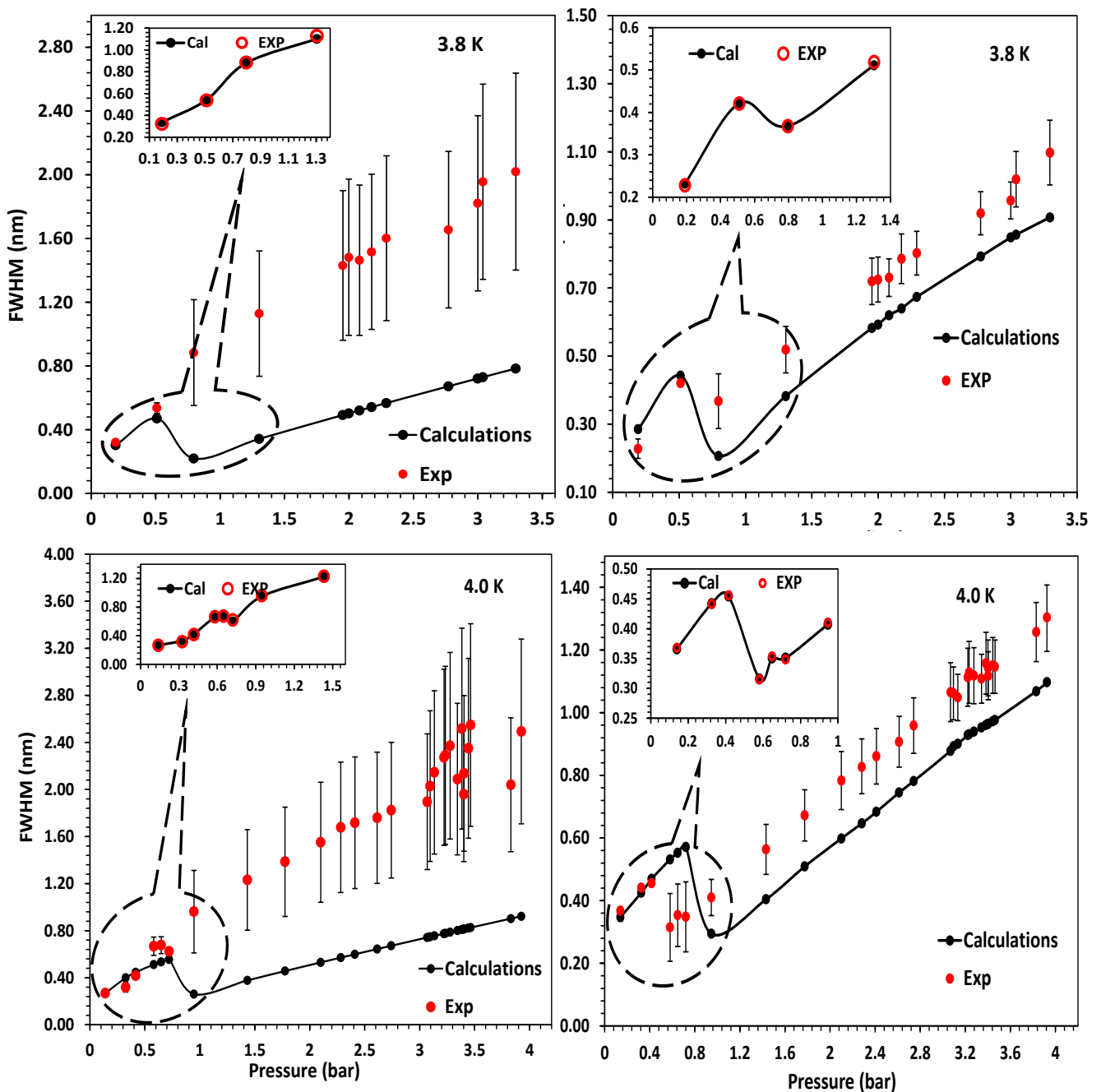
$n_{He}$ : the number density of the gaseous and liquid helium

### 4.10.1 Theoretical Linewidth for the singlet and triplet transitions

It is of interest to compare our experimental measurements with simulated parameters of linewidths and lineshifts. The results of calculations such as those presented in this section were carried out at four isotherms, 3.8, 4.0, 4.5 and 5.0 K. It is notable that the value of the  $n_{He}$  in reference [57] was constant in their calculations with a value of  $2.2 \times 10^{22} \text{ cm}^{-3}$  for  $LHe$  at 4.2 K, whereas in the current calculations, the magnitudes of number densities of helium vary for each measurements depending on phase, pressure and temperature.

The results of calculation are reflected in Figure 4.18 for the atomic  $2p \ ^1P \leftarrow 3s \ ^1S$  singlet transition on the left, and  $2p \ ^3P \leftarrow 3s \ ^3S$  triplet transitions on the right, of Figure 4.18 for

the linewidth. It can be seen from this figure that the pressure dependence of the simulated linewidth is similar to the experimental trends for all isotherms, where the linewidths are proportional to gas number density. On the other hand, the measured broadening of the triplet transition is in a closest agreement with calculations, and is significantly larger than the broadening observed for the corresponding singlet lines. This is because of the absence of the resonance interaction in the broadening mechanism in the triplet transition, whereas for the singlet lines, the effects of higher-order interaction terms are restricted by its much stronger resonance interaction [112]. Thus, numerous investigations of line broadening and some of the associated theoretical aspects were very difficult for singlet transitions affected by this resonance.



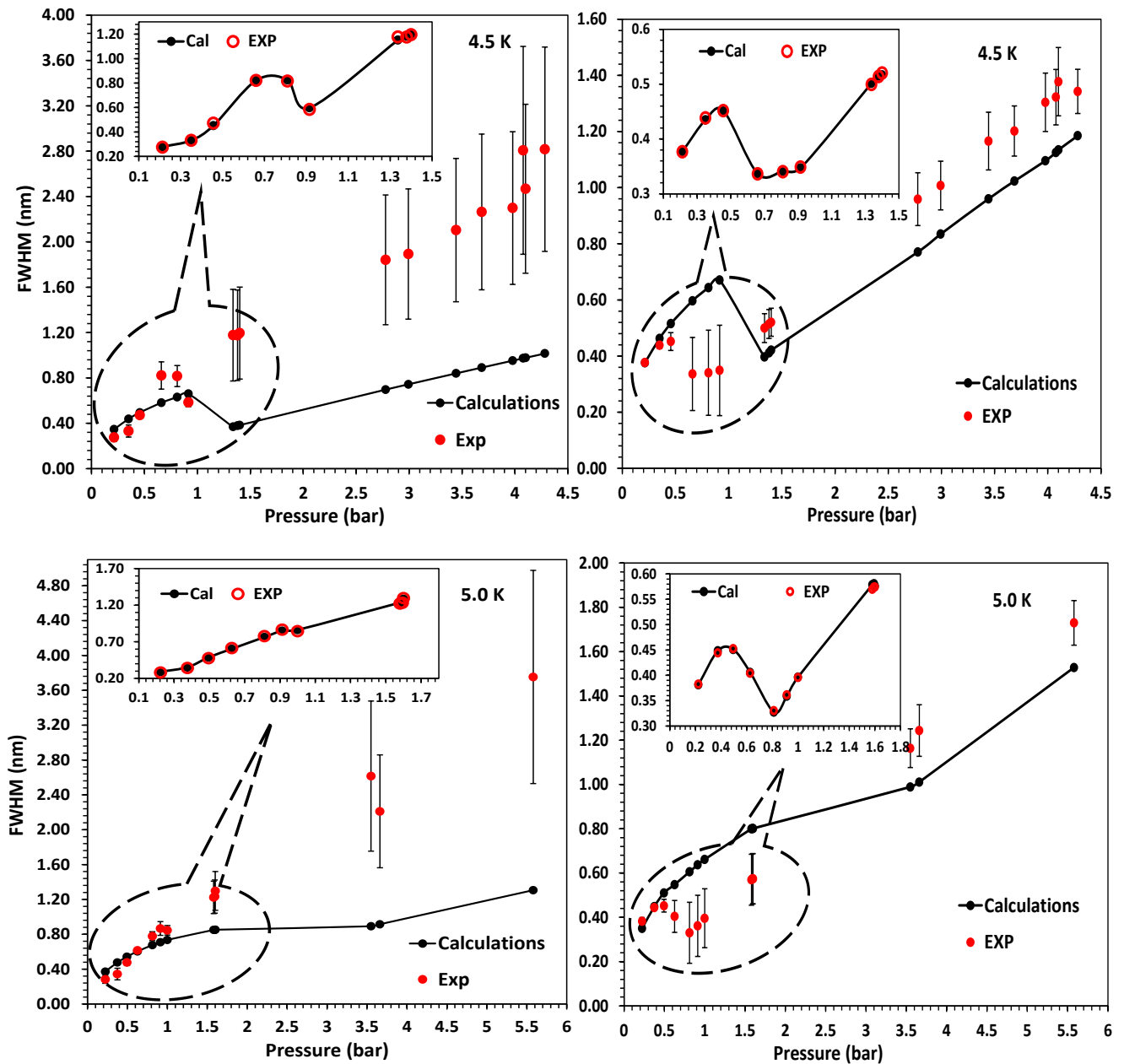


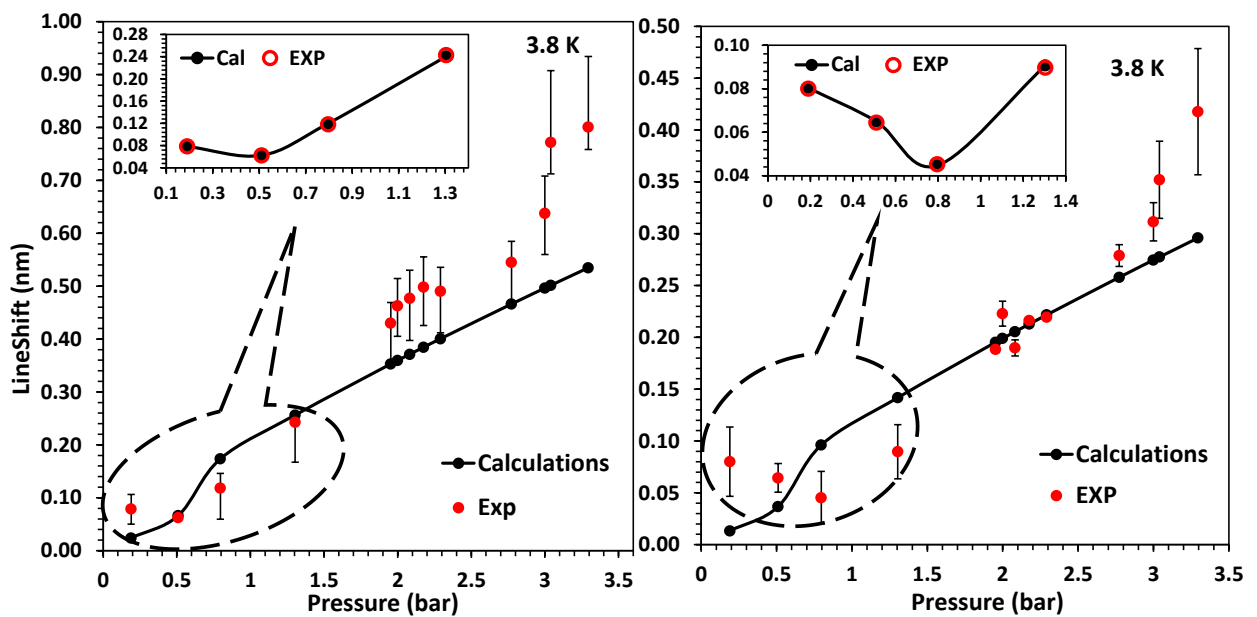
Figure 4.18: FWHM of the 728 nm (on the left-hand side) and 706 nm (on the right-hand side) atomic lines as a function of pressure in gas and liquid helium. Red dots are experimental data. Solid and black lines with dots represent the static approximation calculations. The inset shows the gas region corresponding to the data inside the dashed oval callout where there excellent agreement between the measured and simulated data can be achieved by changing helium number density. These comparisons were found at 3.8, 4.0, 4.5 and 5.0 K.

This is because some of the lowest pressure data points in the gas phase fit with theory, whilst slightly higher pressure data showing deviations from theory for all isotherms. Therefore, the helium number density was changed with temperature to find the conditions at which the theory could be fit to the data. We subsequently realized that the temperatures at the beginning of gas regime are higher than the isotherms being studied,

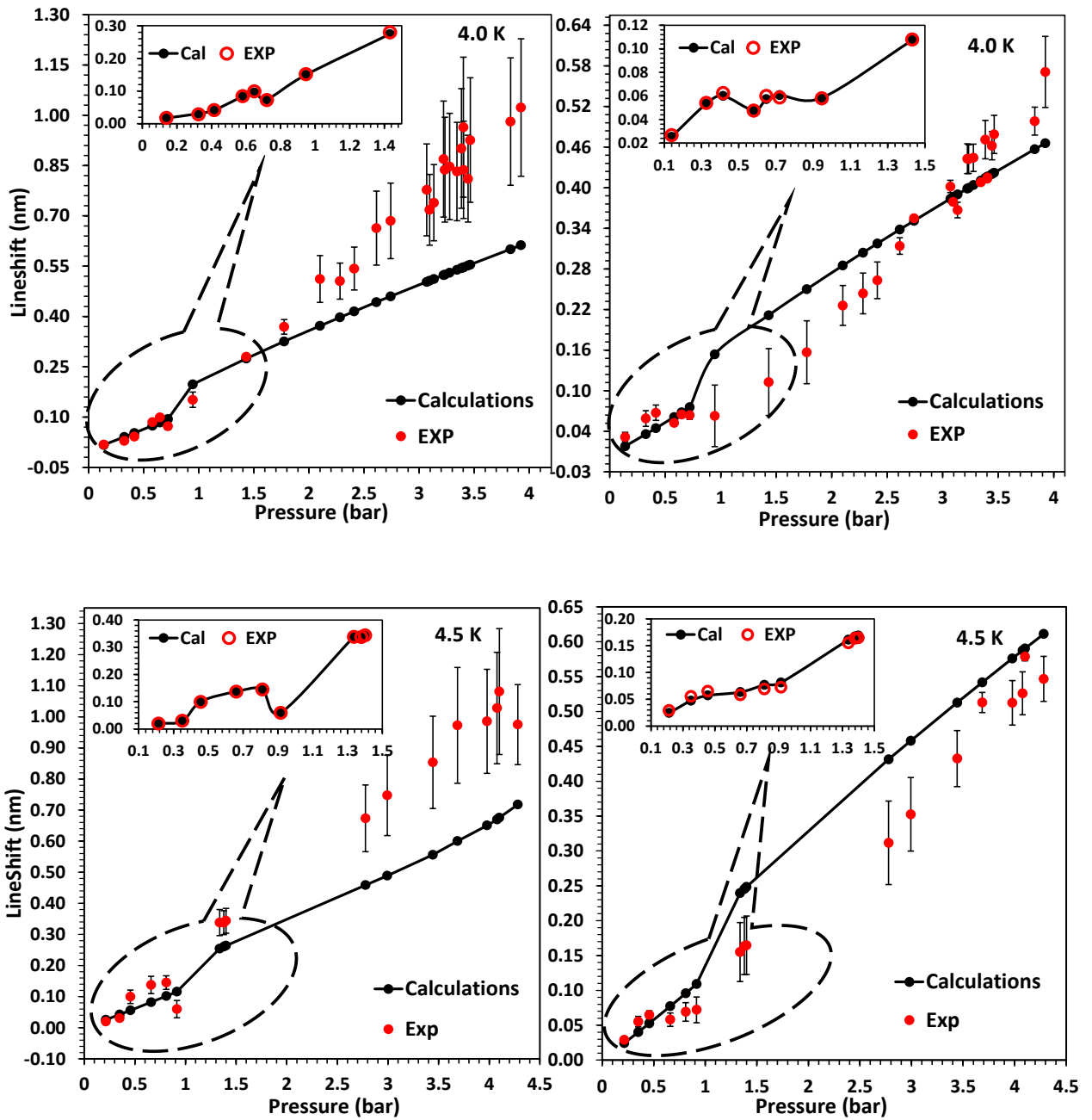
i.e., the temperature is 8.64 – 10.9 K at pressures of less than 500 mbar for all isotherms due to the local heat produced by high electrical field applied. With regards to the data found at pressures before the SVP line, the density was too high to obtain a good fit with theory and in return though this density is high and corresponds cold region, it still in the gas phase. The insets in Fig. 4.18 clarify the data points that show a good fit with theory in the regime below SVP<sup>6</sup>. As a consequence, it is expected that a layer of cluster probably forms around the excited atoms at point which is before the region of SVP curve of helium and it is likely that there is phase transition earlier.

### 4.10.2 Theoretical lineshift for the singlet and triplet transitions

Predominantly, in the instance of emission, uncertainty to somewhat in the measured line broadening is common due to the likelihood of lineshape distortion due to contributions from non-thermalized atoms in the upper excited state of the transition [108]. However, this does not affect lineshift measurements where the symmetric lineshapes do not suffer from such uncertainty. Hence, this would provide an excellent means of performing such a comparative study. In this section, we present measurements of the pressure shift of the helium singlet line at 728 nm and triplet line at 706 nm as compared with the results of our calculations.



<sup>6</sup> P.S.; this part of calculation has not conducted in publication of the spectral atomic lines that we mentioned in the beginning of this chapter, so this is first trying specially for singlet transitions we will indicate in this chapter.



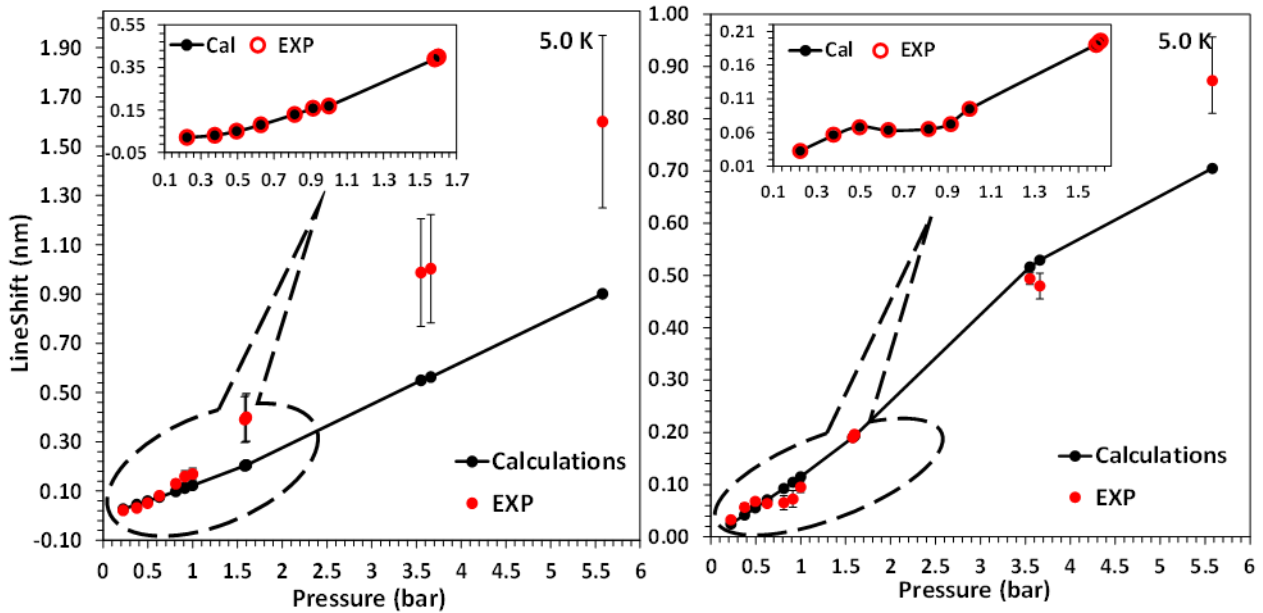


Figure 4.19: Comparison between measured lineshifts and theory for the singlet line at 728 nm (on the left side of the panel) and the triplet line at 706 nm (on the right) as a function of pressure at 3.8, 4.0, 4.5 and 5.0 K. The agreement between parameters are closest to theory for the triplet state. The insets in each isotherm show measured data points in the gas phase show a good fit with theory in the regime below SVP.

From Figure 4.19, the calculated lineshifts, as represented by black, solid lines, increase with temperature in both the singlet and triplet transitions. The red dots represent experimental data that is in a good agreement with calculations in both the gas and liquid phases but which then deviate from theory upon increasing the temperature from 3.8 K to 5.0 K. Again, as illustrated in the previous section for the linewidth, we focused on the data in the gas phase and recalculated the relationship with the lineshift by changing the helium density numbers to obtain a perfect fit, as shown in the inset in each isotherm. As expected, the temperatures that correspond with the density numbers in terms of obtaining a good fit were higher than the temperature measured in the cell. This was found for the first three data points in the gas phase. The others, which lie before crossing of phase transition were at lower temperature indicating the growth of clusters around the excited helium atoms<sup>7</sup>.

Table 4.7 reports the comparison of our calculations using the static approximation of the broadening and shifts in the He 706 nm triplet transition in wavenumbers with those

<sup>7</sup> The standard error deviation of theoretical treatments data for the singlet 728 nm and triplet 706 nm transitions, covering lineshifts and linewidths can be found in the Appendix G and H

of other publications. The calculations were performed at  $T = 4$  K for  $n_{He} = 2.65 \times 10^{22}$   $\text{cm}^{-3}$ , which is close to the asymptotic value of the helium density for  $P = 3.5$  MPa.

Table 4.8: Comparison of line parameters determined from static profiles and other approximations at  $T = 4$  K,  $P = 3.5$  MPa and  $n_{He} = 2.65 \times 10^{22}$   $\text{cm}^{-3}$ .

	FWHM ( $\text{cm}^{-1}$ )	$\Delta\nu$ ( $\text{cm}^{-1}$ )
This Work-Static approximation	20.03	80.14
MRCI [145]	39.50	-140.00
CI truncated [145]	42.60	86.50
Bonifaci <i>et al.</i> [120]	140.00	200.00

## 4.11 Conclusion and structural model

We have demonstrated a new design for the efficient acquisition of fluorescence spectra of helium excited by corona discharge over a wide range of pressures at cryogenic temperatures covering both the gas and liquid phases. Several thousand spectra were recorded, including some in the previously unexplored region of dense cryogenic helium gas, from which the atomic fluorescence lines emerging from the  $n = 3$  singlet and triplet states were analysed. The dependence of lineshifts and linewidth on pressure supported the supposition that a significant number of atoms are solvated in the liquid phase. In the gas phase, no appreciable dependence on the cell temperature was observed, indicating that plasma properties dictated the excitation mechanisms, the energy transfer and the emission processes. The fluorescence from triplet levels is dominated by that from the singlet levels by an intensity ratio of up to two orders of magnitude. This exceptionally high conversion rate was attributed to vibrationally excited molecular ion precursors undergoing dissociative recombination.

The long-range  $\text{He-He}^*$  repulsive potential has been used to calculate the lineshift and linewidths as based on the framework of the static approximation theory. It has been shown that such lineshapes are the result of the creation of a microcavity around the

excited helium atom,  $\text{He}^*$ . A comparison between data derived from experimental spectroscopic fluorescence and theory proved the accuracy of the potential in describing the interaction for  $\text{He}^*(3s)\text{-He}$  in both the singlet and triplet states. Both linewidth and lineshifts were found to be proportional to gas density and are effectively defined by the repulsive interaction between an excited helium atoms and surrounded by ground state helium atoms. Hence, it can be seen that lineshifts and broadening in the singlet and triplet lines are particularly sensitive to the helium density and temperature. Consequently, information on the conditions in the medium of helium is thus provided. Therefore, we can say the analysis of atomic lines represents a powerful tool because it is used as a means to understand on the processes occurring in the cell.

The fluorescence pressure dependence of lineshifts and linewidths were determined from the experimental data and compared to the theoretical predictions, demonstrating that the nascent excited helium  $\text{He}^*$  atoms reside in a bubble state within the liquid. In Figures 4.18 and 4.19, linewidth and lineshift parameters can be seen to increase with pressure for singlet and triplet lines both experimentally and theoretically from static line broadening calculations performed for all isotherms.

Furthermore, from the comparison with theory is that better agreement with experiment was observed for the gas phase than the liquid phase. Therefore, we concentrated on the gas phase; there has been no attempt to interpret the liquid phase because it contains a mixed and complex system of excited helium atoms in liquid helium.

On the other hand, the points that slightly deviate in the gas phase were recalculated for linewidth and shift to correspond with the actual conditions (pressure, temperature and helium number densities,  $n_{\text{He}}$ ). In this step, the helium number densities were taken into account, in that they were altered to correspond to the actual  $P$  and  $T$ . We realized that  $n_{\text{He}}$  was at a greater temperature than that measured, requiring adjustment from 8.7 K to 16 K to gain good agreement between theory and experiment. Hence, we can argue that the corona discharge heats the gas locally, and in fact this method of comparison is promising in terms of measuring localized temperatures. This implies that obtaining a good fit supports the interpretation that the local temperature is higher than the temperature of the cell. Furthermore, it is interesting that the data points between 500 mbar and 1200 mbar, and are below *SVP*, were found to achieve good agreement with theory by increasing  $n_{\text{He}}$ . This is likely to constitute confirmation of cluster formation of helium atoms around the bubble before crossing the *SVP* phase transitions, followed by subsequent growth as a solvated shell in LHe. So, we can presume that there are different

objects with different densities along the gas-liquid curve because the helium cluster densities are not as the same as the LHe densities.

A basic hypothesis of our model is that, according to a discontinuity of the slopes of the coefficients of linewidths and lineshifts between the gas and liquid phases, a structural change is obtained which can be interpreted to the existence of two contributions of spectral lines of  $\text{He}^*$ . First one when the excited helium atom resides in gas bubble that generated by repulsion force between the  $\text{He}^*$  and surrounding ground state helium atoms. The second contribution upon increase the pressure, layers of helium ground state clusters were formed around  $\text{He}^*$  and according to the simulation, it was found that the number of  $n_{\text{He}}$  becomes larger in closed region to the SVP, providing an evidence of cluster formation before helium liquefies. By continuing of increase pressure, the growth of cluster around  $\text{He}^*$  increases resulting to create solvation layer around  $\text{He}^*$ . Therefore, considerable increase in the coefficients of linewidths, line shifts and intensities in liquid phase indicating to the strong interactions between  $\text{He}^*$  and a solvation shell.

These observations were found to be in a similar manner of excimers. As a consequence, the question that raised in introduction has been answered about the possibility to apply the assumptions of solvated excimers to excited helium atoms as well, and to the first time

Fig 4.20 shows a schematic of an excited helium atom,  $\text{He}^*$ , in different species: firstly,  $\text{He}^*$  sites within a cavity (in a state referred to as a Rydberg state, represented as a red dot on the orbital) in the gas phase close to the tip electrode where the temperature is expected to be 8 – 10 K; the second case, when  $\text{He}^*$  is caged or solvated in the bubble within the liquid helium. The other species possible is that of He atoms clustered around  $\text{He}^*$  in the gas phase and below SVP, as shown in Fig. 4.21. A mix of two such  $\text{He}^*$  species in LHe is possible when LHe has been heated due to an excitation process such as an electron beam or electrical discharge which causes the formation of a bubble of gaseous helium around  $\text{He}^*$  in the liquid helium.

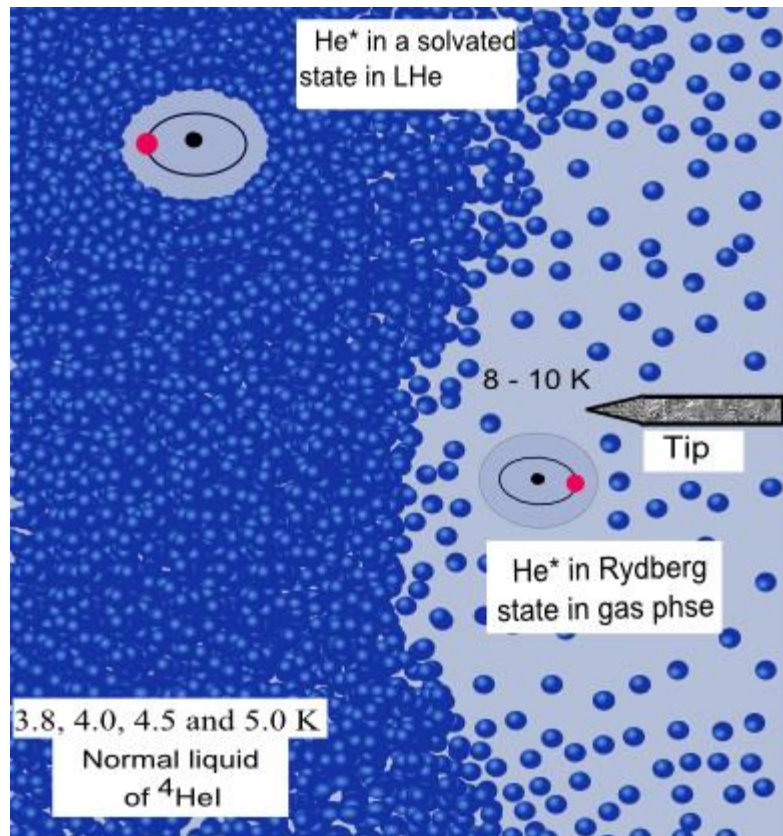


Figure 4. 20: Schematic diagram of an excited helium atom  $\text{He}^*$ : the first case is within Rydberg state in the gas phase, represented as a red dot. The second case is when it resides within a cavity that is solvated in normal liquid helium (LHe).

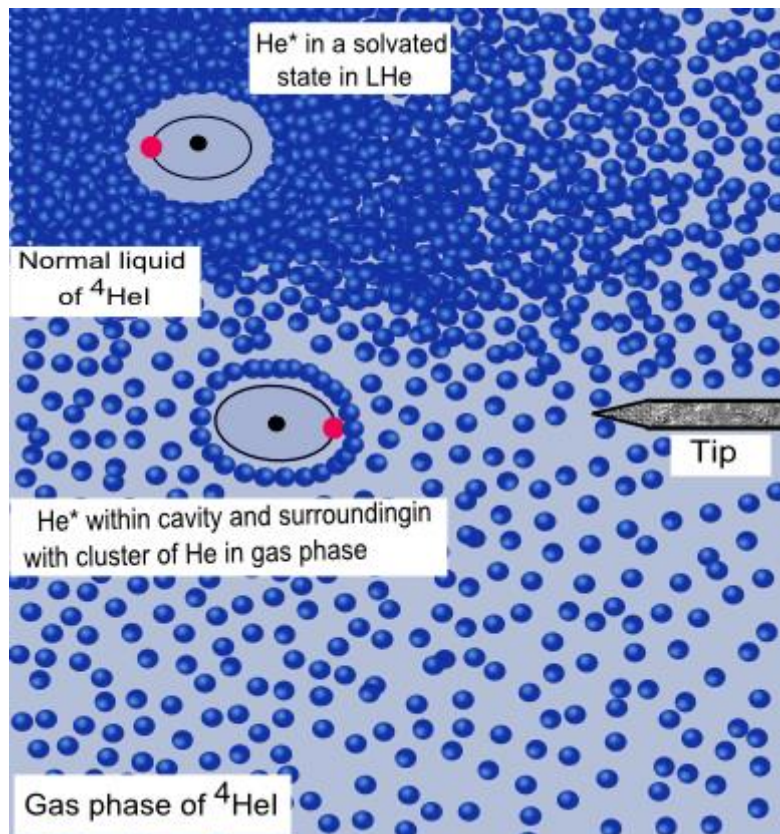


Figure 4. 21: Schematic diagram of excited helium atom  $\text{He}^*$  enclosed in a bubble that has formed a cluster with ground state helium atoms in the gas phase before *SVP*. The second model here is when  $\text{He}^*$  is caged or solvated in a bubble within a liquid helium medium.

## Chapter 5

### Results and discussion

# Pressure and Temperature dependence of Excimer-Cluster formation, Solvation and Boiling within Liquid Helium

This chapter is a complement to the work originally published in

[J. Phys. Chem. Lett. 2016, 7, 4666–4670](#)

DOI: [10.1021/acs.jpcllett.6b02081](https://doi.org/10.1021/acs.jpcllett.6b02081)

## Abstract

Helium excimers  $\text{He}_2^*$  generated in a corona discharge were investigated in the gas, normal liquid and supercritical phases of helium as a function of temperature and pressure between 3.8 and 5 K and 0.2 and 6 bar. Intense fluorescence in the visible and near infrared regions showed the rotationally resolved  $d^3 \Sigma_u^+ \rightarrow b^3 \Pi_g$  and  $D^1 \Sigma_u^+ \rightarrow B^1 \Pi_g$  transitions of  $\text{He}_2^*$ . With increasing pressure the rotational lines merged into single features. Spectra showed sharp, discrete rotational lines; upon increasing the pressure, the lines broadened and ultimately evolved into broad, poorly resolved features. Furthermore, the intensity distribution shifted toward the lowest rotational state. As this was only seen in the liquid phase, and with a different lineshifts than the rest of the spectrum, it was clear that the  $\text{He}_2^*$  spectrum is a superposition of features from gas-phase and solvated excimers. This means that solvated excimers not only exist but also can be identified via their spectroscopic fingerprint. The observed pressure dependence of linewidths, shapes and shifts established phases of coexistence and separation of excimer-helium mixtures, providing detailed insight into nucleation, solvation and boiling of  $\text{He}_2^*-\text{He}_n$  cluster.

The structure of this chapter is as follows: Section 5.1 gives a concise introduction to molecular bands and rotational spectroscopy. Experimental data are reported in Section 5.2. The treatment of the spectra, including calibration and fitting processes, is described in Section 5.3. Section 5.4 presents molecular bands of the  $d^3 \Sigma_u^+ \rightarrow b^3 \Pi_g(0-0)$  transition with its analysis in 5.4.1, and the  $D^1 \Sigma_u^+ \rightarrow B^1 \Pi_g(0-0)$  transition in 5.4.2, as recorded at 3.8, 4.0, 4.5 and 5.0 K that covers the analysis of the lineshifts, widths and intensities. Section 5.5 discusses the predicted phase transition of the SVP of LHe and reviews our hypothesis regarding the associated phase transition. A set of concluding remarks our observations through structural model are presented in Section 5.6, and in Section 5.7, error determinations for the data are discussed

## 5.1 Introduction

The ability to resolve rotational lines at low temperatures provides exceptional sensitivity for investigating molecule-solvent interactions. For example, infrared spectra of molecules embedded in 0.4 K cold  $^4\text{He}$  droplets [32] display sharp, discrete lines, indicating both free rotation and the superfluidity of the  $^4\text{He}$  droplets [19]. A decreased B-constant and a degree of line broadening reflect an interaction of the molecule with the normal component of helium at the interface [168, 169] with the otherwise superfluid helium. Mixed  $^3\text{He}$ - $^4\text{He}$  droplets with more than 60  $^4\text{He}$  atoms are also superfluid and have an even lower temperature of only 0.15 K. Remarkably, in this ultracold environment the linewidth of the rotational features is three times [19] smaller than in pure  $^4\text{He}$  droplets [13, 34].

In view of these exciting features and distinct temperature effects, this would seem a very promising starting point from which to perform rotationally resolved spectroscopy with control over a wide range of temperatures, beyond 0.15 and 0.4 K, particularly where additional control over pressure might also be possible. While this control is difficult to accomplish in helium droplets in free beams, it is quite readily possible using bulk helium. However, embedding single foreign molecules directly into bulk helium is challenging because at the temperatures of liquid helium all other substances are themselves frozen, [36] and sophisticated techniques are required to achieve this [37-39]. Short-lived helium excimers ( $\text{He}_2^*$ ) as single-molecule probes represent an alternative means of investigation; they have been used both recently [45, 46, 48, 170] and in the past to probe the bulk phases of helium by imaging [49] and spectroscopy. Dennis et al. have bombarded 1.7 K cold superfluid helium with electrons and observed fluorescence in the visible spectral range, which originated from transitions between various electronically excited singlet and triplet states of  $\text{He}_2^*$  [9]. Despite an environment of superfluid helium, the spectra did not show discrete rotational lines but rather features that resembled the rotational envelope of P, Q and R transitions. However, in a similar experiment, Hill, Heybey and Walter observed discrete rotational lines in the transient absorption spectrum of  $\text{He}_2^*$  [50] of 1.7 K cold superfluid helium. These lines were shifted from their associated emission-in-helium and gas phase values, though changes in the effective moment of inertia were not reported. Li et al. excited normal-liquid helium with a corona discharge and observed the fluorescent emission of  $\text{He}_2^*$ , similar to Dennis et al., but in this instance sharp, discrete lines were observed [8].

In all these experiments, however, the effects of temperature and the pressure have not been addressed.

To advance the understanding of solvation in liquids, we have recorded fluorescence spectra of excimers  $\text{He}_2^*$  for the  $d^3 \Sigma_u^+ \rightarrow b^3 \Pi_g(0-0)$  and the  $D^1 \Sigma_u^+ \rightarrow B^1 \Pi_g(0-0)$  transitions in a helium solute over a wide range of hydrostatic pressures between 0.2 and 5.6 bar and at temperatures between 3.8 and 5.0 K, covering the gas and normal liquid phases of helium, as will present in coming sections.

## 5.2 Experimental data of Molecular bands

As mentioned in chapter 4.2, a corona discharge electronically excites and ionises He atoms under a wide range of pressures. As a result, intense fluorescence can be observed in the visible region. Figure 4.1 shows a pressure and temperature (*PT*) diagram of the data we collected below supercritical points ( $T_C$ ,  $P_C$ ) from 3.89 K to 5.2 K. Each point represents a fluorescence spectrum in the range 300 – 1000 nm. Emission spectra were recorded in the gas and liquid phases by varying the hydrostatic pressure. With a view to gaining accuracy and consistency in the data, spectra were recorded several times under the same conditions.

The rotationally resolved  $d^3 \Sigma_u^+ \rightarrow b^3 \Pi_g(0-0)$  and  $D^1 \Sigma_u^+ \rightarrow B^1 \Pi_g(0-0)$  transitions of  $\text{He}_2^*$  that are observed due to the transitions between electronically excited states were investigated in this chapter. The wavelengths ( $\lambda$ ) corresponding to the transitions at 639.87 nm and 659.42 nm, respectively. Each molecular band includes Q, P and R branches.

Table 5.1 shows a comparison of the rotational lines positions observed in the current study and a previous analysis conducted by Ginter [79, 80]. It was found that the molecular transitions of our data are blue-shifted with respect to the Ginter values by approximately  $9 \text{ cm}^{-1}$ , or 0.45 nm, for the triplet  $d-b$  transition and  $8 \text{ cm}^{-1}$ , or 0.39 nm, for the singlet  $D-B$  transition. Actually, we have no explanation for this deviation, but it looks to be in good agreement regarding the position of all rotational lines.

Table 5. 1: Positions of Q and P branches of the triplet  $d-b$  and singlet  $D-B$  rotational transitions obtained with a glow discharge. Observed values of these positions in wavenumbers were compared with previous data reported by Ginter [79, 80], where  $\nu_0$  is the central position of each peak and  $\Delta\nu$  is the difference between our value and the equivalent value reported in [79, 80].

Branch	$d\ ^3\Sigma_u^+ - b\ ^3\Pi_g (0 - 0)$			$D\ ^1\Sigma_u^+ - B\ ^1\Pi_g (0 - 0)$		
	Ginter [79] $\nu_0/\text{cm}^{-1}$	Current value $\nu_0/\text{cm}^{-1}$	Current- Ginter $\Delta\nu/\text{cm}^{-1}$	Ginter [80] $\nu_0/\text{cm}^{-1}$	Current value $\nu_0/\text{cm}^{-1}$	Current- Ginter $\Delta\nu/\text{cm}^{-1}$
Q	15623.87	15632.23	8.36	15161.72	15168.99	7.27
P(2)	15594.63	15604.22	9.59	15132.70	15140.80	8.10
P(4)	15564.60	15573.85	9.25	15103.46	15111.68	8.22
P(6)	15534.14	15543.35	9.21	15074.25	15082.47	8.22
P(8)	15503.33	15512.46	9.13	15045.12	15053.53	8.40
P(10)	15472.23	15481.36	9.13	15016.11	15023.99	7.88

## 5.5 Treatment of the spectra

### 5.3.1 Calibration using glow discharge spectra

As mentioned in chapter4 section 4.3.1 and 4.3.2 and as an important step after collecting spectra, calibration of spectra is required. For such, glow discharge spectra were recorded at room temperature and low pressure where every experimental setup has a particular discharge spectrum depending on the alignment of optical setup that based on the arrangement of the lenses and mirrors to focus emitted lines on the CCD of spectrometer (see chapter3- experimental part). The process of calibration explained in chapter 4, in particular that the results of calibration, in terms of gradients and intercepts found for the singlet  $D-B$  transition being different from the triplet  $d-b$  transition, as shown in Table 5.2. This is because the experiment for  $D-B$  was conducted in another date and under conditions differs from  $d-b$  which led us to record spectrum of glow discharge for each case and doing calibration. Additionally, the glow discharge spectrum is used as a reference by measuring the differences between the positions and shapes of identical features in the collected spectra and discharge spectrum to investigate associated changes in spectral parameters.

Table 5. 2: The values of the experimental setup that made to record spectra of glow discharge for calibration of the singlet  $D-B$  and  $d-b$  transitions after gas line evacuation at room 300 K.

T = 296 K	$d\ ^3\Sigma_u^+ - b\ ^3\Pi_g (0 - 0)$	$D\ ^1\Sigma_u^+ - B\ ^1\Pi_g (0 - 0)$
Slope (m) / mm/row	0.05799	0.05795
Intercept (b) / nm	289.28	298.6228
V/ kV	-0.61	-1.07
I / $\mu$ A	-67	-94
P / mbar	61	78
Accumulation No.	20	10
Slit opening / $\mu$ m	20	80
Exposure time / seconds	0.1	5.0

### 5.3.2 Fitting with Lorentzian function

As explained in chapter 4.3.1, to assess the changes in lineshape and position with pressure and temperature, rotational branches were systematically and individually fitted to Lorentzian functions. To perform this fitting, the Fityk software [139] was chosen (Version 0.9.8). An example of a good fit, indicating the accuracy that could be achieved by this method, is shown in Figure 5.1. This fit is for the rotational lines of the Q and P branches of the  $d-b$  and  $D-B$  transitions of  $\text{He}_2^*$  in liquid helium, for which it is difficult to gain high-resolution rotational lines. The R branch is not included in this analysis due to its low resolution. Although at high pressures one of the branches merges with the other, the fitting process allowed individual lines to be deconvoluted. For instance, from Fig 5.1 it can be seen the P(2) line of the triplet  $d-b$  transition had merged with the Q branch at a pressure of 2.6 bar, hence it difficult to determine the associated peak position and linewidth. The fitting process, however, allowed for deconvolution of the lines, allowing an accurate analysis of features for each branch, except the R branch.

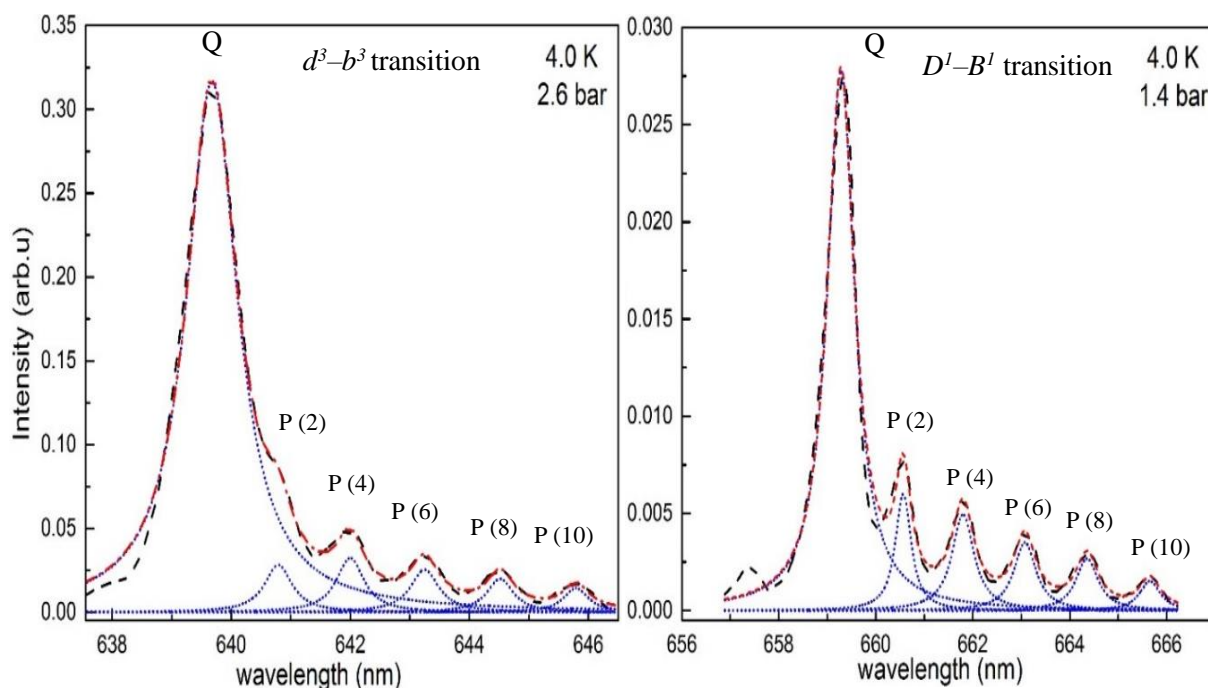


Figure 5.1: Fit of spectra using Lorentzian functions provided in the Fityk program [34] showing a perfect fit in LHe for the triplet  $d-b$  and singlet  $D-B$  transitions at  $P = 2.6$  bar and 1.4 bar respectively, at  $T = 4.0$  K. The black-dashed line represents the measured and calibrated spectra, the overall fit is represented by a red-dashed line, and the blue dotted lines show the individual Lorentzian components.

## 5.6 Molecular band

### 5.6.1 $d^3\Sigma_u^+ - b^3\Pi_g$ transition

It is noteworthy that the first part of analysis of molecular band was investigated in principle by a colleague at the University of Leicester, Luis Mendoza-Luna [3]. To complement his studies due to his lacking of time, however, further analysis at 4.5 K was undertaken for  $d-b$  transition. Moreover, line intensities were investigated in addition to the lineshifts and widths to confirm our group's previous quadratic component exploration into the formation of helium excimers in different environments [59]. Therefore, the analysis of this triplet fluorescence, as will be presented in this

section, are a collaborative work achieved by team work between myself and my colleague [3].

Fluorescence spectra were recorded at 3.8, 4.0, 4.5, and 5.0 K, showing the  $d^3 \Sigma_u^+ \rightarrow b^3 \Pi_g$  transition of  $\text{He}_2^*$  in the  $n = 3$  Rydberg state [79], as shown in Fig 5.2, for various different hydrostatic pressures, covering both the gas and the liquid phases of helium. A glow discharge spectrum recorded in the gas cell at very low pressure is shown as a reference for the line-positions under vacuum conditions [79] and to demonstrate the resolution of the spectrometer. The spectrum shows typical features with P, Q, and R rotational lines defined by the selection rules  $\Delta N = -1, 0, \text{ and } 1$ , respectively. The quantum number,  $N$ , denotes the lower rotational state of the transition and starts with the electronic angular momentum quantum number, which is one for the  $b^3 \Pi_g$  state.  $N$  refers to *Hund's* coupling case (b), where  $N$  is the total angular momentum,  $J$ , minus the electron spin,  $S$  (i.e.,  $N = J - S$ ). P and R lines are resolved; the Q lines lie almost on top of each other and are thus too closely spaced to be fully resolved by our spectrometer. All lines are split into groups of six energetically close transitions due to spin–spin and spin–orbit interactions of the triplet levels in Hund's case (b) [171]. As before, however, these splittings cannot be observed at our resolution.

At low cell pressures, sharp, discrete lines were observed, similar to the spectra reported by Hill *et al.* [50] and Li *et al.* [8]. With increasing pressure, the lines shift in frequency, broaden and become increasingly asymmetric. By comparison with the glow discharge spectrum, it can be clearly seen that at lower pressures the P(2) line and Q-branch quickly gain intensity compared to the other P lines. Additionally, the P(2) line merges at a certain, distinct pressure for each given isotherm, with the Q-branch. At 3.8 K, this occurs between 0.2 and 0.6 bar, at 4.0 K between 0.7 and 0.9 bar, at 4.5 K between 1.3 and 2.8 bar, and at 5.0 K between 1.6 and 3.6 bar, as shown in Fig 5.2.

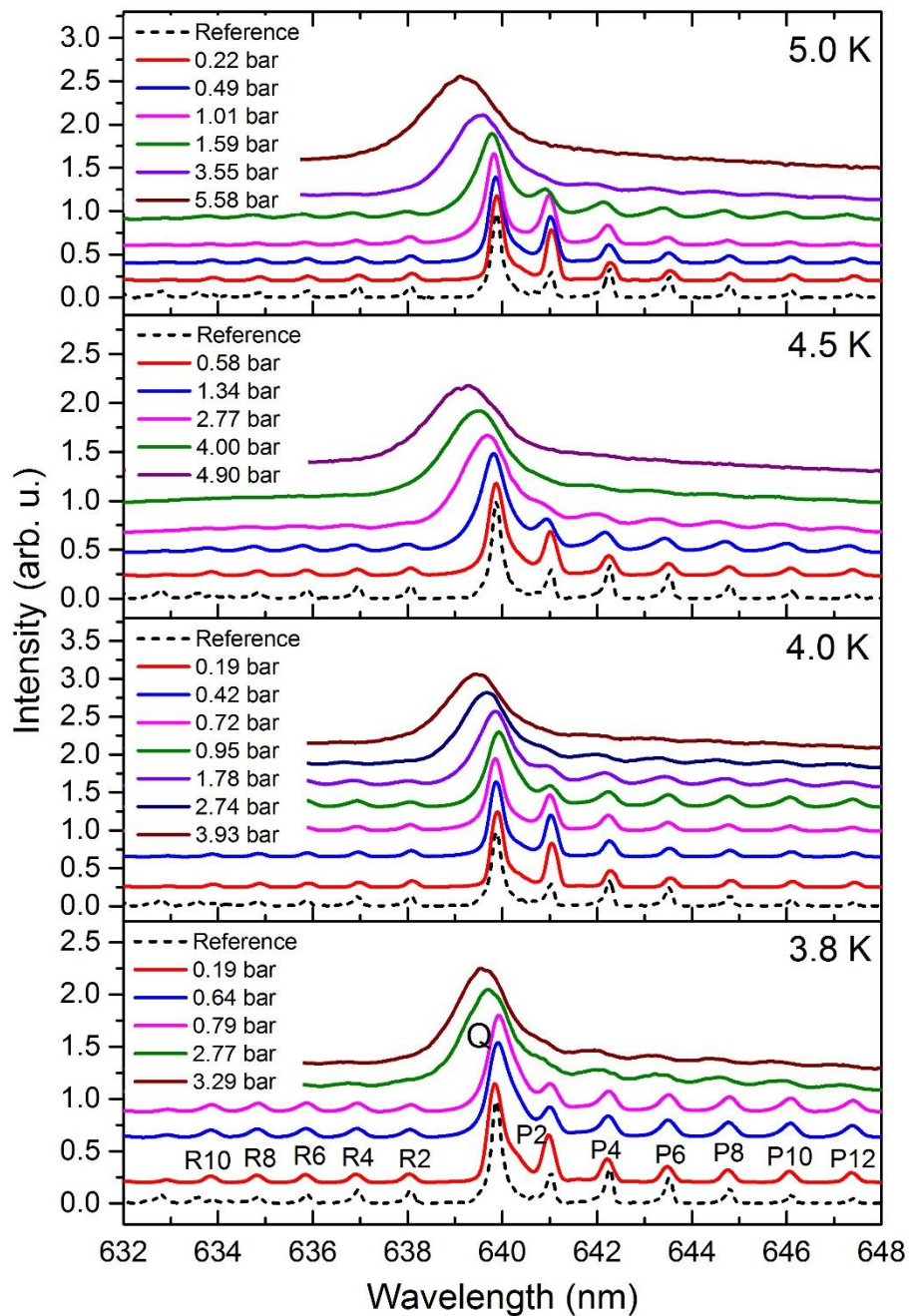


Figure 5.2: Selection of spectra of  $\text{He}_2^*$  in helium as a function of pressure for four isotherms (the measured temperature deviated by no more than 0.1 K from the isotherm). The lines of a glow discharge reference spectrum are labeled R, Q, and P as a function of quantum number  $N$  (Hund's case (b)). With increasing pressure, the lines broaden and shift. Note also that with increasing pressure the Q and P(2) lines gain more intensity compared to other lines, and ultimately merge. The intensities and offset have been scaled for better visualization. Within the resolutions observed, the rotational  $B$  constant for  $\text{He}_2^*$  was unchanged.

Rotational resolution is no longer apparent when pressures increase much beyond the saturated vapor pressure (SVP, which increases from 0.6 bar at 3.8 K to 1.9 bar at 5.0 K) of *pure* helium, and at a lower pressure for R lines than for P lines. At higher pressures, the spectrum is similar to that reported by Dennis *et al.* [9]. Fig 5.3 demonstrates our data in comparison with Dennis *et al.*'s analysis in the gas and liquid phases for the triplet 639.87 nm (b) and singlet 659.42 nm (a) transitions, where both sets of data are highly resolved for all rotational lines in the gas phase under 4.2 K and 0.2 bar. In LHe, the P and R branches disappear and only the Q branch of both transitions is observed. Most of the intensity is concentrated around the band in the centre. We assign these features to the envelope of the Q(1) and P(2) transitions. The fact that these two transitions are not resolved can be attributed to the liquid environment, which was found to hinder rotation and produce a collapsed spectrum, for instance, for OCS [13, 34].

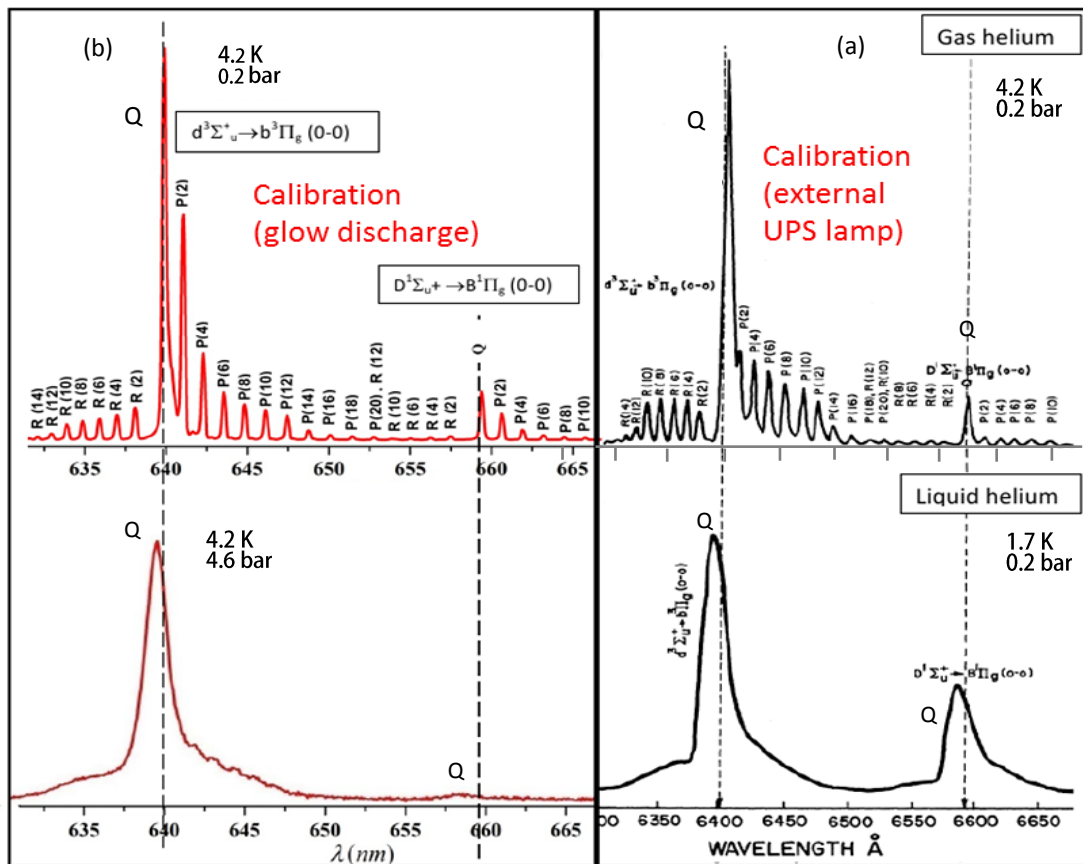


Figure 5.3: Comparison of the  $d^3\Sigma_u^+ \rightarrow b^3\Pi_g$  and  $D^1\Sigma_u^+ \rightarrow B^1\Pi_g$  bands at high resolution in the gas and liquid phases for (a) Dennis's experiment by electron-bombardment [14], (b) current experiment by corona discharge, showing the difference in intensity between these two transitions. The structure changed substantially after increasing the pressure in the liquid phase, where the rotational lines of the P- and R-branches vanished, indicating the restriction to free rotation of helium excimers in liquid He.

Also, the resolution of R branches decreases at lower pressures than the P-branch. Generally, the intensity of the  $D-B$  transition is much lower than for the  $d-b$  transition. Hence, this makes the Q branch of  $D-B$  transition look like a shallow ‘curve’ at high pressures. Conversely, for the  $d-b$  transition, the Q branch retains the appearance of a broadened line with a high peak intensity. As shown in Fig 5.3, the difference in intensity between these two transitions is considerable, and is similar to the observations of Dennis [9]. However, rotational motions have not been resolved in this study in the liquid helium, but which were observed in our study under wide range of pressures.

Fig 5.4 shows the spectra recorded for the triplet  $d-b$  transition at 3.8 K under a variety of pressure values, covering the rotational R, Q and P branches. These lines shifted in energy and broadened pressure until they could no longer be resolved.

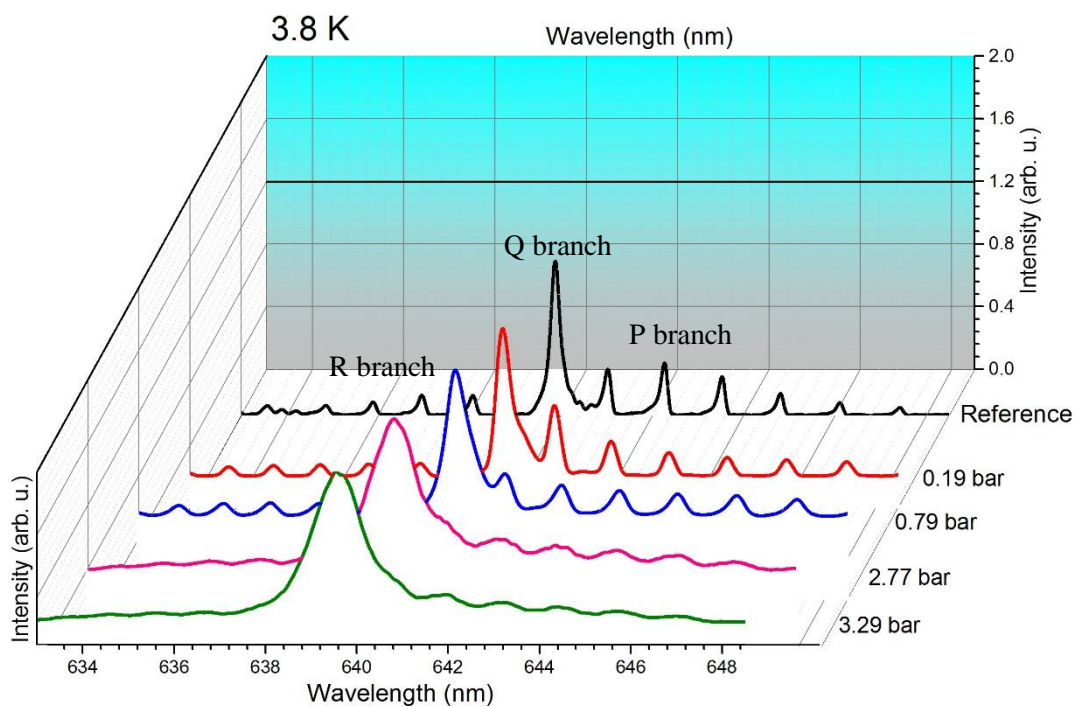


Figure 5.4: Spectra of the triplet  $d-b$  transition at 3.8 K as a function of pressure. The lines from a glow discharge reference spectrum are labeled by black lines for R, Q, and P as a function of quantum number  $N$ . Rotational lines are blue-shifted, broadened and resolution was progressively lost with increasing pressure.

### 5.6.1.1 Analysis of the $d^3\Sigma_u^+ - b^3\Pi_g$ transition

#### 5.6.1.2 Line-Shift versus pressure

To analyse the changes in line position, broadening and intensity (i.e., the same parameters as in chapter 4), the lines were individually fitted using Lorentzian functions. Over a large range of pressures, the lines remain symmetrical; hence, fitting to a Lorentzian line shape represents a reasonable means by which to assess and quantify line intensities, lineshifts and linewidths at 3.8, 4.0, 4.5 and 5.0 K.

Fig 5.5 shows the Q and P lineshifts,  $\Delta\lambda(p)$ , as a function of pressure. The lineshifts of all sharp P lines are similar, but they are dissimilar to those of the Q lines. The lineshifts can be grouped into different pressure regions; at pressures below the SVP of liquid helium, the Q lines show small and only slightly increasing shifts with increasing pressure. When the pressure is higher than the SVP of liquid helium, and when subsequently further increased, the Q lines exhibit a stronger lineshift, which we attribute to a stronger perturbation. Interestingly, at 4.0 K and 950 mbar, a small but abrupt red shift is seen close to the SVP of liquid helium, as can be seen in the Fig 5.2. The same red shift appears to be present at 3.8 K, but more data would be needed to substantiate this supposition. These abrupt changes correlate with the increase of the intensity ratio of the Q and P lines, which will be presented in coming sections. Lineshift coefficients,  $\partial\Delta\lambda / \partial p$  and  $\Delta\lambda_0$ , were obtained for the gas and solvated phases separately by fitting the function  $\Delta\lambda(p) = (\partial\Delta\lambda / \partial p) + \Delta\lambda_0$  to the data. Lineshift data was fitted by a simple linear fit in the Origin program via  $y = a + b*x$ , where  $y$  and  $x$  are the input data and represent lineshifts and pressures respectively, and  $a$  and  $b$  are the intercepts ( $\Delta\lambda_0$ ) and gradient ( $\partial\Delta\lambda/\partial p$ ), as shown in Table 5.3; data for the 3.8 K isotherm at pressures before the red shift occurs were not analysed due to insufficient data being available. Hence, the fitting in the gas phase has not been considered.

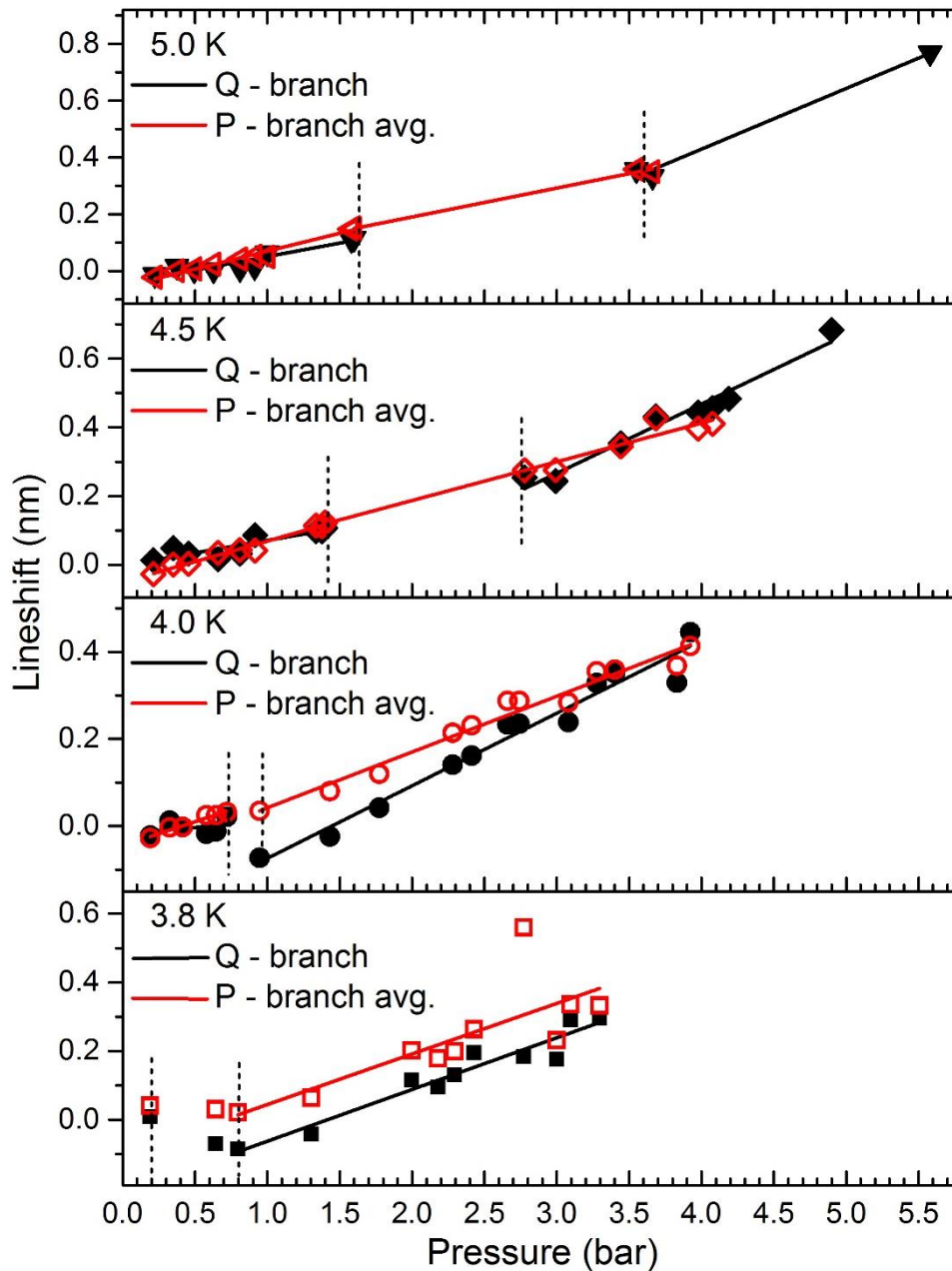


Figure 5.5: Lineshifts as obtained through fitting with Lorentzians. Filled symbols represent Q transitions, while hollow symbols represent P transitions averaged over all  $N$  except  $N = 2$  (see text). The lineshifts can be grouped according to the gas and liquid phases of the helium. The  $P_{\text{avg}}$  lineshift coefficients (gradients of straight lines) do not change between the gas and liquid phase, but the Q lineshift coefficients are consistently larger in the liquid phase, indicating a stronger perturbation. Dashed lines represent regions in which these coefficients change and where we suspect the phase transition takes place.

Table 5.3 shows similar lineshift coefficients for Q and  $P_{\text{avg}}$  transitions in the gas phase, as expected. In the liquid phase, however, the lineshift coefficients of the Q and  $P_{\text{avg}}$  transitions differ and diverge, as they have different gradients. This indicates that the P and Q features must originate from different species, i.e., species in different environments, because in molecular spectra the positions of the P and Q lines are mutually dependent, as defined by the appropriate rotational constants (and hence structure), and therefore cannot diverge.

Table 5. 3: Lineshift coefficients for Q and averaged P ( $N > 2$ ) lines in the gas phase and liquid regions<sup>8</sup>

T [K]	branch	phase	slope, $\frac{\partial \Delta \lambda}{\partial P}$ [nm/bar]	intercept, $\Delta \lambda_0$ [nm]
4.0	(Q)	gas	$0.029 \pm 0.040$	$-0.018 \pm 0.021$
4.0	(P) <sub>avg.</sub>	gas	$0.110 \pm 0.011$	$-0.045 \pm 0.006$
4.5	(Q)	gas	$0.073 \pm 0.015$	$-0.002 \pm 0.014$
4.5	(P) <sub>avg.</sub>	gas	$0.119 \pm 0.007$	$-0.050 \pm 0.006$
5.0	(Q)	gas	$0.095 \pm 0.011$	$-0.044 \pm 0.012$
5.0	(P) <sub>avg.</sub>	gas	$0.126 \pm 0.006$	$-0.056 \pm 0.006$
3.8	(Q)	liq.	$0.151 \pm 0.015$	$-0.213 \pm 0.035$
3.8	(P) <sub>avg.</sub>	liq.	$0.147 \pm 0.043$	$-0.103 \pm 0.104$
4.0	(Q)	liq.	$0.167 \pm 0.010$	$-0.241 \pm 0.029$
4.0	(P) <sub>avg.</sub>	liq.	$0.128 \pm 0.007$	$-0.086 \pm 0.020$
4.5	(Q)	liq.	$0.201 \pm 0.016$	$-0.337 \pm 0.061$
4.5	(P) <sub>avg.</sub>	liq.	$0.113 \pm 0.011$	$-0.038 \pm 0.038$
5.0	(Q)	liq.	$0.214 \pm 0.021$	$-0.426 \pm 0.091$

### 5.6.1.3 Linewidth versus pressure

Linewidth is a further parameter that was investigated to understand the physical origin of our observations. According to the physical perturbation, the line broadening can have different sources; it can be due to collisions in the gas phase or thermal motion in the

<sup>8</sup> Coefficients could not be determined at 3.8 K,  $Q_{\text{gas}}$ ,  $P_{\text{gas}}$  (too few data) and 5.0 K,  $P_{\text{liq}}$  (unresolved lines).

condensed phase, where the perturbation shifts the energy levels and leads to line broadening. Therefore, the linewidth of the Q and averaged P ( $N > 2$ ) Lines was analysed as a function of pressure of isotherms of interest in the gas and liquid phases.

Fig 5.6 shows the analysis of the Q and P linewidths,  $\Delta\omega(p)$ , as a function of pressure. As in the lineshifts, the linewidths can be classed into two regions of pressures; in the gas phase at low pressure, below SVP, where the linewidth coefficients of the  $\frac{\partial\Delta\omega}{\partial P}$  of Q and  $P_{\text{avg}}$  lines are similar; in the high pressure region, however, the deviation of the linewidth increases between the Q and  $P_{\text{avg}}$  lines above the SVP of liquid helium. Moreover, at higher pressures than SVP the rotational P(2) line becomes asymmetric, which makes the fitting difficult and not accurate due to merging with the Q branch. As a consequence, the averaged P branch ( $N > 2$ ) was considered most suitable for analysis, i.e., where the P(2) line was excluded. The pressures at which the P(2) line merges with the Q branch varies with each given isotherm. At 3.8 K, this occurs between 0.2 and 0.6 bar, at 4.0 K between 0.7 and 0.9 bar, at 4.5 K between 1.3 and 2.8 bar, and at 5.0 K between 1.6 and 3.6 bar, as shown in Fig 5.2.

Table 5.4 reports the values of linewidth coefficients of the Q and  $P_{\text{avg}}$  lines of the isotherms of interest. The difference between  $Q_{\text{gas}}$  and  $Q_{\text{liq}}$  lines can be seen, whilst the difference becomes smaller and did not much change (nearly straight line) between  $P_{\text{gas}}$  and  $P_{\text{liq}}$  lines with pressure. Broadly speaking, the linewidth coefficients,  $\partial\Delta\omega/\partial p$ , of these Q branches were found to be greater than those for  $P_{\text{avg}}$  lines in the liquid phase, indicating changes of structure. At 3.8 K, more data would be needed in the gas phase to confirm this observation, and also at 5.0 K,  $P_{\text{liq}}$  (unresolved lines).

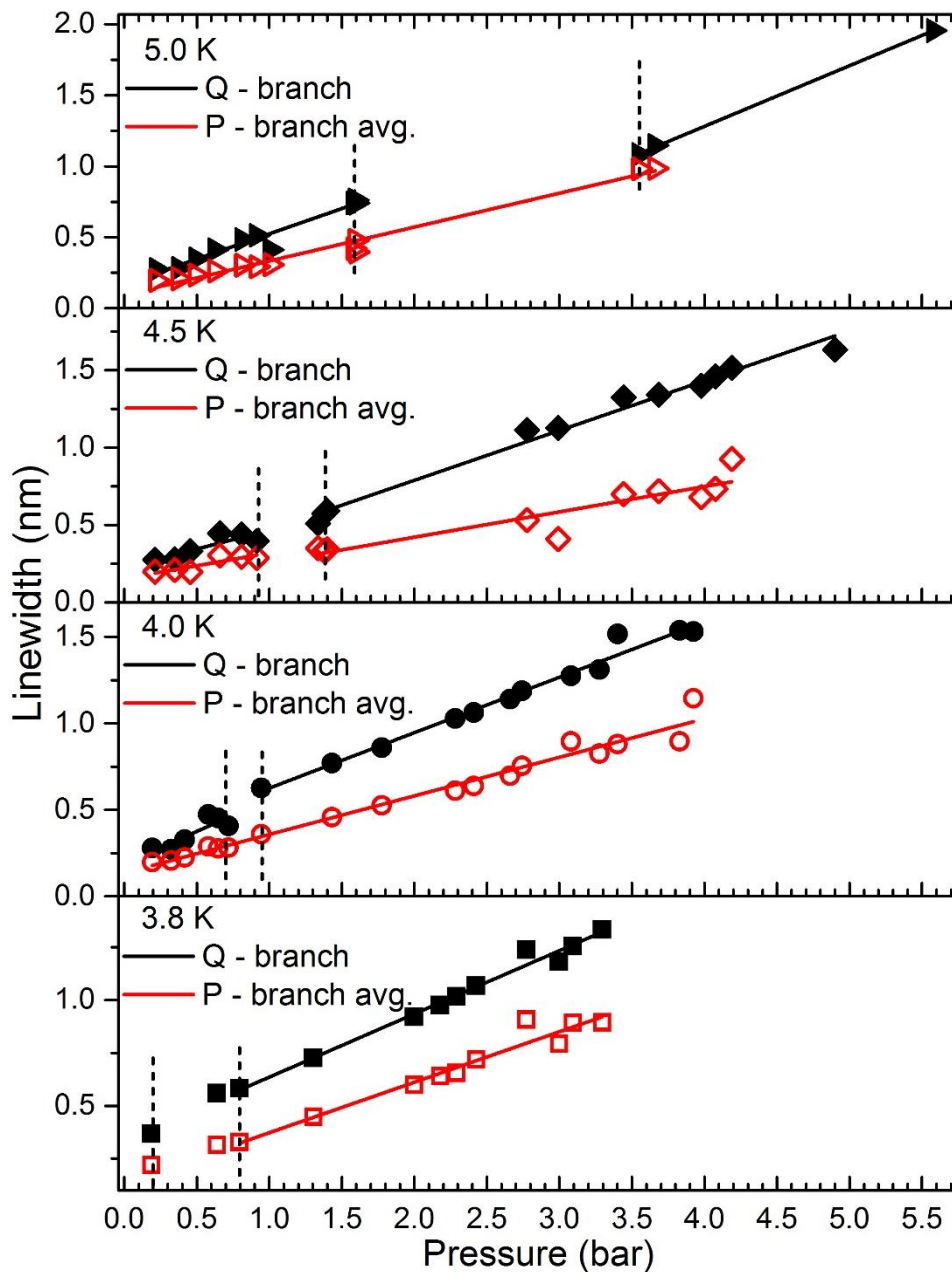


Figure 5.6: As a consequence of fitting with Lorentzians, linewidths can be obtained as a function of pressure of the triplet  $d$ - $b$  transition for different isotherms. The Q branch is represented by black filled symbols; red hollow symbols are the averaged P linewidths excluding the P(2) line. The pressure is divided into two regions, which are the gas phase at low pressure and the liquid phase at high pressure above the SVP, whilst the region in between, in which we expect to find the phase boundary, is indicated by vertical dashed lines.

Table 5. 4: Linewidth coefficients for Q and averaged P ( $N > 2$ ) lines in the gas phase and liquid regions <sup>9</sup>

T [K]	branch	phase	slope, $\frac{\partial \Delta\omega}{\partial P}$ [nm/bar]	intercept, $\Delta\omega_0$ [nm]
4.0	(Q)	gas	$0.321 \pm 0.014$	$0.305 \pm 0.039$
4.0	(P) <sub>avg.</sub>	gas	$0.191 \pm 0.032$	$0.154 \pm 0.017$
4.5	(Q)	gas	$0.243 \pm 0.072$	$0.223 \pm 0.045$
4.5	(P) <sub>avg.</sub>	gas	$0.165 \pm 0.046$	$0.154 \pm 0.029$
5.0	(Q)	gas	$0.355 \pm 0.029$	$0.169 \pm 0.031$
5.0	(P) <sub>avg.</sub>	gas	$0.176 \pm 0.015$	$0.147 \pm 0.016$
3.8	(Q)	liq.	$0.299 \pm 0.014$	$0.337 \pm 0.033$
3.8	(P) <sub>avg.</sub>	liq.	$0.238 \pm 0.019$	$0.134 \pm 0.048$
4.0	(Q)	liq.	$0.371 \pm 0.108$	$0.189 \pm 0.056$
4.0	(P) <sub>avg.</sub>	liq.	$0.229 \pm 0.019$	$0.117 \pm 0.055$
4.5	(Q)	liq.	$0.349 \pm 0.013$	$0.145 \pm 0.044$
4.5	(P) <sub>avg.</sub>	liq.	$0.164 \pm 0.025$	$0.093 \pm 0.079$
5.0	(Q)	liq.	$0.427 \pm 0.007$	$-0.427 \pm 0.032$

#### 5.4.1.4 Line Intensity versus pressure

Line intensity was another parameter analysed by fitting rotational lines using Lorentzian functions. The intensity ratio in the  $d-b$  transition was taken between the line intensity of the Q branch and the averaged P lines, excluding the P (2) line.

For solvated, and hence cold,  $\text{He}_2^*$ , only the lowest allowed quantum state,  $N = 1$ , will be populated because the next highest allowed level,  $N = 3$ , is  $75 \text{ cm}^{-1}$  higher in energy. Only odd  $N$  rotational states are allowed in the  $d^3 \Sigma_u^+$  state because of exchange symmetry. For the  $d^3 \Sigma_u^+$  state of  $\text{He}_2^*$ , the only transitions emerging from the  $N = 1$  state are the Q(1) and P(2) lines. The intensity ratio between the Q(N) and P(N) lines ( $NP > 2$ ) therefore qualitatively reflects the degree of rotational cooling. Fig 5.7 shows the ratio of the line intensity of the Q lines and the averaged line intensity of the P lines. The intensity of the P(2) line has been excluded from the average because it changes line shape as it merges with the Q branch. For all four isotherms shown in Fig 5.7, the Q/P intensity ratio is roughly constant in the gas phase but increases linearly in the liquid phase of helium with pressure. Presumably, the rotational energy is transferred into

<sup>9</sup> Width coefficients could not be determined at 3.8 K, Q<sub>gas</sub>, P<sub>gas</sub> (more data needed) and 5.0 K, P<sub>liq</sub> (unresolved lines).

collective modes of the solvation shell and liquid environment [172, 173]. In superfluid helium droplets, this type of energy transfer was found to cause rotational line broadening [174, 175]. A simple explanation of the linear dependence of the Q/P intensity ratio on pressure is that molecules coexisting in the gas phase are rotationally cooled by collisions with the liquid. Additionally, the use of electronically excited He excimers as molecular probes means that our ability to observe rotational cooling is limited by the excimer's radiative lifetime. An upper limit to the fluorescence lifetime has been found as  $\tau \sim 10$  ns [51]. The fact that solvated excimers may cool from several hundred Kelvin to 4 K over this time frame would give a lower limit to the rotational cooling rate of  $\sim 10^{-10} - 10^{-11} \text{ K s}^{-1}$ .

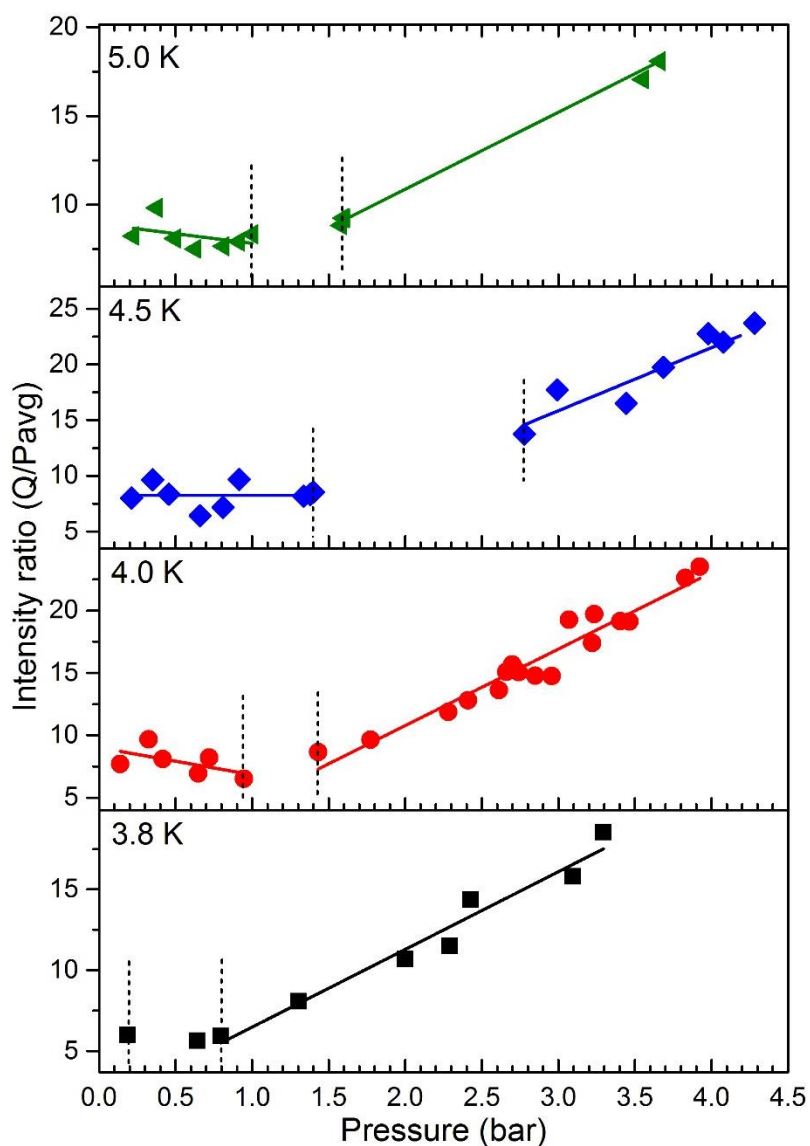


Figure 5.7: Pressure dependence of the intensity ratio of the Q branch and averaged P lines, excluding P(2), for 3.8, 4.0, 4.5, and 5.0 K. The ratio is roughly constant in the gas phase, but increases linearly with pressure in the liquid phase of helium.

### 5.6.2 $D\ ^1\Sigma_u^+ \rightarrow B\ ^1\Pi_g$ transition

This section presents another interesting transition which follows the triplet  $d-b$  transition in wavelength. Although, the intensity of  $D-B$  transition is much lower than  $d-b$  transition and sometimes it is difficult to observe in spectra, we have found from the best to analyse this band. This is because: (a) the structure of rotational lines is relatively simple, (b) it does not overlap strongly with other transition except the hydrogen line at 545 nm, (c) sufficient data set were obtained including this transition, and (d) it was discussed by literatures of electronically excited bulk liquid helium  $^4\text{He}$  [7, 9, 54]. However, pressure and temperature dependence of the lines shape were not sequentially investigated in different phases by literatures. Fluorescence spectra recorded at 3.8, 4.0, 4.5 and 5.0 K show the  $D\ ^1\Sigma_u^+ - B\ ^1\Pi_g$  transition of  $\text{He}_2^*$  in the  $n=3$  Rydberg state [79]. The rotational transitions up to  $J=10$  for the P and  $J=8$  for the R branches were detected at low pressure. Although the resolution and intensity of the singlet  $D-B$  transition is very low compared to the triplet  $d-b$  transition, the emission is nevertheless intense enough for spectral analysis to be carried out.

Additionally, excitation of LHe by electron bombardment by Dennis [9] was compared with the current spectra produced by corona discharge in the gas phase and LHe, as shown in Fig 5.3, covering the R, Q, and P branches. The  $D-B$  transition was not investigated extensively due to difficulties in observing these transitions in the gas phase, and which could not be resolved in LHe. For instance, in [176] the  $D-B$  band has been resolved and displayed a rotational structure at  $P=0.2$  bar, low gas density, and  $T=4.2$  K, but not in LHe. In other studies, well-resolved rotational structure was observed for this band was observed in LHe at low applied pressure ( $P\sim 1.0$  bar), but which disappeared for  $P>4$  bar [55]. To the best of our knowledge, there are no studies in the literature reporting the pressure dependence of lineshifts, widths and intensities of this transition, with the exception of a single study that investigated line broadening of three rotational lines in excimers produced by corona discharge at three different pressures and 80 K [54]. Another set of research investigated the lineshifts of the Q branch only at 4.2 K and up to 7 bar [56], while there was a strong overlap for the rotational lines at 2.0 bar that made deconvolution of lines impossible. Broadly, however, none of these studies have considered the effects of pressure and temperature. However, the current technique enabled us to record and analyse hundreds of spectra in this wavelength range

in the gas and LHe states over a wide range of pressures. Therefore, we consider these data worthwhile and supportive of the results of previous studies.

Fig 5.8 shows a comparison between the set of the rotational Q, P and R branches from corona discharge with a negative polarity, at four isotherms and for different hydrostatic pressures, covering the gas and the liquid phases. A glow discharge spectrum was recorded in the evacuated cell at low pressure, 78 mbar, as a reference for the linepositions under vacuum conditions [80]. The dashed black lines represent a glow discharge reference involving the Balmer alpha line ( $H_\alpha$ ) [177] emitted from atomic hydrogen which are attributed to H impurities unavoidably obtained in N6.0 purity He, which is frozen out and thus disappears from the spectrum at low temperature.

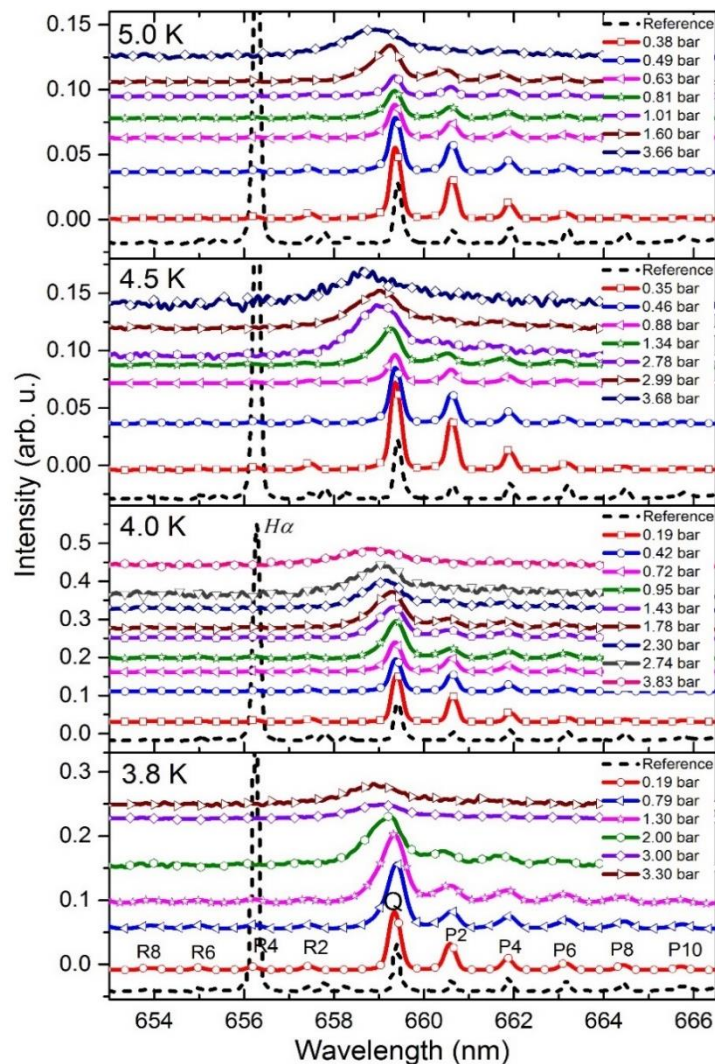


Figure 5.8: Spectra of  $\text{He}_2^*$  in helium as a function of pressure for four isotherms. The glow discharge reference spectrum is represented by a dashed black line, where the R, Q, and P lines are labelled as a function of quantum number  $N$  (Hund's case (b)), involving the Balmer alpha line emitted ( $H_\alpha$ ) [47] from atomic hydrogen due to H impurities present in the N6.0 purity He used. With increasing pressure, the lines broaden, shift and the Q and P(2) lines gain more intensity compared to other lines, and which ultimately merge. The intensities and offset have been scaled for better visualization.

Similar to our observation of the rotational lines features of the triplet  $d$ - $b$  transition in section 5.4, by increasing the pressure in the cell, the lines broaden, shift towards shorter wavelengths, change their shape (particularly the P(2) line), and a blue shift is often observed with respect to the reference value, as shown in Fig 5.8. By comparison with the glow discharge spectrum, it is clear that the P(2) line gains in intensity compared to other P lines. Alongside this, the P(2) line ultimately merges with the Q branch at a particular pressure, as depending on isotherm. At 3.8 K, this happens between 0.2 and 0.8 bar, at 4.0 K between 0.7 and 0.95 bar, at 4.5 K between 0.9 and 1.34 bar, and at 5.0 K between 1.6 and 3.6 bar. On the other hand, the R branch becomes unresolved at lower pressures than the P branch. The rotational B constant for  $\text{He}_2^*$  was unchanged throughout the above.

### 5.6.2.1 Analysis of the $D \ ^1\Sigma_u^+ - B \ ^1\Pi_g$ transition

#### 5.6.2.2 Lineshift versus pressure

To analyse the changes in linewidth, line position and intensity, the lines were separately fitted with Lorentzian functions at 3.8, 4.0, 4.5 and 5.0 K. Over a large range of pressures the lines remain symmetrical, hence the fits with Lorentzian functions represents a good way to assess and quantify lineshifts by subtracting the maximum peak position of the rotational Q and P lines from the position of the glow discharge spectrum (as a reference) over a wide range of pressures for each given isotherm. The average of the shift of each of the P rotational (4, 6, 8 and 10) lines has been considered. However, P(2) was excluded from the average due to being superimpose on the Q branch. In Fig 5.9, the lineshifts of the Q and  $P_{\text{avg}}$  branches for the  $D$ - $B$  transition as a function of pressure at 3.8, 4.0, 4.5 and 5.0 K are shown.

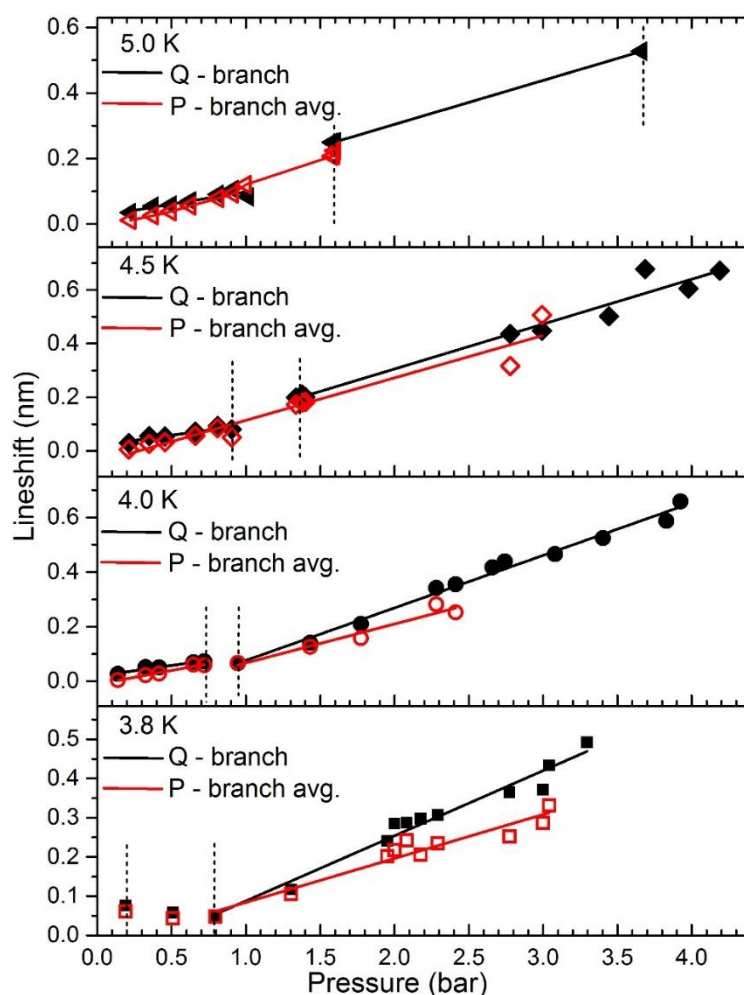


Figure 5.9: Lineshifts gained by fitting with Lorentzian lineshapes as a function of pressure of the  $D^1\Sigma_u^+ \rightarrow B^1\Pi_g$  transition at 3.8, 4.0, 4.5 and 5.0 K. Black and filled symbols represent the Q branch, red and hollow symbols are the average P lineshifts excluding P(2). These lines were classified into two regions; the gas phase, where the lineshift coefficients,  $\partial\Delta\lambda/\partial P$ , of the Q and the  $P_{\text{avg}}$  lines were found to be identical; the liquid phase, in which Q- $\partial\Delta\lambda/\partial P$  coefficients are considerably larger compared to the  $P_{\text{avg}}$ , indicating the change in structure in LHe. The dashed lines show the region where the lineshift coefficient changes and phase transition was believed to occur. Note the decreasing lineshift with pressure at 3.8 K in the gas phase.

Fig 5.9 shows the Q and  $P_{\text{avg}}$  lineshifts  $\Delta\lambda(p)$  as a function of pressure. The lineshifts can be classified into two pressure regions: pressures below the SVP of liquid helium, where the Q-lines show small, and only slightly increasing shifts when the pressure is increased. With further increases in pressure, the Q-lines exhibited abrupt blue-shifts that were larger than those observed at lower pressures. The observed abrupt change indicates a change in the structure of the perturbing environment, and is attributed to the formation of a dense solvation shell. Lineshift coefficients,  $\partial\Delta\lambda/\partial p$  and  $\Delta\lambda_0$ , were obtained for the gas and solvated phases separately by fitting the function  $\Delta\lambda(p) = (\partial\Delta\lambda/\partial p) + \Delta\lambda_0$  to the data in the Origin program, as shown in Table 5.5.

For all isotherms, lineshift coefficients of the Q and P<sub>avg</sub> branches in the gas phase are similar, while in the liquid phase the slopes indicate the formation of a dense solvation shell. These observations indicate that the P and Q features must originate from different species because in molecular spectra the positions of P and Q lines are mutually dependent, as defined by rotational constants.

Table 5. 5: Lineshift Coefficients for Q and Averaged P ( $N > 2$ ) Lines in the Gas Phase and Liquid Regions.

T [K]	branch	phase	slope, $\frac{\partial \Delta \lambda}{\partial P}$ [nm/bar]	intercept, $\Delta \lambda_0$ [nm]
4.0	(Q)	gas	$0.097 \pm 0.009$	$0.019 \pm 0.005$
4.0	(P) <sub>avg.</sub>	gas	$0.101 \pm 0.009$	$-0.011 \pm 0.005$
4.5	(Q)	gas	$0.078 \pm 0.015$	$0.019 \pm 0.009$
4.5	(P) <sub>avg.</sub>	gas	$0.087 \pm 0.026$	$-0.006 \pm 0.016$
5.0	(Q)	gas	$0.095 \pm 0.015$	$0.023 \pm 0.010$
5.0	(P) <sub>avg.</sub>	gas	$0.104 \pm 0.006$	$-0.037 \pm 0.006$
3.8	(Q)	liq.	$0.196 \pm 0.010$	$-0.078 \pm 0.024$
3.8	(P) <sub>avg.</sub>	liq.	$0.112 \pm 0.011$	$-0.028 \pm 0.024$
4.0	(Q)	liq.	$0.192 \pm 0.007$	$-0.116 \pm 0.019$
4.0	(P) <sub>avg.</sub>	liq.	$0.133 \pm 0.019$	$-0.075 \pm 0.036$
4.5	(Q)	liq.	$0.167 \pm 0.013$	$-0.029 \pm 0.038$
4.5	(P) <sub>avg.</sub>	liq.	$0.140 \pm 0.038$	$-0.044 \pm 0.081$
5.0	(Q)	liq.	$0.134 \pm 0.001$	$0.036 \pm 0.002$

The lineshift coefficients of the Q and P<sub>avg</sub> lines are listed in Table 5.5, with the exception of the 3.8 K isotherm where too few data points below SVP were available for reasonable analysis, and for the 5 K isotherm in the liquid phase, where the P-branch lines were unresolved. The intercepts of the lineshift coefficients are negative, indicating that the molecules are in a different environment than the gas phase. Also, the magnitude of the intercept increases with temperature for the rotational Q and P lines in the liquid phase, showing a greater sensitivity to the environment than the gas phase.

### 5.6.2.3 Linewidth versus pressure

Similar to the lineshifts scenario, to investigate the changes in line broadening, the lines of the Q and P<sub>avg</sub> branches were separately fitted with Lorentzian functions for each isotherm. Over a large range of pressures, the lines remain symmetric, hence fitting to Lorentzian functions represent a good way to assess and quantify line broadening using

the linewidth as the sole parameter. Fig 5.10 shows the linewidths obtained from the fitting procedure as a function of pressure at 3.8, 4.0, 4.5 and 5.0 K. Q lines were found to broaden more rapidly than  $P_{\text{avg}}$  lines. Line broadening constants essentially increased continuously with increasing temperature. Also, it is noticeable that linewidth of the Q branch in the singlet  $D-B$  and triplet  $d-b$  transitions is larger than the lineshift by a factor of about 1.5. The abrupt change in the linewidths of the Q branch occurs in the pressure region that represented the phase boundaries for each given isotherm.

For the sake of clarity of our conclusion, the coefficients of the linewidth  $\partial\Delta\omega/\partial P$  of the Q and  $P_{\text{avg}}$  lines are listed in Tables 5.6. Likewise, the intercepts,  $\Delta\omega_0$ , of the linewidth coefficients are negative, indicating that the molecules exist in a different environment. Also, the magnitude of the intercept of the Q-branches is larger in the liquid phase than the gas phase, showing a greater sensitivity to the condensed shell than the gas phase.

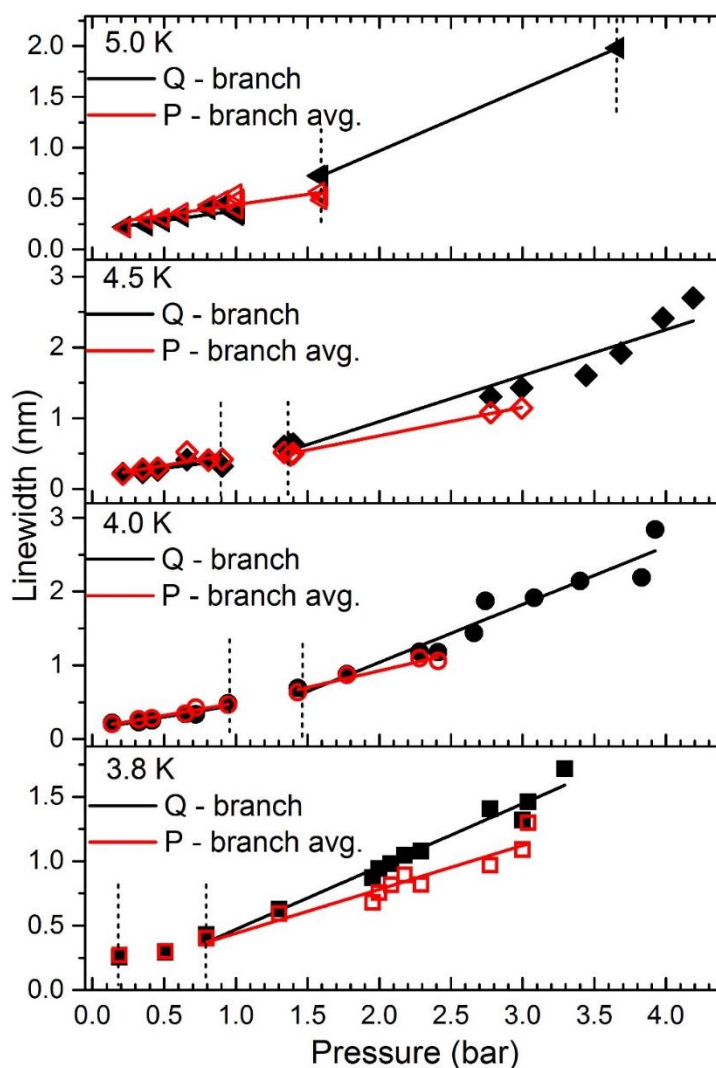


Figure 5.10: Pressure dependence of the linewidth of the Q- and  $P_{\text{avg}}$  branches features (after deconvolution, see above text) in the gas and liquid phases at 3.8, 4.0, 4.5 and 5.0 K. The line broadening of the Q-transitions with pressure is larger than for the  $P_{\text{avg}}$  lines. The dashed lines indicate the crossover regions.

Table 5. 6: Line broadening coefficients,  $\frac{\partial\Delta\omega}{\partial P}$ , for the Q and the averaged P branch ( $N > 2$ ) lines in the gas and liquid phases at 3.8, 4.0, 4.5 and 5.0 K. For 3.8 K,  $Q_{\text{gas}}$  and  $P_{\text{gas}}$  coefficients could not be determined due to insufficient data. At 5.0 K, the rotational lines of P branch could not be resolved due to hindering of rotational motion at high pressure. All slopes found for the Q branch in the liquid phase are greater than those found for gas phase.

T [K]	branch	phase	slope, $\frac{\partial\Delta\omega}{\partial P}$ [nm/bar]	intercept, $\Delta\omega_0$ [nm]
4.0	(Q)	gas	$0.326 \pm 0.053$	$0.137 \pm 0.032$
4.0	(P) <sub>avg.</sub>	gas	$0.331 \pm 0.032$	$0.156 \pm 0.019$
4.5	(Q)	gas	$0.247 \pm 0.096$	$0.169 \pm 0.059$
4.5	(P) <sub>avg.</sub>	gas	$0.342 \pm 0.124$	$0.161 \pm 0.077$
5.0	(Q)	gas	$0.195 \pm 0.052$	$0.185 \pm 0.040$
5.0	(P) <sub>avg.</sub>	gas	$0.204 \pm 0.038$	$0.236 \pm 0.039$
3.8	(Q)	liq.	$0.488 \pm 0.029$	$-0.017 \pm 0.071$
3.8	(P) <sub>avg.</sub>	liq.	$0.341 \pm 0.038$	$0.099 \pm 0.084$
4.0	(Q)	liq.	$0.786 \pm 0.078$	$-0.531 \pm 0.223$
4.0	(P) <sub>avg.</sub>	liq.	$0.449 \pm 0.078$	$0.026 \pm 0.158$
4.5	(Q)	liq.	$0.649 \pm 0.063$	$-0.347 \pm 0.191$
4.5	(P) <sub>avg.</sub>	liq.	$0.404 \pm 0.015$	$-0.056 \pm 0.032$
5.0	(Q)	liq.	$0.609 \pm 0.007$	$-0.248 \pm 0.015$

#### 5.6.2.4 Line Intensity versus pressure

A further spectroscopic parameter to analyse is the ratio of the line intensities. As opposed to the  $d-b$  transition, the intensity ratio of the singlet  $D-B$  transition is taken between the line intensity of the Q and the P(2) lines. This is because the intensity of the averaged P branch fluctuates with pressure, hence the averaged P branch was ignored in this analysis. The pressure dependence of the intensity of molecular bands has been studied previously [51]. This study found that the intensities of atomic and molecular emissions decrease exponentially with increasing pressure, indicating that most of the excited states are non-radiatively quenched by the surrounding ground state liquid. In the current experiment, however, we have found that the intensity ratio increases in proportion to pressure. This indicates a change in the structure of the perturbing environment, showing rotational population transfer to lower energy states. For all isotherms, line intensity ratios (Q/P2) appear to be essentially constant in the gas phase

at low pressures below the SVP. However, after crossing the phase boundary into the liquid phase above the SVP, the line intensity ratio increases in proportion to pressure, as shown in Fig 5.11.

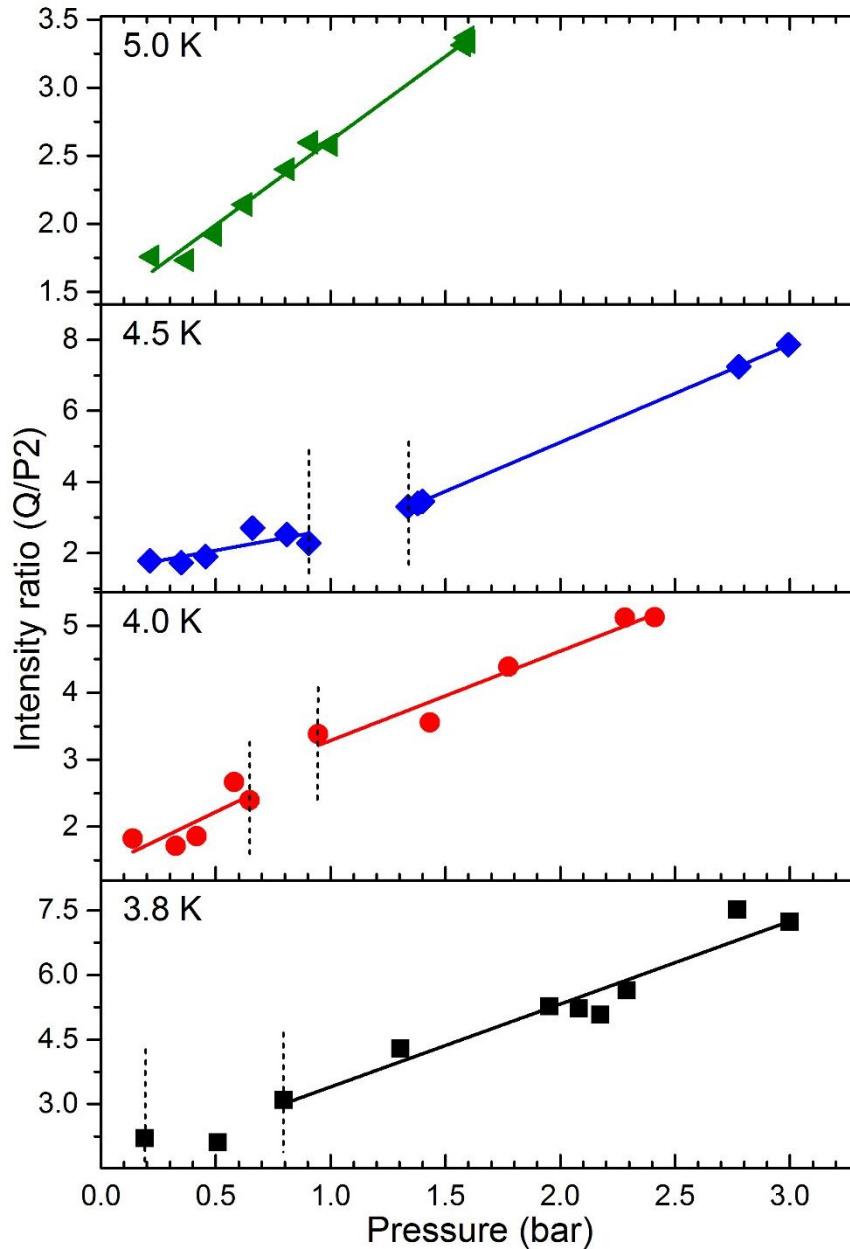


Figure 5.11: Pressure dependence of the line intensity ratio of the Q branch and the P(2) line (Q/P2), at 3.8, 4.0, 4.5 and 5.0 K. The intensity ratios increase slightly with pressure in the gas phase, whereas in the liquid phase of helium it increases linearly and strongly with pressure. The abrupt change between the liquid and gas phases is taken to be the phase transition, as depicted by the vertical dashed lines.

For 5.0 K and at pressure greater than 1.66 bar, the line intensity of the P branch was increasingly more difficult to measure because the spectral resolution progressively decreases or is distorted at higher pressure via stronger environmental perturbations. Hence, the line intensity ratio (Q/P2) was impossible to measure in the liquid phase of helium. Consequently, the intensity ratio coefficient in Fig 5.11 at 5.0 K is solely in the gas phase. This investigation of line intensity provides us with further evidence of this intriguing region between the gas and liquid phases of helium, indicating the phase boundary at a given pressure, as it turns out by the dashed vertical lines.

## 5.5 Predicted phase transition of the SVP of LHe

As mentioned in chapter 4.6, the limited regions between the gas and liquid phases that shown in Figs 5.5, 5.6, 5.7, 5.9, 5.10, and 5.11 in between the dashed lines are likely to represent phase transition regions. The phase transition was thought to occur at pressures lower slightly than the actual SVP curve of  $^4\text{He}$ , as dependent on the analysis of parameters. Thereafter, a comparison between the actual SVP curve [137] and expected regions of the studied parameters was made, as shown in Fig 5.12, where the values of pressures in which the crossing phase occurs for each isotherm are fitted with an exponential function (see text in 4.6).

Upon comparison of Fig 5.12 with the actual SVP curve, it was found that for the  $d-b$  transition, the linewidth and lineshift data implies a phase transition below the actual SVP curve, whilst line intensity data suggest a phase transition slightly above the SVP at 3.8 bar, as consistent with SVP in the other isotherms. Regarding the  $D-B$  transitions, all data derived for all parameters imply phase transitions at pressures below that of the actual SVP curve. This means that below the phase transition, clusters form around the helium excimers at these points. After crossing the phase boundary, and with subsequently increasing pressure, excimers are solvated (as can identified by a stronger interaction with the environment or, in other words, a greater gradient for the various parameters so determined). Table 5.7 reports the pressures at which the estimated regions of the phase transition are. It is worth remarking that to improve the accuracy of this feature more data is required, especially in the regions confined between the gas and liquid phases.

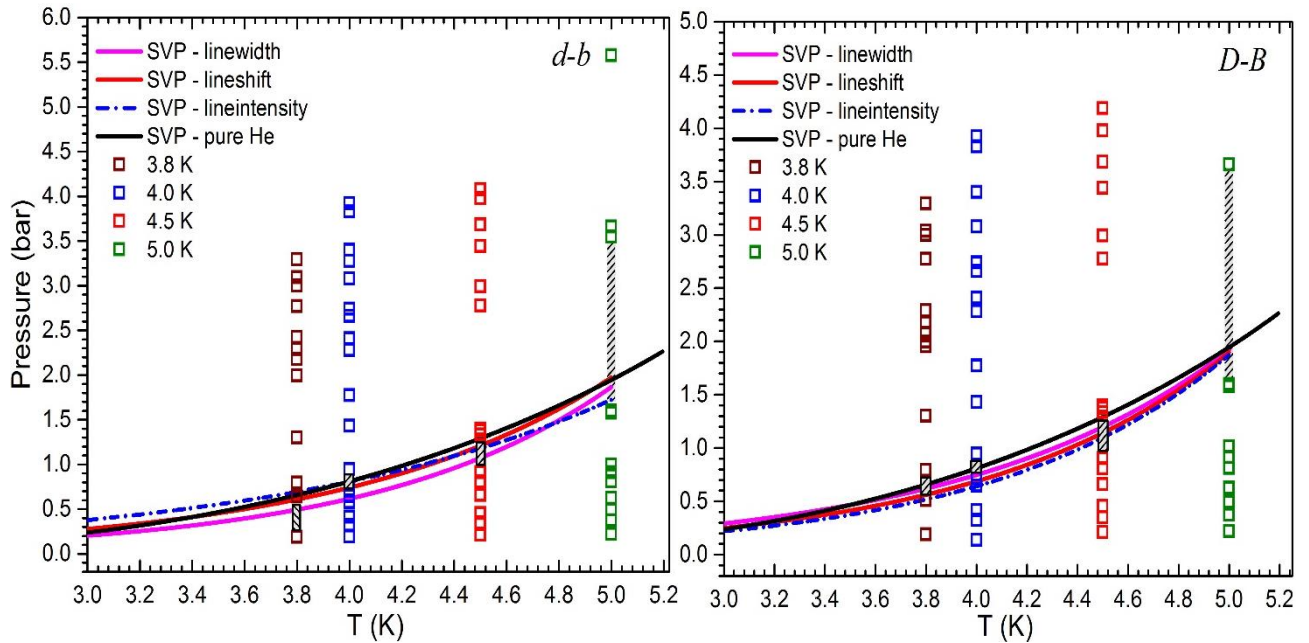


Figure 5.12: Hypothetical phase diagram for the excimer-helium mixed system showing the comparison between the saturated vapour pressure (SVP) of pure  $^4\text{He}$ , and the hypothetical thermodynamic phase transition obtained by an exponential fit of different parameters (linewidth, lineshift and line intensity ratio of the  $d-b$  and the  $D-B$  transitions) at 3.8, 4.0, 4.5 and 5.0 K. Hollow points represent spectra measured for each of the indicated isotherms. The shaded region between the hollow points represents the region in the P-T diagram where the hypothesized thermodynamic transition for the excimer-helium mixed system is located.

Table 5. 7: The values of pressure that quantify the hypothetical thermodynamic transition for the excimer-helium mixed system for the  $d-b$  and the  $D-B$  transitions at 3.8, 4.0, 4.5 and 5.0 K.

Molecular band	Parameter	3.8 K	4.0 K	4.5 K	5.0 K
		Suspected pressure transition/bar	Suspected pressure transition/bar	Suspected pressure transition/bar	Suspected pressure transition/bar
$d-b$	Linewidth	0.190 – 0.796	0.720 – 0.950	0.905 – 1.337	1.600 – 3.550
	Line Shift	0.190 – 0.796	0.720 – 0.950	1.400 – 2.780	1.600 – 3.550
	Line Intensity	0.190 – 0.796	0.950 – 1.430	1.400 – 2.780	1.000 – 1.600
$D-B$	Linewidth	0.190 – 0.796	0.950 – 1.430	0.905 – 1.337	1.600 – 3.660
	Line Shift	0.190 – 0.796	0.720 – 0.950	0.905 – 1.337	1.600 – 3.660
	Line Intensity	0.190 – 0.796	0.648 – 0.946	0.905 – 1.337	–

## 5.6 Conclusion and General observations

In conclusion, we have investigated the spectra of  $\text{He}_2^*$  in normal liquid helium as a function of pressure and temperature. At low pressure, rotationally resolved  $D^1 \Sigma_u^+ \rightarrow B^1 \Pi_g$  transition of  $\text{He}_2^*$  were observed. Upon increase the pressure the lines shifted in energy and broadened until they completely vanished. Analysis of lineshifts, linewidths and line intensities, of the  $\text{He}^*$  in chapter 4, show analogous evidence for what observed for the triplet  $d$ - $b$  lines for the presence of (i) cold excimers solvated in helium, (ii) hot excimers in gas pockets within liquid helium due to the joule heating of discharge and –when the pressure is low enough – (iii) in the gas phase. The excimers rotate freely in the gas pockets, while the solvated excimers are thermalised and hindered in their rotation. Our work establishes a phase diagram for a mixed phase of  $\text{He}_2^*$  and ground-state helium, explaining the release of energy by formation of microscopic gas bubbles, the desorption of excimers from electronically excited helium clusters, and the nucleation and stabilization of  $\text{He}_2^*-\text{He}_n$  at temperatures low temperatures. The exploration of helium in different phases at the nanoscale with the great precision inherent to rotational spectroscopy should therefore be possible. This is promising for the investigation of molecular superfluidity.

The general trends of the rotationally resolved  $d^3 \Sigma_u^+ \rightarrow b^3 \Pi_g(0-0)$  and  $D^1 \Sigma_u^+ \rightarrow B^1 \Pi_g(0-0)$  transitions of  $\text{He}_2^*$  can be listed as following;

- High rotational quantum states are populated; for the triplet  $d$ - $b$ , up to  $J = 18$  and 14 for P(18) and R(14) respectively, while for the singlet  $D$ - $B$  up to P(10) and R(8).
- The relative separation between rotational lines is constant, as a result the B rotational constant does not change, at least insofar as we have been able to determine. However, the P(2) line is a distinct case where in the  $d$ - $b$  transition, it merges with Q branch and becomes asymmetric at high pressures, whereas for the  $D$ - $B$  transition, the P(2) line remains separated from Q before merging, and this why the latter was taken into account in intensity ratio analysis.
- For both transitions, the rotational resolution of the R branch was lost at lower pressures than the P branch. The rotational motions of the P branch of the  $D$ - $B$  band have been hindered ultimately at pressures less than  $d$ - $b$  band for each

isotherm, and the consequent effect on rotational B constant, whose effect on the spectrum is to condense the line spacing. As a results these rotational lines disappear at specific pressure; for the  $D-B$  band at 3.8 K, this happens at 2 bar, 2.8 bar this happens while for  $d-b$  transition, at 2.8 bar disappeared. At 4.0 K, the P branch can no longer be resolved at 1.78 for the singlet, but for the triplet this occurs at 2.74. At 4.5 K and for  $D-B$ , it prevented at 1.34 bar whereas this occurs for  $d-b$  band at 2.77 bar. Finally, for both transitions at 5.0 K, there was not enough data in liquid to recognize, so this happened around 1.6 bar, as can be seen in Fig 5.2 and 5.8.

- All spectral lines gain blue-shift toward short wavelength as a function of pressures with respect to the glow discharge spectrum. However, a red shift was observed for some isotherms when crossing the phase transition, which can be interpreted as the signature of a structural change of the medium around the excimers. Then, again blue-shift is significant at high pressures in LHe.
- Again, the dashed vertical lines mark the gap in the data where we have reason to suspect the crossover region between gas and liquid to lie, assuming that for electronically excited helium the phase transition may not be exactly identical to that of pure helium. Our assumption is due to the changing slopes of the linewidth, lineshift and intensity coefficient trend lines, and from the observation that this trend is not always exactly coincident with the SVP. We thus postulate the existence of a phase transition at certain pressures on isotherms pertaining to the phases of helium described above. Interestingly, the phase transition was found to occur at slightly lower pressures than the actual SVP curve for  $^4\text{He}$ , as is clear from Fig. 5.12 for the  $d-b$  and the  $D-B$  transitions.
- Similarly, for the observed atomic lines, linewidth values are always greater than lineshifts for both the singlet and triplet transitions. Additionally, the linewidths and shifts for the singlet  $D-B$  band are larger than the triplet  $d-b$  band by a factor of around two.
- The abrupt changes that have been seen in the lineshifts, widths and in the intensity ratio molecular transitions, indicate a change in the structure of perturbing environment, therefore, attributed to the formation of a dense solvation shell.
- The difference in the gradients of the coefficients of all parameters in each of the two phases can be readily explained by a superposition of spectra from excimers in

different types of environments: (i) in a fully solvated state (ii) in hot gas cavities. Both species contribute a different spectral weight to the Q and P lines of the spectrum. These different contributions are apparent in the significantly larger intensities of the Q and P(2) features compared to the P and R lines of higher  $N$ , as can be seen in Fig 5.2 and 5.8.

- The coexistence of  $\text{He}_2^*$  in the gas phase under conditions where the helium should be liquid is not unreasonable. Similar to the electron beams used in the past, corona discharge excitation in a point-plane geometry concentrates excitation energy within a small spatial volume, which may lead to local heating and boiling in the vicinity of the tip electrode.
- The establishment of the spectral fingerprint of solvated helium excimers in liquid helium and the associated pressure and temperature-dependent lineshifts is encouraging for use of molecular probes in the investigation of superfluid helium, for which a number of techniques for the injection of molecules are currently being pursued [36-39]. In a broader context, such experiments may lead to a better understanding of molecular solvation in related systems [44-46] in particular, and fluids in general [178-180].

Fig 5.13 shows a schematic picture of an excimer (excited helium molecule,  $\text{He}_2^*$ ) in different species. Firstly (a) represents all cases discussed before in the cell, when excimer sits within a cavity (bubble), (in a state referred to as a Rydberg state, represented as a red dot in the orbital) in the gas phase, Secondly a picture of  $\text{He}_2^*$  is given where the helium atoms are clustered around the excimer in the gas environment and below phase transition SVP, and a final species when excimer resides in a cavity in a solvated shell in the normal liquid helium. (b) the small set of helium excimers caged within a cavity in a liquid helium environment (solvated layer).

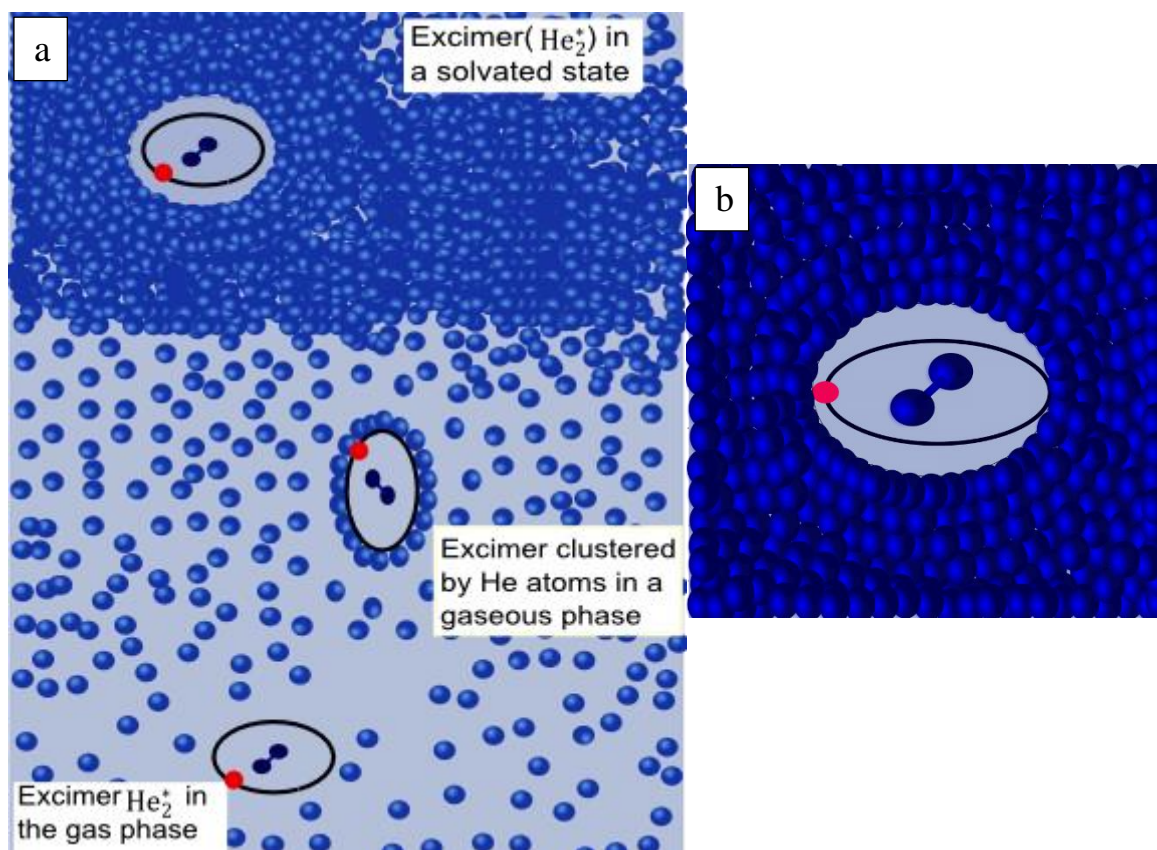


Figure 5.13: Schematic diagram of an excited helium molecule ( $\text{He}_2^*$  excimer) in different species; (a) excimer (a Rydberg state) in the gas phase, an excimer forming a cluster with helium atoms in the gas phase but close to the SVP, and an excimer residing within a cavity in the fully solvated state in normal liquid helium (LHe). (b) Image of the LHe environment when the excimer is fully solvated by ground state helium atoms.

## 5.7 Error determination

The reasons of error determination that arise from different sources (see text in chapter 4.8) for analysis of atomic lines, are similar to that undertaken in the analysis of molecular bands. Table 5.8 is an example of the goodness of the fit to the linewidths of the rotational Q and  $P_{\text{avg}}$  lines of the triplet  $d-b$  transitions. The magnitudes of the coefficients of the parameters studied in the molecular transitions, namely the intercept and the gradients for given isotherms along with standard error (Std. Error) of every fit

are listed. Additionally, this analysis includes the standard errors of each value and the magnitudes of the R-squared factor ( $R^2$ ), which represent the goodness of the linear fit. The scattering of the lineshifts, widths and intensities have the most dominant effects on magnitude of any error, and this scattering is affected by the changes in pressure and temperature to a greater extent than any other sources of error.

Table 5. 8: The results of the standard error of the linear fit of linewidths of the *d-b* transition. These results include the gradients (nm/bar) and intercept (nm) in the gaseous and liquid phases for each given isotherm. The accuracy of the linear fit is quantified by the  $R^2$  factor.

T / K	Branch	Phase	Intercept Value	Intercept Std. Error	Slope Value	Slope Std. Error	Statistics Adj. R-Square
3.8	Q	Liquid	0.337	± 0.033	0.298	± 0.014	0.982
3.8	P	Liquid	0.134	± 0.048	0.239	± 0.019	0.942
4.0	Q	Gas	0.189	± 0.056	0.373	± 0.108	0.684
4.0	Q	Liquid	0.305	± 0.039	0.321	± 0.014	0.979
4.0	P	Gas	0.154	± 0.017	0.191	± 0.032	0.873
4.0	P	Liquid	0.117	± 0.055	0.229	± 0.019	0.924
4.5	Q	Gas	0.223	± 0.045	0.243	± 0.072	0.673
4.5	Q	Liquid	0.145	± 0.044	0.322	± 0.013	0.983
4.5	P	Gas	0.154	± 0.029	0.165	± 0.046	0.699
4.5	P	Liquid	0.093	± 0.079	0.164	± 0.025	0.821
5.0	Q	Gas	0.169	± 0.031	0.355	± 0.029	0.941
5.0	Q	Liquid	-0.427	± 0.032	0.427	± 0.007	0.999
5.0	P	Gas	0.147	± 0.016	0.176	± 0.015	0.936

## Chapter 6

### Results and discussion

# Spectroscopic investigations of corona discharge in helium at room temperature (300 K)

## Abstract

Gaseous helium was excited at room temperature (300 K) using a corona discharge with negative polarity. Fluorescence spectra recorded in the visible and near infrared regions between 0.2-26 bar show the rotationally resolved  $d^3\Sigma_u^+ \rightarrow b^3\Pi_g$  and  $D^1\Sigma_u^+ \rightarrow B^1\Pi_g$  transitions of  $\text{He}_2^*$ , and the atomic  $2p^1P \leftarrow 3s^1S$  and  $2p^3P \leftarrow 3s^3S$  transitions. The analysis of observed transitions showed line shifts, spectral broadening and intensity changes whose magnitudes were dependent on pressure. Symmetrical shapes of the atomic 706 nm and 728 nm, and rotational 639 nm and 650 nm lines, were observed and described by Lorentzian profiles. A comparison between the experimental 706 and 728 nm lines and their simulation by the impact theory of broadening and shifts in spectral lines was made. Other features were analysed such as the electron mobility, pressure effects on the current discharge and applied voltages.

The structure of this chapter is as follows: Section 6.1 gives a concise introduction to the chapter. Experimental data are reported in Section 6.2. The relationship between the current and voltage discharge with pressure is described in Section 6.3. Section 6.4 presents fluorescence spectra that were resolved at room temperature, covering the singlet and triplet transition regions. The analyses of said spectra are presented in Sections 6.5, including lineshifts, widths and intensities as a function of pressure, and a comparison with results at low temperature is made. A theoretical treatment of the spectra is given in Section 6.6, including simulations of the singlet 728 nm and the triplet 706 nm lines. Section 6.7 presents molecular bands for the singlet and triplet transitions. The analyses of said molecular bands are presented in Sections 6.8, including lineshifts, widths and intensities as functions of pressure, in addition to the comparison with results at low temperature. A number of concluding points are presented in Section 6.9.

## 6.1 Introduction

Spectroscopic emission is an excellent means through which to gain information on discharge plasmas at low and high pressures. Although electrical discharge is a complicated process in dense liquids and high-pressure gases, the point-plane geometry

can help control and determine corona discharge after applying a high voltage to a tip electrode and avoiding breakdown between the electrodes (see chapter-3).

With a high electric field close to a tip electrode, the density of the corona current which is dominated by the mobility of electrons – increases considerably. Light emitted from the electronically excited states of atoms and molecules near an ionization region was observed in this experiment. The interaction between excited atoms or molecules and their environment in the cell yields the fluorescence spectra that give details and information about the pressure and temperature effects of a helium gas. This information can be obtained by investigating the line position and shape. Studies similar to those described above have investigated the profile of spectral lines emitted due to discharge in low pressures gases [181, 182] through the interaction of excited atoms with surrounding ground state atoms that leads to the broadening and shift of emitted spectral lines. Other research efforts have analysed the blue shift of the triplet 706 nm line ( $3s-2p$  transition) of atomic helium at 77 and 300 K, using a scanning Fabry-Perot interferometer [112, 130, 183]. However, these measurements were made in low-pressure helium gas at less than 10 Torr (0.013 bar). Another type of interaction that has been investigated was the singlet 728 nm line ( $3s-2p$ ) transition, which was found to broaden with pressure, but not shift, the associated spectral lines [107, 110]. A corona discharge has been utilized to investigate these transitions up to 5 MPa [184], while associated measurements have detected a considerable asymmetry in observable lines. Our measurements at 298 K using pressures of up to 30 bar, have allowed us to observe He I atomic and molecular emissions using corona discharge. The symmetric lines of these transitions supported our analysis of lineshift and linewidth parameters across this range of pressures. Then, comparison with simulation using the impact approximation has predicted the gas temperature in the ionization zone to be high  $\leq 500$  K, whereas in reference [184] the agreement between experimental line profiles and simulation occurs when a temperature in the ionization zone of 500 K is assumed. Finally, to examine the general trends of these parameters, a comparison with the results of the low temperature experiments discussed in chapters 4 and 5 will be given.

## 6.2 Experimental data

A corona discharge allows for the electronic excitation and ionisation of helium atoms at 298 K and over a range of pressures, from a small fraction of a bar up to 30 bar. The high-pressure helium cell used at room temperature is made of stainless steel metal, differing from that used for low temperatures (which was made of copper - see chapter 3). The excited helium atoms and molecular-excimers undergo transitions between electronically excited states. Intense fluorescence in the visible and near infrared regions was observed in the wavelength range from 300 - 1000 nm. The mechanisms by which the excited states of molecules and atoms were populated are deduced through the spectroscopy. An Andor Solis Technology Shamrock SR303i spectroscopy was used to record and collect the light emitted from the corona discharge in the vicinity of the tip of the top electrode through an optical setup similar to the one described in chapter 3. Spectroscopic results recorded at 300 K are displayed in Fig 6.1, showing the atomic and molecular transitions of the excited helium atoms ( $\text{He}^*$ ) and the excimers ( $\text{He}_2^*$ ).

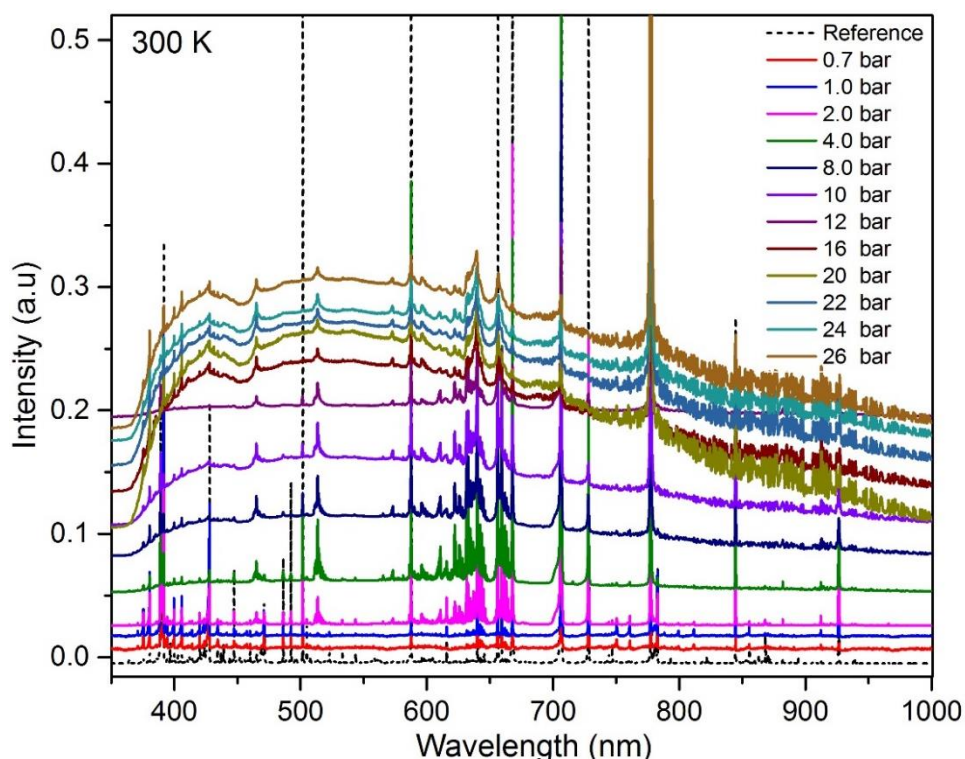


Figure 6.1: Overview of the spectra of He gas at 300 K and up to 26 bar of pressure. The spectra have been moved upwards by 0.1-0.2 a.u. for clarification. The discharge current changed during recording of spectra, and consequently the baselines are not completely equivalent and consistent, especially at high pressure.

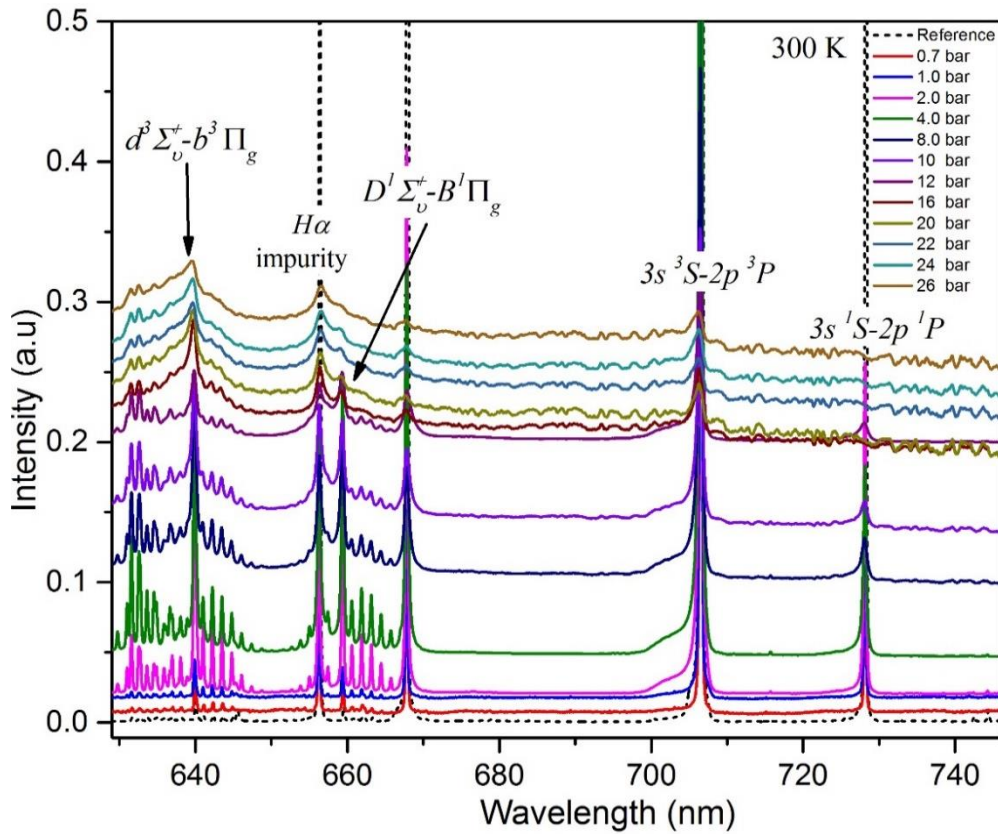


Figure 6.2: Expanded wavelength range from Fig. 6.1, focussing on the transitions of interest in this chapter including the singlet and triplet  $3s - 2p$  transitions of the atomic lines of  $\text{He}^*$ , and the singlet and triplet  $D-B$  and  $d-b$  transitions, respectively, of the molecular bands of  $\text{He}_2^*$ .

A section of the entire wavelength range was selected so as to concentrate on the electronic transitions of the excited helium atoms and molecules, as shown in Fig 6.2. In this wavelength region, ranging from 630-740 nm, the triplet  $d-b$  and singlet  $D-B$  transitions of the molecular bands of  $\text{He}_2^*$ , and the singlet with triplet  $3s - 2p$  atomic transitions of  $\text{He}^*$  are illustrated. These transitions were selected to compare with the analogous results investigated at low temperature (3.8, 4.0, 4.5 and 5.0 K) in chapters 4 and 5. A glow discharge spectrum designated by a dashed black line is shown as a reference for the other spectra where, before pressurising with helium gas, the cell was evacuated to 0.07 mbar using a scroll-pump at room temperature and then recording a discharge glow spectrum after applying a voltage with a negative polarity. Because the glow discharge spectrum was used in the calibration process, and as a reference to investigate line position and shape, any change in optical setup obliges us to record a new glow discharge spectrum. Table 6.1 shows the details of the experimental setup used to record the glow discharge spectrum under different conditions.

Table 6.1: The experimental conditions under which glow discharge spectra were recorded for calibration of the atomic lines and molecular transitions after gas line evacuation at room temperature.

T = 300 K	Reference/ atomic lines	Reference/ molecular bands
Slope (m) / mm/row	0.05767	0.05796
Intercept (b) / nm	299.361	299.442
V/ kV	-0.2	-14
I / $\mu$ A	-9.5	-0.5
P / bar	0.1	0.1
Accumulation No.	20	20
Slit opening / $\mu$ m	100	100
Exposure time / seconds	0.1	2

### 6.3 Current and voltage relationship with pressure

The ionization region, which is confined near the tip of the tip electrode and was extremely intense in this region, leads to the ionization of the fluids and gases, as well as light emission at a much smaller maximum length than the tip-plane distance. This happens when the tip is held at a negative potential, resulting in electrons being ‘injected’ through the tip and the formation of an ionized area in the immediate vicinity of the tip.

The ionization region and excitation process depend on the voltage applied and varies from one plasma to another. In the present experiment, the voltage was applied from a DC power supply (Spellman/MPS15N10/24/DCC2) under negative polarity. No current was directly measurable after applying a low voltage to the point electrode. However, by increasing the voltage, at some point a current was detected which increases rapidly with voltage. Remarkably, the initial observation to the reading of a measurable current is always correlated with discharge ignition and light emission near the tip. In other words, when we observe a current, this means the start of the discharge and beginning of fluorescence, which can then be used for spectroscopic purposes.

Changing the pressure during operation was found to affect the discharge current and temperature of the cell. The range of voltages, as affected by the number density of

helium atoms, was found to vary between 0.6 and 3.7 kV, and the discharge current between 8.0 and 120  $\mu\text{A}$ , over the course of the experiment.

The  $I - V$  curves for the space charge-controlled region are shown in Figure 6.3. The average-voltage current curves are moved to higher voltages with increasing pressure. The currents measured at  $P = 1.0$  bar were sometimes unstable, but this phenomenon reduces rapidly, again with increasing pressure. This relationship has effects on the mobility of electrons in the medium of the cell, as will be explained in the following section.

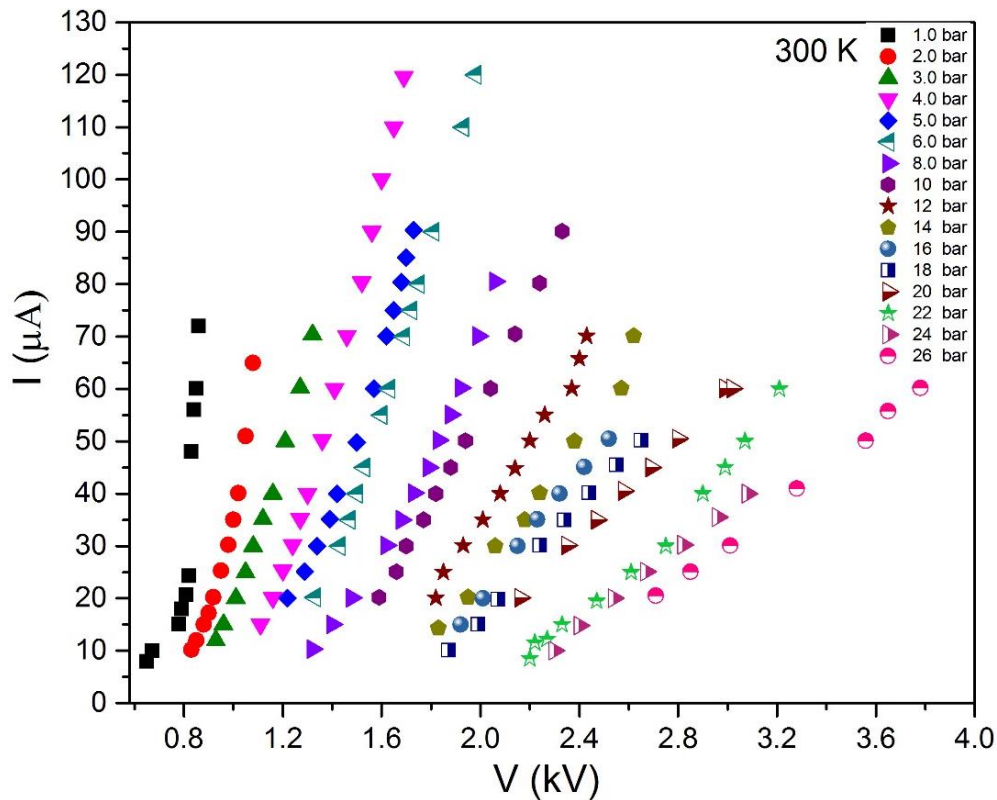


Figure 6.3: Voltage versus current as a function of pressure at room temperature. At 1.0 bar the current was unstable.

## 6.4 Spectral lines of the $3s \ ^1,^3S \rightarrow 2p \ ^1,^3P$ transitions

In this section, the atomic lines are presented that were observed at room temperature in the range 700-730 nm covering the atomic  $3s \ ^1S \rightarrow 2p \ ^1P$  and  $3s \ ^3S \rightarrow 2p \ ^3P$  transitions. Fig 6.4 presents the spectra at 300 K for a range of pressures between 0.7 and 26 bar. All of these lines were calibrated with respect to a glow discharge spectrum, as indicated

previously. As is known, the triplet transitions are more intense than the singlet transitions. It can be seen that the resolution of the singlet was lost due to pressure earlier than the triplet where, at 14 bar, the singlet line disappears, while the triplet line retained some shape, albeit shifted and broadened, up to 26 bar.

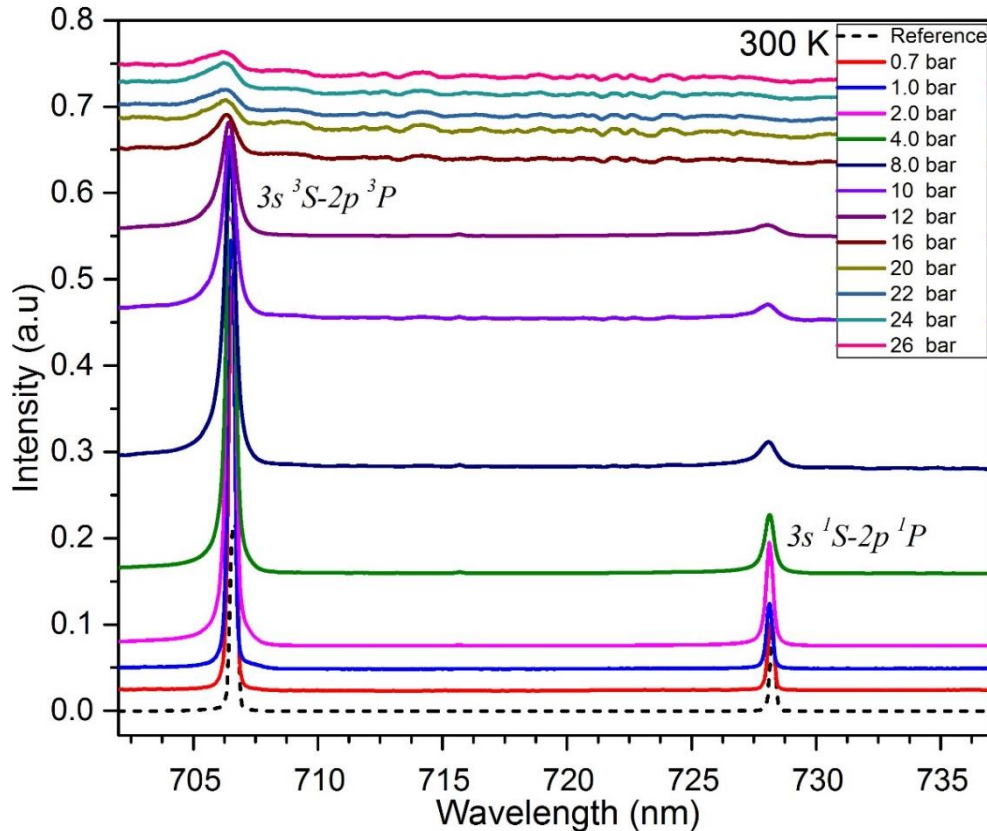


Figure 6.4: Spectra of atomic lines of the singlet and triplet  $3s-2p$  transitions at 300 K and up to 26 bar. Different spectra have been displaced vertically by 0.05-0.7 a.u. for reasons of clarity.

## 6.5 Analysis of atomic lines

### 6.5.1 Line shift, width and intensity vs pressure

To better compare line profiles, the intensities have been normalized. Figure 6.5 shows the transitions in the singlet and triplet regions, where spectra have been recorded at various pressures. For comparison, a glow discharge spectrum of atomic helium is also shown (dashed line) in Fig. 6.5. As pressure is increased, the line broadens and begins to develop a blue-shifted wing (i.e., towards shorter wavelengths); as pressure is increased further, this wing becomes a separate band that takes on a symmetric line

profile. However, at very high pressures the line profile becomes to some extent asymmetric and its blue wing is more intensive than its red wing. The blue shift indicates a strong repulsive interaction between excited He atoms and the ground state atoms.

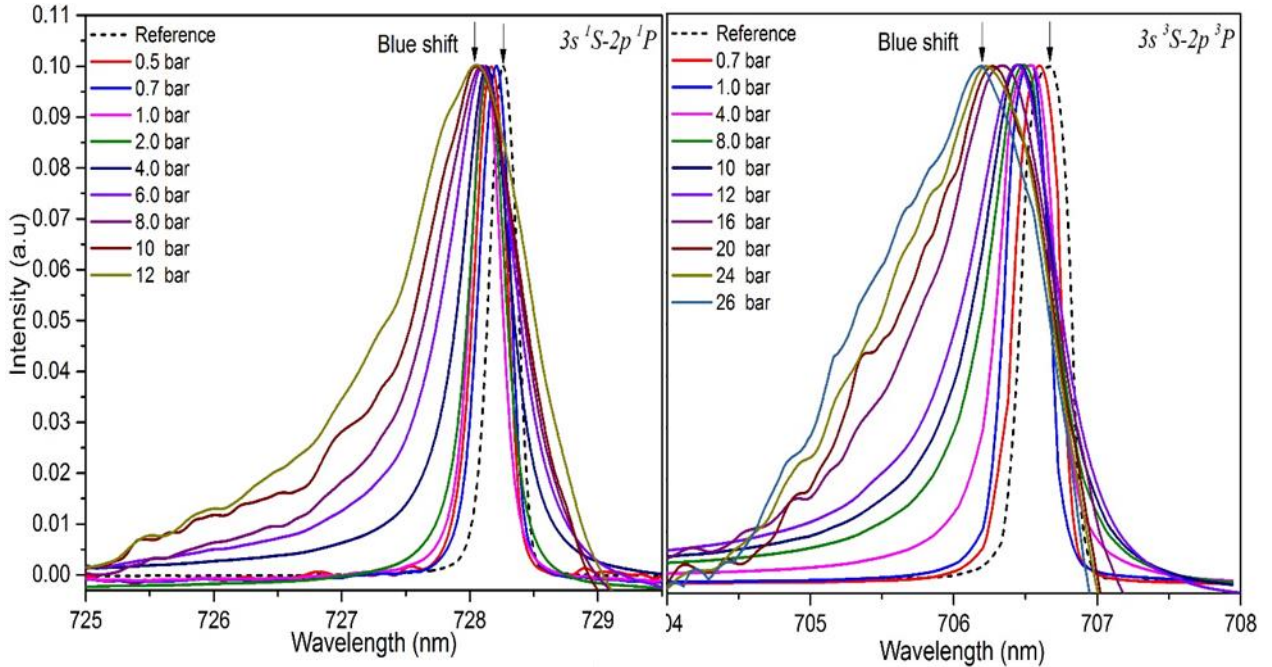


Figure 6.5: Fluorescence spectra of helium excited by a corona discharge at 300 K in the region of the atomic  $3s\ ^1S \rightarrow 2p\ ^1P$  transition of singlet helium and triplet transition  $3s\ ^3S \rightarrow 2p\ ^3P$ . All intensities have been normalised. A dashed black line represents the reference spectrum obtained from the glow discharge at room temperature. At 14 bar, the singlet line disappears, while the triplet line maintains its shape, albeit shifted and broadened, up to 26 bar.

To estimate lineshift, broadening and intensity, the spectral lines were first calibrated, normalized and fitted to a Lorentzian function using the Fityk software, which produced good fits to the data. The shifts in spectral lines for the singlet transition were measured from their maximum positions relative to the maximum of the glow discharge line as a reference over a range of pressures (0.5–27 bar). Fig. 6.6 shows the lineshifts obtained from this fitting procedure as a function of pressure at 300 K for the singlet and triplet transitions.

Correspondingly, Fig. 6.7 shows the linewidths for the 728 and 706 nm lines as a function of pressure at 300 K. The symmetry retained in most of the atomic lineshapes allowed us to quantify the linewidths as a function of full width at half maximum (FWHM).

Line intensities, as obtained from fitting the spectral data with Lorentzian functions, were examined. It is apparent from Fig 6.4 that there was a difference in the intensity ratio between the triplet and singlet, where the intensity of the singlet lines was much lower than that of the triplet lines and this ratio varies with pressure. Hence, an analysis without meaningful calibration is rather pointless. We have therefore divided the intensity of the triplet by that of the singlet lines prior to normalisation, which eliminates the effects of changes in intensity due to external factors such as current and voltage. Fig. 6.8 shows the effects of intensity ratio after fitting the spectral lines with Lorentzian functions for spectra recorded at room temperature as a function of hydrostatic pressures.

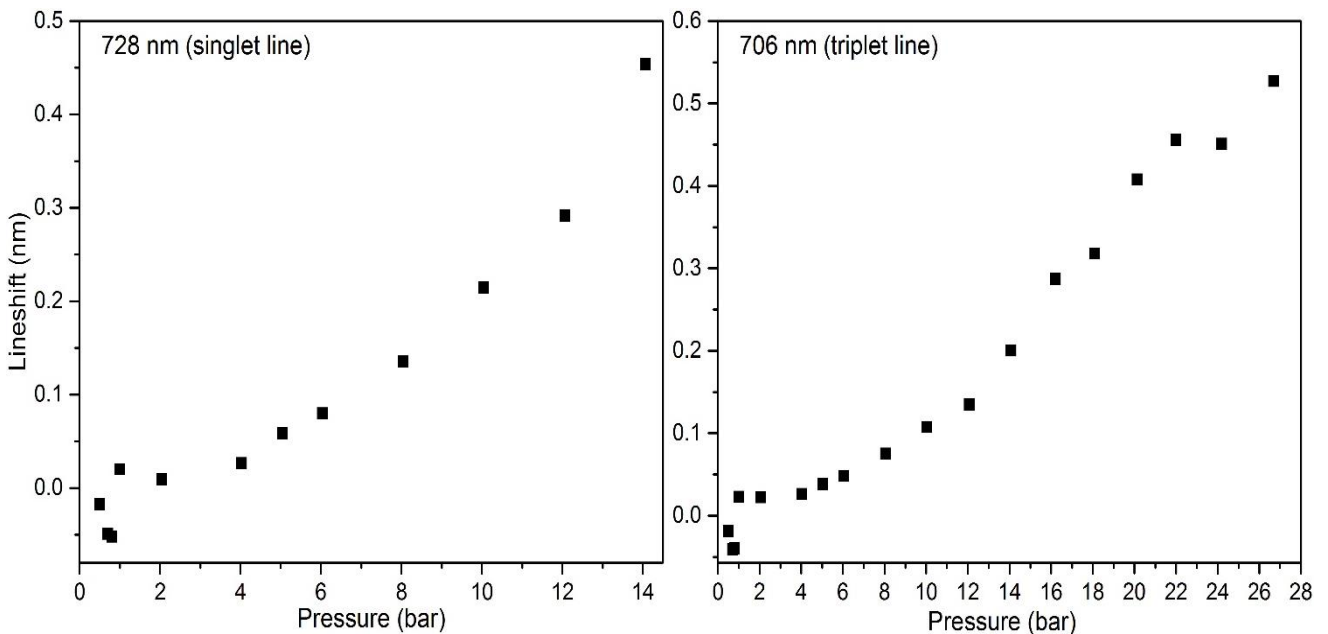


Figure 6.6: Pressure dependence of the  $3s\ ^1S \rightarrow 2p\ ^1P$  atomic singlet and triplet transitions as a function of pressure at room temperature. Both transitions show a linear dependence on pressure. The lineshifts for the singlet are greater than for the triplet.

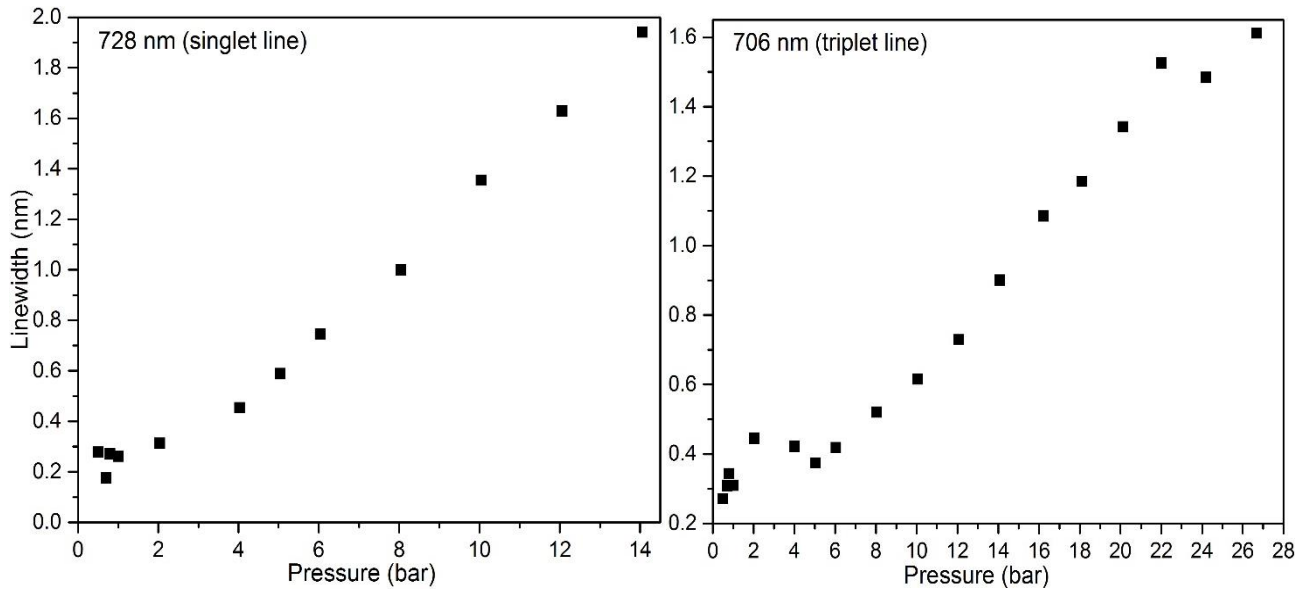


Figure 6.7: Pressure dependence of the linewidth of the  $3s\ ^{1,3}S \rightarrow 2p\ ^{1,3}P$  atomic singlet and triplet transition at 300 K. Similar to the lineshift analysis, the linewidths for both transitions are proportional to the hydrostatic pressure, where the linewidth for singlet line is greater than that of the triplet line by a factor of two.

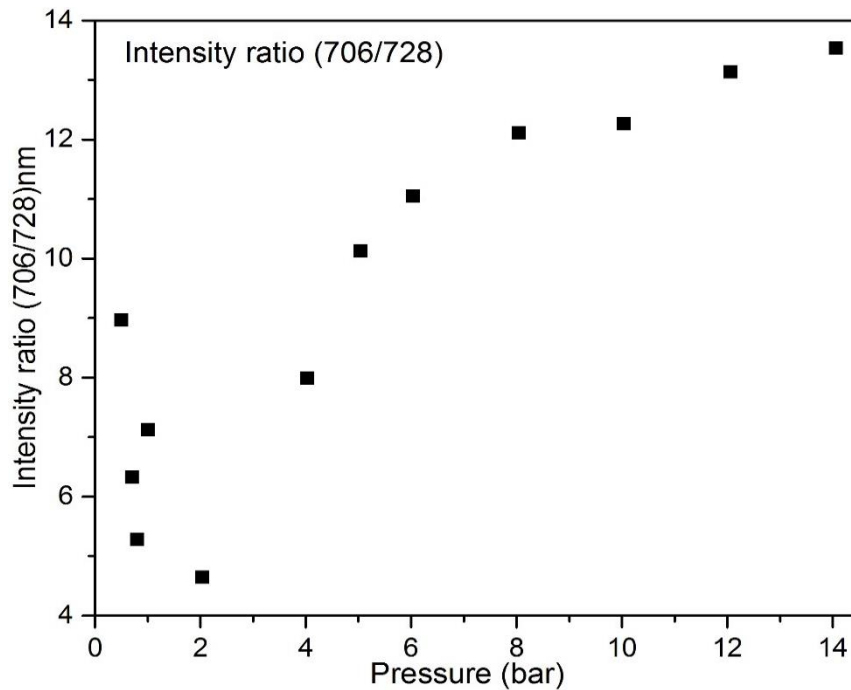


Figure 6.8: Pressure dependence of the intensity ratio of the triplet 706 nm and singlet 728 nm lines at 300 K. The intensity ratio shows a linear dependence on pressure.

All the parameters analysed, the widths, shifts and intensities of lines, are proportional to gas density and are characterized by the repulsive interaction between an excited helium atom and its surrounding ground state atoms. Also, it can be seen that at low

pressure, from 0.5 to 2 bar, the data fluctuate and are unstable; at pressures greater than 2 bar, the data show an essentially linear increase with pressure. Additionally, although the atomic lines of the singlet at 728 nm vanished at lower pressures than the triplet 706 nm line, the values of its lineshifts and linewidths are greater than the value of triplet line by a factor of two. But generally, the values of linewidths for both transitions are greater than the values of lineshifts. These observations are similar to features of the atomic lines at low temperature ( $\leq 5$  K).

## 6.5.2 A comparison with results obtained at low temperature

A comparison between the results of analysis of the lineshifts and linewidths at 300 K and the results for low temperatures reported in chapter 4 and 5 is given herein. Fig. 6.9 shows a comparison of the (wavenumber) shifts of the triplet 706 nm lines at 3.8, 4.0, 4.5, 5.0 and 300 K. At low temperatures, the pressure dependence of lineshifts is exhibited much more clearly than at room temperature.

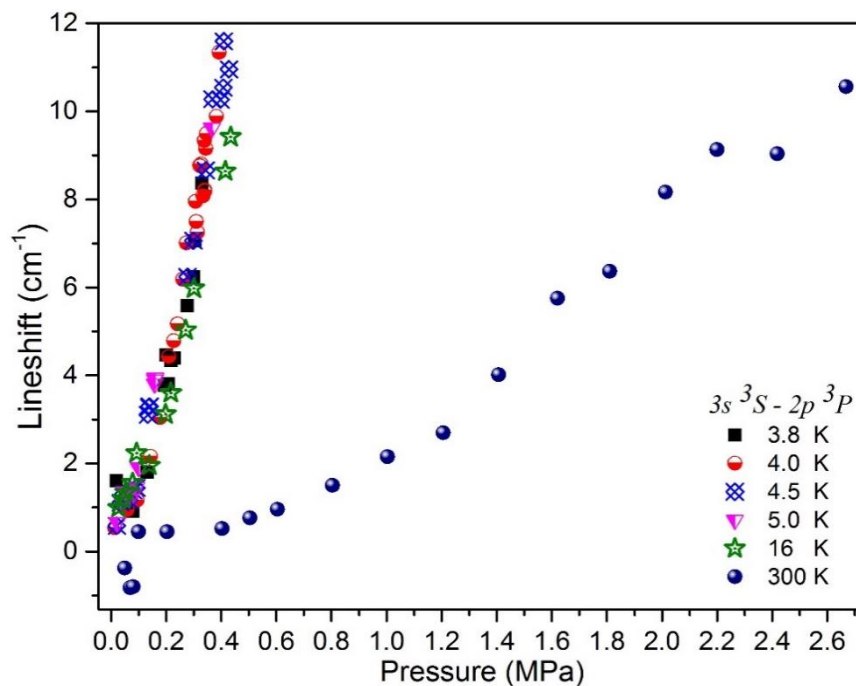


Figure 6.9: Comparison of the lineshifts observed for the atomic triplet line as a function of pressure up to 26 bar between low isotherms (3.8, 4.0, 4.5 and 5.0 K) and room temperature (300 K). The change in trend in the shifts is significant between low and high temperatures.

Fig. 6.10 clarifies also the gradient of the linewidth strongly in wavenumbers for the triplet  $3s - 2p$  transition as a function of pressure between low isotherms (3.8, 4.0, 4.5, 5.0 and 16 K) as reported in chapter 4 for the gas and liquid phases, and at room temperature (300 K).

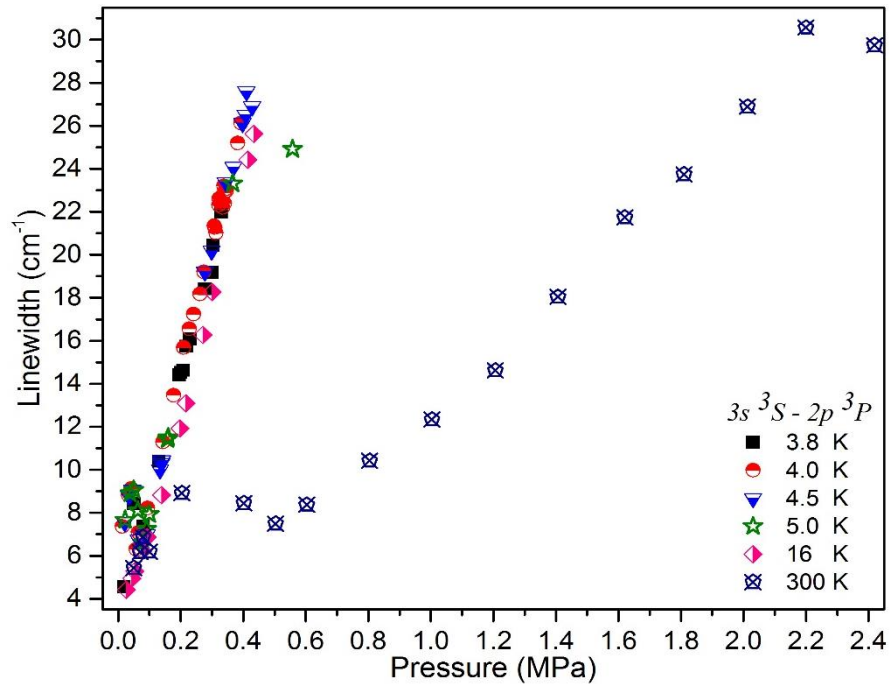


Figure 6.10: Linewidths of the triplet line as a function of pressure in the gas and liquid phases at low temperatures compared to the findings at room temperature (300 K). A considerable difference can be seen between these isotherms.

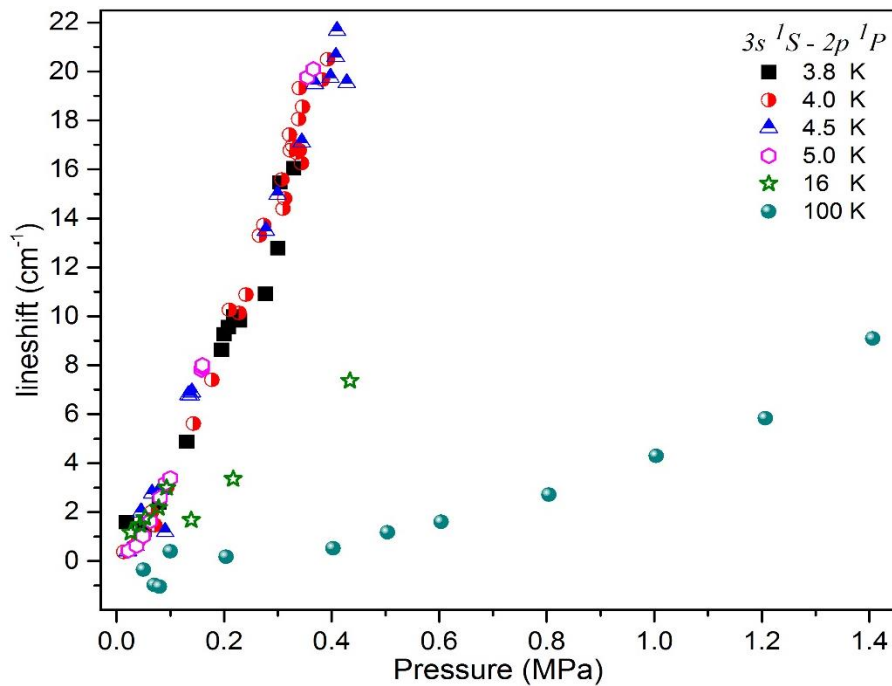


Figure 6.11: Comparison between the lineshifts that measured low temperatures and 300 K as a function of pressure for the singlet line. A large deviation is observed when we go from low to room temperature.

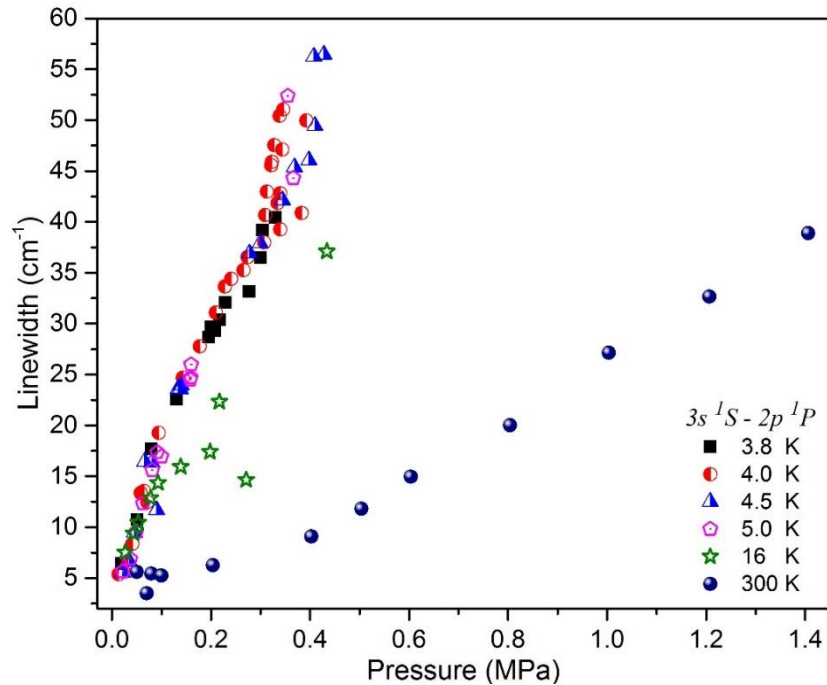


Figure 6.12: Linewidth as a function of pressure for the singlet line in for measurements at cryogenic temperatures and at room temperature. The gradients of the associated lines decrease towards high temperature.

For all comparisons in Figs 6.9-6.12, it can be seen that the gradients of the lineshifts and linewidths for both the singlet and triplet lines at 300 K are significantly lower than at cryogenic temperatures. As such these comparisons of the pressure dependence of the lineshift and linewidth for a liquid versus a gas indicate to the effects of high density of helium atoms at low temperatures strongly than room temperature. Hence, strong interactions between dense helium and excited helium atoms ( $\text{He}^*$ ) at low temperatures lead to large linewidths and lineshifts.

In Figs. 6.13 and 6.14, further comparisons of lineshift and linewidth between our experimental results and findings of our collaborators in Grenoble-Alpes University, France, at low temperatures and 300 K are made. In this study [15], the analysis of lineshift and linewidth of triplet 706 lines were carried out only at 4.2 K in the liquid phase and a supercritical gas phases at different temperatures and at pressures ranging from 0.1 to 6 MPa. The atomic lines recorded in this study showed an asymmetry in the shape with increasing pressure. Furthermore, analysis of the singlet 728 nm lines were not obtained. However, in current study a symmetric shape enhances the analysis of the lineshift and linewidth for both transitions, and the slight asymmetry observed only occurs at higher pressures.

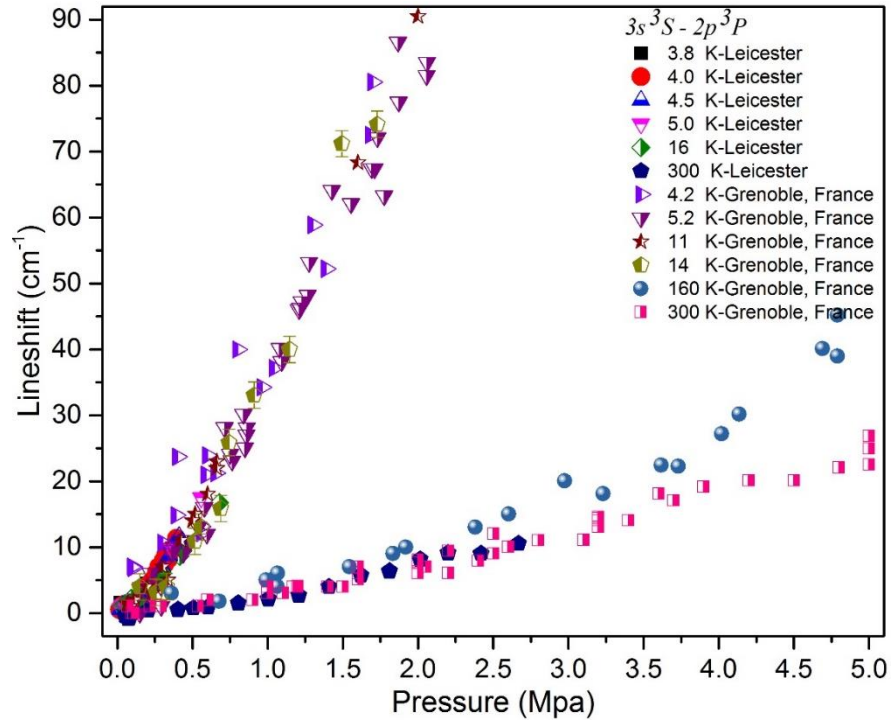


Figure 6.13: Comparison of the lineshifts for the 706 nm line as a function of pressure showing data from previous and current studies at low and room temperatures.

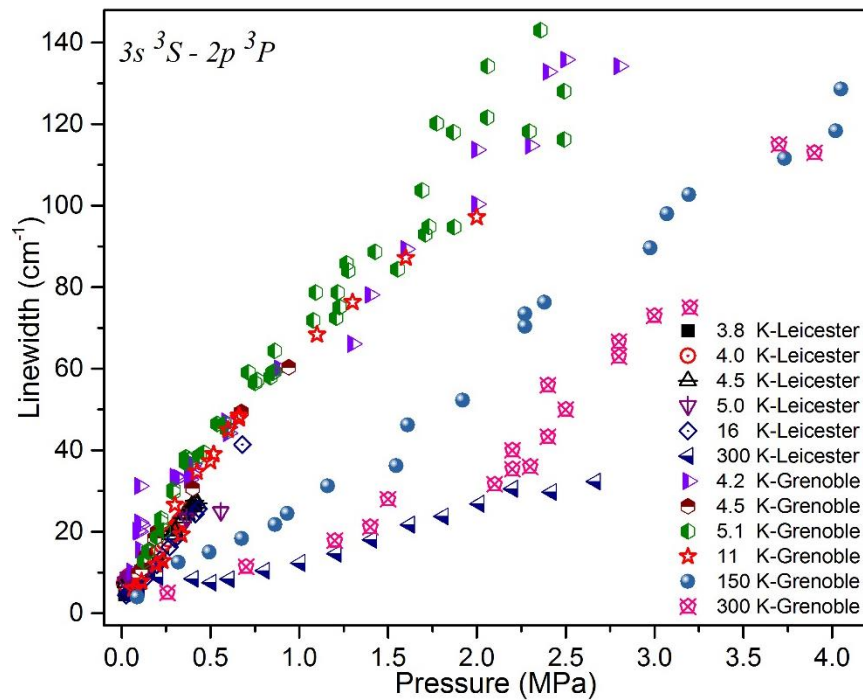


Figure 6.14: Comparison of the linewidths for the triplet  $3s-2p$  transition as a function of pressure between previous and current studies at low and room temperatures.

## 6.6 Theoretical treatment

It is of interest to compare our experimental measurements with simulated parameters of linewidths and lineshifts of atomic lines. The shift and broadening of the atomic triplet line at 706 nm was studied theoretically by Leo [185], who indicated a linear relationship of the lineshift and broadening as a function of density ( $N$ ). Primarily, the density and temperature of a gas in the ionization zone of discharge were assumed to allow calculations using the approximation of impact theory to investigate the shift and width of spectral lines. This theory describes the collisions of the excited helium atom with atoms in their fundamental state using impact approximation.

On the other hand, for the asymmetric profile of the spectral lines observed with more blue-shifted wings than the red wings at high pressure, a quasi-static approximation was required in addition to impact theory [184]. Here, impact theory was dependent on the temperature and pressure of the gas, while the quasi-static profile was predicated on the gas density,  $N$ , only, where the spectral line centre is described by impact theory, while the wings were described by the quasi-static model. Hence, using these approximations, provided us with more information about the experimental data.

The object of the analysis was to estimate the temperature of the helium gas within the ionization zone and to properly describe the differences in lineshift and linewidth compared to low temperature. Here, the gas number density,  $N$ , can be calculated from the ideal gas equation for a given pressure and temperature in order to use the fitting parameters of the simulation:

$$PV = nRT = NkT \dots \dots \dots (6.1)$$

- P = absolute pressure
- V = volume
- T = absolute temperature
- n = number of moles
- R = universal gas constant = 8.3145 J/mol K
- $N$  = number of atoms and molecules
- k = Boltzmann constant =  $1.38066 \times 10^{-23}$  J/K
- $k = R/N_A$
- $N_A$  = Avogadro's number =  $6.0221 \times 10^{23}$  mol<sup>-1</sup>

### 6.6.1 Simulation of the triplet 706 nm line

A symmetric Lorentzian profile of spectral lines was used in the analysis of the impact broadening theory with widths and shifts being proportional to a gas density,  $N$  [181, 182]. According to a Lennard-Jones interaction potential between radiator and perturbators [167], the analysis of the line distortion depends on the nature of the interaction. Therefore, the repulsion interaction ( $U(r) = \hbar C_{12} r^{-12}$ ) which dominates the interaction between the radiator and perturbators was assumed. For a repulsive interaction, the equations used to calculate lineshift ( $S_L$ ) and line broadening ( $\Delta\lambda_L$ ) within the impact approximation can be given as follows [184]:

$$S_L = 0.922 \left( \frac{\lambda^2}{2\pi c} \right) w^{9/11} C_{12}^{2/11} N \dots \dots \dots (6.2)$$

$$\Delta\lambda_L = 6.44 \left( \frac{\lambda^2}{2\pi c} \right) w^{9/11} C_{12}^{2/11} N \dots \dots \dots (6.3)$$

where  $\lambda = 706$  nm is the wavelength of the triplet  $3s-2p$  line,  $C_{12}$  is the repulsive coefficient of the Lennard-Jones potential in  $\text{cm}^{12}/\text{sec}$ ,  $w = 10^4 \times T^{0.5}$  is the relative velocity (in  $\text{cm}/\text{sec}$ ) of the He atoms,  $T$  is the gas temperature in K and  $N$  is the gas number density (in  $\text{cm}^{-3}$ ), was taken from NIST. As mentioned, a symmetric Lorentzian profile was assumed for the spectral lines in the calculation, with a lineshift to linewidth ratio of 0.143. In fact, this ratio is close to that of our experimental data with helium gas at 300 K for both the 706 and 728 nm lines at low pressure. The deviation increases between experimental data and simulation with increasing pressure.

Simplifying equations (6.1) and (6.2) by substituting the values of constants and treating the repulsive potential with value of constant  $C_{12} = 1.6 \times 10^{-72} \text{ cm}^{12}/\text{sec}$ , the magnitudes of the shift and FWHM (in nm) of the 706 nm line can be given respectively as:

$$S_L = 0.384 \cdot 10^{-21} \cdot N \cdot \left( \frac{T}{300} \right)^{\frac{9}{22}} \dots \dots \dots (6.4)$$

$$\Delta\lambda_L = 2.9 \cdot 10^{-21} \cdot N \cdot \left( \frac{T}{300} \right)^{\frac{9}{22}} \dots \dots \dots (6.5)$$

The results of calculation are reflected in Figs. 6.15 and 6.16 for the atomic  $2p\ ^3P \leftarrow 3s\ ^3S$  triplet transition for the linewidth and lineshift, respectively, and are compared with our experimental results.

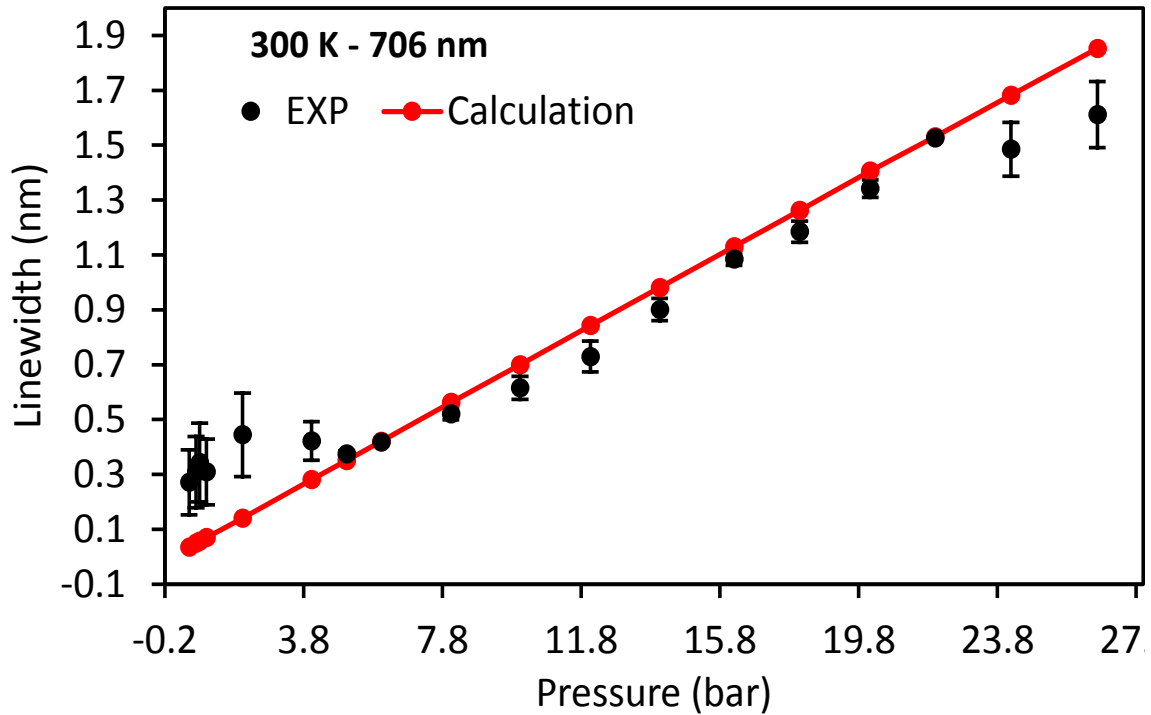


Figure 6.15: Linewidth of the 706 nm line of helium gas at 300 K and various pressures. Black points represent the experimental data whilst the red line represents the results of the simulation.

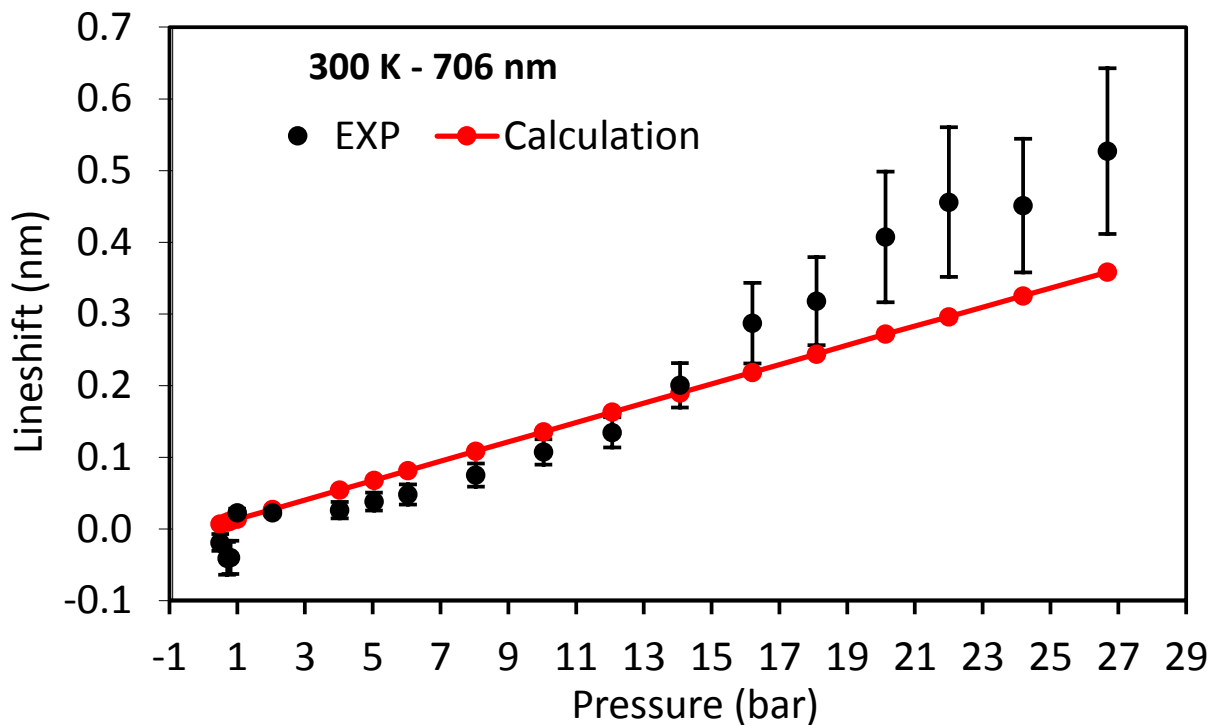


Figure 6.16: Lineshift of the 706 nm line as a function of pressure of the helium gas at 300 K. Black points represent experimental data and the red line represents the results of the simulation.

It is notable in the above figures that our values only seem close to those of Leo at low to medium pressures between 1-19 bar, according to the lineshift to linewidth ratio of about 0.143. In the region below 1 bar, the lineshift and broadening fluctuate due to instability in the current, which affects the corona discharge and thus the spectra. From 19 bar, our experiments show a nonlinear relationship between lineshift and pressure and same behaviour for linewidth, therefore the impact approximation can no longer be applied for higher pressures. The determination of the density of the He perturbators thus proved very complex and cannot be simply deduced from the broadening and shift of the line. It is therefore expected that the line profile will need to be calculated using the quasi-static approximation. This step will be discussed for future, however; the current focus will remain on the lineshift and linewidth for the moment.

### 6.6.2 Simulation of the singlet 728 nm line

The resonance broadening  $\Delta\lambda_{res}$  of the line at 728 nm is characterized by an oscillator strength,  $f = 0.276$  of the resonance transition of the line at 58.4 nm [184], and is given by;

$$\Delta\lambda_{res} = 1.44 \frac{\lambda^2 r_0 f \lambda_r}{8} \cdot N \dots \dots \dots (6.6)$$

Here  $\lambda$  is the wavelength (728 nm),  $f = 0.276$ ,  $\lambda_r = 58.4$  nm, the classical radius of an electron is  $r_0 = e^2 / 4\pi \epsilon_0 mc^2 = 2.8 \times 10^{-13}$  cm, and N is the gas number density in  $\text{cm}^{-3}$  which was taken from NIST. The expressions for the resonance width and shift of the atomic lines at 728 nm are given by:

$$\Delta\lambda_{res} (728nm) = 4.3 \cdot 10^{-21} \cdot N \dots \dots \dots (6.7)$$

$$S_{res} (728nm) = 1.05 \cdot 10^{-21} \cdot N \dots \dots \dots (6.8)$$

The results of the simulations are presented in Figs. 6.17 and 6.18 together with the experimental data.

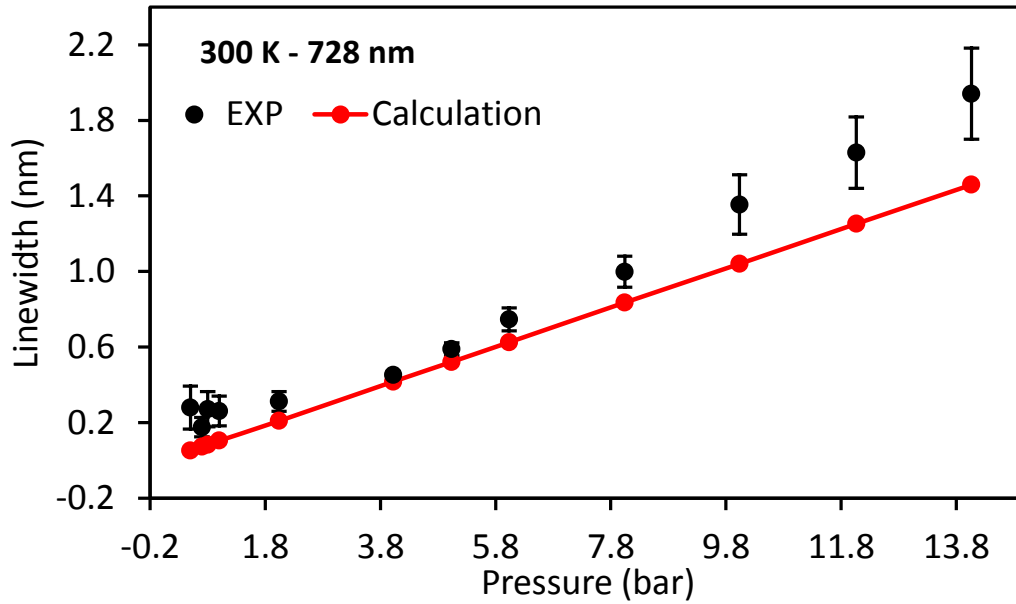


Figure 6.17: Broadening of the 728 nm line of helium gas at 300 K at different pressures. Black points represent the experimental data and the red line represents the result of the simulation.

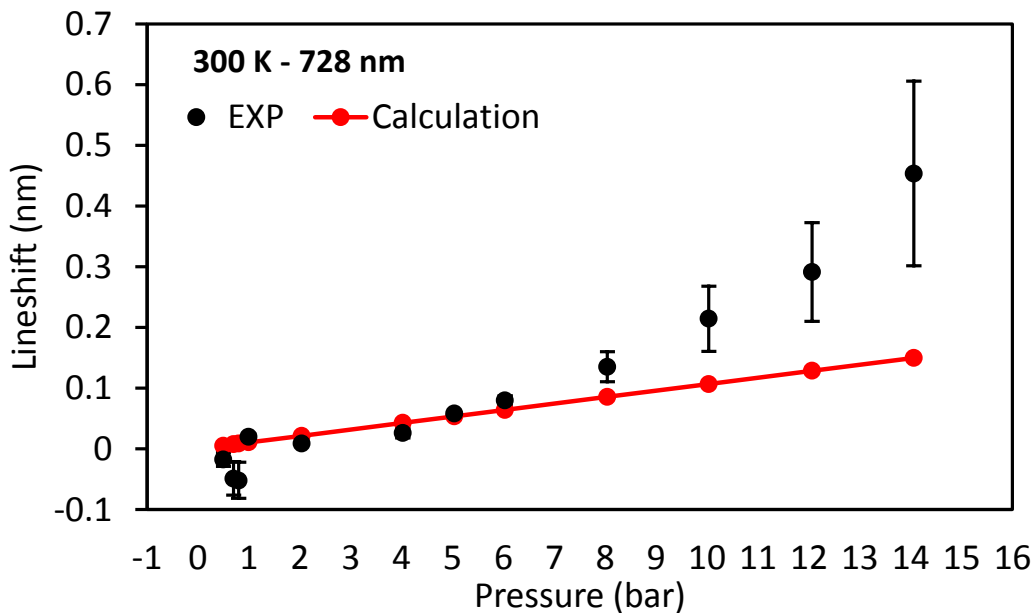


Figure 6.18: Lineshifts of the 728 nm line as a function of pressure of helium gas at 300 K. Black points represent experimental data whilst the red solid line represents the results of the simulation.

From Fig 6.17 and 6.18, and similarly for our observations of the calculations for the 706 nm line, there is a linear relationship at low pressure between the lineshift and broadening of the 728 nm line as a function of pressure. However, at pressures greater than 8 bar the experimental results deviate from the calculation for both lineshift and linewidth, indicating that the impact approximation can only be applied at lower

pressures. We have therefore undertaken to calculate the line profile using the quasi-static approximation.

Additionally, the results of the linewidth for both simulation and experiment are greater than those for the lineshift, as for the 706 nm line.

## 6.7 Molecular bands

This section presents fluorescence spectra recorded at 300 K showing the  $d^3\Sigma_u^+ \rightarrow b^3\Pi_g$  and  $D^1\Sigma_u^+ \rightarrow B^1\Pi_g$  transitions of excited helium molecules  $\text{He}_2^*$ . Fig 6.19 shows the molecular singlet and triplet transitions for various different hydrostatic pressures ranging between 0.5 and 26 bar at room temperature in the range 630 – 667 nm. A glow discharge spectrum was recorded and is shown as a reference for the line positions under vacuum conditions and the conditions listed in Table 6.1 for molecular bands. From Fig 6.19, the spectrum shows typical features with P, Q, and R rotational lines defined by the selection rules  $\Delta N = -1, 0,$  and  $1,$  respectively, upon the radiative transfer between electronically excited states of  $\text{He}_2^*$ .

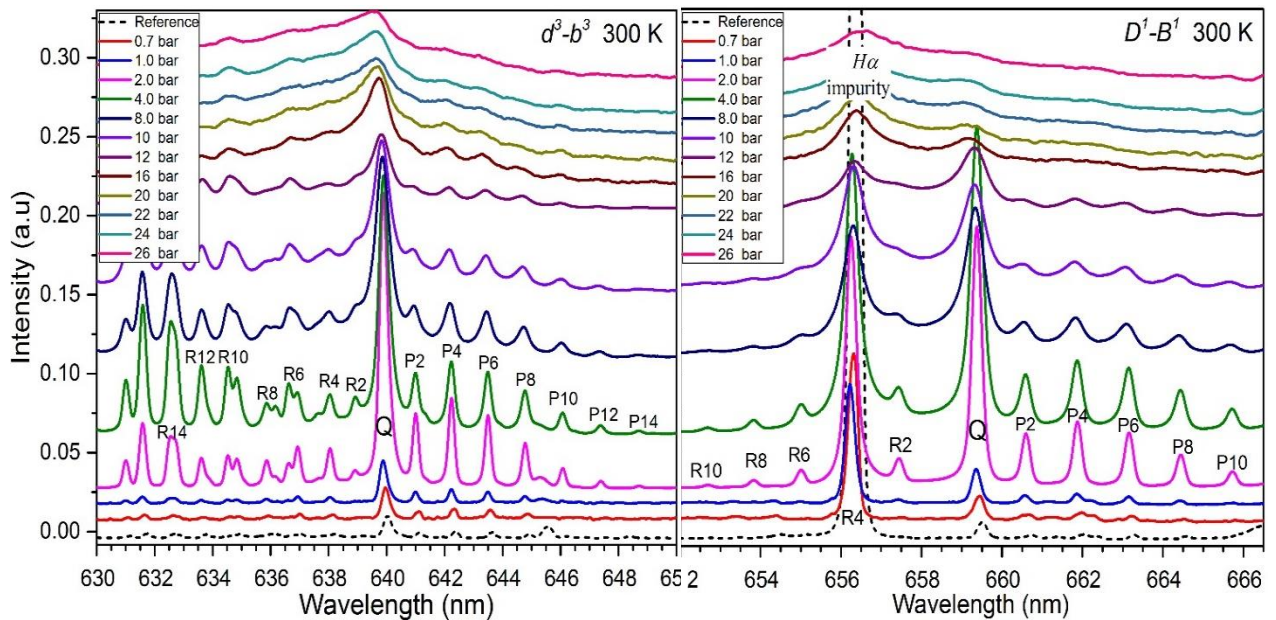


Figure 6.19: Spectra of the triplet  $d$ - $b$  (left) and singlet  $D$ - $B$  (right) transitions of the  $\text{He}_2^*$  excimer as a function of pressure at room temperature. Rotational lines are labelled R, Q, and P as a function of quantum number  $N$  (Hund's case (b)). The Balmer series hydrogen alpha line ( $H$ - $\alpha$ ) due to hydrogen impurities in the N6.o He, overlapped the  $D$ - $B$  spectra at the R(4)-branch. The glow discharge spectrum is represented by a dashed black line as a reference.

It was found from Fig 6.19 that with increasing pressure, the lines broaden, shift and the Q, P(4) and P(6) lines increase in relative intensity compared to other lines, while at low temperatures (see chapter 5) the rotational Q and P(2) lines gained in relative intensity and ultimately merged. The intensities and offset have been scaled for better visualization. The atomic Balmer series Hydrogen alpha ( $H-\alpha$ ) was also observed due to H impurities in the N6.0 He, in which overlapped the D-B spectra at the R(4) branch. The intensity of this line was also affected by pressure. Within the resolutions observed, the rotational B constant for  $He_2^*$  was unchanged.

It is noted that the intensity of R-branches decreases at lower pressures than the P-branch for both transitions. Moreover, it was observed that the rotational P-branches of the singlet D-B transition were unresolved) at pressures between 10-12 bar, which is lower than the case for the triplet d-b transition (which became unresolved between 20-22 bar). Generally, the absolute intensity of the  $D-B$  transition is much lower than that of the  $d-b$  transition. Hence, this makes the Q-branch of the  $D-B$  transition

## 6.8 Analysis of molecular bands

### 6.8.1 Lineshift, linewidth and intensity versus pressure

Similar to the previous analysis of molecular bands in chapter 5, rotational lines were normalized, calibrated and fitted to Lorentzian functions to assess lineshifts, line broadening and intensities. The results of analysis are shown in Fig. 6.20, which presents two panels as a comparison of the lineshift and linewidths for the singlet D-B and triplet d-b transitions as a function of hydrostatic pressure. In both parameters of lineshift and widths were analysed for the Q-branch and  $P_{avg}$ -branch, where the latter considers all lines of the P-branch from P(2) to P(10). It can be seen that the linear relation between those parameters and pressure holds for the Q- and  $P_{avg}$ -branches, however, the coefficients of lineshift and width for Q-branch are larger than the  $P_{avg}$  in both transitions. In similar manner to these transitions at low temperatures, D-B transitions disappear at pressure lower than d-b lines, where Q-lines were hindered at 20 bar and at 14 bar for  $P_{avg}$  lines. In contrast, the rotational lines for the triplet d-b transition were started to vanish at 26 bar for the Q-branch and up to 22 bar for  $P_{avg}$ .

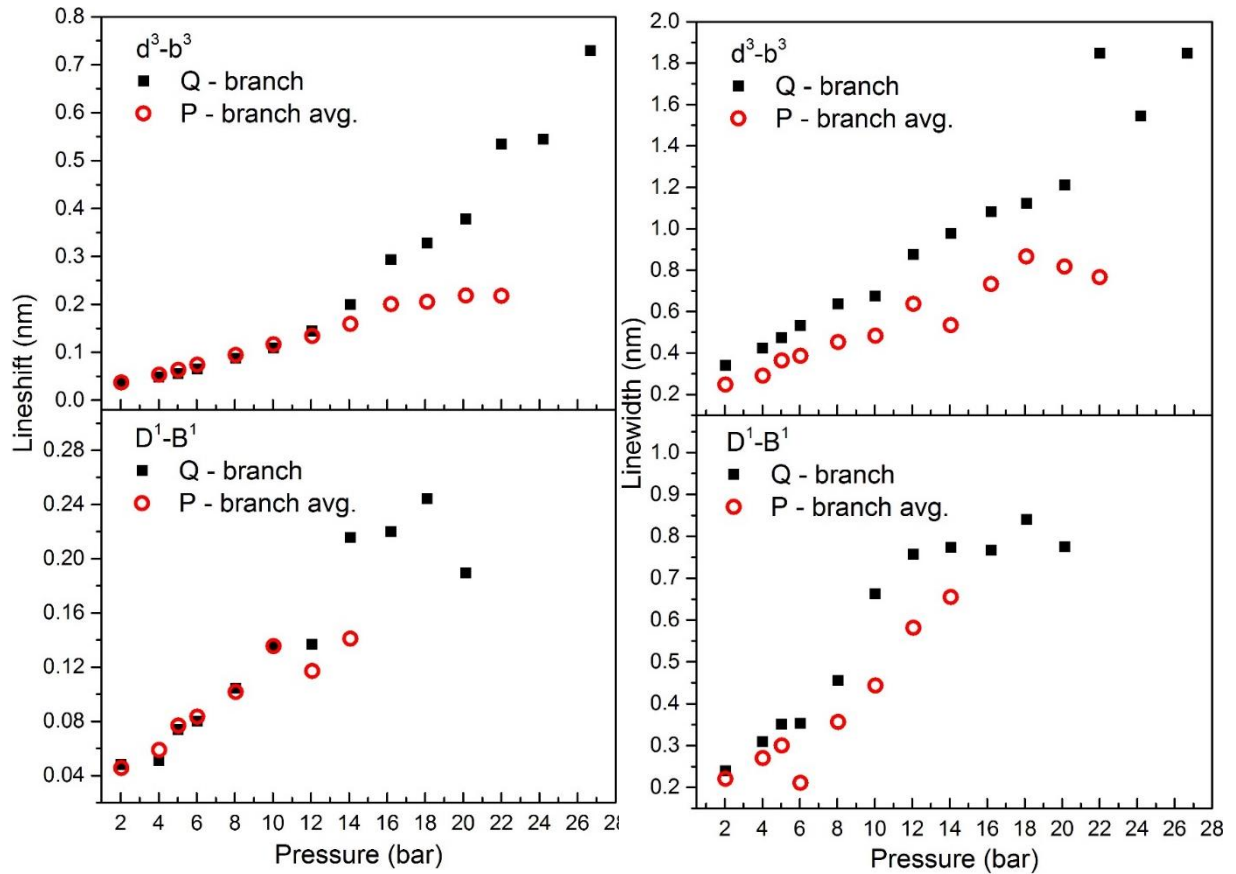


Figure 6.20: Lineshifts (left panel) and linewidths (right panel) as obtained by fitting with Lorentzians at 300 K as function of pressure for  $d$ - $b$  and  $D$ - $B$  transitions. Black squares represent “Q-branch transitions”, while red circles represent P-branch transitions averaged over all  $N$ .

The last parameter analysed through the fitting process was the line intensity ratio of the Q lines and  $P_{\text{avg}}$  lines. The fluorescence intensity was observed to change with pressure and temperature, so an analysis without meaningful calibration is inappropriate. We have therefore divided the line intensity of the Q-branch by that of the  $P_{\text{avg}}$ -branches prior to normalisation, which eliminates the effects of intensity changes due to external factors.

Fig 6.21 shows the ratio of the line intensity of the Q lines and the averaged line intensity of the P lines over all  $N$  lines, for the singlet  $D$ - $B$  and triplet  $d$ - $b$  transitions. From Fig. 6.21, the Q/P intensity ratio increases linearly with pressure. However, at high pressure the increment of the line intensity ratio fluctuates for both transitions.

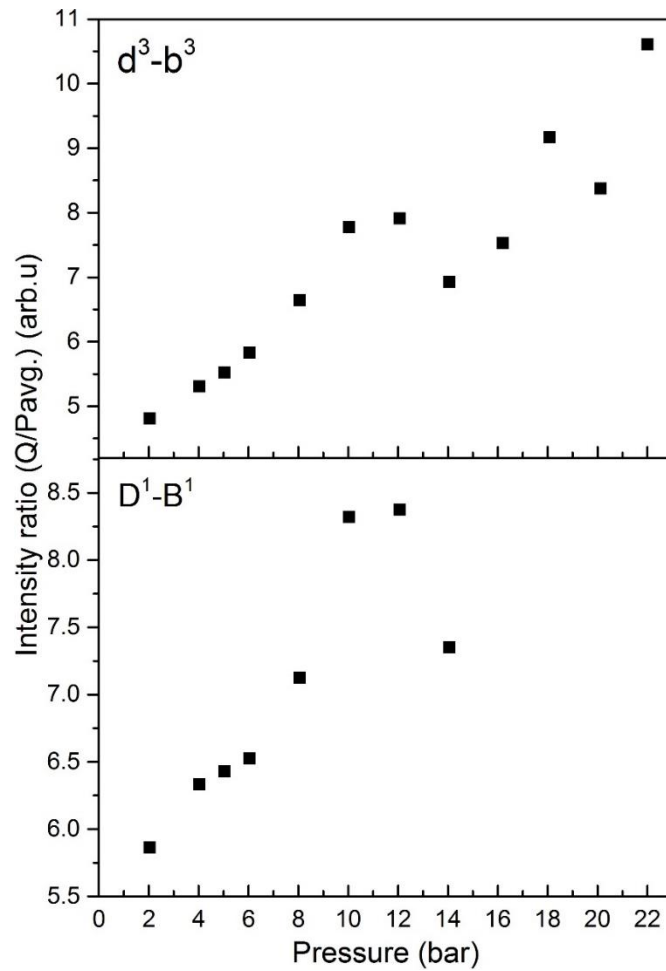


Figure 6.21: Pressure dependence of the intensity ratio of the Q-branch and  $P_{\text{avg}}$ -branch excluding P(2), for 3.8, 4.0, 4.5, and 5.0 K.

## 6.8.2 A comparison with results at low temperature

In this section, a comparison between the results of the analysis of lineshifts and linewidths at low and high temperatures for the molecular bands is given. Also, a comparison with the previous results from our collaborators in Grenoble, France [15], will be made. The latter comparison was for lineshift only as no line broadening results were available.

Fig 6.22 shows the linewidths (in nm) of the molecular singlet  $D-B$  and triplet  $d-b$  bands at the 4.0, 5.0 and 16 K isotherms compared to results at 300 K as a function of pressure. The line broadening of the singlet transition is greater than that of the triplet at low

temperatures. Contrary to the room temperature results, it was found that the singlet is less pressure dependence than the triplet.

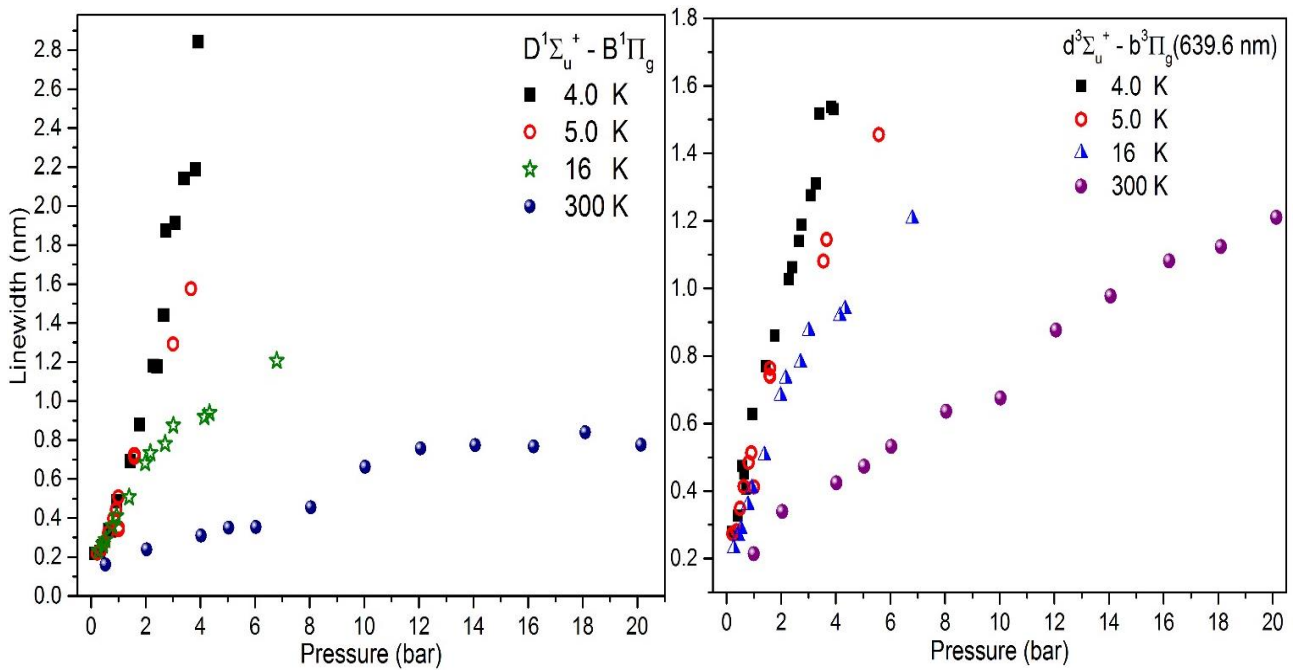


Figure 6.22: Measurements of linewidth as a function of pressure in different temperatures for the singlet D-B and triplet d-b transitions. The gradient of the linewidth increases at low temperature.

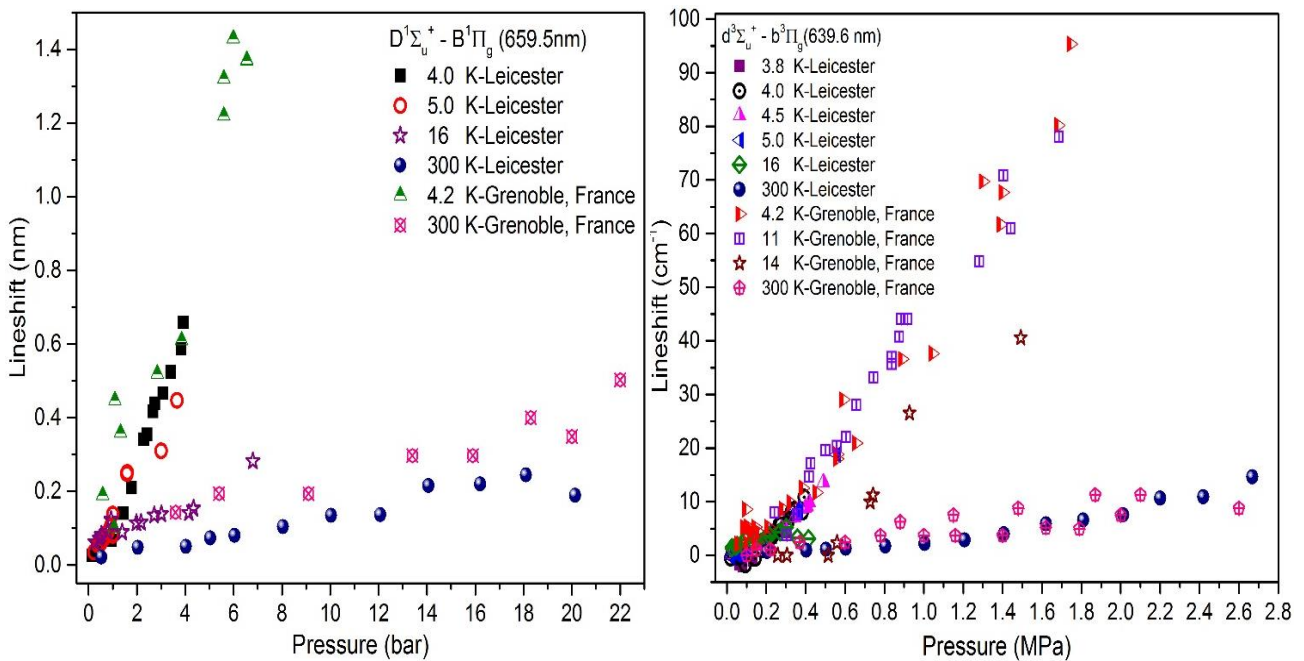


Figure 6.23: Comparison of the lineshift for the 706 nm line as a function of pressure between previous and the current studies at low and room temperatures.

A similar comparison was made for lineshift under identical conditions to the above and for the same transitions (including the results of the Grenoble group), as shown in Fig. 6.23. According to the reference calculation, lineshifts for the triplet lines were in wavenumbers, while nanometres was used for the singlet line. Again, similar to the linewidth, the lineshift for the triplet rotational lines was smaller than for the singlet at low temperatures, whereas at 300 K, the shift observed for the triplet lines is greater than for the singlet.

It is clear from Fig 6.22 and 6.23 that the gradients of the lineshift and linewidth for the molecular bands decrease with increasing temperature; the effects of pressure are reduced at increased temperature due to the consequent reduction in helium atom density at high temperature

## 6.9 Conclusion

We have presented a study of atomic lines and molecular bands emitted from excited helium atoms ( $\text{He}^*$ ) and excimers ( $\text{He}_2^*$ ). We have shown well-resolved spectra can be produced using a corona discharge that is well-suited with another high pressure cell differs from the cell that use with liquid helium phase to excite visible and near infra-red fluorescence of gas helium at 300 K and investigate pressure dependence.

The atomic and rotational lines for both singlet and triplet transitions shifted in energy and broadened as the helium pressure was increased. The parameters for the spectral lines were compared with the collisional broadening and shifts calculated using impact theory, from which good agreement was found with experimental results at low pressures. However, this approximation was found to break down with the increasing pressure assuming that impact theory can clearly be seen to be invalid for calculating line position at an increase in helium atoms density  $n_{\text{He}}(T,P) = 5.7 \times 10^{20} \text{ cm}^{-3}$  [184]. Another assumption is that the heating of the gas in the ionization zone is to temperatures greater than 300 K (due to the effects of the large discharge current near the tip of the electrode), where a good agreement between the measured linewidths and lineshifts with simulations was found to be at 500 K for ionization zone [184]. Other

comparisons of line parameters for the excited atoms and molecules are made between the results for liquid helium at low temperatures, and the gas at room temperature.

Although at 300 K the density of gas helium is lower than for the liquid phase, spectral lines of excited helium atoms and rotational lines of excimers are shifted to some extent but broadened significantly due to the frequent collisions with other He atoms in the gas phase. In contrast, a strong lineshift and broadening for all transitions of interest were observed at high density in the liquid phase. These features indicate into effects of pressures and temperatures on interactions between both species, excited atoms and molecules, with environment providing evidence of ability to control the interaction in different conditions by changing pressures and temperatures.

## Chapter 7

### Results and discussion

# Using corona discharge for detection of the emission spectroscopy of different plasmas at room temperature

## Abstract

A corona discharge was generated by DC source under a negative polarity in a stainless steel high pressure cell at room temperature. By the injection of pure helium, pure air, an unspecified perfume and mixture of these three materials was used as the gaseous medium to generate a corona discharge, with emission spectroscopy subsequently carried out to investigate the discharge characteristics and determine the plasma parameters. Atomic lines of He I, (Ar I, II), O and N atoms, as well as molecular bands of due to  $N_2$ ,  $N_2^+$  and He I were identified, presenting in the spectral range 300-1000 nm. Because the fluorescence spectra composition gives insight into the ongoing plasma chemistry, in this chapter, a corona discharge coupled with optical emission spectroscopy in the UV, visible and near infrared regions was used as a diagnostic means of examining atmospheric pressure air, and a mixture of helium with air and perfume, which could be relevant to bio-medical, explosive detection and environmental applications. This is just the beginning of a project that is far from being complete.

The structure of this chapter is as follows: Section 7.1 gives a concise introduction to the chapter. Experimental data are reported in Section 7.2. The analyses of spectra are presented in Sections 7.3, including the analysis of atmospheric pressure air with a plasma of helium and an unknown perfume. General observations and future plans are given in Section 7.4.

## 7.1 Introduction

Recently, considerable attention has been devoted to methods of efficient analysis and investigation of atmospheric pressure (atm) air plasmas at different gas temperatures. This field of research is motivated by various applications, such as activated reflectors and absorbers of electromagnetic radiation, polluted air detoxification, and as surface treatments [186-188]. One such study used a radiofrequency plasma source method to deconvolute the constituents of air ( $N_2$ , Ar and  $O_2$ ) [189], for instance. Interestingly, however, DC glow discharge appears to be an effective and promising method by which to efficiently obtain a plasma [190]. A DC electric field was applied to efficiently produce a glow discharge [191, 192] atmospheric pressure air plasmas at gas temperatures below 2000 K. Often, it is believed that atmospheric pressure air plasmas represent cases of local thermodynamic equilibria due to the rapid interspecies collisions that occur at high pressure. However, optical diagnostic techniques of emission spectroscopy cannot rely upon this assumption because the electrical discharges affect the velocity gradients of flowing plasmas and the elevated temperature of electrons can result in large departures from chemical and thermal equilibria [192].

The production of stable sources of homogeneous atmospheric-pressure plasma is a complicated challenge. A major obstacle in the generation of glow discharge plasmas in gases at atmospheric pressure (APGD) is raised from instabilities. As a consequence, this leads to the glow-to-arc transition (GAT) [193-196]. Also, in some excitation processes of gaseous plasma, a high electric field is required to emit electrons from the cathode through ion impact. To overcome this instability, a microhollow cathode discharge (MHCD) was used as the electron source to support and extend the range of stable operation between the microhollow anode and a third positively biased electrode, as the density of the discharge electrons is expected to extend [193, 194]. Moreover, the process of converting an atmospheric-pressure glow discharge (APGD) into a filament discharge can be realized through the use of noble gases and high-frequency electric sources.

Although a high cost of the noble gases plasmas, it is still focussing and required by researchers. This is because a sustainable discharge of atmospheric air can be obtained through use of the noble gases [197]. Also, other researchers found glow discharges were easier to generate with pure inert gases [198, 199], though the possibility of

producing a sustained DC glow discharge in a mixture of helium with air was explored by Arkhipenko *et al.* [195, 200].

The current experiment is similar to that used in chapter 6 with only a few alterations, as explained in chapter 3. The high efficiency of our high-pressure cell suggests that we can employ a corona discharge in different, and potentially quite varied, environments. As mentioned previously, this is in fact not a new method, as many researchers have run corona discharges at room temperature in different environments for the purposes of emission spectroscopy. With a slight different in setup design, we were able to reproduce their results. However, the efficiency is very high in terms of how much light we were able to get out in our method, as our spectra could be recorded, with a good to excellent signal-to-noise ratio, in short time. A high discharge voltage is necessary to generate a stable plasma in air, but the introduction of He gas improves the stability of the plasma at high pressures for reasonable discharge voltages. Hence, those two conditions have supported our experiment to allow for straightforward observation of spectra.

The technique of an atmospheric-pressure glow discharge (APGD) described in this chapter was applied for four types of air or helium plasmas. The first case (1) corresponds to glow discharges generated by a DC electric field in air at atmospheric pressure. The second case (2) consists of a mixture of air and helium that is exposed to the glow discharge. The third case (3) is a mixture of air with an unspecified perfume. Finally, case (4) corresponds a mixture of air, helium and perfume.

In order to investigate further, the processes associated with air operating in a helium and in unspecified perfume mixture are investigated spectroscopically in this chapter. This effect might find an application for the detection of small quantities of the impurities in helium gas and also to detect spectra emitted from samples during their destruction by the discharge process.

Broadly, this experiment idea reviews diagnostic techniques based on optical emission spectroscopy, and it should be noted from the outset that this is just the beginning of a new research topic and not the key point of this thesis. The objective in this chapter and these experiments is to use helium or air at atmospheric pressure whilst employing a corona discharge as a means detect unknown transitions over chemical interactions.

## 7.2 Experimental data

The layout of the experiment and optical alignment used in this chapter is similar to that described in chapter 6 for the room temperature experiment with a few minor alterations (see chapter 3 for experiment at room temperature, section 2.4). The procedure required evacuation of the cell and pipes to 6 mbar on a Pirani gauge before initiation of the discharge, followed by filling the cell with dry air and then mixing with helium or perfume at atmospheric pressure (1 bar). The plasma was established with a glow discharge at atmospheric pressure. Therefore, the discharge was ignited for each case near to the tip electrode by applying a high voltage under negative polarity from a DC power supply (Spellman/MPS15N10/24/DCC2). Obtaining a stable discharge was initially difficult, but atmospheric-pressure glow discharge (APGD) was obtained after with a degree of experimentation with increasing the discharge current. Moreover, it was subsequently realized that the discharge current decreases over time, leading to a reduction in intensity of the associated spectral lines, requiring us to change the value of current on occasion to maintain experimental conditions. Fluorescent light was recorded using an Andor Solis Technology Shamrock SR303i spectrometer for different plasmas, as described in the following sections.

The DC power supply was applied across the electrodes under negative polarity. The power required varies depending on the plasma, and the associated plasma concentration, under consideration, the size of the gap between the electrodes and the temperature of the gas. Table 7.1 shows the discharge characteristics used in this experiment.

The acquisition time for each individual spectrum was 2 s for all measurements, except for the spectrum of air plus helium for which the acquisition time was 1 s. The acquisition was repeated 20 times, during which the spectra were accumulated and corrected for noise (cosmic event removal, etc.). This led to an effective exposure time,  $t_{\text{eff}} = t_{\text{exp}} \times N_{\text{accu}} = 20 \text{ s}$  or  $40 \text{ s}$ , as shown in Table 7.1.

Table 7.1: Experimental conditions required to ignite discharges through plasmas at atmospheric pressure in air, and details of effective time required to record each spectrum.

Plasma	Air	Air + He	Air + perfume	Air + He + perfume
- V / kV	6.11	7	8.15	6-8
- I / $\mu$ A	0.5	1-2	4-5	3
Power / mW	3.1	14	32.6 – 40.8	18 – 24
Exposure time /s	2	1	2	2
N. accumulation	20	20	20	20
$t_{\text{eff}}$	40	20	40	40

It seems that the mixture of air and helium plasma required greater power for ignition and the air less the least among these species.

## 7.3 Analysis of Spectra

### 7.3.1 Spectra of air and air plus helium at atmospheric pressure

The spectra from the various kinds of plasma at atmospheric pressure were collected at specific voltages and currents and then analysed and compared via emission spectroscopy. The emission spectra span the wavelength region 300-1000 nm, covering the UV, visible and near infrared regions for each plasma.

A corona discharge was ignited at atmospheric pressure, although this process was started by allowing the cell to pressurise to 0.5 bar and then filled gradually to 1 bar. Fig 7.1 shows the spectra of these two cases of atmospheric-pressure glow discharge (APGD). From this comparison, it is clear that some lines are missing at 0.5 bar that were present at high intensity at 1 atm. The signs (symbol) of the transitions observed are not given in this figure, but rather in subsequent figures when they become more intense after mixing with He.

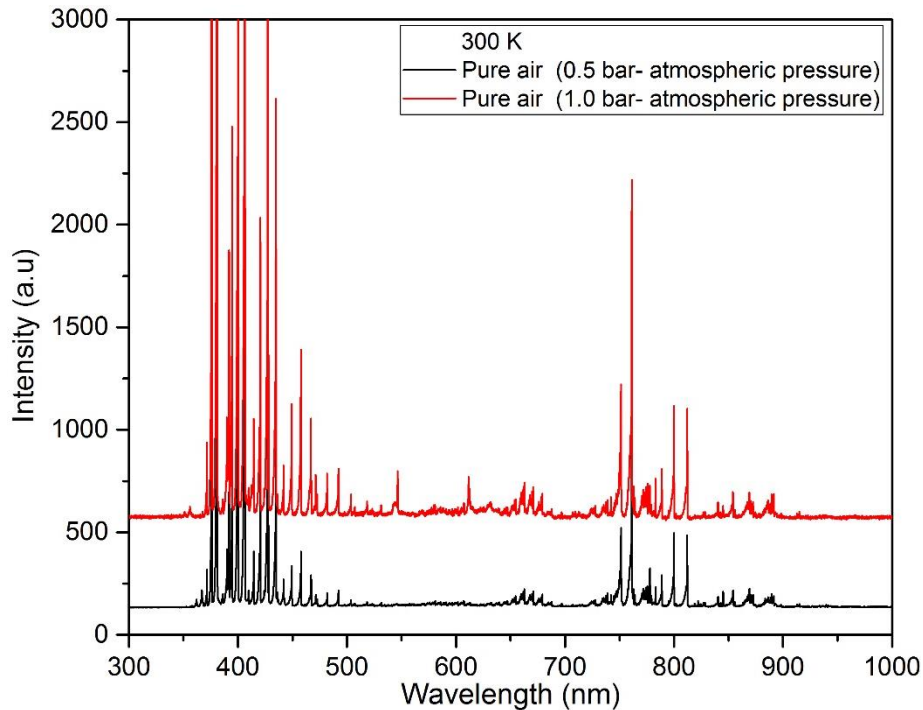


Figure 7.1: The emission spectrum obtained by atmospheric-pressure glow discharge (APGD) at 0.5 and 1 atm at 300 K.

The next step was the addition of pure helium to gain a mixture of helium and air at room temperature and atmospheric pressure. Stabilising the discharge was to some extent easier after adding helium to the air. In the case of air, the discharge frequently broke down due to arcing across the plasma, though after many attempts a stable discharge in air was achieved. A review of spectra recorded for a mixture of helium and air compared to the spectra recorded for 1.0 bar of pure helium is shown in Fig. 7.2, where the spectra for pure helium was taken from the result in chapter 6 (for pure helium excited by corona discharge under negative polarity in the cell after the evacuation process described above). Regarding plasma formation in ‘pure’ air, the cell was filled with helium, evacuated, and then filled with dry air, which was then exposed to a high voltage to obtain an atmospheric-pressure glow discharge (APGD). It can be seen from Fig 7.2 that some transitions do not appear in the plasma of air, nor in the plasma of pure helium. However, they are observed in the spectra recorded for a mixture of air plus helium, as shown inside dashed circles over the red spectrum. On the other hand, some lines in the spectra of pure helium are significantly reduced in intensity and hidden after mixing the helium with air plasma, as indicated by the dashed ellipses over blue spectrum. Moreover, numerous transitions were either observed, or became stronger, when mixing pure helium with air at atmospheric pressure, as represented by red

spectrum; these bands will be fully identified in subsequent figures (7.4 and 7.5). With this observation, helium gas as a trace can be assumed to detect missing atomic and molecular lines. Most of the transitions that can be resolved in pure helium are labelled for the blue spectrum in Fig. 7.2 below.

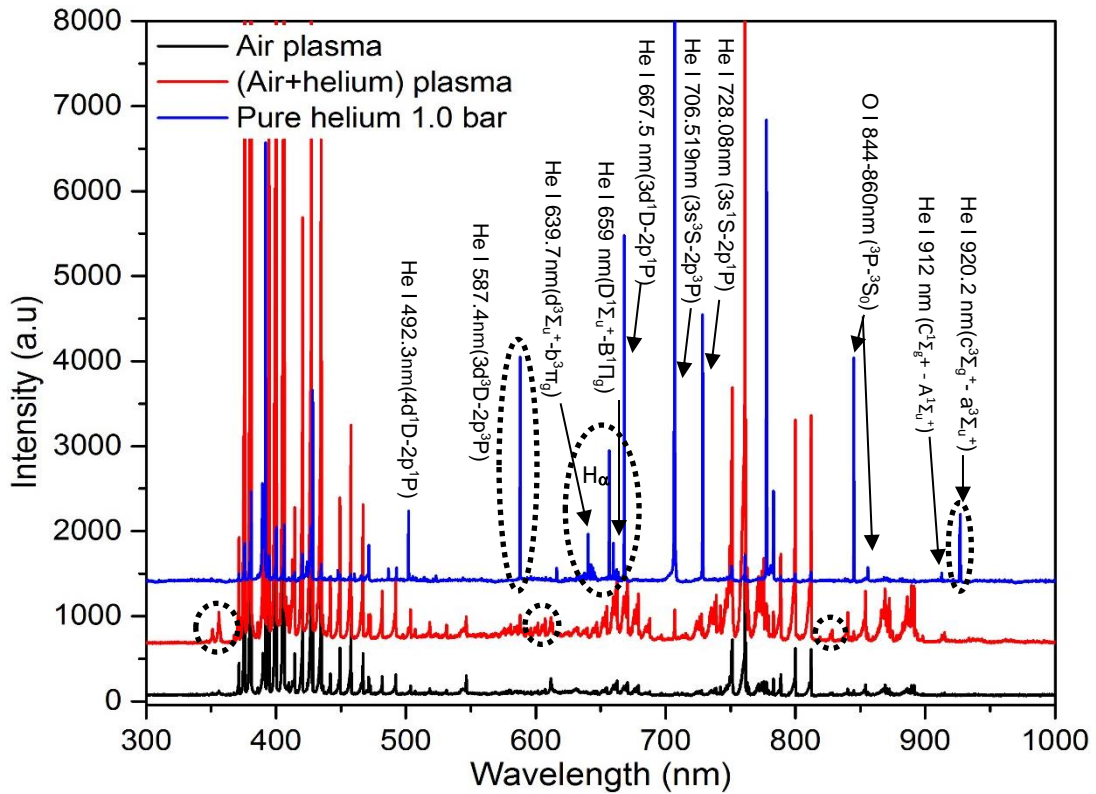


Figure 7.2: Overview of the spectra at room temperature of the plasma of pure helium at 1 bar, dry air at atmospheric pressure and a mixture of air with helium produced using corona discharges. The spectra have been moved upwards by 500-1000 a.u. for clarification purposes.

$N_2^+$  is produced when the helium plasma expands into the ambient air. Where the spectra are dominated by bands of the second positive system of  $N_2$  which is then ionized due to excited metastable helium atoms,  $He^*$ , forming nitrogen molecule ion ( $N_2^+$ ) according to the reaction [201]:



### 7.3.2 Spectra of air and air plus perfume plasmas

The second case investigated was the emission spectra of a mixture of an unspecified perfume with air. Here, the pressure cell was evacuated to 0.6 mbar to remove the helium. After that, atmospheric-pressure glow discharge (APGD) was run and a

spectrum of air recorded at 300 K. Then, an unknown perfume was introduced through the inlet (a Dragon leak valve), to merge with the air plasma. Hence, a corona discharge was established across the electrodes under a negative voltage polarity. Fig. 7.3 shows the spectrum of air compared to that of a mixture of air and perfume.

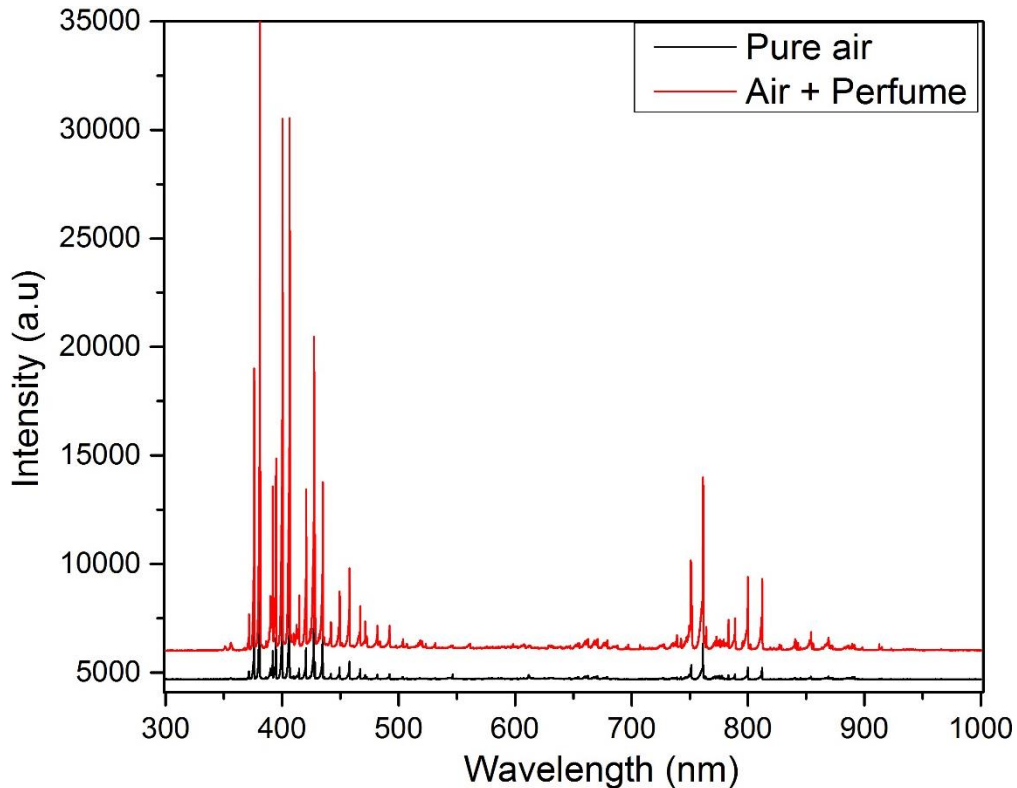


Figure 7.3: A comparison between the spectrum of air and spectrum of an unspecified perfume and air mixture at atmospheric pressure. Some transitions were hidden in the air plasma spectrum while, after mixing with perfume, were observed, such as the atomic nitrogen (N) group.

From Fig. 7.3, various transitions were either extremely weak or unresolved in the pure air plasma spectrum. However, these bands were observed after subsequent mixing of air with perfume at atmospheric pressure. We realized that the cell pressure had increased to be 1.2 bar after adding the perfume to the air in the cell, means that the estimate value of pressure of perfume ( $\sim 0.2$ ) was added to the atmospheric pressure (1 bar). We used perfume merely to see the effect on the discharge of a material containing chemical elements that might conceivably need to be distinguished. Some of these transitions can be recognized according do assignments given in the literature. To gain a precise description, the spectral range, 300-1000 nm, was divided into regions that were recorded at higher resolution and zoomed in to show the difference between these two

cases. The first region, 350-400 nm, as shown in the Fig. 7.4, contains a large group of transitions associated with molecular nitrogen. Also, it can be seen the spectral lines how are developing by corona discharge and mixing with helium at atmospheric pressure, where these lines gain more intense, broadening and observed after mousing such as N<sub>2</sub> C-B (0-1) transition. All transitions are labelled corresponding to each group from element in figures below.

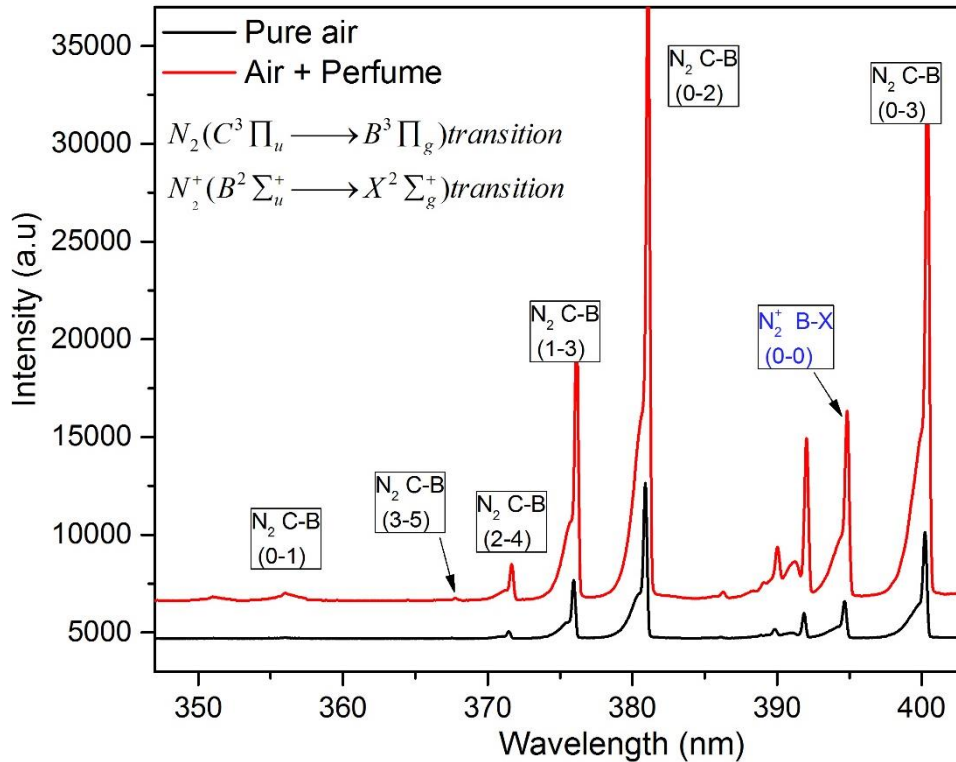
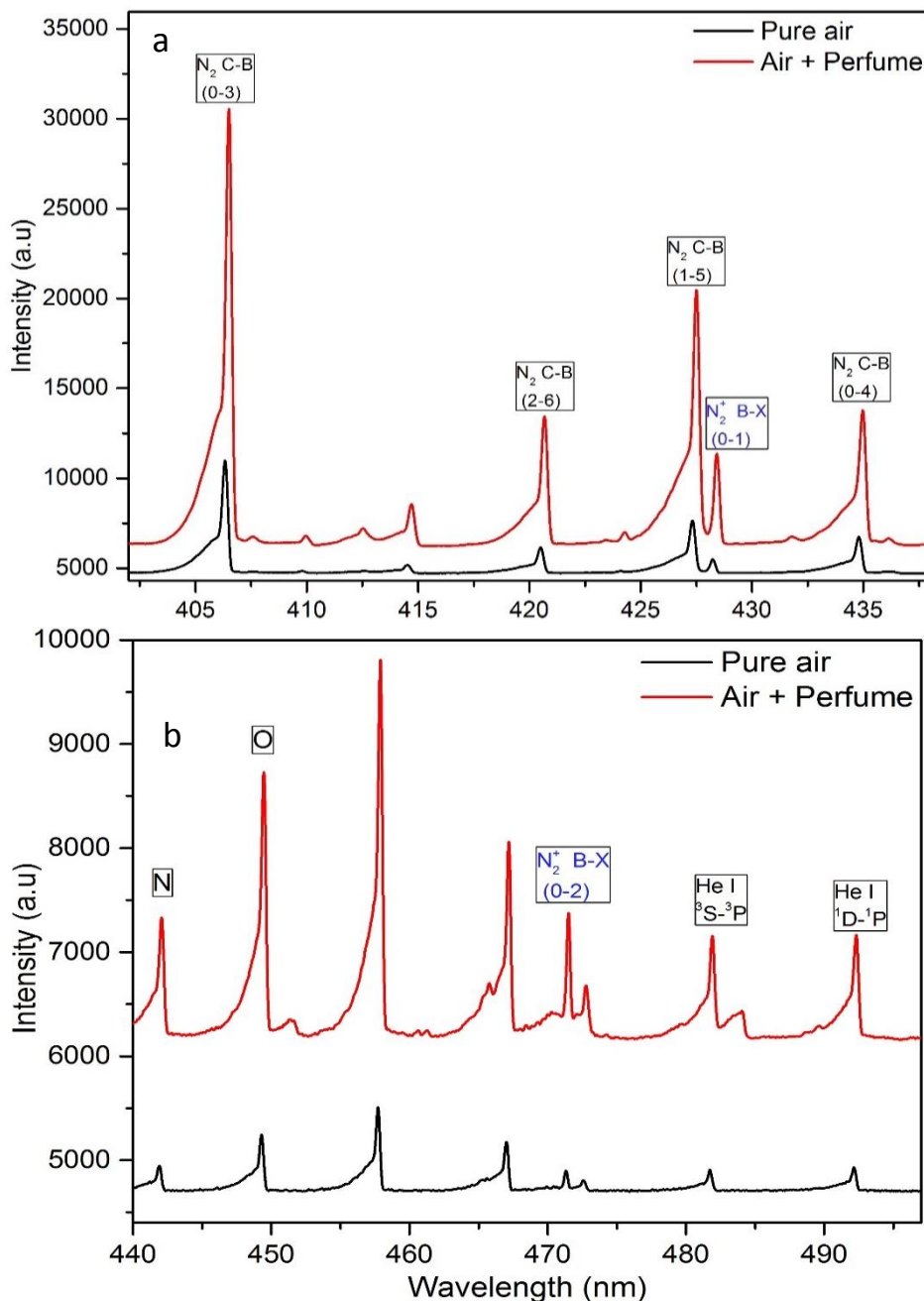


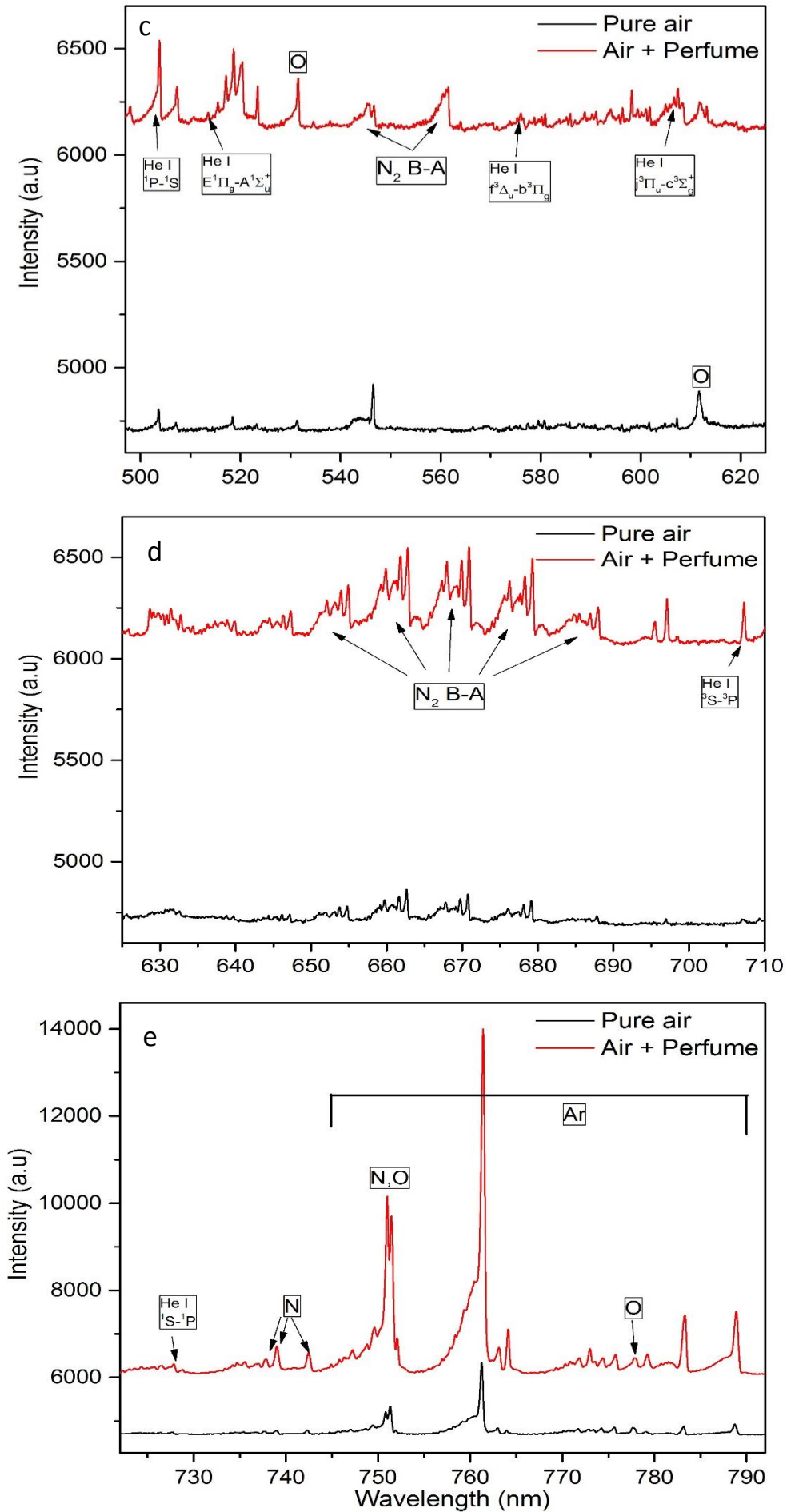
Figure 7.4: High resolution spectrum of the range 350-400 nm of Fig. 7.3 to show emission features from plasmas of air and a mixture of air and perfume. Such plasmas are readily produced by means of the electrical discharge due to the formation of corona discharges. Various transitions of N<sub>2</sub> and N<sub>2</sub><sup>+</sup> were observed.

Diverse molecular transitions of N<sub>2</sub> (C→B) and N<sub>2</sub><sup>+</sup> (B→X) appeared in the air plasma at room temperature depending on plasma excitation level (power applied on tip electrode). On the other hand, these transitions become particularly intense, and previously unseen transitions could be observed after adding the perfume, such as the N<sub>2</sub> (C→B) (0-1) feature at around 355 nm. Spectroscopic measurements of the N<sub>2</sub> (C→B) transition were reported in figures 8 and 9 of ref. [202] by Yu *et al.*, which shows a spectrum obtained

from a glow discharge. Where in such study, the vibrational temperature of the C state can be determined by the structure of the vibrational sequences (0,3), (0,2), (1,3), (2,4), (3,5) and (0,1) of the N<sub>2</sub> (C→B) system. The rotational temperature of the spectra reported in this study [202], was found by fitting the spectrum in the range 260–382 nm, in which corresponds to the vibrational band sequence of N<sub>2</sub> C→B with NEQAIR2 simulations. The best fit between the measured spectrum and simulated one yields a rotational temperature of 2200 ± 50 K [202]. Hence, our next step will be conducting such simulations to identify the rotational temperature of any level.

Fig. 5.7 (a) - (g) completes the presentation of the spectra in the 300-1000 nm range for the air and perfume plasmas as produced by a corona discharges.





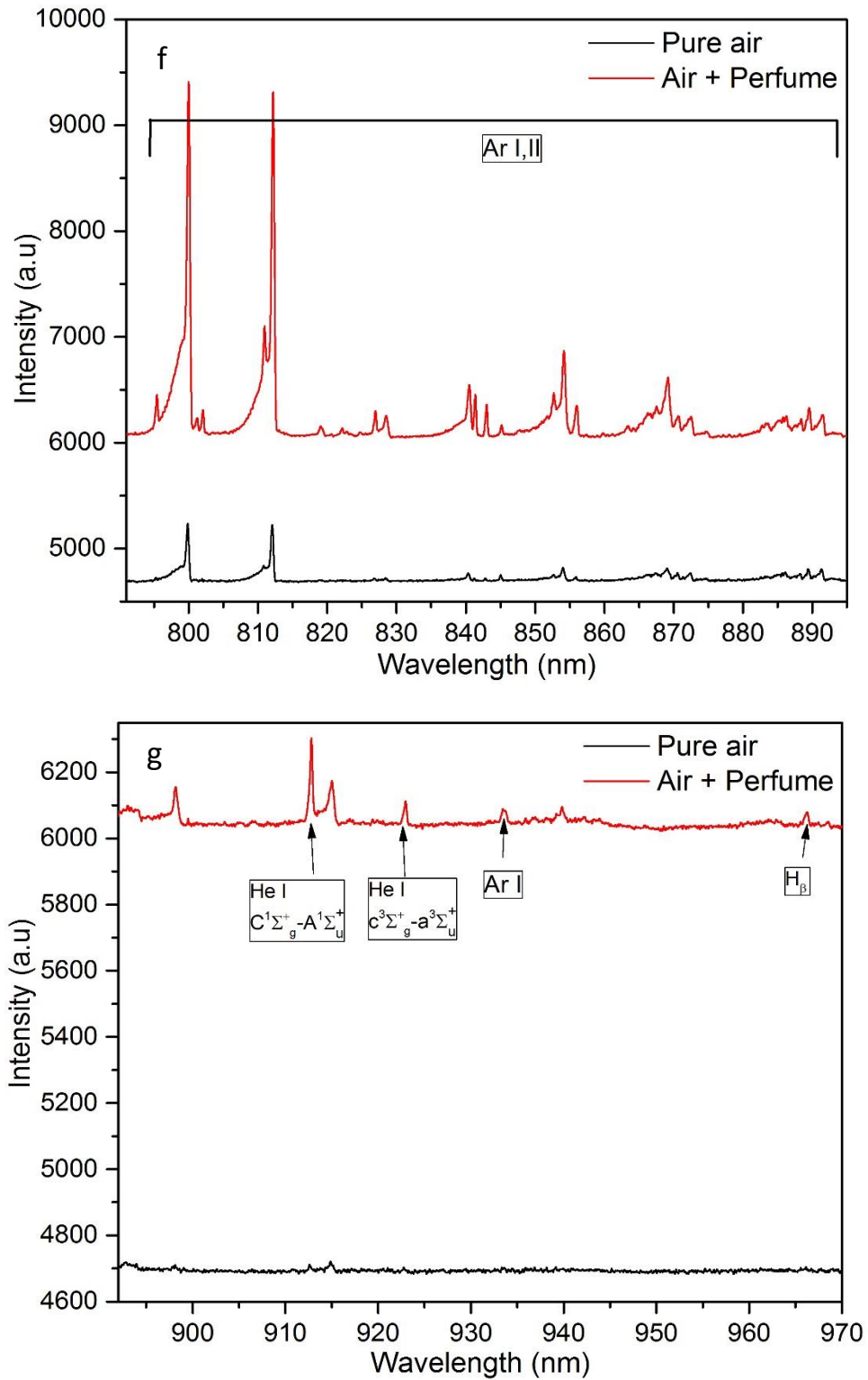


Figure 7.5: Typical emission spectra of air and perfume at atmospheric pressure from a corona discharge in the UV, visible and NIR regions (300-1000 nm). Expanded views of the ranges are given to clarify the differences between the air and perfume plasmas presented in Fig 7.3.

From the comprehensive presentation of the entire spectral range, as divided into short ranges, in Fig. 7.5 (a-g), atomic lines that can be attributed to O I, N and He I atoms were observed. Additionally, molecular bands for the He<sub>2</sub> I, N<sub>2</sub> and N<sub>2</sub><sup>+</sup> were also observed using a corona discharge. Transitions of Ar I, II was also observed in the 750-930 nm region, as shown in Fig. 7.5 (e), (f) and (g).

Intense atomic and molecular spectra due to nitrogen and oxygen make it difficult to observe the weak H and OH emissions.

### **7.3.3 Spectra of air, helium and perfume plasmas**

The final case of the use of atmospheric-pressure glow discharge (APGD) was that of a mixture of the plasmas presented in previous sections, namely air, perfume and helium plasmas, at room temperature and atmospheric pressure.

The most surprising observation in this experiment, as mentioned previously, was the differences between spectra substantially during separating of the samples studied, before and after the helium to the mixture. Fig. 7.6 presents the spectra recorded for dry air, air plus perfume, air plus helium and a mixture of air plus perfume plus helium plasmas. Indeed, the effect of excitation in the corona discharge of the plasmas in Fig. 7.6 is clear, especially before and after adding air and helium. For instance, the designated areas within circles from 1-4 for the spectrum of air indicate the spectral lines observed, or otherwise. Then on injecting the perfume to air at atmospheric pressure, these lines either appear, or increase or decrease in intensity. Remarkably, in the region labelled circle-3 at ~5.60 nm range in Fig. 7.6, there are no features in neither the spectra of plasma of air (black line), nor air plus helium (blue line); however, the plasma of air at atmospheric pressure with perfume allows observation of this transition, which can be assigned to the molecular transition of N<sub>2</sub> (B-A). On the other hand, on diluting this mixture of air and perfume with the addition of helium, the intensity of the N<sub>2</sub> band decreases. Broadly, the development in the spectra observed allows us to conclude that helium plasma can used to identify transitions or reduce the intensity of some lines, or we can depend on air at atmospheric pressure as a means to detect and explore elements and transitions.

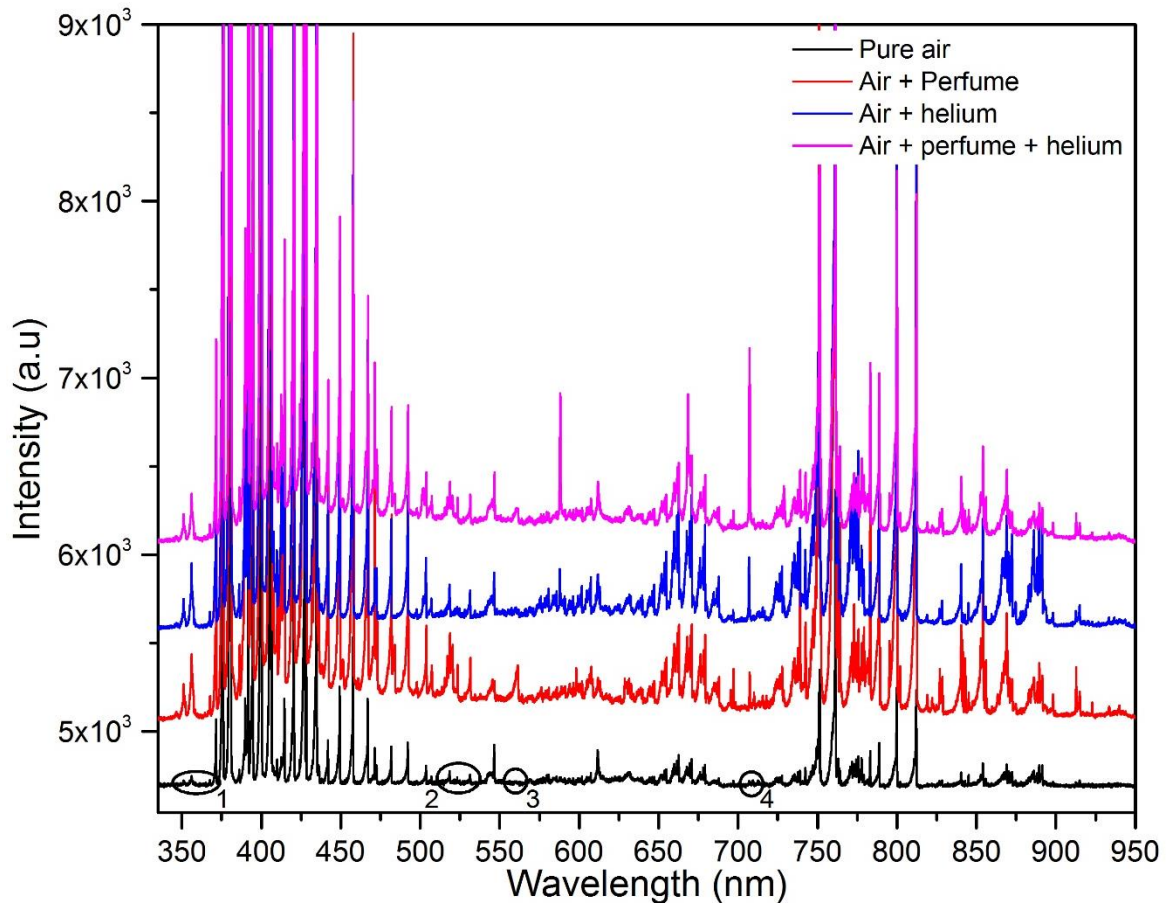


Figure 7.6: Development of the spectra for atmospheric pressure glow discharges of different cases of plasma; dry air, air plus perfume, air plus helium, and a mixture of air plus perfume and helium. Examples of some of the transitions observed, or otherwise, in the air plasma spectrum are highlighted by black circles 1-4, which become either less or more intense on mixing with perfume and helium at room temperature and using corona discharges.

## 7.4 General observations and plan

Optical emission spectroscopy was used in the UV, visible and NIR regions as a diagnostic of atmospheric pressure air with perfume and helium. Corona discharge has been employed for this purpose using a negative polarity voltage at room temperature. Some of the key points that we realized in this experiment are as follows:

- One of the main reasons the atmospheric pressure plasma is a complicated challenge is due to the lack of knowledge regarding the fundamental properties of atmospheric pressure glow discharges (APGDs).
- A major challenge that we faced during these experiments was in initiating the discharge in atmospheric pressure air, where numerous attempts were required before gaining a stable discharge.
- Arcing occurred when mixing atmospheric pressure air with perfume, and the strong spark in the cell that resulted in repeated arcing with each attempt at achieving a stable discharge in the cell before such was actually achieved.
- Helium gas was used to enhance and identify a number of the transitions that were either missing or observed in only weak intensity in other plasmas such as perfume and air at atmospheric pressure.
- The measured gas temperature does not noticeably increase when the discharge is applied.
- We can use this discharge mechanism of the plasma to understand the species generated in the air and other plasmas.
- This project needs further analysis and investigation to deconvolute the various – and numerous – emission transitions.
- We need to change the concentration of helium (pressure of He) with air or perfume and same thing for perfume (pressure of perfume), in order to see what happens for emitted lines features.
- The experiment needs to be repeated using a well-characterised material with a known concentration in air and helium.
- The use of simulations to determine the rotational and vibrational temperature.
- Different discharge currents are required to increase the chance to reaching higher electronic levels, allowing for the exploration of more transitions of the species present.

Finally, this study and results are evidence of using corona discharge and helium to detect another transitions or reduce their intensity, to be an answer on one of our questions in this thesis whether we are able to employ discharge or helium in different field.

# Chapter 8

## Summary and outlook

Whilst each results chapter includes its own set of conclusions, in this chapter we highlight the main points in this work with suggested future work. Broadly speaking, in this project a rich series of fluorescence spectra for  $^4\text{He}$  were investigated involving atomic and molecular transitions under different experimental conditions. Therefore, this thesis was divided into two sections:

The first section covers the data at cryogenic temperatures and we have found that; in this part new data at various pressures and temperatures have been reported that, to the best of our knowledge, have not been previously investigated, including in the region below SVP.

The spectroscopic investigation of localized atomic  $\text{He}^*$  and molecular excited helium  $\text{He}_2^*$  (excimers) states can be carried out using corona discharge as the excitation source in the gaseous and normal liquid phases. Intense fluorescence spectroscopy in the visible and near infrared regions was observed due to transitions between electronically excited states, and showed the rotationally-resolved  $d^3\Sigma_u^+ \rightarrow b^3\Pi_g$  and  $D^1\Sigma_u^+ \rightarrow B^1\Pi_g$  transitions of  $\text{He}_2^*$ . We also observed fluorescence from the  $3s^3S \rightarrow 2p^3P$  and  $3s^1S \rightarrow 2p^1P$  atomic transitions ( $\text{He}^*$ ). Spectra were recorded at 3.8, 4.0, 4.5 and 5.0 K over a range of pressures from 0.1–6.0 bar.

The analysis of the observed shifts, widths and intensity of molecular bands show a distinct difference in the gradients of the coefficients of these parameters for each given isotherm between the gas phase and liquid phase. Remarkably, similar behaviour was observed for the analysis of atomic lines. This abrupt change in lineshifts and linewidths with pressure that occurred by crossing the SVP curve of helium was indicative of the change in structure of the helium environment around the  $\text{He}^*$  and  $\text{He}_2^*$  species. This provides evidence as to the linear superimposition of the two different contributions to the emission lines, and enabled us to disentangle those contributions as arising from the existence of  $\text{He}^*$  or  $\text{He}_2^*$  emitters residing in different environments: (i) cold emitter

resides in a solvated shell of helium, (ii) hot emitter existing in a gas pocket in normal liquid helium, providing new insight into solvation phenomena at the nanoscale.

A further interesting observation was that inhibition of the free rotation of molecule was identified at pressures and temperatures in the region below the saturated vapor pressure (SVP) of helium (vapor phase), i.e., before helium liquefies. This could be an indicator of the high sensitivity of the  $\text{He}_2^*$ -He interaction more than that of the He-He interaction, and for the  $\text{He}^*$  emitter the interaction of  $\text{He}^*$ -He is stronger than for the He-He interaction. Consequently, clusters around the  $\text{He}^*$  or  $\text{He}_2^*$  emitters were expected to form below the SVP curve region of helium upon increasing the pressure. This study will contribute to a better understanding of collisional processes in different phases, including studies that are relevant to an understanding of microsolvation

The set of cryogenic systems in this experiment needs further development to increase cooling power, enabling us to obtain temperatures lower than 3.5 K and allowing the investigation of the superfluidity of helium and the transitions in this regime. More data are needed to elucidate the gap in the data when crossing the region of the SVP curve of helium (see Fig. 4.1) to determine the pressure and temperature conditions favouring clusters formation with high precision.

Simulation is also required to simulate transitions by the different emitters in the cryogenic cell to determine the rotational temperature of molecules and to distinguish between different contributions obtained for these transitions. Additionally, calculations of the mobility of electrons in liquid helium represent another target for future work.

The second part of this thesis was the room temperature experiment. As a further advantage of the application of the corona discharge technique, it was employed to form plasmas from pure air, an unspecified perfume and helium. The idea here was to collect the spectra of these substances separately, then after mixing them with helium. After that, a comparison between these spectra was carried out to explore and understand some of the emitting species generated in this mixture of plasmas at atmospheric pressure for the first time.

Some transitions in these spectra disappeared after injecting helium into the discharge region; by contrast, other transitions became either stronger or weaker with helium. As a result, helium gas can be used to enhance and identify a number of the transitions that were either missing or observed only weakly in other plasmas such as perfume and air

at atmospheric pressure for the first time. Molecular transitions of  $N_2$  (C $\rightarrow$ B) and  $N_2^+$  (B $\rightarrow$ X) and spectral atomic lines of N, H, O, Ar I and He I were observed in spectra at room temperature.

A corona discharge at atmospheric pressure air coupled with optical emission spectroscopy can be employed in different environmental applications such as; a diagnostic means for various plasma sources, bio-medical and explosive detection. In medical aspect, it will be planned to collect several samples from breath of patients, then analyse emitted spectra of a mixture of the gas helium with breath of patients after applying corona discharge at atmospheric pressure air.

The idea of this experiment is new and was carried out over only a short period (due to lack of time), therefore it needs further analysis to disentangle and deconvolute the various – and numerous – spectral features.

Minor modifications to the equipment such as the gas inlet (perfume or any other material) enhances the ability to control the concentration of this gas at any given time.

# Publications

## 1- Excimers in the Lowest Rotational Quantum State in Liquid Helium

Luis Guillermo Mendoza-Luna, **Nagham M. K. Shiltagh**, Mark J. Watkins, Nelly Bonifaci, Frédéric Aitken, and Klaus von Haeften, *J. Phys. Chem. Lett.* 2016, 7, 4666–4670.

DOI: 10.1021/acs.jpcllett.6b02081

## 2- Atomic fluorescence emitted from a corona discharge in helium above and below saturated vapour pressure

**Nagham M. Shiltagh**, Luis G. Mendoza Luna, Mark J. Watkins, Stuart C. Thornton, and Klaus von Haeften, *Eur. Phys. J. D* (2018) 72: 5

DIO: org/10.1140/epjd/e2017-80322-4

## 3- Nucleation, solvation and boiling of helium excimer (D-B transition) clusters

**Nagham M. Shiltagh**, Luis G. Mendoza Luna, Mark J. Watkins, Stuart C. Thornton, and Klaus von Haeften, in writing process to be submitted to PRL

# Activities

- Contribution in the SDG conference, in University of Nottingham for period 6<sup>th</sup>-8<sup>th</sup> of January/ 2015, Contributed Talk entitled "**Observation of free rotation and pressure dependent line-broadening of single molecules in normal liquid helium**".
- Contribution in the SDGM2016 conference (RSC Spectroscopy and Dynamics Group Meeting 2016), in University of Warwick, 5<sup>th</sup> – 7<sup>th</sup> January 2016. Contributed poster entitled "**Excimer-cluster formation, solvation and boiling studied by rotationally resolved fluorescence spectroscopy in gaseous and liquid helium**".
- Contribution in the European conference on the Dynamics of Molecular Systems (UCM – MOLEC 2016), in Toledo (Spain), in September 11<sup>th</sup> – 16<sup>th</sup>, 2016. Contributed poster entitled "**Identification of phase transitions of a mixed system of electronically excited species and liquid helium by studying the pressure dependence of lineshift, linewidth and line intensity of visible and near infrared fluorescence**".

# Appendix A

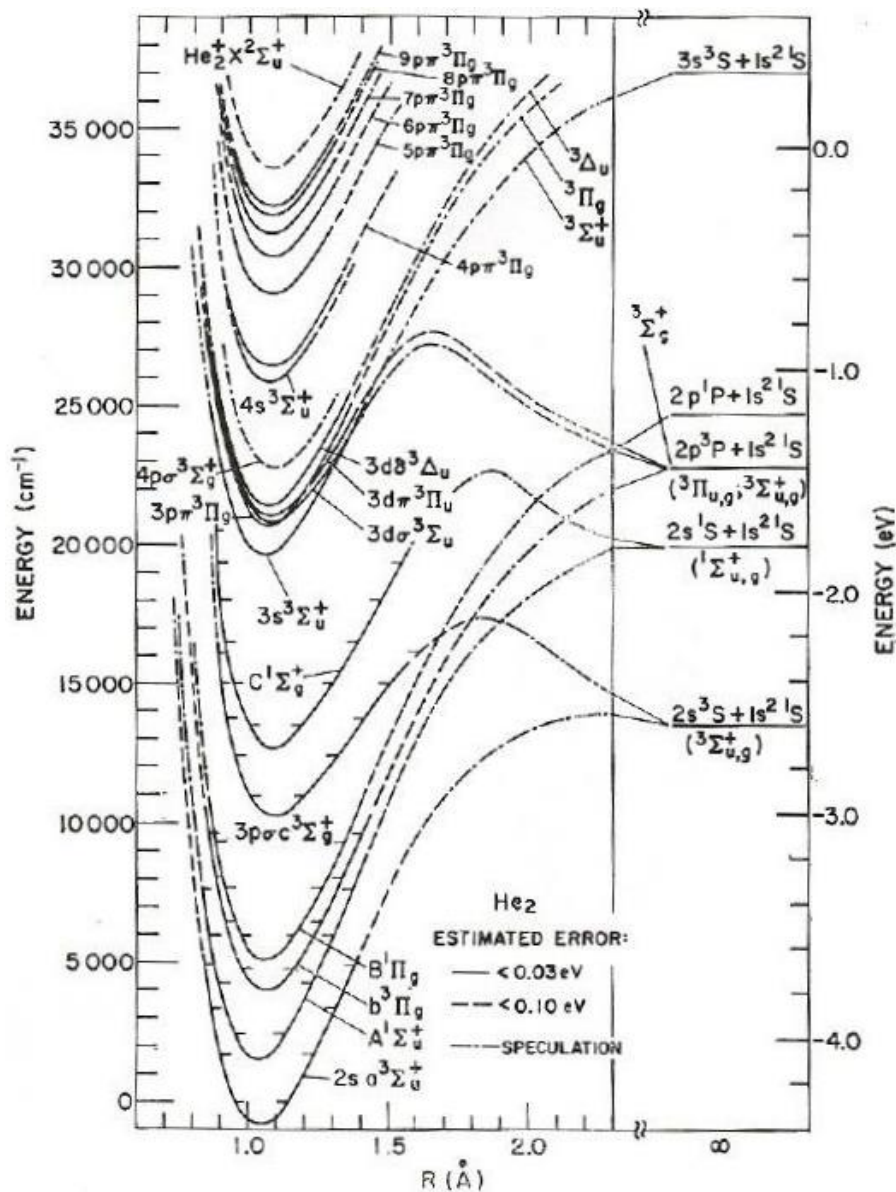
## Atomic and molecular transitions of helium

The atomic and molecular transitions of He\* and He<sub>2</sub>\* [203]

Transition	Wavelength or band-head (nm)
$e^3\Pi_g \rightarrow a^3\Sigma_u^+$ (0-0)	465.0
$d^3\Sigma_u^+ \rightarrow b^3\Pi_g$ (0-0)	640.1
$D^1\Sigma_u^+ \rightarrow B^1\Pi_g$ (0-0)	659.6
$f^3\Sigma_u^+ \rightarrow b^3\Pi_g$ (0-0)	596.0
$C^1\Sigma_g^+ \rightarrow A^1\Sigma_u$ (0-0)	911
$C^1\Sigma_g^+ \rightarrow A^1\Sigma_u$ (1-1)	930
$C^1\Sigma_g^+ \rightarrow A^1\Sigma_u$ (2-2)	950
$c^3\Sigma_g^+ \rightarrow a^3\Sigma_u$ (0-0)	919
$3^1P \rightarrow 2^1S$	501.6
$3^1D \rightarrow 2^1P$	667.8
$3^1S \rightarrow 2^1P$	728.1
$3^3P \rightarrow 2^3S$	388.9
$3^3D \rightarrow 2^3P$	587.6
$3^3S \rightarrow 2^3P$	706.1
$4^1P \rightarrow 2^1S$	396.5
$4^1D \rightarrow 2^1P$	492.2
$4^1S \rightarrow 2^1P$	504.8
$4^3P \rightarrow 2^3S$	318.8
$4^3D \rightarrow 2^3P$	447.2
$4^3S \rightarrow 2^3P$	471.3

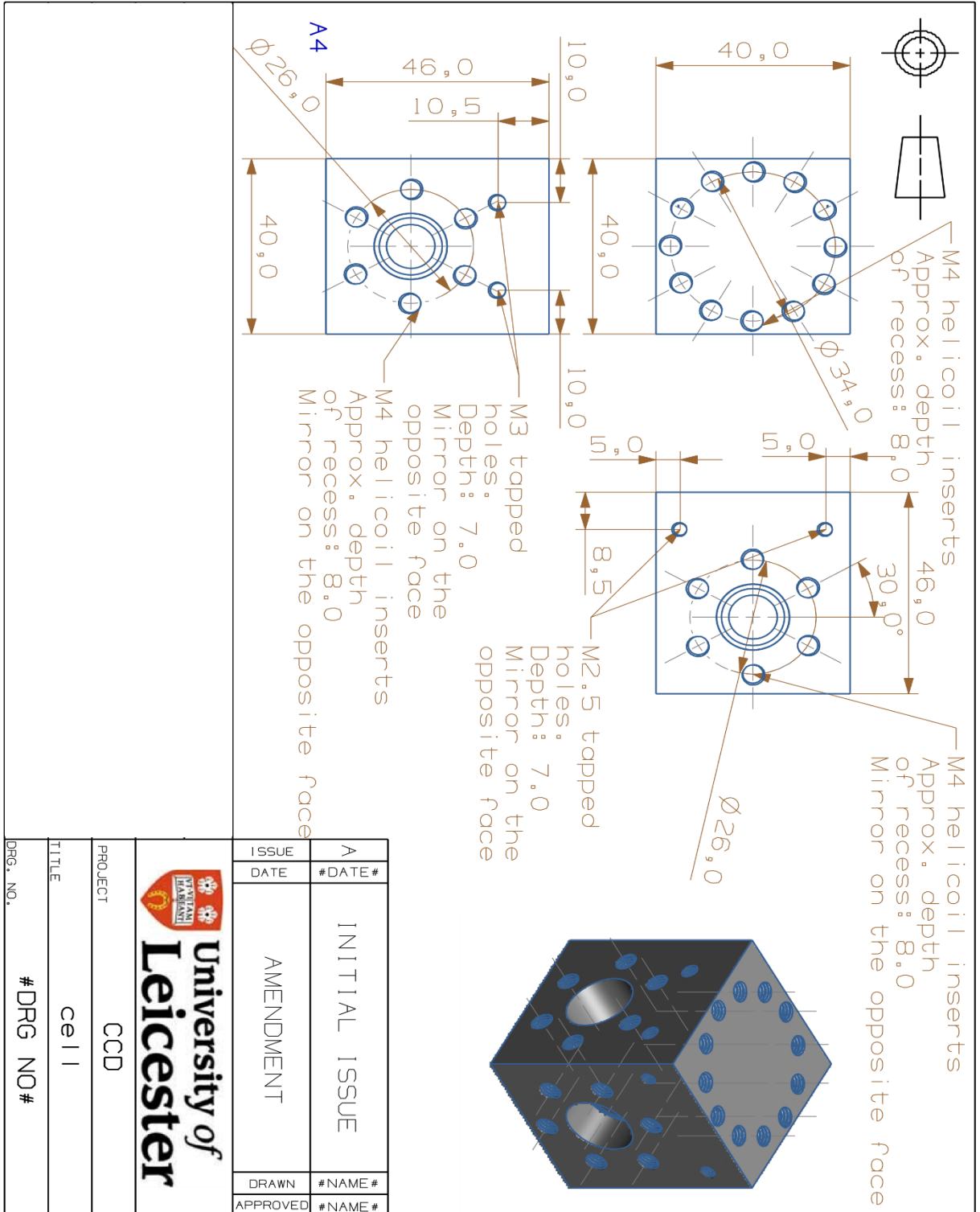
# Appendix B

Potential energy curves for states of He<sub>2</sub>. Reproduced from Fig. 1 of [204]



# Appendix C

Drawing of copper high pressure cell (low temperatures) [3]



# Appendix D-1

## Technical drawings of the tip bearer electrodes

0.28 mm diameter channel  
38,0  
M3 thread Length: 17  
SECTION B - B  
Edge filletting to 0.25 mm radius  
Ø 4,3  
1,5  
5,0  
5,5  
1,25  
Ø 3,0

A4

SCALE 1:1		DIMENSIONS ARE IN MILLIMETERS		SHEET 1 OF 1	
DRAWN	# NAME #	DATE	# DATE #	USED ON	# USED ON #
DESIGNED	# NAME #	DATE	# DATE #	DRAWING TYPE	# DRAWING TYPE #
CHECKED	# NAME #	DATE	# DATE #	MATERIAL	# MATERIAL #
APPROVED	# NAME #	DATE	# DATE #	FINISH	# FINISH #
DO NOT SCALE			TOLERANCE EXCEPT WHERE STATED OTHERWISE		
			± 0.1		
PROJECT		# PROJECT NAME #			
TITLE		tip-electrode-bearer			
DRG. NO.		# DRG NO #			

ISSUE	A	INITIAL ISSUE
DATE	# DATE #	
		AMENDMENT
DRAWN	# NAME #	
APPROVED	# NAME #	

# Appendix D-2

## Technical drawings of the flat electrodes

Technical drawing of a flat electrode. The drawing includes a 3D perspective view, a side view with dimensions, and a top view. Dimensions are as follows:

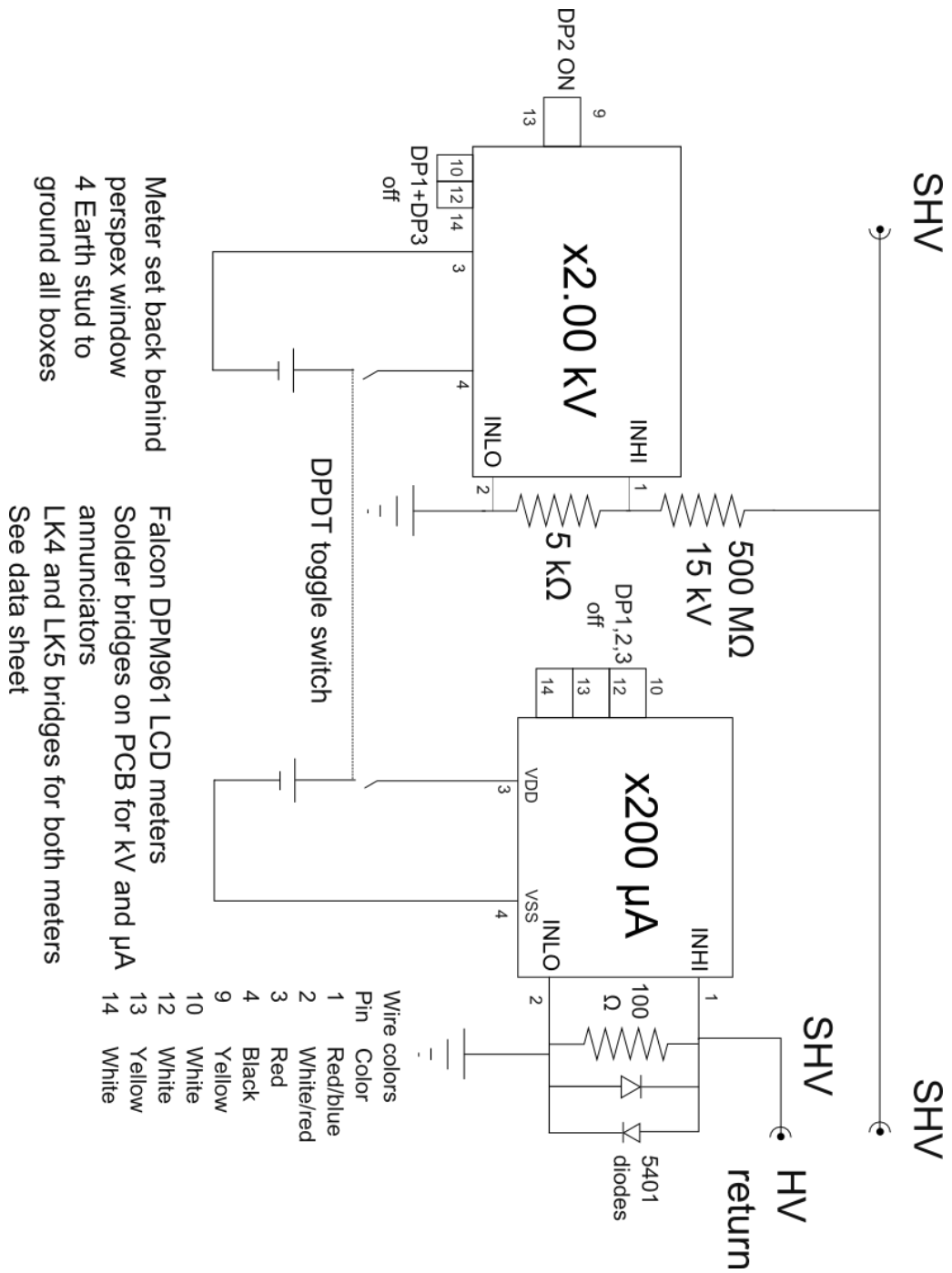
- Top diameter:  $\varnothing 8,0$
- Inner diameter:  $\varnothing 4,3$
- Outer diameter of the middle section:  $\varnothing 3,0$
- Length of the top section: 1,5
- Length of the middle section: 7,2
- Length of the bottom section: 2,8
- Total length: 37,0
- Thread: M3 thread, Length: 17
- Note: Filletted to 0.25 mm radius

**A4**

SCALE 1 : 1		DIMENSIONS ARE IN MILLIMETERS		SHEET 1 OF 1	
DRAWN	# NAME #	DATE	# DATE #	USED ON	# USED ON #
DESIGNED	# NAME #	DATE	# DATE #	DRAWING TYPE	# DRAWING TYPE #
CHECKED	# NAME #	DATE	# DATE #	MATERIAL	# MATERIAL #
APPROVED	# NAME #	DATE	# DATE #	FINISH	# FINISH #
DO NOT SCALE				TOLERANCE EXCEPT WHERE STATED OTHERWISE	
± 0,1					
PROJECT		# PROJECT NAME #			
TITLE		flat_electrode			
DRG. NO.		# DRG NO #			
ISSUE	A	DATE	# DATE #	INITIAL	ISSUE
AMENDMENT					
DRAWN	# NAME #	APPROVED	# NAME #		

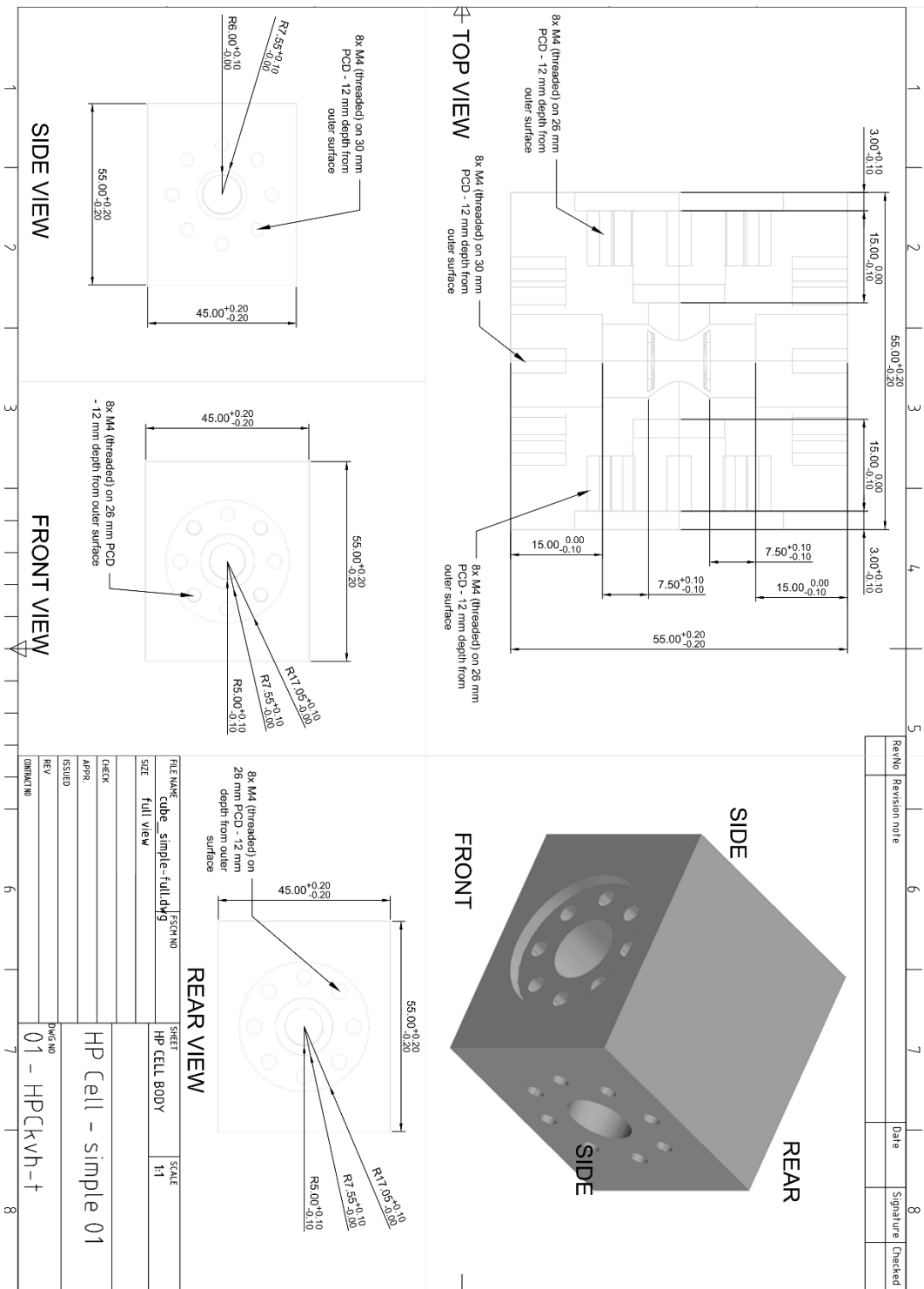
# Appendix E

## High-Voltage monitor



# Appendix F

## Drawing of stainless steel cell (room temperature)



# Appendix \_\_\_\_\_

## Appendix G

The standard error deviation data for the simulation treatment of the lineshifts for the atomic singlet and triplet transitions.

Singlet								Triplet							
Shift								Shift							
3.8 K		4.0 K		4.5 K		5.0 K		3.8 K		4.0 K		4.5 K		5.0 K	
P	STDE V	P	STDE V	P	STDE V	P	STDE V	P	STDE V	P	STDE V	P	STD EV	P	STD EV
0.19	0.03	0.14	0.00	0.21	0.00	0.22	0.00	0.19	0.03	0.14	0.01	0.21	0.00	0.22	0.00
0.51	0.00	0.33	0.01	0.35	0.02	0.37	0.01	0.51	0.00	0.33	0.01	0.35	0.01	0.37	0.01
0.79	0.03	0.42	0.01	0.46	0.02	0.49	0.00	0.79	0.06	0.42	0.01	0.46	0.01	0.50	0.01
1.30	0.01	0.58	0.01	0.66	0.03	0.63	0.00	1.30	0.08	0.58	0.01	0.66	0.01	0.63	0.00
1.95	0.04	0.65	0.01	0.81	0.02	0.81	0.02	1.95	0.07	0.65	0.01	0.81	0.01	0.81	0.01
1.99	0.05	0.72	0.01	0.92	0.03	0.91	0.02	1.99	0.06	0.72	0.01	0.92	0.02	0.91	0.01
2.08	0.05	0.95	0.02	1.34	0.04	1.00	0.02	2.08	0.08	0.95	0.06	1.34	0.04	1.00	0.01
2.18	0.06	1.43	0.00	1.38	0.04	1.58	0.09	2.18	0.08	1.43	0.08	1.38	0.04	1.58	0.00
2.29	0.04	1.78	0.02	1.40	0.04	1.59	0.09	2.29	0.08	1.77	0.08	1.40	0.04	1.59	0.00
2.77	0.04	2.10	0.07	2.79	0.11	1.60	0.09	2.77	0.08	2.10	0.06	2.78	0.06	1.00	0.00
3.00	0.07	2.28	0.05	2.99	0.13	3.55	0.22	3.00	0.08	2.28	0.07	2.99	0.05	3.55	0.01
3.04	0.14	2.41	0.06	3.44	0.15	3.66	0.22	3.04	0.06	2.41	0.07	3.44	0.04	3.66	0.02
3.29	0.13	2.61	0.11	3.69	0.20	5.58	0.40	3.29	0.04	2.61	0.05	3.69	0.01	5.58	0.06
		2.74	0.11	3.98	0.19					2.74	0.04	3.98	0.03	0.22	0.00
		3.07	0.14	4.08	0.20					3.07	0.04	4.08	0.03	0.38	0.01
		3.09	0.11	4.10	0.23					3.09	0.05	4.10	0.01	0.50	0.01
		3.13	0.11	4.28	0.16					3.13	0.06	4.28	0.00		
		3.22	0.17							3.22	0.03				
		3.23	0.16							3.23	0.03				
		3.28	0.16							3.28	0.03				
		3.34	0.15							3.34	0.05				
		3.38	0.18							3.38	0.02				
		3.40	0.21							3.40	0.05				
		3.40	0.15							3.40	0.05				
		3.44	0.13							3.44	0.03				
		3.46	0.19							3.46	0.02				
		3.83	0.19							3.83	0.04				
		3.93	0.21							3.93	0.01				

# Appendix H

The standard error deviation data for the simulation treatment of the linewidths for the atomic singlet and triplet transitions.

Singlet								Triplet							
Width								Width							
3.8 K		4.0 K		4.5 K		5.0 K		3.8 K		4.0 K		4.5 K		5.0 K	
P	STD EV	P	STD EV	P	STD EV	P	STD EV	P	STD EV	P	STD EV	P	STD EV	P	STD EV
0.19	0.01	0.14	0.00	0.21	0.03	0.22	0.05	0.19	0.03	0.14	0.06	0.21	0.03	0.22	0.02
0.51	0.03	0.33	0.04	0.35	0.05	0.37	0.07	0.51	0.01	0.33	0.03	0.35	0.01	0.37	0.00
0.79	0.33	0.42	0.01	0.46	0.01	0.49	0.03	0.79	0.08	0.42	0.02	0.46	0.01	0.50	0.03
1.30	0.39	0.58	0.07	0.66	0.12	0.63	0.01	1.30	0.09	0.58	0.08	0.66	0.11	0.63	0.08
1.95	0.47	0.65	0.07	0.81	0.09	0.81	0.05	1.95	0.13	0.65	0.07	0.81	0.13	0.81	0.15
1.99	0.48	0.72	0.03	0.92	0.04	0.91	0.08	1.99	0.13	0.72	0.09	0.92	0.14	0.91	0.15
2.08	0.47	0.95	0.35	1.34	0.40	1.00	0.06	2.08	0.12	0.95	0.08	1.34	0.08	1.00	0.15
2.18	0.48	1.43	0.43	1.38	0.39	1.58	0.19	2.18	0.14	1.43	0.11	1.38	0.08	1.58	0.12
2.29	0.51	1.78	0.46	1.40	0.41	1.59	0.19	2.29	0.13	1.77	0.12	1.40	0.08	1.59	0.11
2.77	0.49	2.10	0.51	2.79	0.57	1.60	0.22	2.77	0.14	2.10	0.14	2.78	0.15	1.00	0.11
3.00	0.54	2.28	0.55	2.99	0.57	3.55	0.86	3.00	0.14	2.28	0.15	2.99	0.15	3.55	0.16
3.04	0.61	2.41	0.56	3.44	0.63	3.66	0.65	3.04	0.17	2.41	0.15	3.44	0.19	3.66	0.19
3.29	0.61	2.61	0.56	3.69	0.69	5.58	1.22	3.29	0.18	2.61	0.15	3.69	0.18	5.58	0.25
		2.74	0.57	3.98	0.67					2.74	0.16	3.98	0.20	0.22	0.02
		3.07	0.58	4.08	0.92					3.07	0.18	4.08	0.20	0.38	0.00
		3.09	0.64	4.10	0.75					3.09	0.18	4.10	0.23	0.50	0.03
		3.13	0.69	4.28	0.90					3.13	0.17	4.28	0.19		
		3.22	0.75							3.22	0.19				
		3.23	0.76							3.23	0.20				
		3.28	0.79							3.28	0.19				
		3.34	0.64							3.34	0.18				
		3.38	0.85							3.38	0.20				
		3.40	0.57							3.40	0.19				
		3.40	0.66							3.40	0.18				
		3.44	0.76							3.44	0.19				
		3.46	0.86							3.46	0.19				
		3.83	0.56							3.83	0.20				
		3.93	0.78							3.93	0.22				

# Bibliography

---

## Bibliography

- [1] E. Andronikashvili, *A direct observation of two kinds of motion in liquid helium II*, in: Z.M. Galasiewicz (Ed.) *Helium 4*, Pergamon, Oxford, 1971, pp. 154-165.
- [2] J. Wilks, *An introduction to liquid helium*, Clarendon Press, Oxford, 1970.
- [3] L.G.M. Luna, FREE AND HINDERED-ROTATION OF HELIUM EXCIMERS IN LIQUID HELIUM VIA A BULK EXPERIMENT, Ph.D. thesis, University of Leicester, Leicester, UK, (2015) 45ff.
- [4] Z. Li., Corona discharge in liquid helium and dense gas in intense field: pre-breakdown, charge transport, emission spectroscopy, Ph.D. thesis, University of Joseph Fourier - Grenoble 1, France, (2008) 93.
- [5] *Heliox AC-V <sup>3</sup>He Refrigerator. System manual.*, *Heliox AC-V <sup>3</sup>He Refrigerator. System manual.* Oxford Instruments, (2005).
- [6] D. Min, W. Hailing, W. Qin, Y. Jianping, Dependences of Q-branch integrated intensity of linear-molecule pendular spectra on electric-field strength and rotational temperature and its potential applications, *Scientific Reports*, 6 (2016).
- [7] K. Von Haeften, T. Laarmann, H. Wabnitz, T. Möller, Bubble formation and decay in <sup>3</sup>He and <sup>4</sup>He clusters, *Physical Review Letters*, 88 (2002) 2334011-2334014.
- [8] Z.L. Li, N. Bonifaci, F. Aitken, A. Denat, K. Von Haeften, V.M. Atrazhev, V.A. Shkhatov, Spectroscopic investigation of liquid helium excited by a corona discharge: Evidence for bubbles and "red satellites", *EPJ Applied Physics*, 47 (2009) 22821-22821.
- [9] W.S. Dennis, E. Durbin, W.A. Fitzsimmons, O. Heybey, G.K. Walters, Spectroscopic identification of excited atomic and molecular states in electron-bombarded liquid helium, *Physical Review Letters*, 23 (1969) 1083-1086.
- [10] N.P.r. M. Hartmann, B. Sartakov, J. P. Toennies, and A. F. Vilesov, High resolution infrared spectroscopy of single SF<sub>6</sub> molecules in helium droplets. I. Size effects in <sup>4</sup>He droplets, *J. Chem. Phys.*, 110, No. 11 (1999) 5109-5123.
- [11] W. Vinen, *The physics of superfluid helium*, (2004).
- [12] S. Grebenev, M. Hartmann, M. Havenith, B. Sartakov, J.P. Toennies, A.F. Vilesov, The rotational spectrum of single OCS molecules in liquid <sup>4</sup>He droplets, *Journal of Chemical Physics*, 112 (2000) 4485-4495.

## Bibliography\_\_\_\_\_

- [13] B.G. Sartakov, J.P. Toennies, A.F. Vilesov, Infrared spectroscopy of carbonyl sulfide inside a pure  $^3\text{He}$  droplet, *J. Chem. Phys.*, 136 (2012) 134316.
- [14] G. Herzberg, *Molecular spectra and molecular structure., Spectra of diatomic molecules*, 2nd ed.. ed., Krieger, Malabar, Fla., 1950.
- [15] T.H.V. Nguyen, in, Grenoble Alpes, France, 2015
- [16] P. Scharlin, R. Battino, E. Silla, I. Tuñón, J.L. Pascual-Ahuir, Solubility of gases in water: Correlation between solubility and the number of water molecules in the first solvation shell, *Pure and Applied Chemistry*, 70 (1998) 1895-1904.
- [17] J. Wilks, *The Properties of Liquid and Solid Helium*, Oxford University Press, Science, 1967.
- [18] A.F. Borghesani, *Ions and electrons in liquid helium*, 2008.
- [19] J.P. Toennies, A.F. Vilesov, Superfluid Helium Droplets: A Uniquely Cold Nanomatrix for Molecules and Molecular Complexes, *Angewandte Chemie International Edition*, 43 (2004) 2622-2648.
- [20] K. Mendelssohn, Superfluids, *Science (New York, N.Y.)*, 127 (1958) 215.
- [21] L. Landau, Theory of the superfluidity of helium II, *Physical Review*, 60 (1941) 356-358.
- [22] D.M. Brink, S. Stringari, Density of states and evaporation rate of helium clusters, *Zeitschrift für Physik D Atoms, Molecules and Clusters*, 15 (1990) 257-263.
- [23] W. Bendiner, D. Elwell, H. Meyer, Properties of  $^3\text{He}$  near the critical point, *Physics Letters A*, 26 (1968) 421-422.
- [24] W.F. Vinen, Macroscopic quantum effects in superfluids, *Reports on Progress in Physics*, 31 (1968) 61-121.
- [25] W.F. Vinen, *Chapter I Vortex Lines in Liquid Helium II*, in: C.J. Gorter (Ed.) *Progress in Low Temperature Physics*, Elsevier, 1961, pp. 1-57.
- [26] L. Tisza, Transport Phenomena in Helium II, *Nature*, 141 (1938) 913.
- [27] A.C. Hollis-Hallett, Oscillating Disc Experiments in Liquid Helium II, *Proceedings of the Physical Society. Section A*, 63 (1950) 1367.
- [28] K. Von Haeften, T. Laarmann, H. Wabnitz, T. Möller, Observation of atomiclike electronic excitations in pure  $^3\text{He}$  and  $^4\text{He}$  clusters studied by fluorescence excitation spectroscopy, *Physical Review Letters*, 87 (2001) 153403/153401-153403/153404.

## Bibliography

---

- [29] J.P. Toennies, A.F. Vilesov, *Spectroscopy of atoms and molecules in liquid helium*, in: *Annual Review of Physical Chemistry*, 1998, pp. 1-41.
- [30] B. Tabbert, H. Gunther, G. Putlitz, Optical investigation of impurities in superfluid  $^4\text{He}$ , *Journal of Low Temperature Physics*, 109 (1997) 653-707.
- [31] A.N. Gerritsen, J. Koolhaas, X-ray ionization in liquefied gases, *Physica*, 10 (1943) 49-56.
- [32] M. Hartmann, R.E. Miller, J.P. Toennies, A.F. Vilesov, Rotationally Resolved Spectroscopy of  $\text{SF}_6$  in Liquid Helium Clusters: A Molecular Probe of Cluster Temperature, *Phys. Rev. Lett.*, 75 (1995) 1566-1569.
- [33] J. Harms, M. Hartmann, B. Sartakov, J.P. Toennies, A.F. Vilesov, High resolution infrared spectroscopy of single  $\text{SF}_6$  molecules in helium droplets. II. the effect of small amounts of  $^4\text{He}$  in large  $^3\text{He}$  droplets, *Journal of Chemical Physics*, 110 (1999) 5124-5136.
- [34] S. Grebenev, J.P. Toennies, A.F. Vilesov, Superfluidity within a small helium-4 cluster: The microscopic Andronikashvili experiment, *Science*, 279 (1998) 2083-2086.
- [35] J.P. Toennies, A.F. Vilesov, K.B. Whaley, Superfluid helium droplets: An ultracold nanolaboratory, *Physics Today*, 54 (2001) 31-37.
- [36] V. Kiryukhin, B. Keimer, R.E. Boltnev, V.V. Khmelenko, E.B. Gordon, Inert-gas solids with nanoscale porosity, *Physical Review Letters*, 79 (1997) 1774-1777.
- [37] V. Lebedev, P. Moroshkin, J.P. Toennies, A. Weis, Spectroscopy of the copper dimer in normal fluid, superfluid, and solid ( $^4\text{He}$ ), *J Chem Phys*, 133 (2010) 154508.
- [38] V.V. Khmelenko, S. Mao, A. Meraki, S.C. Wilde, P. McColgan, A.A. Pelmenev, R.E. Boltnev, D.M. Lee, Luminescence of oxygen atoms stimulated by metastable helium at cryogenic temperatures, *Physical Review Letters*, 111 (2013).
- [39] E. Popov, J. Eloranta, Copper dimer interactions on a thermomechanical superfluid  $^4\text{He}$  fountain, *Journal of Chemical Physics*, 142 (2015).
- [40] J.B. Birks, Excimers, *Reports on Progress in Physics*, 38 (1975) 903.
- [41] S.L. Fiedler, J. Eloranta, Interaction of helium rydberg state atoms with superfluid helium, *Journal of Low Temperature Physics*, 174 (2014) 269-283.
- [42] J.J. Hopfield, Excimer of He, *Phys. Rev.*, 35 (1930a) 1133.
- [43] J.J. Hopfield, Excimer of He, *Astrophys.*, 72 (1930b) 133.

## Bibliography\_\_\_\_\_

- [44] J.J. Hopfield, Absorption and emission spectra in the region 600-1100 [9], *Physical Review*, 35 (1930) 1133-1134.
- [45] A.V. Benderskii, R. Zadoyan, N. Schwentner, V.A. Apkarian, Photodynamics in superfluid helium: Femtosecond laser-induced ionization, charge recombination, and preparation of molecular Rydberg states, *Journal of Chemical Physics*, 110 (1999) 1542-1557.
- [46] D.N. McKinsey, W.H. Lippincott, J.A. Nikkel, W.G. Rellergert, Trace detection of metastable helium molecules in superfluid helium by laser-induced fluorescence, *Physical Review Letters*, 95 (2005) 111101.
- [47] W.G. Rellergert, S.B. Cahn, A. Garvan, J.C. Hanson, W.H. Lippincott, J.A. Nikkel, D.N. McKinsey, Detection and imaging of He<sub>2</sub> molecules in superfluid helium, *Physical Review Letters*, 100 (2008).
- [48] W. Guo, M. La Mantia, D.P. Lathrop, S.W. Van Sciver, Visualization of two-fluid flows of superfluid helium-4, *Proceedings of the National Academy of Sciences of the United States of America*, 111 (2014) 4653-4658.
- [49] J. Gao, A. Marakov, W. Guo, B.T. Pawlowski, S.W. Van Sciver, G.G. Ihas, D.N. McKinsey, W.F. Vinen, Producing and imaging a thin line of He<sub>2</sub><sup>\*</sup> molecular tracers in helium-4, *Review of Scientific Instruments*, 86 (2015) 093904.
- [50] J.C. Hill, O. Heybey, G.K. Walters, Evidence of metastable atomic and molecular bubble states in electron-bombarded superfluid liquid helium, *Physical Review Letters*, 26 (1971) 1213-1216.
- [51] J.W. Keto, F.J. Soley, M. Stockton, W.A. Fitzsimmons, Dynamic properties of neutral excitations produced in electron-bombarded superfluid helium. I. The He(2 S<sub>3</sub>) and He<sub>2</sub>(a 3) atomic and molecular metastable states, *Physical Review A*, 10 (1974) 872-886.
- [52] J.W. Keto, F.J. Soley, M. Stockton, W.A. Fitzsimmons, Dynamic properties of neutral excitations produced in electron-bombarded superfluid helium. II. Afterglow fluorescence of excited helium molecules, *Physical Review A*, 10 (1974) 887-896.
- [53] F.J. Soley, W.A. Fitzsimmons, Pressure shifts and quenching of atomic and molecular states produced in electron-bombarded liquid helium, *Phys. Rev. Lett*, 32 (1974) 988-991.
- [54] L.G. Mendoza-Luna, M. Watkins, K.V. Haefen, N. Bonifaci, F. Aitken, Line broadening of excimers bound to the surface of 4He clusters investigated by comparison with corona discharge excitation spectra, *European Physical Journal D*, 67 (2013).

## Bibliography\_\_\_\_\_

- [55] Z. Li, N. Bonifaci, A. Denat, V.M. Atrazhev, Negative Corona discharge in liquid Helium, *IEEE Transactions on Dielectrics and Electrical Insulation*, 13 (2006) 624-630.
- [56] Z.L. Li, N. Bonifaci, F. Aitken, A. Denat, K. Von Haeften, V.M. Atrazhev, V.A. Shakhmatov, Luminescence from liquid helium excited by corona discharges, *IEEE Transactions on Dielectrics and Electrical Insulation*, 16 (2009) 742-750.
- [57] Z.L. Li, N. Bonifaci, A. Denat, V.A. Shakhmatov, K. Von Haeften, V.M. Atrazhev, Atomic and molecular spectra emitted by normal liquid  $^4\text{He}$  excited by corona discharge, *Fizika Nizkikh Temperatur (Kharkov)*, 37 (2011) 484-490.
- [58] N. Bonifaci, F. Aitken, H. Van Nguyen, V.M. Atrazhev, K. Von Haeften, R. Rincon, Shape of atomic lines emitted by cryoplasma in helium, *Journal of Physics: Conference Series*, 397 (2012).
- [59] L.G. Mendoza-Luna, N.M.K. Shiltagh, M.J. Watkins, N. Bonifaci, F. Aitken, K. Von Haeften, Excimers in the Lowest Rotational Quantum State in Liquid Helium, *Journal of Physical Chemistry Letters*, 7 (2016) 4666-4670.
- [60] J.M. Hollas, *Modern spectroscopy*, 4th ed., ed., Wiley, Chichester, 2004.
- [61] K.T. Hecht, *Rigid Rotators: Molecular Rotational Spectra*, in: K.T. Hecht (Ed.) *Quantum Mechanics*, Springer New York, New York, NY, 2000, pp. 152-158.
- [62] G. Herzberg, *Molecular spectra and molecular structure, Infrared and raman spectra of polyatomic molecules*, Krieger, Malabar, Fla., 1945.
- [63] S. Gasiorowicz, *Quantum physics*, 3rd ed., ed., Wiley, Hoboken, N.J., 2003.
- [64] D.A. McQuarrie, *Quantum chemistry*, University Science Oxford University Press, Mill Valley, Calif. : Oxford, 1983.
- [65] C.M. Surko, G.J. Dick, F. Reif, W.C. Walker, Spectroscopic study of liquid helium in the vacuum ultraviolet, *Physical Review Letters*, 23 (1969) 842-846.
- [66] C.M. Surko, R.E. Packard, G.J. Dick, F. Reif, Spectroscopic study of the luminescence of liquid helium in the vacuum ultraviolet, *Physical Review Letters*, 24 (1970) 657-659.
- [67] B.P. Straughan, S. Walker, *Molecular Quantum Numbers of Diatomic Molecules*, in: B.P. Straughan, S. Walker (Eds.) *Spectroscopy: Volume Three*, Springer Netherlands, Dordrecht, 1976, pp. 1-25.

## Bibliography\_\_\_\_\_

- [68] J.M. Brown, *Rotational spectroscopy of diatomic molecules*, Cambridge University Press, Cambridge  
New York, 2003.
- [69] M. Goldman, A. Goldman, R.S. Sigmond, The corona discharge, its properties and specific uses, *Pure and Applied Chemistry*, 57 (1985) 1353-1362.
- [70] F. W. Peek, *Dielectric phenomena in high-voltage engineering*, Third edition ed., McGraw-Hill Book Company, Inc, New York,, 1930.
- [71] R. Payling, D. Jones, A. Bengtson, *Glow discharge optical emission spectrometry*, J. Wiley, Chichester, 1997.
- [72] R.S. Mulliken, The Rydberg States of Molecules. Ia Parts I-VIb, *Journal of the American Chemical Society*, 86 (1964) 3183-3197.
- [73] R.S. Mulliken, The Rydberg States of Molecules. VII, *Journal of the American Chemical Society*, 91 (1969) 4615-4621.
- [74] F.L. Arnot, M.B. M'Ewen, The Formation of Helium Molecules, *Proceedings of the Royal Society of London. Series A, Mathematical and Physical Sciences* (1934-1990), 166 (1938) 543-551.
- [75] F.L. Arnot, M.B. M'Ewen, The Formation of Helium Molecules. II, *Proceedings of the Royal Society of London. Series A, Mathematical and Physical Sciences* (1934-1990), 171 (1939) 106-120.
- [76] O. Tuxen, Massenspektrographische Untersuchungen negativer Ionen in Gasentladungen bei hohen Drucken, *Zeitschrift für Physik*, 103 (1936) 463-484.
- [77] J.S. Cohen, Diabatic-states representation for  $\text{He}^*(n3)+ \text{He}$  collisions, *Physical Review*, A 13 (1976) 86-98.
- [78] N.M. Shiltagh, L.G. Mendoza Luna, M.J. Watkins, S.C. Thornton, K. von Haefen, Atomic fluorescence emitted from a corona discharge in helium above and below saturated vapour pressure, *The European Physical Journal D*, 72 (2018) 5.
- [79] M.L. Ginter, The Spectrum and Structure of the  $\text{He}_2$  Molecule Part III. Characterization of the Triplet States Associated with the UAO's  $3s$  and  $2p\pi$ , *J. Mol. Spectrosc*, 18 (1965) 321-343.
- [80] M.L. Ginter, The spectrum and structure of the  $\text{He}_2$  molecule: Part II. Characterization of the Singlet States Associated with the UAO's  $3s$  and  $2p\pi$ , *J. Mol. Spectrosc*, 17 (1965) 224 – 239.

## Bibliography\_\_\_\_\_

[81] M. Rosenblit, J. Jortner, Dynamics of the formation of an electron bubble in liquid helium, *Physical Review Letters*, 75 (1995) 4079-4082.

[82] J. Eloranta, V.A. Apkarian, A time dependent density functional treatment of superfluid dynamics: Equilibration of the electron bubble in superfluid 4He, *The Journal of Chemical Physics*, 117 (2002) 10139-10150.

[83] A.P. Hickman, W. Steets, N.F. Lane, Nature of excited helium atoms in liquid helium: A theoretical model *The journal of chemical physics* 12 (1975) 3705-3717.

[84] A.P. Hickman, N.F. Lane, Localized excited states of helium in liquid helium, *Physical review letters.*, 26 (1971) 1216-1219

[85] P.D. Goldan, J.A. Berlande, L. Goldstein, Microwave Interactions in Cryogenic Afterglow Plasmas, *Physical Review Letters*, 13 (1964) 182-184.

[86] P.D. Goldan, L. Goldstein, Electron Interactions in Cryogenic Helium Plasmas, *Physical Review*, 138 (1965) A39-A44.

[87] F.I. Y., P.P.L.J. Lett., Diffusion of metastable helium atoms in a cryogenic plasma, *JETP Lett.*, –USSR 3 (1966 ) 254–256.

[88] K. Tomohiro, M. Kazuo, K. Hiroshi, Measurement of a Decaying Plasma with Cryogenic Electron Temperature in 4.2 K Helium Gases, *Japanese Journal of Applied Physics*, 25 (1986) L841.

[89] K. Minami, H. Mitera, S. Takeda, Improved microwave cavity measurements for the density and collision frequency in decaying plasmas, *Japanese Journal of Applied Physics*, 26 (1987) 1153-1158.

[90] K. Minami, S. Watanabe, W. Qin, F. Tomimoto, S. Kuwabara, M.R. Amin, K. Kato, T. Satow, Proposal of cryogenic plasmas in liquid helium ii, *Japanese Journal of Applied Physics*, 34 (1995) 271-276.

[91] A.L. Woodcraft, An introduction to cryogenics, :<http://woodcraft.lowtemp.org>, (2007).

[92] G.K. White, *Experimental techniques in low-Temperature Physics*, third ed., Clarendon Press Oxford, 1979.

[93] H.D. Baehr, K. Stephan, *Heat and mass transfer: Second, revised edition*, 2006.

[94] A. Beiser, *Concepts of modern physics*, 6th ed., McGraw-Hill, London, 2002.

[95] G.K. White, *Experimental techniques in low-temperature physics*, 4th ed.. ed., Clarendon Press, Oxford, 2002.

## Bibliography\_\_\_\_\_

- [96] M. Spivak, *Calculus*, Corrected 3rd ed.. ed., Cambridge University Press, Cambridge, 2006.
- [97] in, Omega Engineering, <https://www.omega.co.uk/pptst/PXM409-USBH.html#description>.
- [98] A. Mandru., Tungsten Tip Preparation, [www.phy.ohiou.edu/~asmith/lab/stm-tip-prep.pdf](http://www.phy.ohiou.edu/~asmith/lab/stm-tip-prep.pdf), (2011).
- [99] R. Coelho, J. Debeau, Properties of the tip-plane configuration, *Journal of Physics D: Applied Physics*, 4 (1971) 1266.
- [100] Macor, Machinable glass ceramic for industrial applications., [http://www.professionalplastics.com/professionalplastics/content/downloads/Macor\\_Brochure\\_2014.pdf](http://www.professionalplastics.com/professionalplastics/content/downloads/Macor_Brochure_2014.pdf), (2015).
- [101] in: MACOR® Machineable Glass Ceramic, <https://www.multi-lab.co.uk/ceramics/macor.htm>, 2014.
- [102] D. Malacara, *Physical optics and light measurements*, Academic Press, Boston, Mass. London, 1988.
- [103] M. Czerny, V. Plettig, ?ber den Astigmatismus bei Spiegelspektrometern. II, *Zeitschrift f?r Physik*, 63 (1930) 590-595.
- [104] in, *Temperature Measurement and Control Catalog. Lake Shore Cryotronics Product Catalog*. Lake Shore Cryotronics, 2013.
- [105] in, Ortech Advanced Ceramics/Alumina Oxide Ceramics Al<sub>2</sub>O<sub>3</sub>. <http://www.ortechceramics.com/>, 2015
- [106] J.M.V. H. G. Kuhn, Radiation width and resonance broadening in helium, *Proc. R.Soc.*, A 277 (1964) 297-311.
- [107] J.M. Vaughan, Self broadening and radiation width in the singlet spectrum of helium, *Proc. R. Soc.*, A 295 (1966) 164-181.
- [108] A.R. Malvern, J.L. Nicol, D.N. Stacey, The effects of excitation mechanisms of spectral profiles in helium, *J. Phys. B: At. Mol. Phys*, 7 (1974) L518-L521.
- [109] A.R. Malvern, R. Damaschini, J. Verges, The pressure broadening of the helium 2.06  $\mu\text{m}$  (2 1P- 2 1S) line, *J. Phys. Lett. A*, 69 (1978) 4-5.

## Bibliography\_\_\_\_\_

- [110] A. Atiola, B.C. Gibson-Wilde, A.C. Lindsay, J.L. Nicol, I.B. Whittingham, Temperature dependence of self-broadening at low densities in singlet spectral lines of helium, *J. Phys. B: At. Mol. Opt. Phys.*, 21 (1988) 249-257.
- [111] A.C. Lindsay, J.L. Nicol, D.N. Stacey, P.E.G. Baird, Absorption measurements of resonance broadening in helium, *Journal of Physics B: Atomic, Molecular and Optical Physics*, 22 (1989) L303-L307.
- [112] J.F. Su, J.L. Nicol, Pressure shift of the helium triplet line  $\lambda 706.5$  nm, *Journal of Physics B: Atomic, Molecular and Optical Physics*, 26 (1993) 255-260.
- [113] K. Von Haeften, K. Fink, A quantum chemical approach towards the electronically excited states of helium clusters, *European Physical Journal D*, 43 (2007) 121-124.
- [114] K.D. Closser, M. Head-Gordon, Ab initio calculations on the electronically excited states of small helium clusters, *Journal of Physical Chemistry A*, 114 (2010) 8023-8032.
- [115] K. Von Haeften, T. Laarmann, H. Wabnitz, T. Möller, K. Fink, Size and isotope effects of helium clusters and droplets: Identification of surface and bulk-volume excitations, *Journal of Physical Chemistry A*, 115 (2011) 7316-7326.
- [116] K.D. Closser, O. Gessner, M. Head-Gordon, Simulations of the dissociation of small helium clusters with ab initio molecular dynamics in electronically excited states, *Journal of Chemical Physics*, 140 (2014).
- [117] K.D. Closser, Q. Ge, Y. Mao, Y. Shao, M. Head-Gordon, Superposition of Fragment Excitations for Excited States of Large Clusters with Application to Helium Clusters, *Journal of Chemical Theory and Computation*, 11 (2015) 5791-5803.
- [118] M. Dehdashti-Jahromi, H. Farrokhpour, Structures and Photoelectron Spectra of Helium Nano Clusters, *Journal of Physical Chemistry C*, 119 (2015) 18641-18649.
- [119] H. Farrokhpour, M. Dehdashti Jahromi, Absorption spectra of small helium Nano clusters ( $4\text{He}_n$ ;  $n = 2-29$ ) and characterization of their low-lying excited states, *Journal of Molecular Liquids*, 230 (2017) 190-199.
- [120] N. Bonifaci, F. Aitken, V.M. Atrazhev, S.L. Fiedler, J. Eloranta, Experimental and theoretical characterization of the long-range interaction between  $\text{He}^*(3s)$  and  $\text{He}(1s)$ , *Physical Review A*, 85 (2012) 042706.
- [121] S.L. Guberman, W.A. Goddard III, On the origin of energy barriers in the excited states of  $\text{He}_2$ , *Chemical Physics Letters*, 14 (1972) 460-465.

## Bibliography

---

- [122] S.L. Guberman, W.A. Goddard III, Nature of the excited states of He<sub>2</sub>, *Physical Review A*, 12 (1975) 1203-1221.
- [123] D. Vrinceanu, S. Kotochigova, H.R. Sadeghpour, Pressure broadening and shift of He(2 3P<sub>0,1,2</sub>)-He(2 3S) lines, *Physical Review A - Atomic, Molecular, and Optical Physics*, 69 (2004) 227141-2271410.
- [124] N.F. Allard, B. Deguilhem, F.X. Gadea, N. Bonifaci, A. Denat, Analysis of the He(3 3S)-He(2 3P) line profile obtained in dense helium plasma, *EPL*, 88 (2009) 53002.
- [125] N.F. Allard, N. Bonifaci, A. Denat, Study of the parameters of the He(3 3S)-He(2 3P) line, *European Physical Journal D*, 61 (2011) 365-372.
- [126] N.F. Allard, B. Deguilhem, A. Monari, F.X. Gadéa, J.F. Kielkopf, Blue satellites on He lines due to He-He collisions, *Astron. Astrophys.*, A 70 (2013) 559.
- [127] J.F. Delpech, J. Boulmer, F. Devos, Transitions between Rydberg levels of helium induced by electron collisions, *Physical Review Letters*, 39 (1977) 1400-1403.
- [128] J. Stevefelt, J.M. Pouvesle, A. Bouchoule, Reaction kinetics of a high pressure helium fast discharge afterglow, *The Journal of Chemical Physics*, 76 (1982) 4006-4015.
- [129] D.R. Bates, Rydberg dissociative recombination in a helium afterglow, *Journal of Physics B: Atomic and Molecular Physics*, 17 (1984) 2363-2372.
- [130] J.F. Su, J.L. Nicol, Measurements of self broadening of the triplet line  $\lambda 706.5$  nm in helium, *Journal of Physics B: Atomic, Molecular and Optical Physics*, 23 (1990) 2215-2222.
- [131] P. Moroshkin, V. Lebedev, A. Weis, Spectroscopy of alkali-metal atoms in dense supercritical 4He at low temperatures, *Phys. Rev.*, A 87 (2013) 022513.
- [132] F. Ferreira Da Silva, P. Waldburger, S. Jaksch, A. Mauracher, S. Denifl, O. Echt, T.D. Märk, P. Scheier, On the size of ions solvated in helium clusters, *Chem. Eur. J.*, 15 (2009) 7101-7108.
- [133] S. Denifl, F. Zappa, I. Mähr, J. Lecointre, M. Probst, T.D. Märk, P. Scheier, Mass spectrometric investigation of anions formed upon free electron attachment to nucleobase molecules and clusters embedded in superfluid helium droplets, *Phys. Rev. Lett.*, 97 (2006) 043201.
- [134] E. Coccia, F. Marinetti, E. Bodo, F.A. Gianturco, Chemical solutions in a quantum solvent: Anionic electrolytes in 4He nanodroplets, *ChemPhysChem*, 9 (2008) 1323-1330.

## Bibliography\_\_\_\_\_

- [135] F.A. Gianturco, E. Coccia, F. Marinetti, E. Bodo, Anionic microsolvation in helium droplets: O H- (He)N structures from classical and quantum calculations, *J. Chem. Phys.*, 128 (2008) 134511.
- [136] F. Marinetti, E. Yurtsever, F.A. Gianturco, HCHO in a cold, quantum solvent: Size and shape of its "Bubbles" in 4He droplets from stochastic simulations, *J. Phys. Chem., A* 114 (2010) 9725-9732.
- [137] V.D.A. Young, *Phase Diagrams of the Elements*, University of California Press, Berkeley, CA (USA), . XI, 291 105 (1991).
- [138] W.H. Press, S.A. Teukolsky, V. Wiliam T, B.P. Flannery, *Numerical recipes in C : the art of scientific computing*, 2nd ed., Cambridge University Press, Cambridge, 1992.
- [139] M. Wojdyr, Fityk: A general-purpose peak fitting program, *J. Appl. Cryst.*, 43, Ver. 0.9.8 (2010) 1126-1128.
- [140] O.J.W.F. Kardaun, *Classical methods of statistics: With applications in fusion-oriented plasma physics*, 2005.
- [141] A. Kramida, Y. Ralchenko, J. Reader, a.N.A. Team., NIST Atomic Spectra Database, NIST Atomic Spectra Database (ver. 5), [Online]. Available: <http://physics.nist.gov/asd> [2015, January 7]. National Institute of Standards and Technology, Gaithersburg, MD., (2014).
- [142] E. Seifert, OriginPro 9.1: Scientific data analysis and graphing software - Software review, *Journal of Chemical Information and Modeling*, 54 (2014) 1552.
- [143] P.H. Zimmermann, J.F. Reichert, A.J. Dahm, Study of the electron spin resonance of negative ions field emitted into liquid helium, *Physical Review B*, 15 (1977) 2630-2650.
- [144] V.M. Atrazhev, J. Eloranta, N. Bonifaci, H. Van Nguyen, F. Aitken, K. Von Haefen, G. Vermeulen, Excited atoms in cavities of liquid He I: Long-range interatomic repulsion and broadening of atomic lines, *EPJ Applied Physics*, 61 (2013) 24302.
- [145] N.F. Allard, Physical interpretation of the blue shift of spectra obtained by corona discharge in liquid helium, *Journal of Physics: Conference Series*, 397 (1), (2012) 012065.
- [146] M.J. Shaw, M.J. Webster, Excitation transfer in the n=4 levels of He following dye-laser pumping to the 41D level in a flowing afterglow, *Journal of Physics B: Atomic and Molecular Physics*, 9 (1976) 2839-2850.

## Bibliography

---

- [147] K. Von Haefen, A.R.B. De Castro, M. Joppien, L. Moussavizadeh, R. Von Pietrowski, T. Möller, Discrete visible luminescence of helium atoms and molecules desorbing from helium clusters: The role of electronic, vibrational, and rotational energy transfer, *Physical Review Letters*, 78 (1997) 4371-4374.
- [148] K. Von Haefen, T. Laarmann, H. Wabnitz, T. Möller, The electronically excited states of helium clusters: An unusual example for the presence of Rydberg states in condensed matter, *Journal of Physics B: Atomic, Molecular and Optical Physics*, 38 (2005) S373-S386.
- [149] J.A. Hornbeck, J.P. Molnar, Mass spectrometric studies of molecular ions in the noble gases, *Physical Review*, 84 (1951) 621-625.
- [150] R.B. Kay, R.H. Hughes, Excitation transfer in helium, *Physical Review*, 154 (1967) 61-69.
- [151] J.D. Jobe, R.M. St. John, Distribution of excitation transfer in helium, *Physical Review. A* 5, (1972) 295-308.
- [152] H.F. Wellenstein, W.W. Robertson, Collisional relaxation processes for the  $n=3$  states of helium. I. Excitation transfer by normal atoms and by electrons, *The Journal of Chemical Physics*, 56 (1972) 1072-1076.
- [153] H.F. Wellenstein, W.W. Robertson, Collisional relaxation processes for the  $n=3$  states of Helium. II. Associative ionization, *The Journal of Chemical Physics*, 56 (1972) 1077-1082.
- [154] H.F. Wellenstein, W.W. Robertson, Collisional relaxation processes for the  $n=3$  states of helium. III. Total loss rates for normal atom collision, *The Journal of Chemical Physics*, 56 (1972) 1189-1197.
- [155] B. Dubreuil, A. Catherinot, Quenching and excitation transfer in the  $n=3$  helium sublevels in a low-pressure glow discharge, *Physical Review. A* 21, (1980) 188-199.
- [156] S.L. Guberman, The doubly excited autoionizing states of  $H_{2^{+}}$ , *The Journal of Chemical Physics*, 78 (1983) 1404-1413.
- [157] R. Deloche, P. Monchicourt, M. Cheret, F. Lambert, High-pressure helium afterglow at room temperature, *Physical Review, A* 13 (1976) 1140-1176.
- [158] M.A. Gusinow, R.A. Gerber, J.B. Gerardo,  $He_{3^{+}}$  and  $He_{4^{+}}$  in 300°K Helium Plasmas: Their effect on recombination loss of electrons, *Physical Review Letters*, 25 (1970) 1248-1250.
- [159] J.F. Delpech, J.C. Gauthier, Electron-ion recombination in cryogenic Helium plasmas, *Physical Review A*, 6 (1972) 1932-1939.

## Bibliography

---

- [160] F. Aitken, N. Bonifaci, A. Denat, K. Von Haefen, A macroscopic approach to determine electron mobilities in low-density helium, *Journal of Low Temperature Physics*, 162 (2011) 702-709.
- [161] F. Aitken, Z.L. Li, N. Bonifaci, A. Denat, K. Von Haefen, Electron mobility in liquid and supercritical helium measured using corona discharges: A new semi-empirical model for cavity formation, *Physical Chemistry Chemical Physics*, 13 (2011) 719-724.
- [162] F. Aitken, N. Bonifaci, L.G. Mendoza-Luna, K. Von Haefen, Modelling the mobility of positive ion clusters in normal liquid helium over large pressure ranges, *Physical Chemistry Chemical Physics*, 17 (2015) 18535-18540.
- [163] F. Aitken, N. Bonifaci, K. Von Haefen, J. Eloranta, Theoretical modeling of electron mobility in superfluid  $^4\text{He}$ , *Journal of Chemical Physics*, 145 (2016).
- [164] K. Hiroike, Electron energy gaps in a one-dimensional liquid, *Physical Review*, 138 (1965) A422-A428.
- [165] J. Eloranta, N. Schwentner, V.A. Apkarian, Structure and energetics of  $\text{He}_2^*$  bubble-states in superfluid  $^4\text{He}$ , *The Journal of Chemical Physics*, 116 (2002) 4039-4053.
- [166] J. Jortner, N.R. Kestner, S.A. Rice, M.H. Cohen, Study of the properties of an excess electron in liquid helium. I. The nature of the electron-helium interactions, *Journal of Chemical Physics*, 43 (1965) 2614-2625.
- [167] W.R. Hindmarsh, A.D. Petford, G. Smith, P. R., Interpretation of collision broadening and shift in atomic spectra, *Soc. , A* 297 (1967) 296-304.
- [168] Y. Kwon, K.B. Whaley, Atomic-scale quantum solvation structure in superfluid helium-4 clusters, *Physical Review Letters*, 83 (1999) 4108-4111.
- [169] Y. Kwon, P. Huang, M.V. Patel, D. Blume, K.B. Whaley, Quantum solvation and molecular rotations in superfluid helium clusters, *Journal of Chemical Physics*, 113 (2000) 6469-6501.
- [170] W. Guo, J.D. Wright, S.B. Cahn, J.A. Nikkel, D.N. McKinsey, Metastable helium molecules as tracers in superfluid  $\text{He}_4$ , *Physical Review Letters*, 102 (2009).
- [171] P.R. Fontana, Spin-orbit and spin-spin interactions in diatomic molecules. I. Fine structure of  $\text{H}_2$ , *Physical Review*, 125 (1962) 220-228.
- [172] R.E. Zillich, Y. Kwon, K.B. Whaley, Roton-rotation coupling of acetylene in  $^4\text{He}$ , *Physical Review Letters*, 93 (2004).

## Bibliography

---

- [173] R.E. Zillich, K.B. Whaley, Solvation structure and rotational dynamics of LiH in  $^4\text{He}$  clusters, *Journal of Physical Chemistry A*, 111 (2007) 7489-7498.
- [174] K. Von Haeften, S. Rudolph, I. Simanovski, M. Havenith, R.E. Zillich, K.B. Whaley, Probing phonon-rotation coupling in helium nanodroplets: Infrared spectroscopy of CO and its isotopomers, *Physical Review B - Condensed Matter and Materials Physics*, 73 (2006).
- [175] R.E. Zillich, K.B. Whaley, K. Von Haeften, Lineshape of rotational spectrum of CO in  $^4\text{He}$  droplets, *Journal of Chemical Physics*, 128 (2008) 094303.
- [176] S.H. Kim, M.S. Yun, K. Yoshino, Y. Inuishi, DIELECTRIC BREAKDOWN OF SUPERFLUID HELIUM, *Technology Reports of the Osaka University*, 33 (1983) 295-299.
- [177] J.J. Balmer, Notiz über die Spectrallinien des Wasserstoffs, *Annalen der Physik*, 261 (1885) 80-87.
- [178] H. Katsuki, T. Momose, Observation of rovibrational dephasing of molecules in parahydrogen crystals by frequency domain spectroscopy, *Physical Review Letters*, 84 (2000) 3286-3289.
- [179] H. Katsuki, M. Fushitani, T. Momose, Quantum property of solid hydrogen as revealed by high-resolution laser spectroscopy, *Low Temperature Physics*, 29 (2003) 832-837.
- [180] B.D. Lorenz, D.T. Anderson, Infrared spectra of  $\text{N}_2\text{O}-(\text{ortho-D}_2)_N$  and  $\text{N}_2\text{O}-(\text{HD})_N$  clusters trapped in bulk solid parahydrogen, *J. Chem. Phys.*, 126 (2007) 184506.
- [181] H.M. Foley, The pressure broadening of spectral lines, *Physical Review*, 69 (1946) 616-628.
- [182] N. Allard, J. Kielkopf, The effect of neutral nonresonant collisions on atomic spectral lines, *Reviews of Modern Physics*, 54 (1982) 1103-1182.
- [183] G.H. Copley, A comparison of self broadening and shift of helium, neon and argon emission lines, *Journal of Quantitative Spectroscopy and Radiative Transfer*, 16 (1976) 553-558.
- [184] N. Bonifaci, Z.L. Li, A. Denat, V.M. Atrazhev, V.A. Shakhatov, Spectroscopic investigations of corona discharge in high pressure helium at 300 K, *EPJ Applied Physics*, 55 (2011).

## Bibliography\_\_\_\_\_

- [185] P.J. Leo, D.F.T. Mullamphy, G. Peach, I.B. Whittingham, Self-broadening of triplet lines of helium, *Journal of Physics B: Atomic, Molecular and Optical Physics*, 25 (1992) 1161-1173.
- [186] A.A.H. Mohamed, R. Block, K.H. Schoenbach, in: *IEEE International Conference on Plasma Science*, 2001.
- [187] J.R. Roth, Z.Y. Chen, Treatment of metals, polymer films, and fabrics with a one atmosphere uniform glow discharge plasma (OAUGDP) for increased surface energy and directional etching, *Acta Metallurgica Sinica (English Letters)*, 14 (2001) 391-407.
- [188] M. Moreau, N. Orange, M.G.J. Feuilloley, Non-thermal plasma technologies: New tools for bio-decontamination, *Biotechnology Advances*, 26 (2008) 610-617.
- [189] E.S. Paller, J.E. Scharer, R. Cao, K.E. Kelly, in: *IEEE International Conference on Plasma Science*, 2001.
- [190] W.E. Amatucci, D.N. Walker, G. Gatling, E.E. Scime, in: *IEEE International Conference on Plasma Science*, 2004, pp. 118.
- [191] L. Yu, D.M. Packan, C.O. Laux, C.H. Kruger, in: *IEEE Conference Record - Abstracts. PPS-2001 Pulsed Power Plasma Science 2001. 28th IEEE International Conference on Plasma Science and 13th IEEE International Pulsed Power Conference (Cat. No.01CH37, 2001, pp. 350.*
- [192] C.O. Laux, T.G. Spence, C.H. Kruger, R.N. Zare, Optical diagnostics of atmospheric pressure air plasmas, *Plasma Sources Science and Technology*, 12 (2003) 125-138.
- [193] R.H. Stark, K.H. Schoenbach, Direct current glow discharges in atmospheric air, *Applied Physics Letters*, 74 (1999) 3770-3772.
- [194] A.A.H. Mohamed, R. Block, K.H. Schoenbach, Direct current glow discharges in atmospheric air, *IEEE Transactions on Plasma Science*, 30 (2002) 182-183.
- [195] V.I. Arkhipenko, A.A. Kirillov, T. Callegari, Y.A. Safronau, L.V. Simonchik, Non-Self-Sustained Atmospheric Pressure Glow Discharges Maintained by the DC Helium Glow Discharge, *IEEE Transactions on Plasma Science*, 37 (2009) 740-749.
- [196] V.I. Arkhipenko, T. Callegari, Y.A. Safronau, L.V. Simonchik, Atmospheric-Pressure Air Glow Discharge in a Three-Electrode Configuration, *IEEE Transactions on Plasma Science*, 37 (2009) 1297-1304.
- [197] W. Liu, J. Niu, S. Zhao, M. Chai, Study on atmospheric pressure glow discharge based on AC-DC coupled electric field, *Journal of Applied Physics*, 123 (2018) 023303.

## Bibliography\_\_\_\_\_

- [198] S. Kanazawa, M. Kogoma, T. Moriwaki, S. Okazaki, Stable glow plasma at atmospheric pressure, *Journal of Physics D: Applied Physics*, 21 (1988) 838.
- [199] V.A. Pinaev, Formation and energy relaxation of a fast electron beam in cathode regions of a glow discharge in helium, *High Temperature*, 55 (2017) 339-345.
- [200] V.I. Arkhipenko, A.A. Kirillov, Y.A. Safronau, L.V. Simonchik, S.M. Zgirouski, Self-sustained dc atmospheric pressure normal glow discharge in helium: From microamps to amps, *Plasma Sources Science and Technology*, 18 (2009).
- [201] V. Léveillé, S. Coulombe, Atomic oxygen production and exploration of reaction mechanisms in a He-O<sub>2</sub> atmospheric pressure glow discharge torch, *Plasma Processes and Polymers*, 3 (2006) 587-596.
- [202] L. Yu, C.O. Laux, D.M. Packan, C.H. Kruger, Direct-current glow discharges in atmospheric pressure air plasmas, *Journal of Applied Physics*, 91 (2002) 2678-2686.
- [203] K. von Haefen, de Castro, A. R. B., Joppien, Discrete visible luminescence of helium atoms and molecules desorbing from helium clusters: The role of electronic, vibrational, and rotational energy transfer., *Phys. Rev. Lett.*, 78 (1997) 4371-4374.
- [204] M.L. Ginter, R. Batting, Potential-energy curves for the He<sub>2</sub> molecule, *The Journal of Chemical Physics*, 52 (1970) 4467-4468.